Femtosecond ablation and characterisation of microfabricated atom chips

A thesis submitted for the degree of

Doctor of Philosophy

by

Holger Wolff

Centre for Atom Optics and Ultrafast Spectroscopy

Faculty of Engineering and Industrial Sciences

Swinburne University of Technology

Melbourne, Australia

Declaration

I, Holger Wolff, declate that this thesis entitled:

" Femtosecond ablation and characterisation of microfabricated atom chips "

is my own work and has not been submitted previously, in whole or in part, in respect to any other academic award.

Holger Wolff

Centre for Atom Optics and Ultrafast Spectroscopy
Faculty of Engineering and Industrial Sciences
Swinburne University of Technology
Melbourne, Australia

Dated this day, January 3, 2010

Abstract

The idea of "atom chips" is a recent innovative concept in the area of quantum physics which promotes the use of miniaturised surface-based elements for trapping, cooling and ultimate control of ultracold atomic gases in close proximity of the surface. Versatile atom chips generate confining magnetic fields for atoms through the use of current carrying microwires or permanent magnetic materials. These microwires or magnetic films can have structured shapes and profiles to produce sophisticated potentials which are controlled in time and space via the application of external magnetic fields, both static and time-varying up to microwave frequencies. Microfabrication of atom chips and the subsequent characterisation of the physical properties of the microwires and the films and of the quality of the generated magnetic field are of paramount significance for potential applications in chip-based atom interferometry and quantum sensors.

This thesis is focused on the application of a new microfabrication technique, femtosecond laser ablation, for the atom chip construction and on the characterisation of the physical and magnetic properties of microwire structures using scanning electron microscopy (SEM), a newly developed magneto-resistance microscopy (MRM), and ultracold atoms as a sensitive probe of magnetic field irregularities. Femtosecond laser ablation can efficiently remove sub-micron thick layers of dielectric, metal or magnetic materials with micron-scale accuracy. Integration of a nano-positioning translation system with a computer controlled automation allows the production of sophisticated structured shapes of microwires in a simple one-step procedure. The major conditions of the ablation process were studied and optimised for a number of materials including gold and copper. The quality of the fabricated microwires is of utmost importance because the edge and surface roughness causes small translational perturbations in the current flow resulting in axial corrugations of the magnetic trapping potential. This deleterious effect can lead to unwanted spatial break up of the ultracold cloud.Ablated wires were characterised using a SEM and the power spectral density of the edge fluctuations was extracted from data analysis.

An exceedingly good root-mean-square (rms) edge deviation of 16 nm was observed in the range of interest of the spatial periods (1-400 µm).

A direct measurement of the magnetic field created above a straight microwire and a sculptured microwire was performed using a MRM. The development, testing and characterisation of this MRM was recently published in Review of Scientific Instruments [Vol08]. The MRM allowed rapid measurement of the atom chip's magnetic potentials in atmosphere with a resolution and sensitivity comparable to ultracold atom techniques. This thesis also elucidates the process of data extraction from the measurement thus yielding a complete three dimensional map of the magnetic field. In addition, the sculptured wire, which generates an array of axially symmetric double-well potentials, is discussed in detail and a motivation for its development is given in the context of the recent demonstration of a BEC-based sensor of magnetic field gradients [Whi07b].

The quality of the straight and sculptured microwires will be tested by using a Bose-Einstein condensate (BEC) to quantify any residual fragmentation. Embarking towards this goal a new experimental apparatus was designed and constructed to utilise the femtosecond ablated atom chip. This apparatus is based on a dual chamber vacuum system with a low velocity intense atom source (LVIS) used to load the atom chip. The vacuum system, laser system, electronics, atom chip and computer control is detailed in addition to measurements of the LVIS operation and initial results from loading the atom chip. While a measurement of the microwire fragmentation using a BEC has not been achieved during this research the steps towards this goal are outlined in addition to future improvements.

In a related experimental investigation, ultracold rubidium atoms were used to characterise the quality of a magnetic potential generated by a grooved magnetic microstructure. A periodic array of magnets produces an exponentially decaying magnetic field which can repel ultracold atoms and serve as an atomic mirror. Any corrugations in the potential cause deviations from specular reflection and lead to diffuse reflection. Time-of-flight imaging of the ultracold cloud before and after reflection provides quantitative data on the change of divergence of the atomic cloud caused by the diffuse component. Two mirrors of periods 1.5 µm and 3 µm coated with magnetic GdTbFeCo films were investigated and the diffuse component was

fully characterised. The experimental data closely matches the results of numerical simulation. This section of the thesis demonstrates the application of ultracold atoms as a probe of micron-scaled magnetic potentials.

Acknowledgements

I still remember my flight to Australia. Sitting on my window seat, having not much more than what I was wearing and what was in the 20 kg bag in the cargohold of the plane, I was anxiously staring down at half the world passing beneath me to where I would meet new challenges for the first time on my own. I knew just that I would have a scholarship, and (seeming more important at that time) that a hotel room had been booked for me for one week, and everything else went along the Australian motto of 'no worries', quite a scary thought back then. Thankfully, I turned out to be not at all 'on my own', I was greeted by many helpful supervisors, colleagues and new friends. Peter Hannaford I had briefly met before at a conference, and he had invited me, and with great commitment had seen to both the scholarship and that ominous hotel room. And since I arrived, he has supported me with all the help I required, from supporting my visits to conferences in Australia, New Zealand and even Europe, up to this final support where I could even on Sunday visit him to get his latest suggestions for the thesis you are reading now.

At the airport I was greeted by Russell McLean, who took great care to ease my transition into the Melbourne culture, and then continued to support me greatly as my supervisor during the first year of my studies. A whole universe of knowledge and tricks was David Gough, who had worked on the project I was to continue during that year.

From the second year on, I worked on the Atom Chip II experiment, an experiment that started from scratch. I cannot stress enough how much both my coordinating supervisor Andrei Sidorov and my supervisor Brenton Hall have supported me during these studies. Brenton's help guided me through the dark times when it seemed that nothing would work, and I have come to deeply respect his skill with the experiment and his tenacity, both with the experiment and with myself. The most fruitful decisions made on that experiment were results of sometimes heated discussions between Andrei, Brenton and myself, with Andrei committed to always compete with our research in the highest circles of physics research, and

Brenton often pointing out our own expertises and strengths.

As colleagues, I was maybe most inspired by Shannon Whitlock, most focused at work, and still able to relax and enjoy private life. While his primary experiment was the Atom Chip I experiment, he was also engaged in a whole lot of other measurements and research. His experiment skills and his initial characterisations of using femtosecond laser ablation for microwire patterning I greatly appreciate. Together with Michael Volk, whom I also thank, he created the Magneto-Resistance Microscope which I used to map the magnetic fields of the microwires. Talking about ablation, nothing would have gone anywhere without Martin Lowe, who devised the ablation apparatus, and who showed me all the nuts and bolts about that method.

Russell Anderson, also working on the Atom Chip I experiment, was often of great help with his expertise in lasers. Two honours students worked on my experiment, and their contributions I dearly appreciate: Tim Mapperson was responsible for the initial LVIS layout; he made simulations and computations of the trapping and average velocities of the cold atomic beam. Michael Pullen later joined me in the characterisation of the LVIS, and some of the results presented in this thesis have been collected when we two worked together.

Also I need to express big thanks to James Wang, who operates the deposition machine, used to deposit both the magnetic films for the magnetic mirrors and all the metal films for the ablation characterisation, and of course the final atom chip, and also the Atomic/Magnetic Force Microscope. And thank you to Hans Brinkies, who operated the Scanning Electron Microscope.

And of course I need to express immense gratitude to Mark 'Do you have your job request?' Kivinen, the in-house specialist in metal machining, for his exceptionally reliable fabrication of various parts needed for the experiment. I was often surprised how quickly he had finished them.

Finally I need to thank Hans Bachor and the ARC (Australian Research Council) Centre of Excellence for Quantum-Atom Optics for funding the project and inviting me to share my results and participate in the wider scientific world at conferences both in Australia and abroad.

And thank you, Barbara. You are by far the best that ever happened to me.

Contents

1 Introduction **1**

1.1 Ultracold Atoms and Bose-Einstein Condensates 1

1.2 Micron-Scale Atom Chips 2

1.3 Organisation of the Thesis 5

2 Trapping and Cooling of Neutral Atoms **8**

2.1 Atom-Light Interaction 9

2.2 Atom-Magnetic Field Interaction 13

2.3 Magnetic Trapping and Evaporative Cooling 17

2.4 Atom Chips 20

3 Femtosecond Ablation **27**

3.1 Microwires: Basic Principles and Microfabrication Techniques 28

3.1.1 Introduction to Microwires 28

3.1.2 Conventional Microfabrication Techniques 33

3.1.3 Femtosecond Laser Ablation 39

3.2 Femtosecond Ablation Apparatus 42

3.2.1 Femtosecond Laser System 42

3.2.2 Alignment 44

3.2.3 Operation 45

3.2.4 Optical and SEM Characterisation of Femtosecond Ablation . 49

3.3 Concluding Remarks 56

4 Magnetic Field Mapping of Microwires **58**

4.1 Magneto-Resistance Microscopy of a Straight, Femtosecond Ablated Wire . . . 58

4.1.1 The Magneto-Resistance Microscope (MRM) . . . 58

4.1.2 Measuring $\Delta B/B$ above the Straight Wire . . . 64

4.2 Sculpting a Wire with Femtosecond Laser Ablation . . . 70

4.2.1 Finite Element Analysis of the Sculptured Wire . . . 73

4.2.2 Mapping the Magnetic Field above the Sculptured Wire . . . 76

4.2.3 Sensing near-surface forces . . . 78

4.3 Concluding Remarks . . . 81

5 Experimental Apparatus **84**

5.1 Dual Layer Atom-Chip . . . 84

5.1.1 Silver Foil Layer of the Atom Chip . . . 85

5.1.2 Microwire Chip . . . 87

5.2 Vacuum Chamber . . . 90

5.2.1 Basic Principles of Vacuum . . . 90

5.2.2 Preparation of Vacuum Components . . . 93

5.2.3 The Vacuum System . . . 95

5.3 Laser System . . . 97

5.3.1 Frequency Locking Scheme . . . 97

5.3.2 Toptica DLX110 . . . 99

5.3.3 Slave Laser . . . 101

5.3.4 Repump Laser . . . 103

5.4 Computer Control of the Experiment . . . 104

5.4.1 Computer 1: The Control Computer . . . 104

5.4.2 Computer 2: The Acquisition Computer . . . 108

5.5 Low Velocity Intense Source of Atoms . . . 110

5.6 Atom Chip Measurements . . . 118

5.6.1 Magnetic Fields . . . 118

5.6.2 Lasers . . . 120

5.6.3 Detection . . . 122

5.7 Conclusion . . . 127

6 Characterisation of Magnetic Mirror Quality 130

6.1 Basic Principles of Magnetic Mirrors . . . 132

6.2 Magnetic Diffraction Gratings for Atoms . . . 135

6.3 Theory of Atomic Reflection from a Corrugated Mirror . . . 138

6.3.1 Angular Spread . . . 138

6.3.2 End-Effects . . . 140

6.4 Monte-Carlo Simulations . . . 142

6.4.1 Overview . . . 143

6.4.2 Determining the Angular Spread . . . 145

6.5 The Magnetic Mirror Experiment Setup . . . 145

6.5.1 The Magneto-Optical Trap . . . 145

6.5.2 Measurement Procedure . . . 147

6.5.3 Experimental Observations with the 10 mm Mirror . . . 149

6.5.4 3 mm Mirror . . . 152

6.6 Conclusion . . . 154

7 Conclusion 156

7.1 Summary . . . 156

7.2 Outlook . . . 158

A Laser Systems 185

A.1 Magnetic Mirror Experiment . . . 186

A.2 Atom Chip Experiment . . . 187

B Numerical Codes 188

B.1 Monte-Carlo Simulations of the Magnetic Mirror Experiment . . . 188

B.2 Calculating the Ablation Laser Path . . . 194

B.3 LabView C Interface Node to Access the Prosilica GigE Camera . . . 195

C Labview Programs 198

D Technical Drawings 202

List of Figures

2.1 Rb energy levels and laser transitions 11
2.2 Principle of the MOT 15
2.3 Layout of a Ioffe-Pritchard magnetic trap 18
2.4 Schematic of the RF evaporation technique 21
2.5 Visualisation of the magnetic field of an atom chip 23
2.6 Illustration of a Z-Wire 25
2.7 Magnetic field strength of a Z-wire and a bias field 25
2.8 Illustration of a U-Wire 26
2.9 Magnetic field strength of a U-wire and a bias field 26

3.1 Schematic of a fragmenting condensate 32
3.2 Comparison of fragmentation 33
3.3 Flow diagram of atom chip fabrication techniques 34
3.4 Different microfabrication techniques 38
3.5 Ablation setup 44
3.6 Illustration of ablation path 46
3.7 Example of a multi-pass ablation result under the SEM 47
3.8 Ablation depth per pulse versus incident laser fluence 50
3.9 Groove width vs laser power 52
3.10 Femtosecond ablated edge 54
3.11 Power spectral density plot of ablated wire edge 56
3.12 Corners of fs-ablated wires 57

4.1 Schematic of the MRM 60

4.2 Comparison of the magnetic fields at different heights 62
4.3 Improvement of the fitting when considering a finite width wire . . . 62
4.4 Reliability measurements of the magnetic tunnel junction sensor . . . 63
4.5 Magneto-resistance measurement on a straight wire 66
4.6 Magnetic field corrugation of a straight wire 67
4.7 Decay of the magnetic noise with distance 69
4.8 Adiabatic splitting of a double well 71
4.9 Mesh for FEA analysis and calculated B_z map 75
4.10 Properties of the double-well system 76
4.11 The measured magnetic fields of the corrugated wire in all dimensions 77
4.12 Magnetic field component B_z above the corrugated wire 78
4.13 $B_z(z)$ at the centre of the wire 79
4.14 Schematic of an adiabatic splitting experiment 80
4.15 Comparison of microfabrication techniques 83

5.1 The silver layer structure of the atom chip 85
5.2 The microwire layer of the atom chip 88
5.3 Photo of the final atom chip 90
5.4 The schematic of the vacuum system 95
5.5 Dependence of the pressure in the atom chip chamber on the pressure in the LVIS chamber 96
5.6 Schematic of the polarisation spectroscopy locking scheme 99
5.7 Resolving a crossover peak by changing the frequency with an AOM . 102
5.8 Representation of a state in the LabView program 104
5.9 Schematic of an LVIS 111
5.10 LVIS laser cage 114
5.11 Magnetic field of the LVIS coils 115
5.12 Measurement of trapped atom fluorescence 116
5.13 Loading of the LVIS 117
5.14 LVIS fill rate versus pressure 118
5.15 LVIS atom number versus laser detuning 119
5.16 Schematic of a Mirror MOT 120
5.17 The magnetic coils around the atom chip chamber 121

5.18 Diagram of the laser cage system of the MOT lasers 122
5.19 Schematic of absorption measurement 123
5.20 Optical density versus probe laser frequency 125
5.21 Loading curve of the MOT loaded by the LVIS 126
5.22 Measurement of the cold atom beam diameter 127
5.23 Expansion of free-falling cloud 128

6.1 Schematic of a magnetic mirror 132
6.2 Reflection of an atom off a magnetic mirror 134
6.3 Hysteresis loop of the GdTbFeCo magnetic film 136
6.4 Magnetic field strength over the mirror 137
6.5 Schematics of a single atom reflection 140
6.6 Effect of end wire 141
6.7 Comparison of different switching techniques 147
6.8 Transverse velocities parallel to the structure 150
6.9 Transverse velocities perpendicular to the structure 150
6.10 Images of the atom cloud 151
6.11 Result of the computer simulation 152
6.12 MFM scan of the 10 mm chip after the experiment 152
6.13 ToF-measurements on the 3 mm mirror 153
6.14 Fluorescence image of cloud bounced off second mirror 154

A.1 Schematic of the trapping laser setup 186
A.2 Diagram of the laser systems 187

C.1 Frontpanel of the experiment control program 198
C.2 Diagram panel of the experiment control program 199
C.3 Frontpanel of the image acquisiton program 200
C.4 Diagram panel of the image acquisiton program 201

D.1 Diagram of the photodiode circuit 202
D.2 Diagram of the FET driver circuit 203
D.3 Mount of the MOT quad coils 204

Chapter 1

Introduction

1.1 Ultracold Atoms and Bose-Einstein Condensates

At very low temperatures atom clouds exhibit strong quantum statistics effects depending on the atoms being bosons (integer spin, even number of neutrons) or fermions (half integer spin, odd number of neutrons). Bosons, named after Satyendra Nath Bose (1894–1974), follow Bose-Einstein statistics (B-E statistics), which allows several indistinguishable particles to exist in the same quantum state [Bos24]. Fermions, named after Enrico Fermi (1901–1954), obey the Pauli exclusion principle, meaning that no two indistinguishable particles can exist in the same quantum state at the same time, and follow Fermi-Dirac statistics (F-D statistics) [Fer26]. Both the B-E and the F-D statistics differ measurably from the classical Maxwell-Boltzmann statistics only at low temperatures, when the number of particles in a system is of the same order of magnitude as its number of possible states.

An effect that was predicted by Einstein in 1924 [Ein24] is the formation of a Bose-Einstein Condensate (BEC) under certain conditions: A gas of non-interacting indistinguishable bosons in a confining potential will undergo a phase transition at a high phase space density, and a major fraction of these bosons will collapse into the ground state. After the development of laser cooling techniques it finally became possible to create a Bose-Einstein condensate. Eric Cornell and Carl Wieman were the first to observe a Bose-Einstein condensate in 1995 [And95], 70 years after its prediction. Because all atoms in a condensate (often thousands or tens

of thousands) share the same wave function, this 'macroscopic' wave function can be directly observed, which was not possible before. Experiments conducted with Bose-Einstein condensates include the formation and observation of vortices [And00] and solitons [Bur99], as well as interference experiments utilising the wave-particle dualism [And97]. Furthermore, the BEC is often closely compared to laser modes in this regard, that a large fraction of the bosonic photons in a laser mode also form a macroscopic population of a single quantum state of the resonator (though usually not the energetically lowest state). This is an indication that many of the laser experiments can be adopted in BEC experiments, using the quantum wave function of the atoms instead of the electromagnetic waves of the photons. This will greatly enhance the resolution of the experiment as the wavelength of the BEC is orders of magnitude smaller than that of light. Examples of this are double-slit or Michelson interferometer [Wan05b], and Sagnac effect [Kas02] experiments. Additionally, atoms can strongly interact with forces that only weakly interact with light, eg. gravity, which can allow these forces to be measured with high precision [Pet99].

A list of research groups focussing in trapping and cooling of neutral atoms is compiled by R. Grimm on the website of the University of Innsbruck at `http://www.uibk.ac.at/exphys/ultracold/atomtraps.html`.

The importance of this field in today's physics is recognised by the bestowing of the Nobel Prize for both laser cooling (1997: Steven Chu, Claude Cohen-Tannoudji, William D. Phillips) and for the creation of BEC (2001: Eric A. Cornell, Wolfgang Ketterle, Carl E. Wieman). To mimic the steep development of lasers, the BEC creation process needs to be optimised greatly.

1.2 Micron-Scale Atom Chips

One of the developments that are now widely used is the so-called atom chip. Current carrying wires close to the atom cloud (distances vary between a few µm to a few mm) can produce traps with a similar and even higher magnetic field gradient and curvature than those produced by external high current coils, which are comparatively far away [Rei99, Haa01]. These high magnetic field gradients

allow for faster cooling of the trapped atoms as will be shown in section 2.3. As an addition, the design of different wire structures allows very complex geometries, and even the possibility of time-dependent potentials [Wei95, Bru00, Hän01a].

It has been shown that a single current carrying wire, together with a homogeneous magnetic bias field perpendicular to the wire direction, produces a two-dimensional quadrupole field, and by only a small change to the wire geometry a 3D quadrupole field can be produced which is necessary for trapping in Magneto-Optical Traps [Den99a, Haa01]. The high magnetic field values and magnetic field gradients result not from high currents or many parallel wires like in coils, but instead from the small distance to the current and from the fact that the magnetic field strength scales as $1/d$ where d is the distance from the wire.

The small inductance and the small currents in turn allow faster switching and more effective scaling of the magnetic fields compared to external coils. However, the close proximity of the wire to the atoms can also have certain disadvantages, mainly additional heating, additional losses, and fragmentation of the atom cloud [For02a, Kou04, Est04]. Thermal fluctuations in the wire result in a shaking of the trap and induce spin flip losses in the magnetically trapped atom cloud [Hen03, Jon03, Lea03]. Fragmentation, in turn, has been shown to be mainly due to deviations of the current path through the wire due to irregularities of the wire's surface and edges [Est04]. Depending on the fabrication method, these irregularities have a noise spectrum starting with a wave number $k < \approx 0.1 - 10\ \mu\text{m}^{-1}$. The higher this wave number the faster the resulting corrugations in the magnetic field become smoothed out with distance d from the wire ($\propto e^{-dk}$). In conventional BEC machines with only external coils they are therefore not observable.

However, with more elaborate and more sophisticated fabrication techniques the effect that small current path deviations change the potential noticeably has been used intentionally. Complex patterns with multiple wires that can be controlled individually have been used to shape the potential in just the right way for various experiments, eg. beam splitters (eg. [Cas00]) and even a conveyor belt for trapped atoms [Lon03]. The smoother the surface and edges of the microwires can be fabricated, the smaller are the structures that can be intentionally shaped in the potential.

This thesis describes results of the research work on two microfabricated atom optical manipulators, a magnetic mirror for cold atoms and a microfabricated atom chip. The magnetic mirror was fabricated by a company using photolithographic techniques and coated in-house with a perpendicular polarised permanent magnetic sandwich structure of TbGdFeCo and Cr. For an ideal mirror, atoms, trapped and cooled above the mirror and then released, would reflect of this mirror in specular reflection, meaning they would not gain any additional spread or change in their horizontal velocity distribution during the interaction with the mirror. Under these conditions, the mirror could be turned into a diffraction grating and work as a beam splitter for cold atoms. However, final results suggest that the permanent magnetic layer was probably degraded during bake-out and was the main limiting factor for the observed quality.

The microfabricated atom chip was constructed in-house using the femtosecond laser ablation technique. The chip is designed to trap a cloud of cold atoms of a BEC in a tight confinement of an intentionally shaped potential. The chip incorporates two major new ideas: Firstly, it has been fabricated with femtosecond ablation, a technique not previously used for atom chips, but which offers certain advantages over photolithographic techniques conventionally used. These include more rapid prototyping, a simpler approach and resulting therefrom a reduced number of sources for defects introduced during production. Secondly, the potential created by the atom chip is no longer due to the particular path of the wires, but due to the shape of the edges of the microwires themselves. As this was the first realisation of an atom chip fabricated in this manner the quality of the process was investigated thoroughly. With an achieved roughness of the edges of $\Delta x_{rms} < 20$ nm, and a power spectral density that stays mainly flat for k vectors between 0.03 and 1 µm^{-1} and drops off sharply thereafter, it has been possible to pattern the wire edges with step sizes of 1 to 5 µm, in order to produce a current distribution in the wire that results in a potential bottom with a string of double wells.

1.3 Organisation of the Thesis

Chapter 2 of this thesis gives a brief background on the trapping and cooling of neutral atoms. Using the example of a standard technique for producing a Bose-Einstein Condensate (BEC) with ^{87}Rb atoms, it details the path towards the lowest temperatures for atomic clouds produced. After explaining the experimental background of BEC and the interest in this very unusual state of matter, it describes the different cooling stages, and their mode of operation. Finally, the chapter describes the use of so-called 'atom chips', where current carrying wires and sometimes other structures such as permanent magnetic films are located close to the experiment region (less than one centimetre) to achieve high magnetic fields and high field gradients. The basic structures of atom chips, namely the U- and Z-wire configurations, are presented and their respective magnetic fields are given.

Chapter 3 focuses on our new method of fabricating atom chips. It details the requirements for atom chips, the advantages and drawbacks and how physicists attempt to optimise the quality of the microstructure. It presents the common microfabrication technique, using photolithography to transfer the pattern onto the chip, and gives different methods to then physically create the pattern on the chip. In the next section, a new method, based on femtosecond laser ablation, where the whole pattern is written in a single step, greatly simplifying and speeding up the fabrication process is compared to conventional microfabrication techniques. A theoretical background to femtosecond laser ablation is given, before our ablation apparatus is described. In the last section of chapter 3, the femtosecond ablation process is analysed using a scanning electron microscope (SEM). Apart from observing the rate, width and accuracy of the ablation, the edge roughness is measured by stitching 43 successive SEM images together. This way the quality of the ablation is not only analysed through the rms roughness, but also through the search for dominant frequencies in the corrugations by Fourier-transforming the shape of the edge.

In chapter 4 the magnetic properties of the femtosecond ablation-created microwires is directly assessed. The magnetic field produced by the microwires was measured using a magneto-resistance microscope (MRM). The setup of this sensor and the results are presented in the first section of this chapter. It can map

the magnetic field with a spatial resolution of down to 5 µm and has a magnetic field noise of less than 2 mG. This is comparable with the sensitivity of cold thermal atom clouds, which allows to make an initial comparison between the quality of the femtosecond ablated microwires and those created by common techniques. A method is presented describing how to infer the full three dimensional magnetic field from measuring just one of its components at a known height above a planar current.

The second part of this chapter focuses on the intentional shaping of the edges of microwires to generate desired potentials, in this case a string of double wells. Initial qualitative considerations are explained to start the search for suitable patterns, which are then tested and optimised on the computer using finite element analysis. After finalising on a pattern, such a microwire is produced using femtosecond ablation and the magnetic field is tested using the MRM. The result of this measurement is compared to the expected outcome of the finite element analysis (FEA).

In chapter 5 the atom chip experiment itself is presented. Ultra-low pressures are required for evaporative cooling and Bose-Einstein condensation, and this section details how this can be achieved in general, and how it is achieved in this experiment. It details both the sources of pressure, as well as the methods and means to neutralise and/or compensate for them. Our two-chamber setting is presented, the bakeout procedure is explained and the pressure differential is measured. The third section of chapter 5 details the laser system. In order to trap, manipulate, and image the atoms, several laser beams are needed, with varying frequencies and detunings. This section explains the three lasers which are used in this experiment, how they are locked, how their frequency and intensity can be adjusted, and what each beam is used for. The fourth section details the 'Low Velocity Intense Source' (LVIS) of atoms. The idea behind using an LVIS is that the limited capture region, one of the major drawbacks of atom chips, could be compensated by injecting a large amount of trappable atoms directly into the trapping region. The layout and mode of operation of an LVIS is explained, and the implementation of the LVIS in this experiment is presented.

Chapter 6 describes a magnetic mirror using permanent magnetic fields. The idea is that a periodic array of magnets produces a magnetic field whose strength decays

exponentially with distance. Thus cold atoms in low-field seeking states are reflected off such a potential. Furthermore, a magnetic mirror with high specularity could be turned into a diffraction grating by applying a bias field. The chapter details the theory behind the magnetic mirrors. A computer simulation (classical Monte-Carlo simulation) of the mirror is presented. Two mirrors were tested, both showing signatures of diffuse reflection when the reflected atom cloud takes a curved form. Results at simulating that behaviour with Monte-Carlo simulations are presented, and compared to recent publications of diffuse reflection of a BEC from an evanescent wave field [Per06].

Chapter 7.1 concludes the thesis. The major findings of each chapter are recapitulated, and possible further experiments suggested.

Chapter 2

Trapping and Cooling of Neutral Atoms

Atom optics is the area of research which investigates the manipulation of cold atoms by magnetic or electromagnetic potentials which show analogous effects to the manipulation of light (eg. mirrors, beam splitters, lenses, gratings, beam guides). In order to measure these effects, the quantum wave character of the atoms has to be observable, which in turn means that the kinetic energy of the atoms has to be greatly reduced. The mean kinetic energy of atoms in a cloud corresponds directly to their temperature T ($\bar{E} = \frac{3}{2}k_B T$, where k_B is the Boltzmann constant), and therefore the process of reducing the kinetic energy is called cooling. This increases the atom's deBroglie wavelength $\lambda_{dB} = h/\sqrt{2\pi M k_B T}$, where M is the mass of the atom and h is Planck's constant (6.626×10^{-34} m^{2}kg/s). In atom optics, scientists focus on the manipulation of the momentum, position and internal state of atoms in various ways, but most commonly using laser light, static and varying magnetic fields, and radio frequency fields.

This chapter describes the basic forms of such atom manipulations and presents the common atom optics methods for producing a Bose-Einstein condensate (BEC). A BEC is a new state of matter, completely unlike the known states of solid, liquid, vaporous or even plasma [Met99, p. 243]. The BEC phase transition occurs when the phase space density ρ of a cloud of non-interacting bosonic particles becomes sufficiently large:

$$\rho = n\,\lambda_{dB}^3 \geq 2.612\ldots, \tag{2.1}$$

where n is the number density of the gas. An illustrative description of this condition is that the wave-packets of the particles need to overlap. For comparison: Gases at

room temperature and atmospheric pressure usually have $\rho \approx 10^{-6}$; however BEC experiments have to start at ultra-high vacuum where the phase space density is many orders of magnitude lower; for example, for Rb at its vapour pressure at room temperature (10^{-7} Torr) $\rho \approx 10^{-17}$. The effect of Bose condensation is profound: A large number of the bosonic atoms coexist in the lowest bound state of the trap whose wave-function spans a large part of the available volume. Since this allows direct observation of the quantum waves, it is of immense interest in experimental physics.

2.1 Atom-Light Interaction

The interaction between atoms and electromagnetic waves is rather complex, and is given in detail in [Met99]. However, to understand the most important mechanics behind the interaction, several assumptions and simplifications can be made to make the situation more accessible. The first and foremost of these is the assumption of a two level atom in a planar electromagnetic wave: Only two levels exist, a ground state $|g\rangle$ and an excited state $|e\rangle$, with an energy difference $\hbar\omega_a$, and the electromagnetic wave with frequency ω_l has constant phase and amplitude in a plane perpendicular to its direction of travel (z direction). In this case it is usual to define the detuning $\delta = \omega_l - \omega_a$. If the light is on resonance ($\delta = 0$), the electron in the atom oscillates between the ground state and the excited state with Rabi frequency Ω, which is proportional to the amplitude of the electric field and the matrix element $\langle e|r|g\rangle$, where r is the position of the electron.

In the more common case that the detuning is non-zero, two things change: First, the oscillation frequency changes to $\Omega' = \sqrt{\Omega^2 + \delta^2}$, and secondly the amplitude of this oscillation reduces to $(\Omega/\Omega')^2$. During the absorption, a photon of the laser field is destroyed, and its energy raises the electron of the atom to the excited state $|e\rangle$. However, the photon also had a momentum, and to conserve momentum, it is transferred to the atom. Stimulated emission is the opposite of this process: A photon is created in the laser field by transferring the electron from the $|e\rangle$ to the $|g\rangle$ state. The momentum of the photon is taken from the atom, which receives a momentum kick in the opposite direction. If an atom first absorbs a photon out of

one light field, then emits a new one again into the same light field, the momentum of the atom is identical to the one it had before. However, the third of the radiative processes, spontaneous emission, allows an atom in the excited state to decay with a decay rate Γ and to emit a photon in a random direction. Over a large number of such 'light scatterings' from the same light field using absorption and spontaneous emission, a change in momentum is observed: Since the momentum transfers from photon absorption are all collinear, they add constructively, while momentum kicks into random directions from spontaneous emission average to zero. The scattering rate γ_p is derived in various books (e.g. [Met99]), and is given by

$$\gamma_p = \frac{\Gamma}{2} \frac{s_0}{1 + s_0 + 4\left(\delta/\Gamma\right)^2}, \tag{2.2}$$

and gives the number of photons scattered by one atom per second where $s_0 = I/I_{sat}$ is the on-resonance saturation parameter, I is the light intensity, I_{sat} is the saturation intensity, and Γ is the linewidth of the transition, which is identical to the decay rate and therefore shares its symbol.

In our experiment, we use ^{87}Rb, which is the atom of choice for many atom optics experiments as its nature, behaviour and characteristics are well known and favourable for laser cooling and Bose-Einstein condensation. A schematic of the energy levels of interest is given in figure 2.1. The transition used for cooling and trapping rubidium is the $5^2S_{1/2}$ $F = 2$ to the $5^2P_{3/2}$ $F' = 3$ cycling transition of the D2 line. Of particular interest in equation 2.2 is the detuning δ; most atomic manipulation techniques work by adjusting its value. The Doppler shift modifies the detuning depending on the velocity of the atom relative to the direction of propagation of the laser, so that equation 2.2 becomes

$$\gamma_p = \frac{\Gamma}{2} \frac{s_0}{1 + s_0 + 4\left(\delta'(\vec{v})/\Gamma\right)^2} \tag{2.3}$$

$$\delta'(\vec{v}) = \delta + \omega_D(\vec{v}) \tag{2.4}$$

$$\omega_D(\vec{v}) = -\vec{k}.\vec{v}, \tag{2.5}$$

where ω_D is the Doppler shift, which depends on the wave vector $\vec{k}$ of the light field and the velocity of the atom $\vec{v}$. For cooling, the laser light should be red detuned ($\delta < 0$), which means that $\omega_D > 0$ so the atoms have to preferentially absorb photons

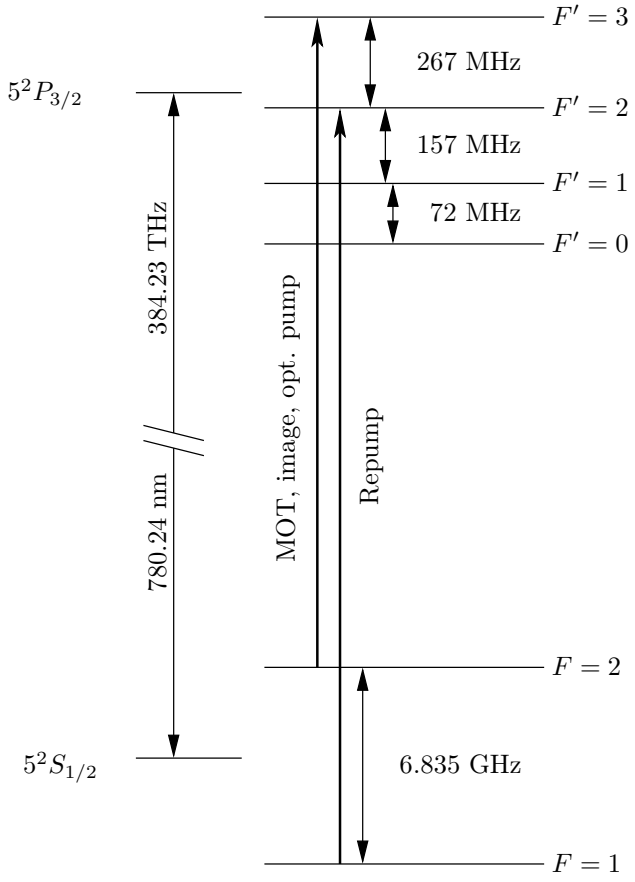

Figure 2.1: Schematic of the energy levels of ^{87}Rb which are important for laser cooling and trapping.

from a counter propagating laser field. An optical molasses uses this effect: Six laser beams, each with the same detuning $\delta < 0$ are guided to intersect from all six mutually orthogonal directions. The detuning is usually set between -1.5 Γ and -4 Γ. A moving atom will, according to equation 2.3, scatter more photons out of a counter propagating beam than out of any other. Regardless of which direction the atom travels, it will always experience a net force which slows it down. As this method uses the Doppler effect for cooling, it is often referred to as Doppler cooling. An important characteristic of optical molasses is the capture velocity v_c, which is the largest velocity an atom may have so that it remains a sufficiently long time inside the molasses region and scatters a sufficient number of photons to be cooled to rest. The capture velocity depends on the fourth power of the diameter of the laser beams and the laser detuning and can be evaluated numerically by modelling atoms with varying velocities and checking which ones remain captured (see [Met99, p.

159f]). The intrinsic heating of the atoms due to the spontaneous emission results in a lower limit for the temperature achievable through Doppler cooling, the so-called Doppler limit T_D.

$$T_D = \frac{\hbar\Gamma}{2\,k_B}, \tag{2.6}$$

In the context of this thesis, the relevant Doppler limit for the rubidium $5^2P_{3/2}$ state is 140 µK. Cold atoms will then perform a random Brownian motion until by chance they leave the volume of the molasses and are lost.

Presence of more than two levels in real atoms plays a role in their interaction with light. The transitions are governed by the frequency of the laser light and a selection rule that states that a single state transition (emission or absorption of a photon) can change the hyperfine level quantum number **F** by 0, 1, or -1. If only a single hyperfine level of the ground state has a hyperfine quantum number within this range, then the atom will always relax into this single state. Such a cycle where the final state after an uncontrolled spontaneous emission is a single known state is called a closed cycle. For the Rb D2 line, such a closed cycle transition is the $F = 2 \rightarrow F' = 3$ transition. However due to the red detuning there is a finite possibility that an atom can undergo an $F = 2 \rightarrow F' = 2$ transition upon absorbing a photon where the rate of excitation is about 1 in 10,000. From there it decays with a probability of around 0.5 into the $F = 1$ state. Once decayed into that state ("dark state"), the molasses laser detuning is far from resonance (> 6.8 GHz) and the atom is no longer cooled on the cycling transition. Considering that every atom undergoes about 200,000 cycles per second, on average it would be pumped into the dark state after about 100 ms. For this reason, a repump laser is added which excites atoms from the $F = 1$ into the $F' = 2$ (or $F' = 1$) state, from where it can decay into the $F = 2$ state and undergo cyclic cooling again. The molasses force is non-conservative; it depends only on the velocity of the atom but not on its position. Thus to trap atoms a position dependent restoration force must be added, which is commonly done using a magneto-optical trap (MOT). This kind of trap was pioneered by Pritchard, Chu and co-workers [Pri86, Raa87].

2.2 Atom-Magnetic Field Interaction

In the presence of a small magnetic field, each of the hyperfine levels splits into 2F+1 magnetic sub-levels noted by $m_F = -F, -F+1, \ldots, F$ which have a linear Zeeman shift of

$$\Delta E_{|F\, m_F\rangle} = \mu_B \; g_F \; m_F \; B \tag{2.7}$$

where μ_B is the Bohr magneton ($\approx 9.274 \times 10^{-24}$ J/T), g_F is the Landé g-factor and B is the magnetic field which defines the quantisation axis. σ^+ circularly polarised light drives the transition between magnetic sub-levels with $\Delta m_F = 1$, whereas σ^- polarised light drives transitions with $\Delta m_F = -1$. Thus in the presence of a magnetic field $\vec{B}(\vec{r})$ and circularly polarised light, the effective detuning δ' now depends on the polarisation of the light and on the strength of the magnetic field:

$$\delta' = \delta + \omega_D(\vec{v}) \pm \frac{1}{\hbar}\, \mu_B\, g_F\, B(\vec{r}) = \delta'(\vec{v}, \vec{r}), \tag{2.8}$$

where the $\pm$ denotes the polarity of the circular polarised light $\sigma^{\pm}$ and $B(\vec{r})$ is the strength of the magnetic field.

This position dependence of the detuning is used in the MOT. A magnetic quadrupole field, produced by a pair of coils in an anti-Helmholtz configuration with its strong axis in the z direction, creates a three dimensional magnetic field gradient, with a field zero the centre of the trap:

$$\left|\vec{B}\,(\vec{r})\right| = A\sqrt{x^2 + y^2 + 4\,z^2} \tag{2.9}$$

$$A = 24\,\mu_0\, \frac{I\; N\; d\; R^2}{\left(d^2 + 4R^2\right)^{5/2}} \tag{2.10}$$

where A is the weak field gradient, usually given in Gauss per cm, I is the current, N is the number of turns per coil, d is the distance between the coils and R is the coil radius. The laser configuration remains unchanged from the optical molasses, having one beam collinear with the z axis (axis of the coils). The x and y axes are typically defined to coincide with the other two molasses beams, since the magnetic field has a rotational symmetry around the z axis. Its beams are circularly polarised as follows: The beams coming from $+x$, $+y$ and $-z$ are polarised σ^+ whereas the beams from $-x$, $-y$ and $+z$ are polarised σ^-. Note that the 'handedness' of the

counter-propagating beams is actually identical. The effect is best explained using a simplified scheme as detailed in figure 2.2: An atom with a trapping transition $F = 0 \rightarrow F' = 1$ with $g_{F'} > 0$ has no magnetic sub-levels in the ground state and three magnetic sub-levels in the excited state. At rest at position $z = z_0 > 0$ ($z = 0$ denotes the location of $B = 0$), its $m_F = -1$ energy level is shifted closer to resonance with the laser frequency, whereas the $m_F = +1$ energy level is shifted further away. This results in the atom predominantly scattering photons out of the σ^- beam, and thus being pushed back into the centre. Similarly, an atom at a position $z < 0$ predominantly scatters photons out of the σ^+ beam and is therefore also pushed into the centre. As in an optical molasses, three of these counter-propagating laser pairs are used for 3D trapping. In the more complex real system of the rubidium D2 line $F = 2 \rightarrow F' = 3$, there are 5 magnetic sub-levels in the ground state and 7 magnetic sub-levels in the excited state. The Lande g-factor g_F is $1/2$ for the ground state and $2/3$ for the excited state, so the effective detuning δ' is different between the different $F = 2, m_F = m \rightarrow F' = 3, m_{F'} = m - 1$ transitions, which are all driven by σ^- polarised light. But the preferred scattering of photons out of a σ^- beam at a position with positive magnetic field and vice versa result in trapping of the atoms regardless of which magnetic sub-state they are in.

A time of flight experiment is commonly used to measure the temperature of a cloud of trapped atoms. This experiment consists of releasing the atom cloud and observing the increase of the diameter of the cloud over time. The atom density of a cooled, thermal cloud projected into a plane follows a two dimensional Gaussian distribution:

$$n(x, y) \propto \exp\left[-\frac{(x - x_0)^2}{2\sigma_x^2} - \frac{(y - y_0)^2}{2\sigma_y^2}\right] \tag{2.11}$$

where x_0 and y_0 are the coordinates of the centre of the cloud, and $\sigma_{x,y}$ is the rms (root mean square) width of the cloud. All four values can be easily obtained by fitting equation 2.11 to an image of the cloud. By repeating the measurement and changing the duration for expansion of the atom cloud, a series of expansions $\sigma(t)$ can be obtained. The measured cloud does not reveal single atoms, but a distribution over many atoms, and therefore statistical methods have to be used, changing the

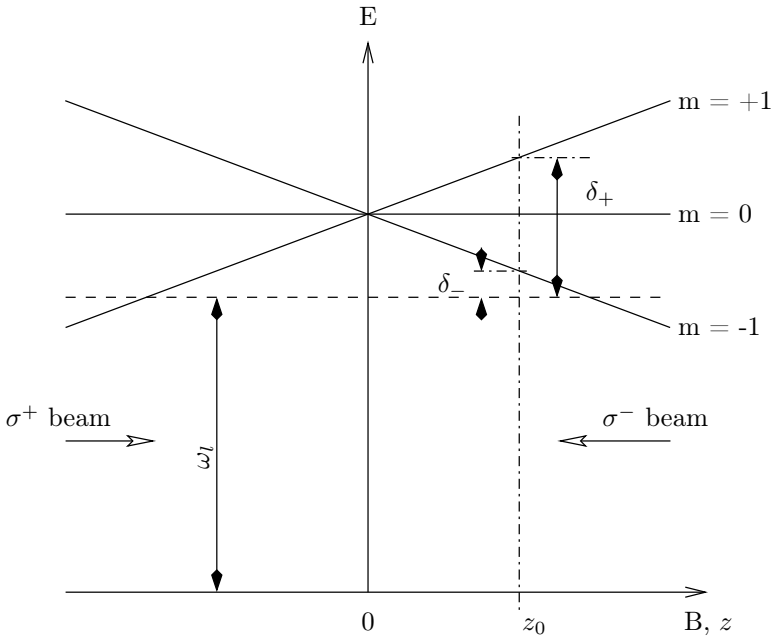

Figure 2.2: Principle of the MOT. The atom is in a magnetic quadrupole field, where the magnetic field is zero at the centre, and linearly changes with distance. The red detuned laser with frequency ω_l corresponds to the dashed line below the energy levels. Because of the Zeeman shift, the m = +1 sublevel increases linearly and is therefore at a positive position z_0 further detuned from the trapping light than the m = -1 sublevel. For this reason, the scattering rate from the σ^- beam (which connects the m = -1 line with the ground state) is considerably stronger than the scattering rate from the σ^+ beam. The opposite is true for negative z, which results in a force pushing atoms towards the centre of the trap.

velocity to its expectation value.

$$\begin{aligned} \sigma^2(t) &= \langle v^2 \rangle t^2 + 2 \langle v \rangle t\sigma_0 + \sigma_0^2 \\ &= \langle v^2 \rangle t^2 + \sigma_0^2 \end{aligned} \tag{2.12}$$

omitting the term $2 \langle v \rangle t\sigma_0$ because $\langle v \rangle$ averages to zero. With $\langle v^2 \rangle$, the temperature can then be calculated:

$$T = \frac{M \langle v^2 \rangle}{k_B} \tag{2.13}$$

where M is the mass of the atoms.

Using this technique, temperatures of laser cooled clouds were observed that were far below the Doppler-limit [Let88]. This groundbreaking observation has since been explained by an effect called Polarisation Gradient Cooling [Dal89]: Counter-

propagating waves interfere in a way that the electric field vectors of each light field at each location are added. If the two lasers have the same frequency, the resulting pattern is stationary in space. If the original waves are co-linearly polarised, their combination is a standing wave with nodes and anti-nodes. If the lasers are linearly polarised in orthogonal directions, the oscillation goes from linearly polarised at 45° to circular polarised to linearly polarised at -45° and circular polarised in the opposite direction, within one wavelength. In the case of the lasers having orthogonal circular polarised fields, as is present in the MOT configuration, the result is a linearly oscillating electric field vector with a direction that rotates around the propagation vector similar to a helix.

It has been shown in [Dal89] that while an atom at rest would be pumped predominantly into the $m_g = 0$ state, an atom moving through such a light field would have a state distribution that slightly lags behind the equilibrium state for each position. An atom moving towards the σ^+ laser beam is populated more in the $m_g = +1$ state than in the $m_g = -1$ state. The $m_g = +1$ state, however, scatters more photons out of a σ^+ beam than out of a σ^- beam and so the atom is slowed down. Atoms travelling in the opposite direction correspondingly have a higher population in the $m_g = -1$ state, and therefore scatter more atoms out of the σ^- beam. While the effect – the preferred scattering of photons out of the counter-propagating beam – is similar to Doppler cooling, the reason for this preferred scattering is different: It relies only on the distribution among the magnetic sublevels for atoms travelling at slow velocities through the standing wave of two counter-propagating circularly polarised beams, and the state's respective preferred scattering from the left- or right-hand circularly polarised beams, and not the Doppler shift. Therefore, the minimum temperature achievable through Polarisation Gradient Cooling is not limited by the Doppler temperature. Instead, sub-Doppler laser cooling is limited by the much lower recoil temperature T_{rc}, which is given by

$$k_B T_{rc} = \frac{\hbar^2 k^2}{2 M}, \tag{2.14}$$

where k is the wave vector of the laser light, and M is the mass of the atom. A short explanation is that the relaxation of the atom due to spontaneous emission imparts a momentum to the atom that can not be eliminated as it is the last effect

in any cycle of the laser cooling process. Even more, satisfying equation 2.1 at the recoil temperature would require a density $n > 10^{13}$ atoms/cm^3. The repulsive force between particles created by re-absorption of previously scattered photons makes such densities impossible to achieve using resonant or near resonant light fields.

To achieve even lower temperatures, the atoms have to be trapped and cooled differently, for example by transferring them into a magnetic trap and cooling evaporatively.

2.3 Magnetic Trapping and Evaporative Cooling

Magnetic trapping of neutral atoms was first suggested in the 1960s [Hee63], but it has taken until after the advent of laser cooling to be first demonstrated [Mig85]. Two main reasons for this are the limited trap depth (even 1 T fields can only hold Rb atoms with a temperature of less than 1 K) and the conservative potential, which means that every atom that falls into the trap thereby acquires enough energy to leave it again. Magnetic trapping utilises the fact that the energy of the magnetic sub-levels changes in the presence of a magnetic field, as described in section 2.2. Sub-levels with $m_F\, g_F < 0$ are called high field seekers, as their energy level decreases with increasing magnetic fields and are therefore accelerated towards locations with large magnetic field values. Similarly, sub-levels with $m_F\, g_F > 0$ are called low field seekers and are repelled by magnetic fields, and therefore can be trapped in local magnetic field minima*. As long as the magnetic moment of the atom can adiabatically follow the direction of the magnetic field, the atom will remain in the same magnetic sub-level and follow the potential which is proportional to the absolute value of the magnetic field at a given point in space.

The simplest magnetic field configuration that has a minimum in three dimensions is a quadrupole field as used for the MOT; however the minimum of the quadrupole field is zero, which means that close to the centre of the trap, the direction of the magnetic field changes very quickly in space. Atoms there can no longer follow the magnetic field vector adiabatically thus flipping their spin. Since these atoms become high-field seekers, they are quickly accelerated out of the trap

*Local magnetic field maxima in all three dimensions, which could trap high field seekers, are impossible to create in free space.

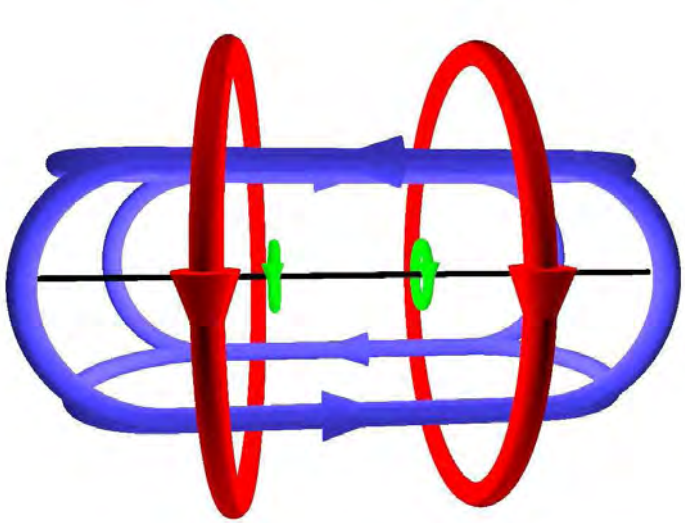

Figure 2.3: Layout of a Ioffe-Pritchard magnetic trap: A homogeneous bias field in the z direction (black rod) is created by a set of Helmholtz coils (red) and overlaid by a 2d quadrupole field created by the four rods of the blue coils. To seal off the ends of the elongated non-zero magnetic field, small end coils (green) are used.

and lost. To minimise these Majorana losses, a magnetic field configuration is chosen where the local minimum has a definite nonzero value. One such configuration is a Ioffe-Pritchard magnetic potential [Pri83]. This consists of a two-dimensional quadrupole field which is superimposed to a homogeneous field in the third direction to allow the trap bottom to be adjusted. A common addition are two 'end currents' that create 1D maxima to seal off the ends of the elongated trap. An implementation of a Ioffe-Pritchard trap is shown in figure 2.3.

As with most potential minima, in a sufficiently small area around this location the magnetic field can be approximated through a Taylor series to second order as a harmonic potential. In such a harmonic potential, the frequency with which a particle oscillates around the minimum does not depend on the amplitude of the oscillation, only on the potential itself and on the particle's mass. This means that this trapping frequency ω_t is constant for all atoms inside the trap, and is therefore a characteristic property of the trap. In elongated traps like the Ioffe-Pritchard trap, the trapping frequencies in the radial and axial directions can be very different, and thus are called the radial trapping frequency ω_{tr} and the axial trapping frequency ω_{ta}. Increasing the trap frequency is also often referred to as making the trap steeper.

Since a magnetic trap is a conservative potential, it is not able to independently cool the atoms or remove their energy without deforming the potential. For this, another method called evaporative cooling is used. Atoms inside a conservative trap will have a velocity distribution given by the Maxwell Boltzmann distribution. This process works by selectively removing atoms which have an energy far larger than the average (those in the 'tail' of the M-B distribution). This can be done by inducing spin flip losses at locations only reachable by atoms with large energies. The remaining atoms rethermalise through elastic collisions, and the cloud gets colder. The time it takes for the atoms to rethermalise depends largely on the number density and the trap frequency.

Once the temperature has equilibriated at a lower value, the cutoff level is reduced again. Typically, the cutoff level is lowered continuously over time in an exponential declining rate. The optimal time constant for this declining cutoff level to retain as many atoms as possible at a given low temperature depends greatly on the experimental conditions of the trap, like the initial number of atoms, but also the background pressure, the steepness of the confinement, the noise in the magnetic potential and many other things. Therefore, the optimal rate has to be found by experimentation and characterisation. If the cutoff level is lowered too quickly, the equilibration can not occur, and the remaining atoms will not be cooled. On the other hand, the evaporation process has to compete with heating and loss processes: The lifetime of atoms in the trap is limited by several factors, the most dominant being background collisions. Even in ultrahigh vacuum, as is used in BEC experiments, a large number of random thermal atoms are present. These can collide with cold atoms in the trap, imparting a momentum to the trapped atoms which easily exceeds the escape velocity of the trap. At the same time, noise in the magnetic coil currents and other effects impart momentum to the trapped atoms, heating them up over time. Experiments therefore strive to achieve long lifetimes and small heating rates to gain time for the evaporative cooling, as well as to confine the atoms in ever tighter traps, which allows quicker rethermalisation and therefore faster evaporation.

The most obvious way to lower the cutoff value is of course to lower the depth of the trap, thereby allowing ever slower atoms to escape. While this is done in some

experiments [Bar01, Luo06], it has a major drawback: As the depth of the trap is lowered, so also is the trap frequency, and this in turn lowers the ability of the cloud to rethermalise. A more convenient way is to keep the trapping potential constant over time, and eject the atoms by other means. This can be done by inducing spin-flip losses. Just like light, electromagnetic waves with a certain frequency can connect atomic levels where the energy difference is equal to the rf frequency, multiplied by Planck's constant h. The photons of the rf field have far less energy than that needed for transitions between the fine or even hyperfine levels. They are high enough, though, to connect different magnetic sub-levels of the ground state with each other. If the frequency of the rf field satisfies the condition

$$\omega_{rf} = \mu_B \, g_F \, |B| \tag{2.15}$$

then the electrons of the atoms will flip into different magnetic sub-levels, quite likely into a non-trapped or even high-field seeking state, at which point they are lost from the trap. Rubidium usually is magnetically trapped in the $F = 2$, $m_F = 2$ state; such an rf field would pump the atoms in the $F = 2$, $m_F = 1$, and then into $F = 2$, $m_F = 0$ state. At this point, they are no longer trapped and fall out of the trap under gravity, or they can be pumped even further into the $m_F = -1$ or $m_F = -2$ states, which are high field seekers. A schematic of this process can be seen in figure 2.4.

By then reducing the frequency, the areas where the atoms are resonant with the rf field move inwards to colder atoms. Since the frequency of the magnetic field can be selected directly, this technique allows full control over the evaporation process.

2.4 Atom Chips

It has been shown that the use of a single wire close to the atomic sample combined with a magnetic bias field can produce very strong magnetic field gradients [Den99b, Rei99]. The $1/r$ dependence of the magnetic field strength of a single wire allows the gradient to be made extremely high even for moderate currents by moving the atoms

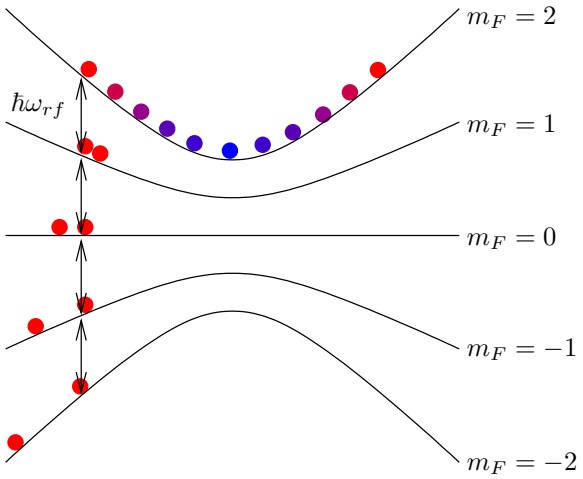

Figure 2.4: Schematic of the rf evaporation technique: An rf field is generated in the trapping region with a frequency that connects the magnetic sub-levels at a certain absolute value of the magnetic field. Atoms which are fast enough to reach such a position are spin-flipped into one of the other magnetic sub-states. If flipped into the magnetically neutral state $m_F = 0$, then they are no longer trapped and fall under gravity out of the trap. If transferred into the magnetic sub-levels with negative $m_F\, g_F$, they are now high field seekers and are actually accelerated out of the trap. Either way, they are lost, and their excess energy with them.

close to the wire itself. Magnetic fields of different sources add up as vectorially:

$$\vec{B}(\vec{r}) = \sum_i \vec{B}_i(\vec{r}) \tag{2.16}$$

The magnetic field produced by a current through a wire in the positive z direction is limited to the x-y plane and is given by

$$\vec{B}_w(\vec{r}) = \frac{\mu_0\, I}{2\,\pi\ |\vec{r}|^2} \begin{pmatrix} -r_y \\ r_x \end{pmatrix} \tag{2.17}$$

where $\mu_0 = 4\,\pi\,10^{-7}$ N/A^2 is the vacuum permeability, and I is the current. By adding a homogeneous bias field $\vec{B}_b = B_b\,\vec{e}_x$, the complete magnetic field is given by:

$$\vec{B}(\vec{r}) = \begin{pmatrix} B_b - \frac{\mu_0\, I\, r_y}{2\,\pi\,|\vec{r}|^2} \\ \frac{\mu_0\, I\, r_x}{2\,\pi\,|\vec{r}|^2} \end{pmatrix} \tag{2.18}$$

The minimum of the absolute value of the magnetic field given in equation 2.18 is zero at $r_x = 0$ and $r_y = r_0$ with

$$r_0 = \left(\frac{\mu_0}{2\,\pi}\right)\frac{I}{B_b}. \tag{2.19}$$

The gradient of the magnetic field at this minimum $\vec{r} = (0, r_0)$ is given by

$$\left.\frac{dB}{dr}\right|_{r_0} = \frac{B_b}{r_0}. \tag{2.20}$$

Increasing the bias field at constant current through the wire moves this minimum closer to the centre and increases the gradient, while increasing the current at constant bias field moves the centre further away and decreases the gradient. To a first approximation, the field around this point resembles a two dimensional quadrupole field with the axes rotated by 45° to the x- and y axis around the z axis. This principle is illustrated in figure 2.5. To prevent Majorana losses (losses due to atoms flipping their spin at zero magnetic field to a non-trappable state), it is necessary to have a magnetic field strength larger than zero at all positions. To ensure this, a second homogeneous bias field B_{OS} can be applied parallel to the wire, so that the absolute value of the magnetic field is greater than zero at all locations. This also changes the potential around the minimum from a linear potential into a harmonic potential with a curvature given by

$$\left.\frac{d^2B}{d\,r_y^2}\right|_{r_0} = \frac{B_b^2}{r_0^2\,B_{OS}}. \tag{2.21}$$

The motion of atoms in the radial direction of this trap is defined by the radial trapping frequency

$$\omega_{tr} = \frac{B_b}{r_0}\sqrt{\frac{\mu_B\,g_F\,m_F}{M\,B_{OS}}}. \tag{2.22}$$

By changing the offset field along the z axis in such a way that it has a minimum in the centre and increases towards both positive and negative z values, the magnetic trap can be closed along this line as well, producing a true three dimensional magnetic trap with strong confinement along the x and y directions and weak confinement along the z direction. A simple method to do this, pioneered by Reichel *et al.* [Rei99], is to use a Z-wire configuration as shown in figure 2.6. For the Z-wire

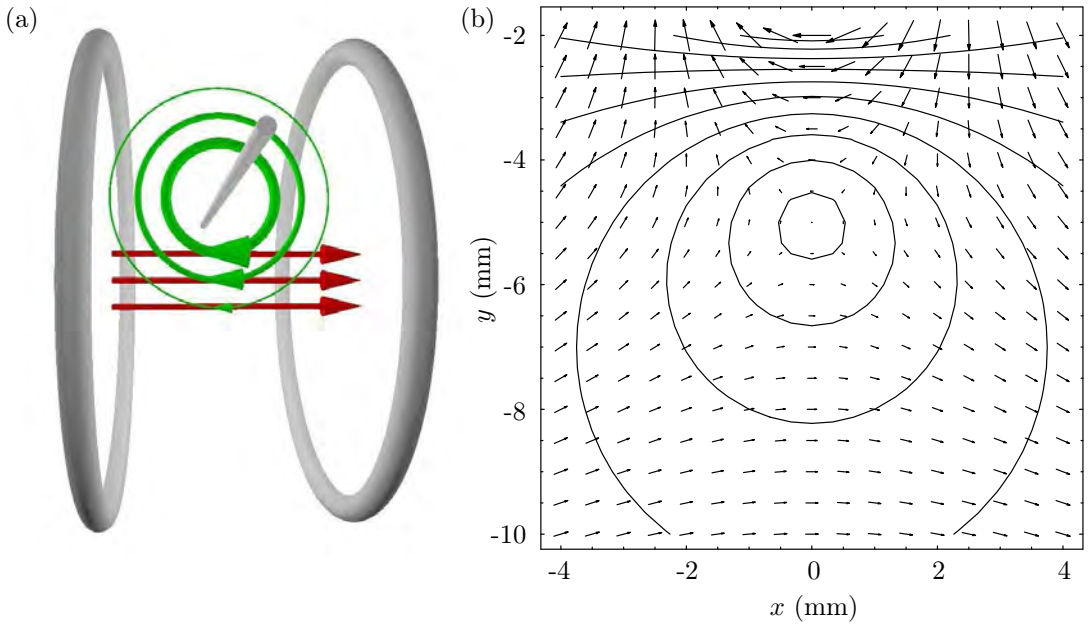

Figure 2.5: Basic idea of an atom chip: (a) A single current produces a circular magnetic field with a strength that decreases as $1/r$ (green). Superimposed by a homogeneous bias field of a certain strength (red), produced for example by a set of Helmholtz coils, these two fields cancel out on one line parallel to the wire. (b) Visualisation of the magnetic field produced by a current (1 A) carrying wire at (0,0) and a homogeneous bias field (0.4 G in positive x-direction) as both $|B|$ contour lines and arrow plot.

configuration, one end of the central wire bends into the homogeneous bias field, the other end bends away from it. The effects of these side-wires add to a magnetic field component in the z direction, thereby increasing the absolute value of the magnetic field above zero. This offset-field increases in strength towards the sides, forming a weak confinement for the trapped atoms. Calculations of the absolute magnetic field strength produced by a Z-wire in combination with a homogeneous bias field in the x direction can be seen in figure 2.7.

A three dimensional quadrupole field is created by a U-wire configuration. It is similar to the Z-wire, except that the second side wire runs anti-parallel to the first side wire, as seen in figure 2.8. The z component of the magnetic fields created by these side wires cancels in the middle between them and increases towards the sides, thereby forming a magnetic field gradient along the z axis. Their non-zero magnetic field component in the y direction, however, slightly shifts the complete magnetic field zero. Calculations of the absolute magnetic field strength produced

by the U-wire in combination with a homogeneous bias field in the x direction can be seen in figure 2.9.

The wires used for these configurations are usually designed to withstand currents of 60–100 A or more to produce tight confinement and effective trapping and cooling of the atoms. For this reason, the cross section of the wires S is is often several square millimetres. While these dimensions are necessary for initial trapping and evaporative cooling, they are unsuited for creating fine micron and sub-micron scale potentials. Microwire atom chips are created to perform such tasks. Their wires often have a cross section of a few tens of μm^2 and can usually conduct less than 1 A. Their limited current and therefore limited trap depth means that atoms to be trapped in microwires have to be pre-cooled to ultralow temperatures. It is therefore not uncommon to have multi-layer atom chips where one layer comprises high current patterns in the U- and Z-configuration, and the other layers incorporate various microwires which create complex potentials. In such a chip, the atoms would be first trapped and cooled in the potentials generated by the high current layer and then transferred into the potential created by the microwire layers. Examples of microwire atom chips include a magnetic conveyor belt for atom clouds [Hän01b], and radio-frequency induced double-well structures for BEC interferometry [Sch05b, Jo07]. A wide variety of applications for atom chips and microwire atom chips are given in [Fol02].

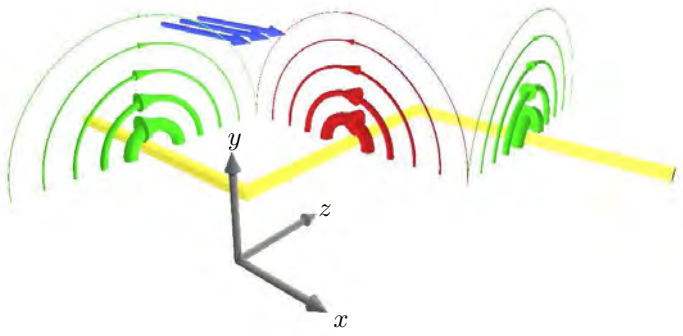

Figure 2.6: Illustration of a Z-wire configuration. The wire itself forms a Z structure, the middle part of which is perpendicular to the bias field (blue). Its magnetic field (red) forms together with the bias field a 2D quadrupole field. The parts of the wires leading to and away from the centre wire produce magnetic fields in the positive z direction above the centre wire, thereby lifting the trap bottom to positive values. Furthermore, the strength of their magnetic fields increases to the sides, thereby sealing the 3D trap.

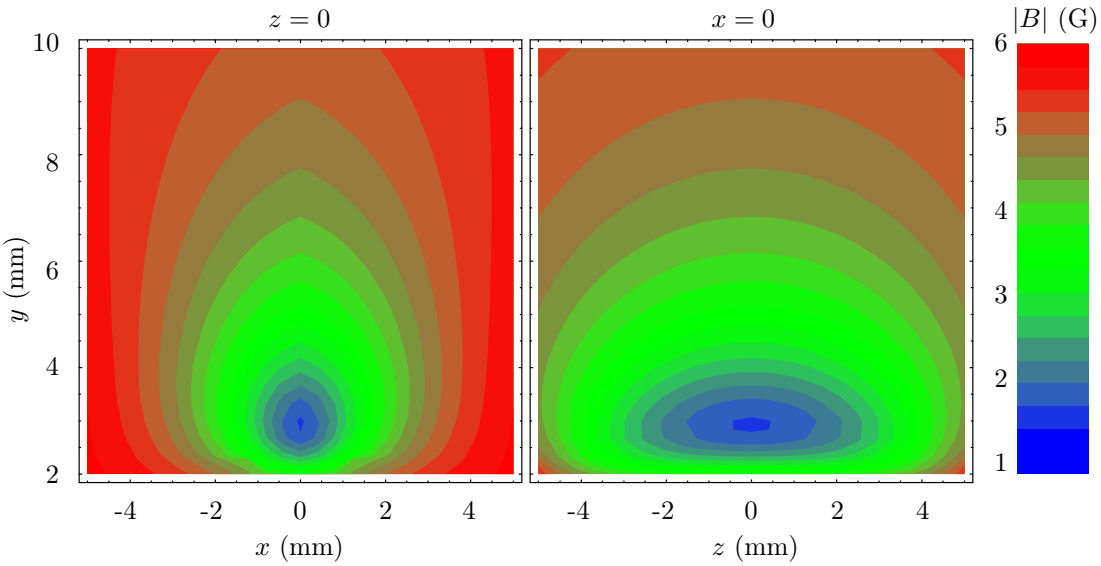

Figure 2.7: Magnetic field strength of a Z-wire and a bias field. The wire in this simulation follows the path ($-\infty$, 0, -5 mm), (0, 0, -5 mm), (0, 0, 5 mm), and (∞, 0, 5 mm), and has a current of 10 A. The bias field has a strength of 5.7 G.

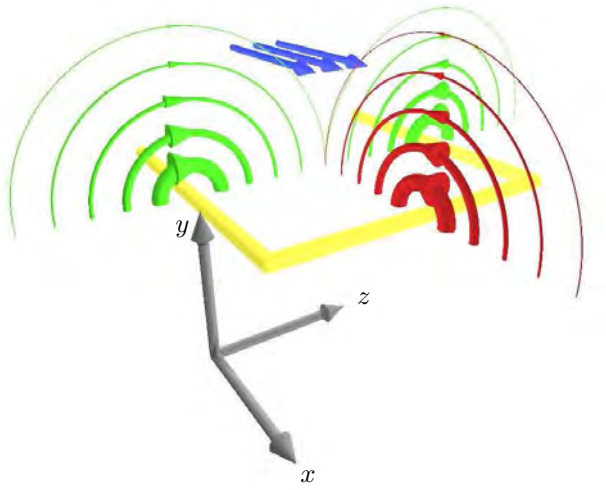

Figure 2.8: Illustration of a U-wire configuration. The wire itself forms a U structure, the middle part of which is perpendicular to the bias field (blue). Its magnetic field (red) forms together with the bias field a 2D quadrupole field. The parts of the wires leading to and away from the centre wire produce a magnetic field gradient in z direction above the centre wire, creating a three dimensional quadrupole field.

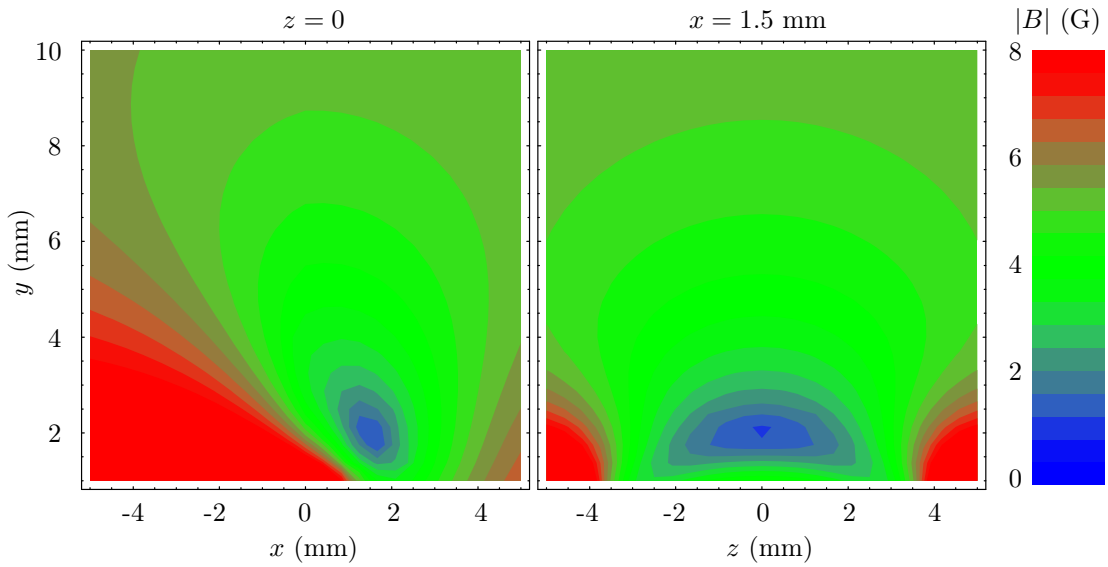

Figure 2.9: Magnetic field strength of a U-wire and a bias field. The wire in this simulation follows the path ($-\infty$, 0, -5 mm), (0, 0, -5 mm), (0, 0, 5 mm), and ($-\infty$, 0, 5 mm), and has a current of 10 A. The bias field has a strength of 5.7 G. As the fields of the wires leading to and from the centre wire produce a field in the negative y direction at the centre, the actual minimum is slightly shifted towards positive x values.

Chapter 3

Femtosecond Ablation: A new tool for Atom Chip Fabrication

This chapter is aimed at the description of major fabrication techniques involved in engineering atom chips [Hän01a, Ott01, Lea02], drawing particular attention to the femtosecond ablation method of writing sophisticated patterns of current carrying microwires to generate magnetic traps for ultracold atoms. While atom chips are a relatively new technology, numerous methods have been pioneered by research groups worldwide to both understand [For02b, Jon04, Est04, Sch05a] and establish [Gro04, Krü07] fabrication processes that deliver the rigorous requirements imposed by atom chips for coherent atom optics with Bose-Einstein condensates. To begin with we introduce the physical effects which govern the *quality* of an atom chip microwire along with an overview of the established benchmarks and methods that have been used to quantify this *quality*. A significant motivational factor underlying the initial pursuit of atom chip development is the large body of knowledge and experience that the semiconductor industry has in the area of lithographic fabrication. Since these methods are currently used by research groups a brief overview is presented which allows our new work to be placed in context regarding the complexity of the overall process.

Following this the physics of femtosecond laser ablation is explored with the assistance of a concise theoretical model that has been elegantly developed elsewhere [Mom97]. The experimental apparatus that was constructed for this project is then introduced with a full description of the femtosecond laser system,

the beam alignment and focussing stages, including the sample vacuum chamber. Then the computer controlled high precision translation stages and their installation required by the apparatus are presented, along with the algorithms used for positioning. To optimise and characterise the ablation thresholds, experiments were performed with a variety of different materials (gold, copper, GdTbFeCo,) and substrates (glass, silicon, sapphire) with the results presented here. Once the optimum ablation conditions were understood, several test microwires were fabricated which were then examined to ascertain their suitability for atom chips. These final tests include a measurement of the wire edge roughness using a scanning electron microscope.

As an additional note it should be mentioned that recently the use of electron lithography for producing atom chips has emerged [Tri08], but this will not be discussed here.

3.1 Microwires: Basic Principles and Microfabrication Techniques

3.1.1 Introduction to Microwires

In Section 2.4 the concept of a conservative magnetic trap for ultracold atoms was introduced along with the typical geometries that have been developed for atom chips, principally the Ioffe-Pritchard type Z-wire trap and the side wire guide [Den99b]. Tight trapping geometries are required in order to achieve high elastic collision rates and runaway evaporative cooling leading to the production of BEC [Dav95, Ket96]. It has been shown that the magnetic field gradient which determines the trap tightness above a wire scales favourably with decreasing wire dimensions at a fixed current density [Wei95]. While initial atom trapping experiments were performed with free standing wires [Haa01], it is straightforward to see that higher currents are achievable when the wires are in good thermal contact with a heat sink to dissipate the ohmic heating of the wire. Combining these two concepts resulted in the idea of what is called an atom chip.

Dimensions and shapes of the microwire on an atom chip are largely determined

by the fabrication technology that is used to create the wire in the first place. However, it is still useful to theorise what an ideal wire would be to understand what limitations the real world imposes on the characteristics of an atom chip. The simplest ideal microwire would be a perfect cylindrical conductor with negligible resistivity such that the magnetic potential could both be solved analytically and would allow for extreme current densities for tight trapping geometries. While the latter could be achieved with low temperature superconducting materials, the complex and expensive cooling systems required for their use were prohibitive for this research. (That said, recently pioneering experiments have been undertaken using superconducting atom chips [Nir06, Ska06].) This leaves metal conductors as the material of choice with atom chip wires being fabricated from gold [Fol00], copper [For02b], silver [Val04], and aluminium [Jon03], with more exotic metal alloys being investigated theoretically [Dik05].

The electrical conductivity σ for the noble metals (silver, copper, gold) used in this research are, in descending order, σ_{Ag} =63.01$\times$ 10^6 S m^{-1}, σ_{Cu} = 59.6$\times$ 10^6 S m^{-1}, and σ_{Au} = 45.2$\times$ 10^6 S m^{-1}. While the electrical resistivity ρ is small, for the microscopic dimensions of atom chip wires this resistivity can easily lead to microwires with resistances of up to 50 Ω.

The typical length of the microwires under investigation was around $\sim$ 5 mm which corresponds to the maximum viewing area of an absorption image in the CCD camera under unity magnification. This leaves the cross section as the major tunable parameter to control the resistance. In real atom chips the microwire cross section is rectangular as opposed to circular, which aids in the dissipation of ohmic heating since one complete side is in good thermal contact with a heat sink. Conventional microwire fabrication utilises vapour deposition of the conductor material and the geometry of this process naturally leads to rectangular wire cross sections. Microwires typically have very small aspect ratios where the height (typically 1 µm) is much smaller than the width (typically 10-20 µm). Thus adding a fixed height to the wire will increase the cross section significantly more than adding to the width. It is therefore important to establish how high a microwire can be made for a given fabrication method.

Once the wire dimensions have been set, the maximum current becomes limited

by the thermal properties of the substrate. If the substrate is unable to dissipate the ohmic heating that occurs during operation (i.e. DC current flow), then the wire temperature can rise rapidly above 400 K where thermal expansion and mechanical stress can result in wire-substrate lift-off or breakage. Both outcomes are undesirable as they can either limit (the former) or terminate (the latter) experiments using that wire. Substrates with a high thermal conductivity λ are thus of interest for atom chip development; however, they must also be electrically insulating and have good bonding properties for the deposited metals.

In this project three substrates were initially used to characterise the laser ablation technique. They were a glass slide ($\lambda_{\text{glass}} = 0.008$ W K cm^{-1}), a sapphire wafer ($\lambda_{\text{sapphire}} = 0.35$ W K cm^{-1}), and a silicon wafer ($\lambda_{\text{silicon}} = 1.457$ W K cm^{-1}) (all thermal conductivity values are given at room temperature). While the poor thermal conductivity of glass is undesirable for use in atom chip experiments, its low cost and abundance proved useful during the initial proof-of-principle experiments of this project. The higher thermal conductivity of sapphire, which is also an optically transparent insulator, is adequate for atom chip experiments. In addition the transparency was advantageous allowing fabrication results to be examined non-destructively under an optical microscope operating in back-light mode.

While silicon has the highest thermal conductivity, the finite resistivity of this semiconductor (160-240 Ω-cm University Wafer, 350 µm thick) requires an insulating layer of silicon oxide to be deposited between the wires and the substrate. This was achieved using a thin film deposition system (Kurt J. Lesker CMS-18) capable of magnetron sputtering and electron beam evaporation in a vacuum with base pressure $< 5 \times 10^{-8}$ Torr. Initially a 25 nm SiO_2 thin film was deposited onto the Si (100) wafer using e-beam evaporation. The accelerating voltage was 7 kV and the evaporation rate was 0.4 nm/s. The distance between the evaporation source and the substrate was 0.7 m. The silicon wafer was held at room temperature and was rotated at 10 revolutions per minute to ensure a uniform coating. This thickness of SiO_2 has been indicated to be an effective insulator for microwires deposited using lithographic methods [Gro04]. However, this was not observed to be the case when insulating grooves were machined using the laser ablation method. Thus for the final atom chip developed during this research project a 400 µm thick sapphire substrate

was used. The combination of a high thermal conductivity substrate and a high electrical conductance metal allows continuous operation of microwires at current densities in excess of 10^7 A/cm^2 [Gro04]. This significantly exceeds the current densities of our existing silver foil atom chip (10^4 A/cm^2) which uses a macroscopic wire of 1 mm $\times$ 0.5 mm cross section [Hal06].

With the development of atom chips researchers were able to produce ultracold atom clouds ($T \approx$µK) or BECs close to current-carrying microwires and observe the interactions between these atoms and the room-temperature surfaces. Initial experiments showed a startling break-up in the shape of the atom cloud as it was moved closer to the wire, and the cloud was described as being fragmented [Kra02, Lea03, Jon04]. Further investigations indicated that this fragmentation was caused by a corrugation of the magnetic potential due to small meandering currents caused by the imperfect, rough edges of a real world wire [Est04, Sch05a, Pau05]. Unlike a geometrically perfect ideal conductor, roughness of the wire edges causes a longitudinal spatial inhomogeneity in the wire resistance, leading to small components of the current to travel perpendicular to the wire direction. These current corrugations produce small ($\sim$ milligauss level) axial magnetic field components $B_{||}$ parallel to the wire and the offset field (in addition to the large azimuthal magnetic field $B_{\perp}$ ($\sim$10 Gauss level) of the wire current), as shown in figure 3.1.

While the magnitude of these modulations of the magnetic field $B_{||}$ is small and can be lowered by reducing the wire current I, this size field is comparable to the energy scales of ultracold atoms. As an example, a magnetically trapped rubidium cloud with atoms in the $F = 2, m_F = +2$ state ($g_F = 1/2$) will experience a Zeeman energy of $\mu_B B$. Using Boltzmann's constant to redefine this energy barrier in terms of temperature yields an equivalence of $\mu_B/k_B \approx 67.2$ µK G^{-1} or 67.2 nK mG^{-1}. While fragmentation appears to be a deleterious effect for atom chips, these experiments suggest a new-found ability to use the ultracold atoms as a probe to measure small scale magnetic field inhomogeneities above microwires and permanent magnetic films [Wil05, Whi07b].

Considerable efforts have been undertaken to reduce the effects of fragmentation to negligible levels. Two approaches have developed simultaneously: i) optimisation

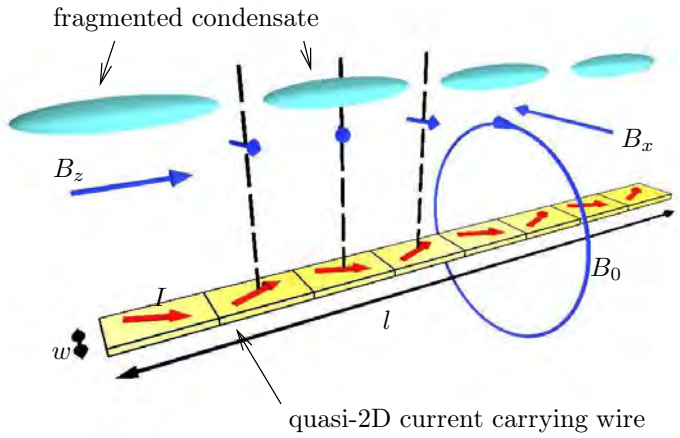

Figure 3.1: Schematic of a fragmenting condensate: Deviations in the current path create components of the resulting magnetic field B_z that are parallel to the wire and therefore corrugate the bottom of the trapping potential given by the offset field such that atoms pool in the local potential minima [Pau05].

of lithographic processes involved in fabricating the microwires [Krü07], and ii) development of novel trapping geometries with high frequency (10 kHz) alternating currents and bias fields [Tre07, Bou08].

The ratio of $B_{||}/B_{\perp}$ is independent of the current but directly reflects the amount of corrugation caused by the wire. Thus it has become one of the figures of merit for determining the *quality* of a microwire and hence the usefulness of a fabrication technique. The state of play of the field is usefully summarised in figure 3.2 which is reproduced here from a recent publication [Krü07]. These data sets were collected using ultracold atom clouds as sensitive magnetic field probes, whereby the extremely low temperature of the cloud can be used to calibrate the potential energy scale of the observed clumps in the cloud [Jon04]. An auxiliary method to using ultracold atoms in determining $B_{||}/B_{\perp}$ was recently demonstrated in our laboratory with a home made magneto-resistance microscope (MRM) which allows in air measurement of the magnetic field above a microwire [Vol08]. This novel MRM augments the cold atom technique as it can measure $B_{||}$ down to 0.1 µT, with a noise floor of $B_{||}/B_{\perp} \sim 10^{-4}$ at heights ≥ 25 µm above a surface.

Another figure of merit that is also useful in determining the quality of the

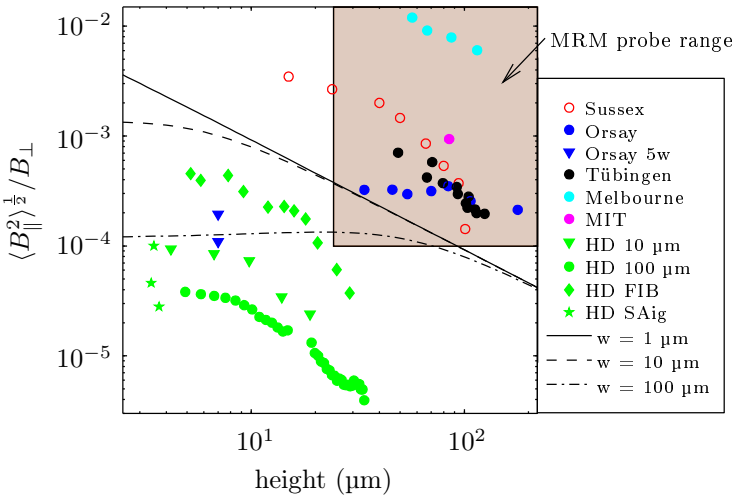

Figure 3.2: Comparison of corrugated components of the magnetic field in different atom chips experiments, reproduced from [Krü07]. The brown hatched area at the top right indicates the measurement space that can be successfully probed with a MRM.

microwire edge is the power spectral density (PSD) of edge fluctuations. This measurement is performed by using a scanning electron microscope (SEM) to acquire a series of high resolution images which are then stitched together via post-processing techniques to form a wire image of around 0.5 to 1 mm in length. Using numerical techniques, elaborated further in section 3.2.4, the PSD of the edge fluctuations is extracted. The PSD yields information on the magnitude and wavelength of dominant edge fluctuations, and the characteristic strength and period of $B_{||}$ at a given distance from the wire can be calculated [Est04]. Since the PSD measurement can be rapidly obtained in less than a day by a commercial SEM it is usually the simplest method available in quantifying the quality of a fabrication method.

3.1.2 Conventional Microfabrication Techniques

When introducing a new technique to perform a given task, it is useful to first elaborate on established methods. This section focuses on the creation of microwires using common microfabrication techniques. A schematic representation of the recipe for conventional microfabrication is shown in figure 3.3, with the multistep lithographic process depicted on the right, and the single step ablation process on the left. The crucial step in the process of writing the wires onto the chip is usually

done by photolithography.

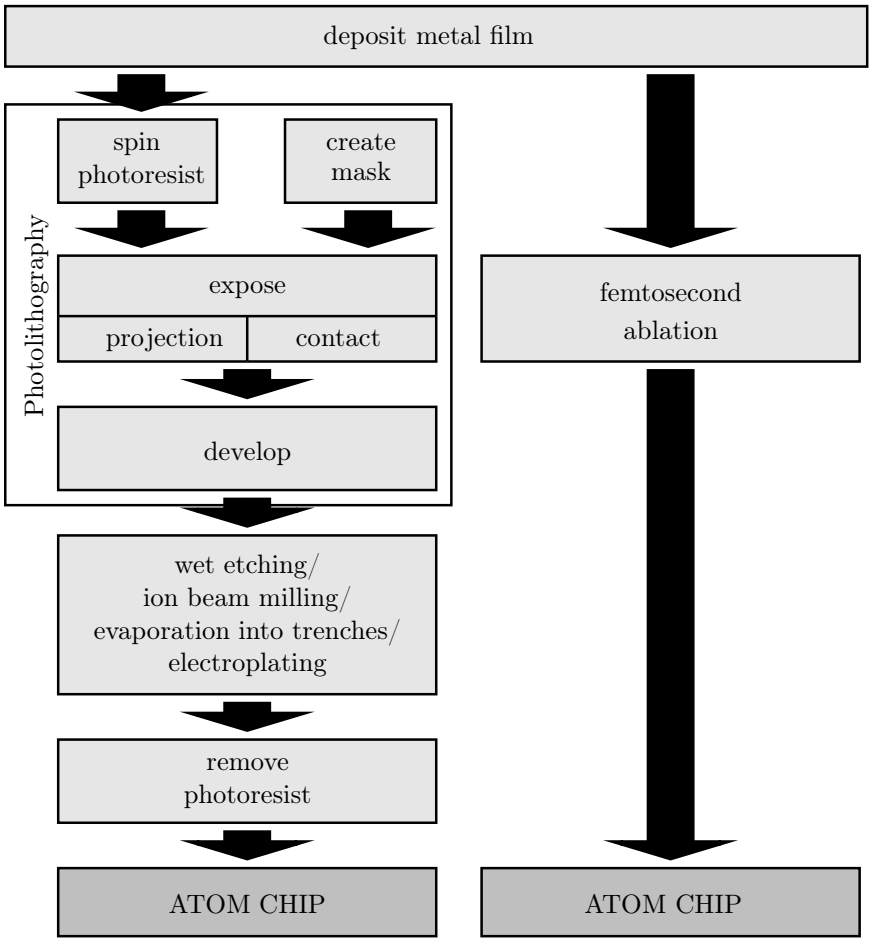

Figure 3.3: Flow diagram of atom chip fabrication techniques: Left: Conventional microfabrication techniques have a complex recipe. Right: Femtosecond ablation is a single step process.

Photolithography

The process of photolithography is based on light-induced changes to a photoresist (usually a light sensitive polymer) by UV light. These changes result in different sensitivity of the exposed and nonexposed parts of the photoresist to developing solvents [Lev03a], with further explanations and specific examples given in [Mad98]. Positive tone photoresists like PMMA (*poly(methylmethacrylate)*) or DQN (a two-component resist consisting of *diazoquinone ester* (DQ) and *phenolic novolak resin* (N)) are weakened by UV exposure, resulting in faster dissolution in the development process, leaving only the unexposed areas remaining. Negative tone photoresists, like

Kodak KTFR, by contrast, become strengthened by the UV exposure, making them more durable during development, thus remaining after the unexposed areas have been dissolved. The photoresist is applied to the sample by spin coating, also called spinning. A liquid solution of photoresist is placed in the centre of a sample which is then spun at high velocity (1.5 – 8 kRPM) such that the centrifugal force spreads the photoresist evenly over the surface. The thickness of the resulting photoresist layer is determined by the polymer concentration in the solution, the viscosity of the polymer, and the rotational velocity. Special photoresists can produce thicknesses of up to 20 µm, and the thickness can be further increased by applying more photoresist onto the surface during the spinning. To evaporate remaining parts of the solution (as opposed to the photoresist), to minimise local stress, and to enhance the adhesion of the photoresist to the substrate, the sample with the photoresist is then usually 'soft baked', or 'pre-baked', for approximately 10 minutes at 75 – 100°C.

The exposed and unexposed areas are defined by a photomask onto which the desired pattern has been written. For microwire atom chips, precision photomasks which are made from quartz plates with a patterned chrome layer are required. The minimum feature sizes of these photomasks are typically 800 nm and are produced by specialised companies [Lev03a], in Australia e.g. the Bandwidth Foundry (`http://www.bwfoundry.com`). The photomask can either be attached directly to the surface of the sample, in which case it will generate a pattern in unity scale, or projected onto the surface by a high-quality optical system, in which case the image of the mask can be miniaturised. The wavelengths used for UV exposure depend on the photoresist, but can range from deep ultraviolet light (DUV, 150 – 300 nm) up to 500 nm. As an example, the maximum sensitivity of PMMA lies at 220 nm and amounts to 150 mJ/cm^2. When the sample has been exposed for the required time to acquire enough energy, the photoresist is developed. This usually consists in immersing the sample in a specific developing solution at a certain temperature for a specific duration. The exposed (positive tone) or unexposed (negative tone) parts of the photoresist are removed by the developer, leaving a relief. After the photolithography, the photoresist forms the exact pattern of the desired chip, either as a positive (when the photoresist remains where the microwires are supposed to be) or negative image (when the photoresist

covers everything except the places where the wires are supposed to be). To transfer the pattern in the photoresist into current carrying wires or other materials, different approaches can be used.

Wet Etching

A common technique for developing positive images is wet etching (figure 3.4a), where a metal-etching solvent (e.g. an aqueous solution of potassium cyanide for gold) is applied to the chip removing metal which is not protected by the photoresist. Afterwards, the remaining photoresist can be removed, leaving the desired wire pattern for the atom chip. Wet etching is highly selective but isotropic meaning that the right acid needs to be selected such that only the metal is removed with the photoresist and wafer remaining. Isotropic means that the dissolving of the material is equally effective in all directions, which in turn results in the metal wires being slowly dissolved from the sides (see third picture from left in figure 3.4a). This issue is of relevance for wires less than $30 - 40$ µm in width or higher than 1 µm.

Dry Etching

Dry etching or reactive ion etching (figure 3.4b) is similar to the wet etching since the positive photoresist protects the metal layer beneath from being removed by a bombardment with ions, typically Ar^+ ions. In a vacuum, the surface is negatively charged while the Ar^+ ions are generated above the sample. The electric potential accelerates these ions towards the surface where their kinetic energy is high enough to eject material. In contrast to wet etching, this is a purely physical process which is anisotropic but not selective: the etching process is effective mostly in one direction, and the wires are not attacked from the side. However; the Ar^+ ions do not discriminate between metal, photoresist or substrate and remove everything. Therefore, the photoresist has to be thick enough to withstand the dry etching longer than the time needed for the film to be completely etched away.

Lift-Off

A technique using a negative photoresist pattern is the so-called lift-off technique. In this case, no metal layer is deposited between the sample and the photoresist.

In its place, a bonding layer that the desired metal can easily adhere to is created (e.g. titanium or chromium). When the metal is then evaporated onto the sample, it will stick to the chip only inside the trenches of the photoresist, forming the wires. The photoresist is then completely removed with warm acetone or isopropanol in an ultrasonic bath [Gro04], taking the unwanted metal along with it. The height of the wires created with this method can not exceed the height of the photoresist.

Electroplating

Similar to thermal evaporation, electroplating can be used to grow wires inside the trenches of a negative photoresist pattern [Est04]. A thin layer of conductive material ('seeding layer') has to be attached to the sample beneath the photoresist layer, so that it can act as a cathode. After the development of the photoresist, the sample is immersed in an electrolyte solution. An anode made from the metal to be used for the wires is also immersed. By applying a current between the anode and the cathode, metal from the anode is ionised and associates with the molecules in the solution. At the cathode (which is to become the atom chip) the process reverses when the metal ions gain electrons from the cathode and deposit on the chip. In this way, the wires are grown inside the trenches. After the process and the removal of the remaining photoresist, the seeding layer has to be destroyed using a short acid bath to insulate the wires from one another.

Post-Processing

While the above mentioned techniques have been used for the fabrication of atom chips, post-processing techniques can also be used to enhance the qualities of the atom chips. For example, in all cases, electroplating can be used to further thicken wires and reduce their resistance, and focused ion beam milling has been used to enhance the edge smoothness of the wires. A summary of the state of play of the field is provided in table 3.1 showing wire dimensions reported, RMS roughness, fabrication method, current density achieved and substrate used.

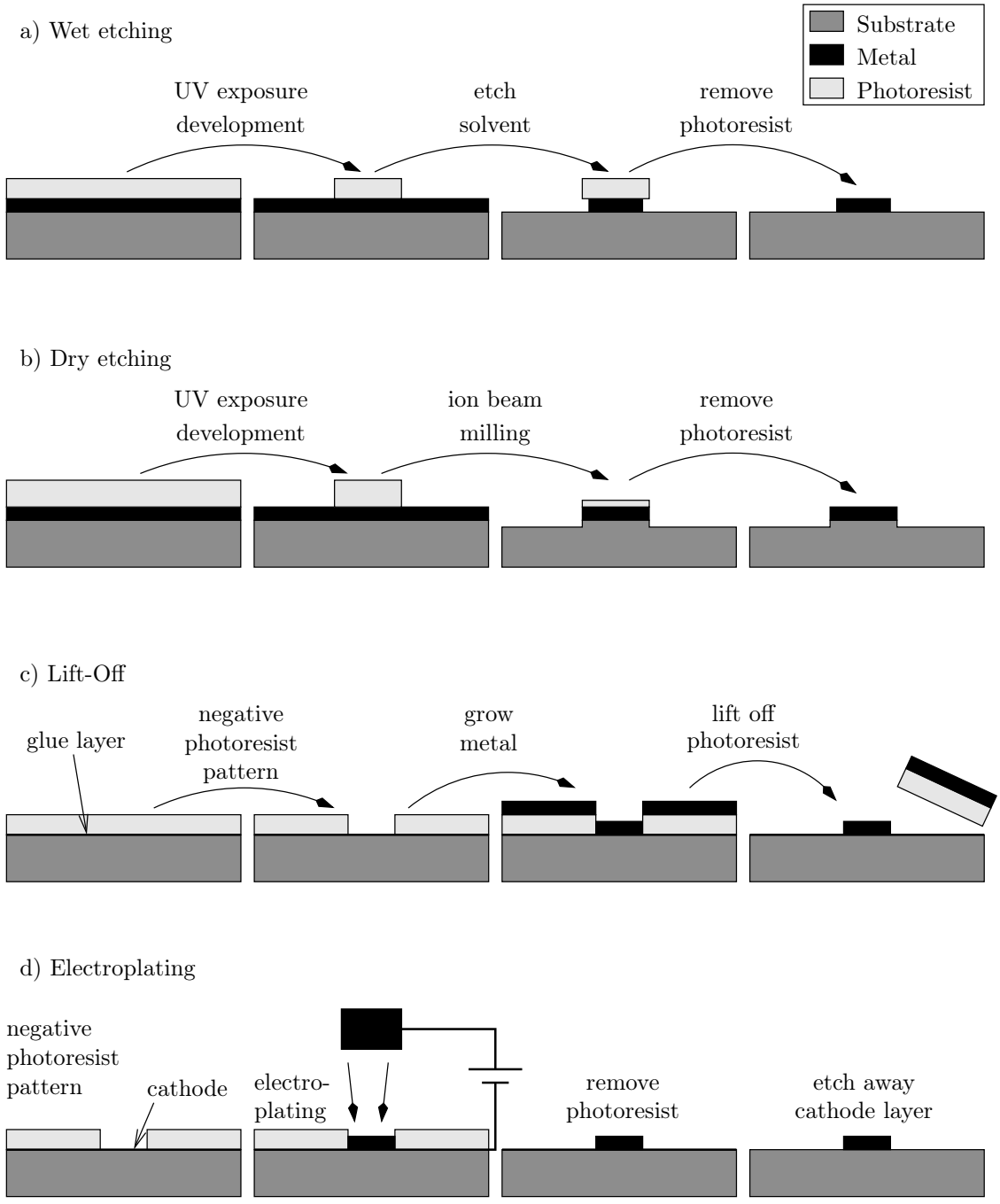

Figure 3.4: Comparison of the major microfabrication techniques using photolithography.

Table 3.1: Comparison of microfabricated atom chips.

Author	Ref	technique	metal	width (µm)	height (µm)	rms deviation	current density
Koukharenko *et al.*	[Kou04]	wet etching	Au	50-100	8.5		
Groth *et al.*	[Gro04]	lift-off	Au	2-100	1-5	50-80 nm	>10 kA/mm^2
Krüger *et al.*	[Krü07]	lift-off	Au		3.1	100 nm	200 kA/mm^2
Esteve *et al.*	[Est04]	electroplating	Au	50	4.5	200 nm	1.3 kA/mm^2

3.1.3 Femtosecond Laser Ablation

The process of laser ablation has a number of possible applications including micromachining, surface cleaning, surface-element analysis, generation of supersonic atomic and molecular beams, and pulsed laser deposition (PLD) of thin films and coatings [Ned04]. In our laboratory we have focused on the development of a one-step micromachining technique for atom chips based upon femtosecond laser ablation of metals to form insulating grooves between conductive wires. Laser ablation describes the effect when a laser pulse transfers its energy into a material faster than the material can disperse it thermally. The local atoms are heated up to far above melting and evaporation temperatures and are subsequently ejected from the bulk material. Clean ablation of metals with nanosecond and picosecond pulsed lasers proved arduous in the past [Wel99]. This is due to the high thermal conductivity of the metal which enables large heat affected zones of molten and re-hardened material to form around the laser impact spot. Recently femtosecond laser systems became available with pulse durations significantly shorter than the thermal diffusion times.

To understand this behaviour, the theory behind the laser ablation of metals has been described with a two-temperature model [Mom97, Wel99]. The laser pulse transfers its energy to the electrons of the metal via an inverse bremsstrahlung process. The energy is then conducted through the material via the thermal diffusion of the electrons and coupled to the atomic lattice. In this simple theory, two partial differential equations that describe the physics are written as [Mom97]:

$$C_e \frac{\partial T_e}{\partial t} = S - \frac{\partial Q(z)}{\partial z} - \gamma(T_e - T_l) \tag{3.1}$$

$$C_l \frac{\partial T_l}{\partial t} = \gamma(T_e - T_l) \tag{3.2}$$

where z represents the direction into the material, $T_{e,l}$ are the temperatures of the electrons and the lattice, respectively, $C_{e,l}$ are the heat capacities per unit volume ($C_e = C'_e T_e$, where C'_e is constant), S describes the laser heating, $Q(z)$ is the electron heat flux, and γ describes the coupling between the lattice and the electrons. S and $Q(z)$ are given by

$$S = I(t)\ A\ \alpha\ \exp[-\alpha z] \tag{3.3}$$

$$Q(z) = -k_e \frac{\partial T_e}{\partial z}, \tag{3.4}$$

where α is the material absorption coefficient, A is the absorbance and k_e is the electron thermal conductivity. The electron temperature increases via the heating process, and decreases due to temperature diffusion into the bulk material and by coupling with the atomic lattice (see eq. 3.1). However, the atomic lattice is only affected by the thermal coupling, and its thermal conductance can be neglected (eq. 3.2). From equations 3.1 and 3.2, two major time scales for equilibration can be defined: $\tau_e = C_e/\gamma$, the electron cooling time, which is usually on the order of 1 ps, and $\tau_l = C_l/\gamma$, the lattice heating time, which is typically much longer ($\approx$ 100 ps). Depending on the pulse duration τ_p, three cases can be observed:

- $\tau_e < \tau_l < \tau_p$ – nanosecond laser pulses: The ablation occurs during the laser pulse. This means that the laser has to traverse a dense cloud of ejected material before arriving at the solid target. This is explained in [Mom96] and will not be discussed in this thesis.

- $\tau_e < \tau_p < \tau_l$ – picosecond laser pulses: The diffusion of the electrons results in a large heat affected zone around the laser impact spot [Mom97], which is disadvantageous for creating fine structures.

- $\tau_p < \tau_e < \tau_l$ – femtosecond laser pulses: In this regime, precise laser ablation with micron and sub-micron resolution is possible. This thesis focuses on femtosecond laser ablation.

In the case of femtosecond laser ablation the process can be analysed by assuming that the electrons are heated first (with $Q(z) = 0$ and $\gamma = 0$), in which case the temperature of the electrons at the end of the (assumed to be square) pulse can be

calculated from equation 3.1:

$$T_e(\tau_p) = \sqrt{\frac{2\,F_a\,\alpha}{C'_e}}\;\exp\left[-\frac{\alpha\,z}{2}\right] \tag{3.5}$$

where F_a is the absorbed laser fluence. Two further simplifications are used to calculate the final lattice temperature: Firstly, the temperature of the electrons is taken to stay constant at its value for the average cooling time

$$\tau_{ec} = \frac{C'_e\,T_e(\tau_e)}{2\,\gamma} \tag{3.6}$$

which is permissible because T_e rises and falls very sharply and can be approximated by a step function. Secondly, the lattice temperature is assumed to rise linearly in time ($T_l(t) = T_e(\tau_p)\;t/\tau_l$), which is permissible as long as $\tau_l \gg \tau_{ec}$. With these assumptions, the lattice temperature may be expressed as

$$T_l(\tau_{ec}) \approx \frac{F_a\,\alpha}{C_l}\;\exp\left[-\alpha\,z\right]. \tag{3.7}$$

For effective ablation, the temperature has to exceed a certain value,

$$T_l\;> \frac{\rho_m\,\Omega}{C_l}, \tag{3.8}$$

where Ω is the specific heat of evaporation per unit mass and ρ_m is the mass density. This in turn gives a sharp threshold for the laser fluence at which the ablation starts. Yang *et al.* gives a more detailed description and differentiation between thermal and non-thermal ablation in [Yan07].

In practise, a femtosecond laser beam is focused onto the metal-coated surface of the sample, thus removing the metal at the specific location. By translating the focal spot over the sample, or more commonly translating the sample under the laser focus, a pattern can be written with many single ablation spots. If the laser, for example, has a repetition rate of 1 kHz and a focal waist diameter of 1 µm, and the sample is moved at a velocity of 100 µm/s, the resulting 10 pulses per diameter create a smooth edge.

3.2 Femtosecond Ablation Apparatus

3.2.1 Femtosecond Laser System

The laser system from which the femtosecond laser pulses are derived consists of a Spectra Physics Tsunami Oscillator and a Spectra Physics Spitfire Regenerative Amplifier. It produces pulses with a wavelength of 800 nm and a spectral bandwidth (FWHM) of 10 nm. The pulse energy exceeds 1 mJ at a repetition rate of 1 kHz. It was first used for femtosecond laser ablation in the research published in [Zha02]. The temporal width of a single pulse τ is measured using a commercial autocorrelation scanner (Positive Light Model SSA-F), which splits the pulse into two spatially separated paths with carefully adjusted same length, before they intersect at an angle $2\,\beta$ inside a BBO frequency doubling crystal. The phase matching condition inside the crystal is such that one photon from either beam must be destroyed to create a photon of the second harmonic wave which then propagates with an angle β to both original beams. As the wave fronts and thereby the positions of the two wave packets are at an angle, the width of the region inside the BBO where the conversion process can happen is directly linked to the width $2\sigma_w$ of the two pulses and the wave front velocity inside the crystal c_{BBO}:

$$\tau = \frac{\sigma_w}{c_{BBO}\sin[\beta]}. \tag{3.9}$$

This width can be simply measured by a CCD chip.

After the autocorrelator the light is split equally into two beams, of which one is used for the femtosecond ablation process and the other is used for a different experiment unrelated to atom optics or microfabrication. The first beam is directed to the ablation apparatus, a schematic is given in figure 3.5. At first, the beam passes a Beta barium borate (β-barium borate or β-BaB_2O_4) crystal. BBO has a wide transparency range (0.19 – 3.5 µm), a high damage threshold, and most importantly a reasonably high nonlinear coupling efficiency (up to six times that of potassium dihydrogen phosphate, or KDP). Though BBO can be temperature controlled for tunable phase matching, in this experiment the crystal was operated at room temperature. The crystal converts the infrared laser light (800 nm) into

near UV light (400 nm) via second harmonic generation with an efficiency of 10%. The advantages of the 400 nm light are a reduction in the diffraction limited spot size, which results in the ability to write smaller structures. A red filter behind the BBO removes the remaining infrared light from the beam. The intensity of the fs pulses can be fine-tuned by rotating an optical neutral density wheel. A microscope lens (Olympus LMPlanFL 50×, N.A. 0.5) focuses the beam down onto the sample. To adjust the distance between the lens and the sample surface, the lens is mounted on a vertical micrometer-screw controlled translation stage. The sample is mounted inside a vacuum chamber. A rotary pump reduces the pressure inside the vacuum chamber to 0.01 mTorr, where the mean free path for collisions ($\Lambda \approx 5$ m) is larger than the chamber size (8 cm by 8 cm, 3 cm height). This allows the ablated atoms to exhibit collision-free motion which results in a significantly reduced debris field about the ablated groove. In addition, the vacuum also reduces the self-focussing effects in air [Pre95, Nol97], so that the focal spot position is independent of laser intensity.

The waist of the laser beam at the focal point ω_0 ($1/e^2$ radius) was measured in vacuum by ablating several grooves with different fluences and corresponding the groove width to the laser fluence to be 0.7 µm (the complete procedure of the measurement is explained in section 3.2.4), resulting in a Rayleigh length of $z_0 = \pi\ \omega_0^2\ /\ \lambda\ \approx 4$ µm. Since it is important for reliable ablation that the surface of the chip is always within the confocal parameter of the beam, special care has to be given to the tilt of the chip with respect to its plane of movement: The distance between the lens and the surface must change by less than 10 µm over the length of the chip (22 x 22 mm^2), which corresponds to a maximum angle between the translation plane and the surface of the chip of 0.4 mrad. Three micrometer screws (80 turns per inch), each with its own counter screw, are used to align the chamber so that the sample is parallel to the plane of translation. To generate the pattern, the vacuum chamber with the atom chip inside is moved by two orthogonal, computer-controlled stepper-motor-operated Newport translation stages (UTM150PP.1) with a resolution of 100 nm. The maximum travel distance of 15 cm exceeds the size of any patterns we want to produce, which are typically of area 25 x 25 mm^2. This allows for the whole atom chip to be patterned in a single writing step.

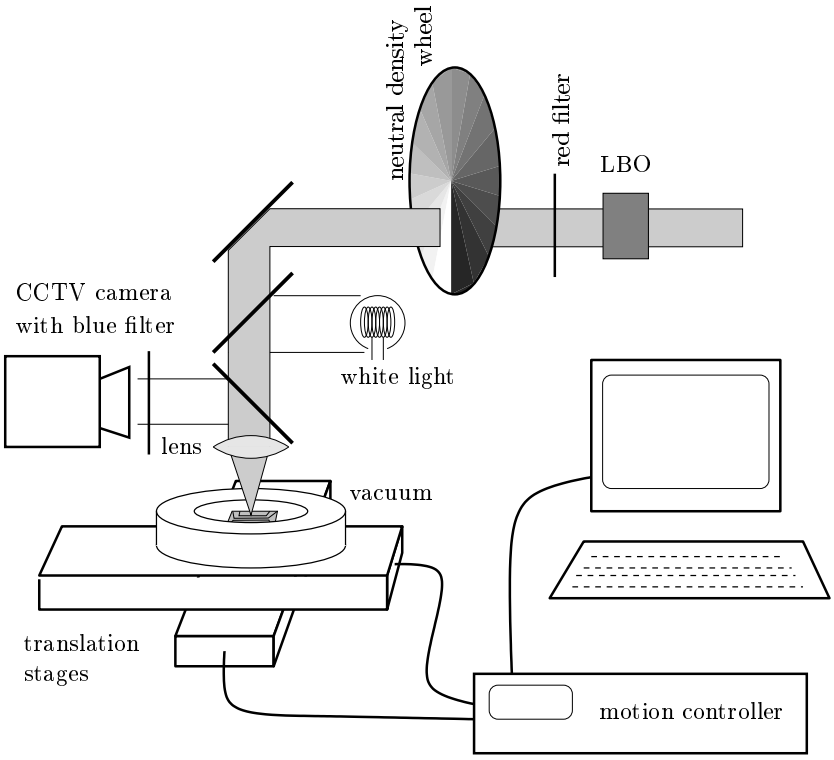

Figure 3.5: The ablation setup: The infrared beam enters the BBO crystal from the right, where UV light is generated via second harmonic generation. The red filter removes the remaining IR light from the beam. A neutral density wheel is used to precisely select the fluence. After the beam is directed vertically down onto the sample, two more glass plate beam splitters (4%) add white light and allow optical imaging using a CCTV camera. The camera is protected from the UV laser light by a blue filter. The beam is then focused by an Olympus LMPlanFL 50× microscope lens (N.A. 0.5) onto the sample inside a vacuum chamber mounted on computer controlled translation stages.

3.2.2 Alignment

To allow real time observation, a white light source and a CCTV camera are also aligned with the beam and through the microscope lens. This is useful for aligning the sample, and for monitoring the ablation process. The first step after placing a sample inside the vacuum chamber is to ensure parallel alignment of the sample's surface with the plane of translation. This is done by adjusting the height of the lens to achieve a reproducible sharp image. This can be the surface of the chip provided there are enough features to distinguish, or the lens is positioned so that an image of the filament of the white light source is focused on the camera. After

having focused the image on one corner of the sample, the chamber is translated along one axis so that another corner is now imaged. This image is focused by tilting the sample using the appropriate micrometer screw of the vacuum chamber. After a few iterations of adjusting the lens height to focus on one side and the chamber tilt to focus on the other side, the sample surface should be parallel along this axis, and the same procedure is repeated for the other axis.

In a similar way, verification of the surface flatness was performed to ensure no bowing of the substrate. Every 5 mm, the sample height is monitored by focussing the surface using the lens' micrometer screw, and the resulting height is read from the micrometer screw's indicator. When using very thin glass samples (100 – 200 µm) the surface height could change by up to 40 µm; however, the final 400 µm thick sapphire substrates had a surface flatness within the uncertainty of the measurement of about 5 µm. After the sample is aligned, it is important to position the lens at the right height for the laser to be focused onto the surface of the sample. At the start a high intensity laser beam is used to ensure ablation takes place even though the surface is out of focus. Then iteratively, the laser intensity is reduced to where ablation is barely observable, and then the focus of the lens is adjusted to maximise the ablation process again. After a few iterations, a minimal laser intensity and best height position of the lens should be found. This adjustment is performed near the centre of the chip to ensure optimum conditions where the quality of the edge is most important, with great care given to the selection of the region so not to interfere with the final operation of the chip.

3.2.3 Operation

Once the sample is aligned, the pattern has to be generated. The first step is to generate a list of points that forms the boundary in an arbitrary coordinate system, which then has to be transformed by translation and rotation to the real coordinates of the sample. For this, the coordinates of one of the corners of the (square) sample is measured, and another coordinate that lies on one of the edges of this corner, preferably more than 10 mm away, is also measured. Knowing which coordinates this corner would have in the initial, arbitrary pattern, the translation vector and rotation angle can be calculated. If the ablation laser were to follow the resulting

pattern, however, the finite diameter $2r$ of the focal spot would result in the edge being ablated to a depth of r. To compensate for this, a new list of points has to be generated that lies always a distance r away from the desired edge (see figure 3.6). The algorithm used to generate these transposed points is given in Appendix B.2.

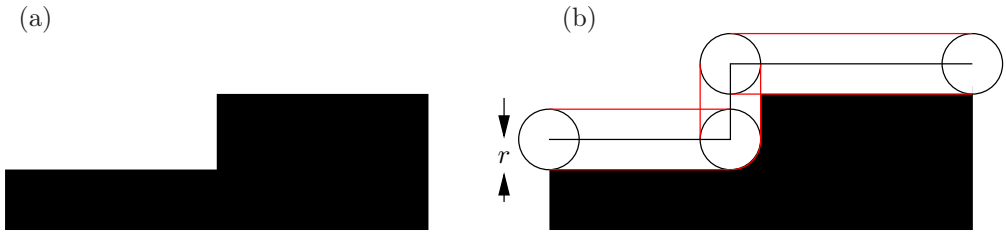

Figure 3.6: Illustration of the ablation path: (a) Desired remaining wire. (b) Actual path of the ablation laser. It has to be transposed by half the diameter of the groove, to achieve the correct edge. Note: The finite diameter does leave round-off effects when ablating inner corners.

In short, for each point in the pattern, it calculates the lines parallel to the lines leading to and away from the point with the right distance, and then calculates where these lines intersect. When using this algorithm, one has to be aware of a few issues:

1. When two successive points are identical, it cannot calculate a parallel line.
2. When the pattern turns back on itself, the algorithm tries to find the intersection of two parallel lines, which would be at infinity.
3. When one point does not have any change in direction (example: (1,0), (2,0), (3,0)) the algorithm may find any point on the resulting lines as the intersection.
4. When the pattern makes a very sharp turn, the intersection point might be a long way off.

The patterns that we used never had a corner sharper than 90°, meaning we could ignore items 2 and 4. However, because the point list was usually computer-generated, we had to make sure that the issues 1 and 3 were addressed. This technique allows the calculation of several ablation pathways for different distances from the desired edge of the pattern. In this way, by ablating on several passes

at different distances, one can achieve wider grooves. This reduces the likelihood of shorts between the wires and the rest of the chip, in addition to reducing the capacitance of the wires which is an important parameter for RF wire currents. Furthermore, this flexibility allows grooves to be cut with different light intensities: lower intensity for smaller spot sizes and finer features and cleaner ablation close to the edge, and higher intensity for guaranteed insulation at faster processing time further apart. An example of this is given in figure 3.7.

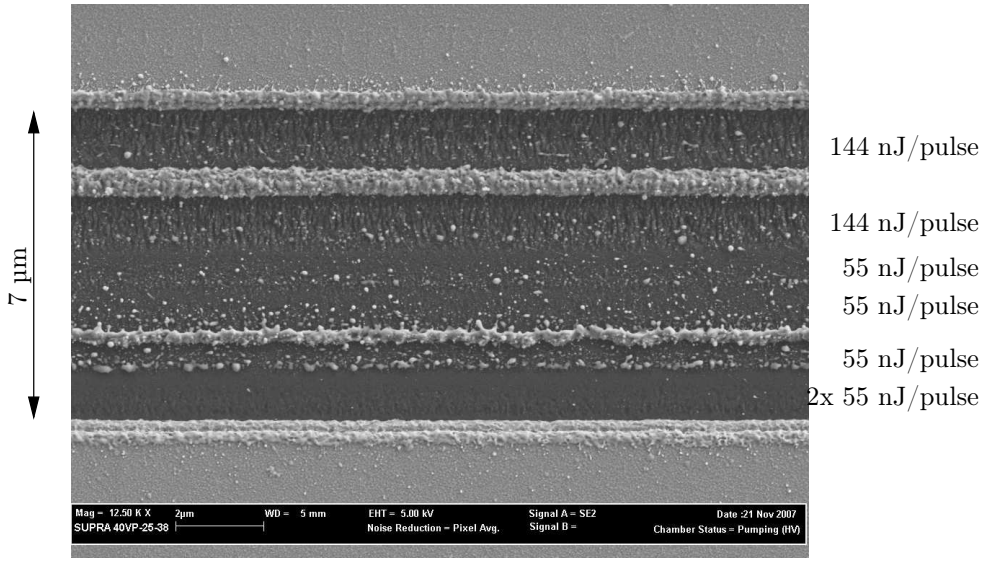

Figure 3.7: A 7 µm wide groove is composed of 7 adjacent 'cuts' with different pulse intensities: The high-power intensities (144 nJ/pulse) ablate the metal completely and damage the surface of the sapphire substrate. The low-power intensities (55 nJ/pulse) create a clean edge with no damage to the substrate; however, some residual metal is left inside the grooves. Ablating twice over the same path (as in the lowest path) results in a clean ablation. Each path was cut with a velocity of 100 µm/s and a repetition rate of 1 kHz.

The controller of the translation stages (Newport ESP 300 motion controller) has a programming mode that is limited but sufficient for this task. An external program transforms the list of points into an ESP compatible command list, similar to the form:

```
5XX
5EP
1HN2,3
1HV0.1;1HA0.5
```

```
1HO
1HL-11.0,11.0;1HW
1HL-9.0,11.0;1HW
1HL-9.0,6.0;1HW
1HL-3.5,0.02;1HW
...
1HX
QP
```

Commands are usually in the form `nCCxx[,yy]` and are separated either by a newline character or by a semicolon. Here `n` is an integer, and `xx` and `yy` are floating point numbers. `CC` is the two-letter command itself. Depending on the command, `n`, `yy` and/or `xx` can be omitted. The algorithm above would first delete a possible program in program slot 5 (`5XX`), and then tell the controller that the following commands are to be stored in the program slot 5, rather than executed immediately (`5EP`). Next, a group is created with group number 1 and translation actuators 2 (as x) and 3 (as y) (`1HN2,3`). This is important because it means that the two actuators are now moved in a synchronised way, so that the result is a straight line with a set velocity and acceleration independent of the direction. The next line sets the velocity to 0.1 units (mm) per second (`1HV0.1`) and the acceleration to 0.5 units per second squared (`1HA0.5`). After ensuring that the actuators are actually switched on (and doing so if they are not) (`1HO`), the important part of the program begins: The command `1HLxx,yy` tells the controller to move the actuators of group 1 in a straight line to position `xx,yy`. It is important to tell the controller to wait for the movement to finish before executing the later commands (`1HW`). In this way, the whole pattern is moved beneath the ablation laser. The last two commands are to delete the group (`1HX`) and to exit the programming mode (`QP`). The program is now stored on the controller and ready to be executed with the command `5EX`. Before starting the program, however, it is important to move the translation stage to a suitable start position and then to unblock the laser.

The ESP 300 occasionally freezes when a long program is stored while a group is assigned. For this reason it is important to always create and delete the groups inside the program, even though the same group will be used for many different programs.

Another issue with the ESP 300 is the limited storage space: only 64 kB are available for all stored programs together. Even 'deleting' specific programs with the `nXX` command does not free the memory that was used by the old program, so that the available memory becomes smaller with successive programming. The command `0XX` can be used to free the memory and delete all programs in the process. More flexible, but also more expensive, is a Newport XPI controller, which is controlled via an Ethernet cable and comes with its own hard disk, a TCL/TK scripting interpreter and National Instruments LabView drivers. For future atom chip development this would be a useful upgrade to simplify the system. It usually takes several hours to ablate a complete atom chip structure, but since the process is mostly automated, it runs with minimal user interaction.

3.2.4 Optical and SEM Characterisation of Femtosecond Ablation

In the established research field of laser ablation a variety of experimental methods have been reported to characterise this process for metals, insulators and of recent interest optically transparent materials. Quantitatively, the parameter of immediate interest is the threshold laser fluence Φ_{th} (units J cm^{-2}), which describes the minimum fluence required to remove material from a given surface. One method, reported in [Nol97], measured the number of fs pulses required to ablate a hole in copper of fixed depth (30 µm) as a function of pulse energy. The results of this study, reproduced here in figure 3.8, show the ablation depth (nm) per pulse plotted versus fluence (mJ cm^{-2}). In this plot two regions can be readily identified, i) at low Φ the amount of material removed per pulse is determined by the optical penetration depth of the material (low gradient fit) and ii) at high Φ (steep fit) indicates a significantly larger energy penetration depth with a correspondingly higher Φ_{th}. Qualitative differences in the material surrounding the hole were also observed for the two ablation regimes, i) the low Φ region showed no heat affected zones while ii) the high Φ region showed considerable collateral damage about the hole. While this characterisation technique was not completely compatible with our aim of ablating thin films (100–500 nm) it shows promise that long pulse trains may be used to ablate to a very large depth (high aspect ratio microwires). This ability stems from

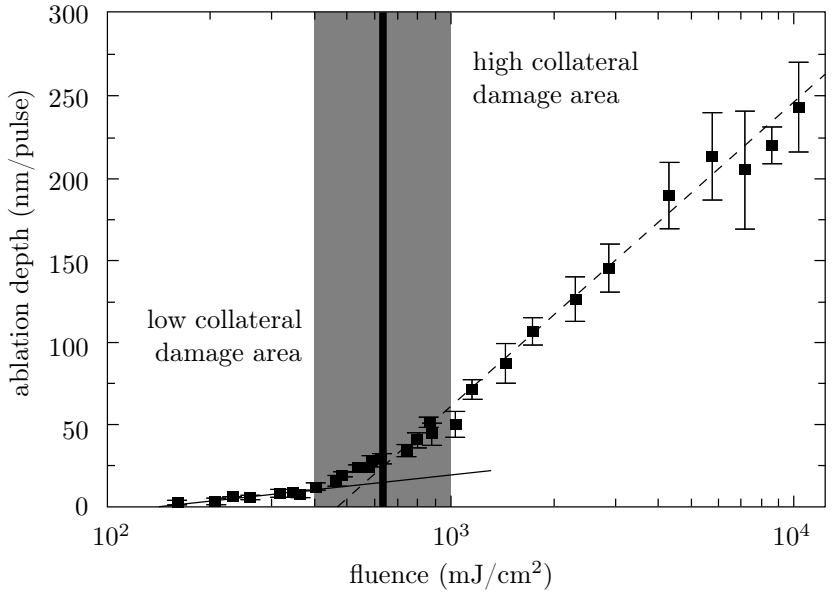

Figure 3.8: Ablation depth per pulse versus incident laser fluence [Nol97]. This characterisation method identifies two regions of ablation. At low fluences, the ablation depth per pulse is slow, but the collateral damage is low. At higher fluences, the ablation depth increases, but at the cost of larger collateral damage areas. At the greyed intermediate area, the ablation cannot be reliably attributed to either regime.

the low repetition rate of fs lasers (1 kHz) such that all thermal energy from the preceding pulse is diffused by the material before the next pulse arrives (i.e. no heat build-up) [Cer07]. Another characterisation technique, reported in [Bon01], studied the ablation morphology of a crater and determined that the square of the diameter of the ablated crater was logarithmically dependent on the laser fluence. We have adapted this technique to quantify the ablation of grooves as opposed to craters, where the square of the diameter of the groove has the same functional dependence on Φ.

This is achieved by assuming the laser beam profile is Gaussian and that the spatial fluence profile Φ(r) is given by

$$\Phi(r) = \Phi_0 \exp\left[-\frac{2r^2}{\omega_0^2}\right], \tag{3.10}$$

where r represents the distance from the beam centre, ω_0 represents the radius of the Gaussian distribution and Φ_0 denotes the maximum laser fluence at the cross

sectional surface. Φ_0 is related to the pulse energy E_{pulse} by

$$\Phi_0 = \frac{2\,E_{\text{pulse}}}{\pi\ \omega_0^2}. \tag{3.11}$$

Rearranging this equation with r^2 as the subject yields

$$r^2 = \frac{\omega_0^2}{2}\ \ln\left[\frac{2\,E_{\text{pulse}}}{\pi\ \omega_0^2\ \Phi(r)}\right]. \tag{3.12}$$

Defining the groove diameter D as $2 \times r$ and fixing $\Phi(r) = \Phi_{th}$ yields the following equation for the square of the groove width as a function of pulse energy

$$D^2 = 2\omega_0^2\left(\ln\left[E_{\text{pulse}}\right] + \ln\left[\frac{2}{\pi\omega_0^2\Phi_{th}}\right]\right). \tag{3.13}$$

Plotting D^2 versus the log of the pulse energy yields a straight line function which can be numerically fitted to extract the focal spot size (from the slope) and the threshold fluence (from the horizontal intercept where D^2 goes to zero). Experimentally this is achieved using the thin film deposition system, described previously (section 3.1), to sputter a variety of materials (Au, Ag, Cu, Ni, Cr, GdTbFeCo, SmCo and CoCr) that are of interest to atoms chips. Each sample consisted of a thin film of ∼100 nm thickness deposited onto a glass microscope slide (1 mm thickness). A series of parallel grooves were then ablated in each material with successive increases in the laser intensity for each new groove. For these experiments the translation stage speed (100 µm/s), the laser repetition rate (1 kHz) and the focal spot size (0.7 µm) result in approximately 7 pulses being incident upon the sample at any given position along the groove. To measure the widths of the grooves each sample was imaged with an Olympus microscope using a 100× optical zoom in both transmission and reflection mode and a Gaussian function is fit to each groove. An example of this data is shown in figure 3.9b containing a microscope image of a series of lines ablated in chromium. By extracting the Gaussian widths from the numerical fits and plotting their squares as a function of the log of the pulse energy (E_{pulse}), a straight line functionality is observed (figure 3.9a). E_{pulse} is determined by measuring the average laser power after the microscope lens (Coherent Field Max) for each groove intensity, and multiplying by 1000 (1 kHz^{-1}) to record the average pulse energy. A linear fit

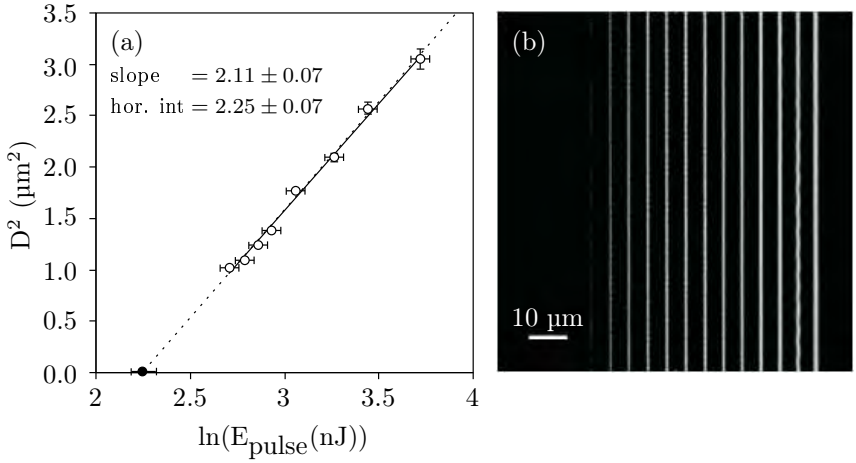

Figure 3.9: (a) Squared diameter D^2 of the ablated lines in 100 nm thick Cr versus the natural logarithm of the pulse energy. The data points (open circles) and errors are obtained using nonlinear regression to fit the Gaussian profiles to the ablated channels imaged using a microscope in a transmission mode, shown in (b). To characterise the ablation process for each material, the minimum beam width ω_0 and the threshold fluence Φ_{th} are extracted from the straight line fit of equation 3.13.

to the data is given by equation 3.13.

To summarise these measurements, the ablation threshold fluence Φ_{th} is tabulated for all the materials studied in table 3.2. In this table rows are ordered by

Table 3.2: Threshold fluences for different materials

Material	Φ_{th}(N=7) [J/cm^2]	ξ	Φ_{th}(N=1)	results from literature
Silver	1.54			
Nickel	1.17	0.96	1.2	
Copper	0.93	0.92	1.0	
TbGdFeCo	0.91			
Chromium	0.87			
CoCr	0.70			
Gold	0.52	0.92	0.608	0.6 [Kau94]
SmCo	0.46			

decreasing threshold fluence with the raw data quoted in column 2. To compare this data with others reported in the literature the average number of pulses used in the ablation must be accounted for, in this case N $\approx$ 7. Initially this may appear suspect as it was claimed that fs ablation is a quick process and the material does not have any memory of the previous pulse, as elucidated in [Cer07]. Hence the threshold for 1 pulse should be the same as for 100 pulses, if the energy is just below threshold,

the material will not ablate regardless of the number of pulses. However, this is just a zero-th order approximation, and some observations ([Güd98]) have indicated that a material dependent 'incubation' effect, or memory of the previous pulse, can alter the observed accumulated threshold fluence Φ_{th}(N) with the following power law [Jee88],

$$\Phi_{th}(N) = \Phi_{th}(1) \times N^{\xi-1} \tag{3.14}$$

Here the exponent ξ is a material specific parameter which appears as a result of the storage cycle of thermal stress-strain energy induced by a laser pulse, where ξ=1 indicates no incubation. A literature search allows a variety of values of ξ to be reported for the table of materials with the trend that for metals this parameter is usually close to unity. In column three we report $\Phi_{th}(1)$, corrected for incubation effects. However, due to the small value of N this only represents on average a 15% departure from the zero-th order model. Column four shows values for $\Phi_{th}(1)$ reported in the literature along with their references.

The higher threshold fluence of copper compared with gold allows more control over the ablation region, making it easier to generate smoother edges. However, as the atom chip is also to be used as a surface MOT, it needs to exhibit high and reliable specular reflection of the MOT beams, a requirement which strongly favours gold over copper. For this reason it was decided to use a dual layer structure of a 300 nm thick copper layer with an 80 nm thick gold layer on top for protection and reflectivity on a 400 µm thick sapphire substrate for thermal conductivity.

To verify the edge roughness of femtosecond ablation of this particular structure, a straight wire was cut into such a sample, and the resulting groove was observed with a scanning electron microscope with a magnification of 12,500, giving images with a resolution of 16.4 nm per pixel. One of these images is shown in figure 3.7. Forty-two of these images were combined manually using the image processing program 'The Gimp' with minimal overlap to create a continuous image of the edge over a length of 630 µm, as seen in figure 3.10. From these images it can also be seen that the ablation edges of the gold and the copper layer are at slightly different locations. This is a result of the lower ablation threshold of gold, which means that at a certain distance from the centre of the ablation laser, the fluence is

high enough to ablate gold, but not high enough to ablate copper. This effect could also be used to construct multi-layer chips out of different materials. This combined image is of considerable size (about 40,000 pixels in length); so the height of the image was constrained to 80 pixels, as the edge is the only feature of interest for this measurement and always remains within these bounds.

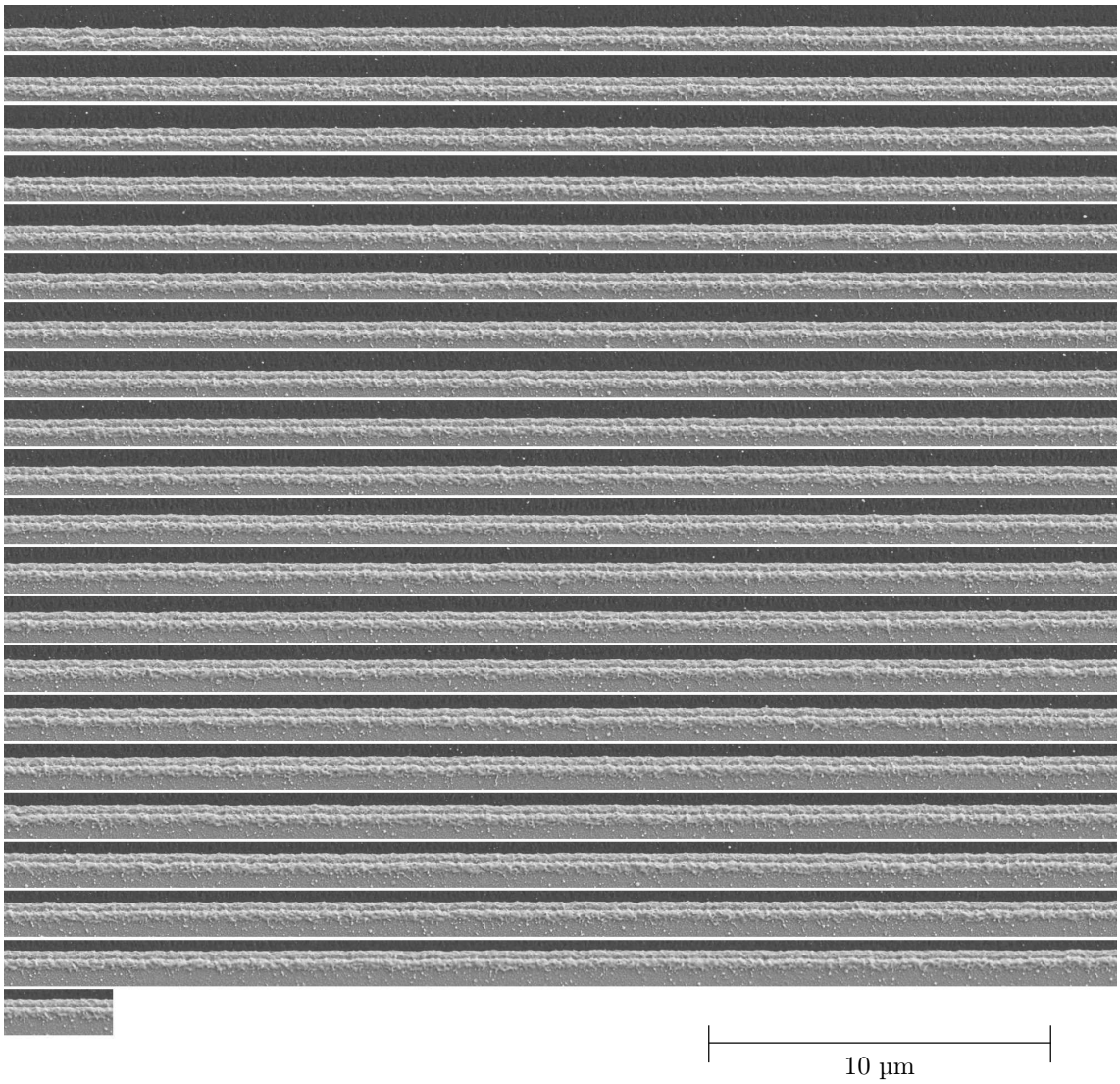

Figure 3.10: Femtosecond ablated edge: SEM images were stitched together to show the edge of a femtosecond ablated wire. The whole length is 650 µm.

An edge-finding algorithm was employed to find the position of the (copper) edge y_n at every pixel column n for the entire edge using the brightness of each pixel. Subtracting a linear fit through all of these values results in the deviation of the edge from the optimum straight line at each pixel column. From this the rms width of the edge fluctuations Δy_{rms} was calculated to be 16 nm, which coincidentally is

also the pixel size. While important for the quality assessment of the wire edge, the rms roughness is not large enough to assess the effects of this roughness on the atoms. As higher spatial frequency fluctuations wash out with distance much quicker ($\propto e^{-kd}$ for $kd \gg 1$), it is important to measure the power spectral density of the edge fluctuations.

The power spectral density (PSD) is calculated by performing a Fourier transformation on the edge positions. Let y_n be the derived position of the position of the edge in the row n. N is the number of rows in the image, and l the length of the edge observed. To calculate the PSD one has to perform a Discrete Fourier Transformation of this kind:

$$PSD_s = \frac{2l}{N^2} \left| \sum_{n=1}^{N} y_n \exp\left(-2\pi i \frac{(n-1)(s-1)}{N}\right) \right|^2 \tag{3.15}$$

$$k_{z_s} = \frac{s}{l} \tag{3.16}$$

Other transformations would produce similar results, but the amplitude might not be comparable. As an example, [Est04] uses a spectral density transformation J_f, which is similar in shape, though different in absolute values, and can therefore only be compared qualitatively. A major characteristic of the transformation used here is that the integration over the PSD will result in the rms width of the noise: $\sum_s PSD_s \; k_{z_s} = \Delta y_{rms}$. The power spectral density is displayed in figure 3.11, it shows three dominant areas: For high frequencies (periods of 300 nm and less) the amplitude of fluctuations drops off. Between 300 nm and about 200 µm the power spectral density indicates mainly white noise. Large fluctuations are in the low frequency region, with periods over 200 µm; however, these are of the same order of magnitude as the whole scan, and the large values might stem from this fact.

Since the corners, both inwards and outwards, are of interest, SEM images were taken of these as well and are shown in figure 3.12. The rounding of the inner corners has a radius of about 0.5 µm while the outer corners exhibit a slightly smaller rounding of 0.4 µm.

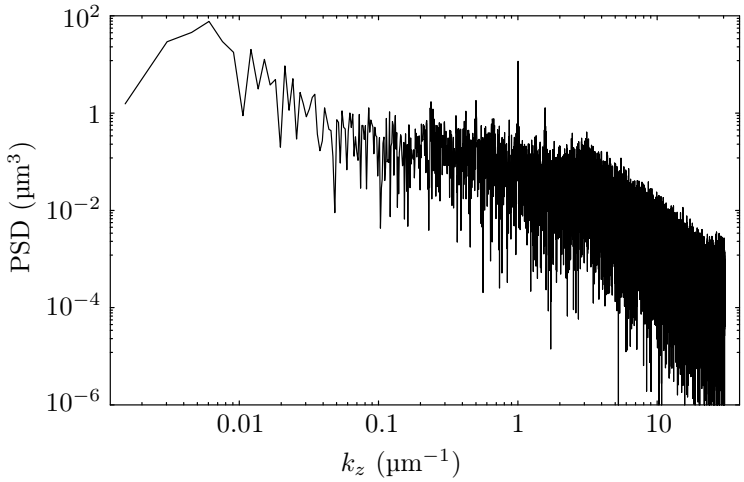

Figure 3.11: Power spectral density plot of ablated wire edge: By stitching together many SEM images, the spectral density of the edge fluctuations was extracted. The absence of any notable spatial components is evidence of the quality of the method.

3.3 Concluding Remarks

In this chapter, femtosecond laser ablation was introduced as a new, quick method for producing microwire atom chips without the need for photolithographic techniques. Several substrate materials and metal films were tested, and the use of copper for good edge characteristics combined with a thin gold layer for protection and reliable reflectivity was chosen for fabricating a microwire atom chip. The edge roughness was measured to be 16 nm, and the analysis of a 650 µm long edge revealed no dominant frequencies. While the adaption of ablation for this goal has just started, these results of the edges already compare femtosecond ablated microwires favourably with some of those that were photolithographically produced. The advantages of femtosecond ablation are mainly in the simplification of the process, reducing the number of possible sources of defects and contamination.

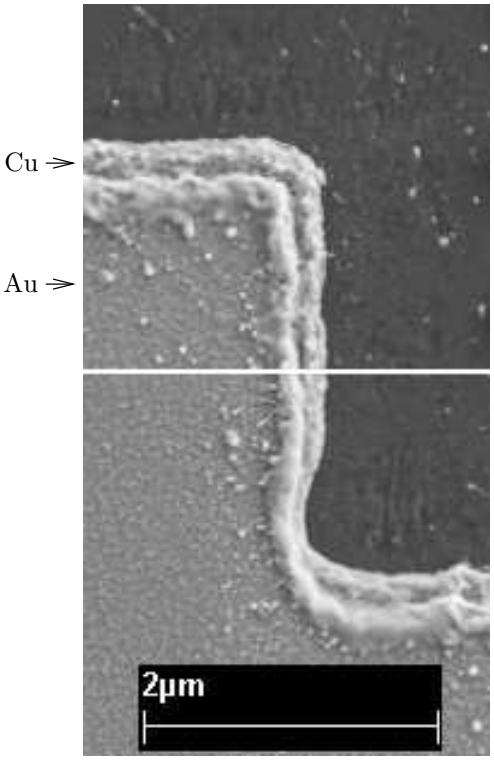

Figure 3.12: The corners of a test wire created with femtosecond ablation. The SEM images were taken with a magnification of 12,500. It shows the imperfections in the corners (both outwards and inwards) are of a magnitude less than 0.5 µm.

Chapter 4

Magnetic Field Mapping of Microwires

4.1 Magneto-Resistance Microscopy of a Straight, Femtosecond Ablated Wire

While scanning electron microscopy is a useful tool to image the edge corrugations, it is insensitive to the magnetic field itself. Many parameters besides the edge quality can have a profound impact on the magnetic potential generated by a current in the microwires. These include defects and inhomogeneities inside the metal layer and changes in the thickness of the metal layer. Therefore a direct measure of the magnetic field produced by the microwire prior to its installation in the experiment is useful. Such a direct measurement was obtained using a home made MRM [Vol08].

4.1.1 The Magneto-Resistance Microscope (MRM)

The MRM directly measures the magnetic field in one direction, in our case perpendicular to the surface of the atom chip (y-direction) to an accuracy of $\Delta B_y/B_y \approx 10^{-4}$, making it comparable to cold atoms when investigating fragmentation above an atom chip. Low temperature Bose-Einstein condensates supersede the accuracy ($\Delta B_y/B_y \approx 10^{-6}$), but are much more complex and expensive than the MRM. Since the measurement can be performed in air, different atom chips can be tested in a short time. Moreover, complete magnetic field mapping above the atom chip can be completely automated with typical scan times (1 mm $\times$ 1 mm, 10 µm resolution) of approximately two hours, so that new designs

can be rapidly prototyped and the best selected for installation.

To characterise the magnetic field of a wire-based atom chip, the chip is first placed on a dual Newport UTM150PP.1 $x - z$ translation stage. This is the same stage that is used in the femtosecond laser ablation apparatus. The magnetic tunnel junction (MTJ) sensor (MicroMagnetics STJ-020) is coupled to a pre-amplifier (MicroMagnetics AL-05) and positioned above the atom chip. The pre-amplifier has a gain of 2500 and a bandwidth of 1 MHz. The distance between the surface of the chip and the tip of the sensor can be set by a manual micrometer screw while being observed with a CCTV camera and a security monitor. The high reflectivity of the atom chip helps to check that the tip and its reflection are converging towards each other and would ultimately touch on the surface of the chip. By comparing relative measurements from the micrometer with the on-screen distance between the tip and its reflection at different heights, we can infer the tip-surface separation to a reasonable accuracy ($\Delta h < 10$ µm). To enhance the signal-to-noise ratio $\Delta B/B$ and to minimise and eliminate other magnetic fields, an AC current (frequency 1.7 kHz, amplitude 10–50 mA) is run through the wire instead of measuring DC magnetic fields. A Lock-In Amplifier (Stanford Research Systems SR830) is used to selectively isolate the magnetic component that oscillates with the same frequency. A computer running LabVIEW 6.1 controls the translation stages via RS232 and reads the signal from the Lock-In Amplifier via GPIB. The whole setup is shown in figure 4.1.

A measurement of the magnetic field along the direction perpendicular to the microwire was used to independently calibrate the sensor tip to the wire separation. The magnetic field along the y-direction (B_y) created by an infinitely thin wire with current I along the z-direction is defined by

$$B_y = \frac{\mu_0}{4\,\pi} \frac{2\;I}{\sqrt{(x - x_0)^2 + h^2}} \;\sin\left[\arctan\left[\frac{x - x_0}{h}\right] + \alpha\right], \tag{4.1}$$

where x_0 is the position of the centre of the wire, h is the height of the sensor above the sample, and α is the angle between the sensor direction and the direction orthogonal to the surface. In the case that the sensor is exactly orthogonal to the surface ($\alpha = 0$) and the wire congruent with the z-axis ($x_0 = 0$), equation 4.1

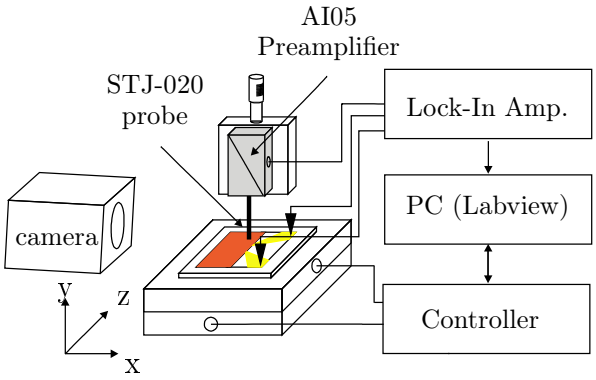

Figure 4.1: Schematic of the magneto-resistance microscope (MRM). The magnetic sample to be characterised is mounted flat on a computer-controlled 2D translation stage (Newport UTM150PP.1). The commercial magnetic tunnel junction probe is attached to the preamplifier built by the same company. A CCD camera is used to verify the proximity of the sample to the chip's surface, as the probe is easily destroyed when scratching over the surface. A lock-in amplifier is used to increase the sensitivity of the measurement.

simplifies to

$$B_y = \frac{\mu_0}{2\,\pi}\; I\; \frac{x}{x^2 + h^2} \tag{4.2}$$

Figure 4.2 demonstrates how the features of the B_y field change with height. When the height increases, the structure flattens and the amplitude decreases. From fitting these curves to a set of data, we can locate the exact position of the wire (x_0) and the distance between the tip and the chip. This is important as it helps to optimise the measurement settings (Gain, Phase, Sensitivity). Figure 4.3 compares the fit to a set of real measurements, with a resolution of 10 µm, and an integration time of 100 ms. The AC current was 25 mA, and the wire had a width of 100 µm. It can be seen that when the tip-chip separation is comparable or smaller than the width of the wire, effects due to the finite width of the wire start to play a role. To calculate the effect of a wire with finite width w, equation 4.2 has to be convolved with a step

function for the wire.

$$f(x) = \begin{cases} \frac{1}{w} & \text{for} \quad |x| \leq \frac{w}{2} \\ 0 & \text{for} \quad |x| > \frac{w}{2} \end{cases} \tag{4.3}$$

$$\begin{aligned} B_y &= \frac{\mu_0}{2\,\pi}\, I \int_{-\infty}^{\infty} dx' f(x') \frac{x - x'}{(x - x')^2 + h^2} \\ &= \frac{\mu_0}{2\,\pi}\, \frac{I}{w} \int_{-w/2}^{w/2} dx' \, \frac{x - x'}{(x - x')^2 + h^2} \end{aligned} \tag{4.4}$$

Figure 4.3 demonstrates how equation 4.4 improves the fitting of a real set of measurement data, taken approximately 50 µm above a 100 µm wide wire.

The reliability and repeatability of the MRM are of importance when the quality of the microfabricated wires is to be assessed. To test this we made many (usually 1000) consecutive measurements at fixed conditions, and calculated the root mean square spread of the results. These measurements were repeated for different time constants of the lock-in amplifier between 1 ms and 1 s. Also, the measurements were performed under different conditions to distinguish between different error sources.

At first, the measurement was performed without applying an actual magnetic field, thus measuring the noise of the tip, the pre-amplifier and the lock-in amplifier. Next, the tip was placed approximately 50 µm above the sample and moved to the position where the signal was maximal ($B_y \approx 1$ G), and the derivative ($\partial B_y/\partial x$) was zero, adding the uncertainty of the measured magnetic field to the background. In the third measurement, the tip was located above the centre of the wire, where the gradient was maximal ($\partial B_y/\partial x \approx 40$ G/mm), which should introduce additional error due to positioning inaccuracy. And finally, between each single measurement the tip was moved between the maximum of the field and the maximum of the gradient, giving the error resulting from the actual movement of the sample below the tip. As suggested by the manual of the lock-in amplifier, in this measurement we waited for 5 time constants after arrival at the new position before measuring. Figure 4.4 shows the results of these error measurements. Below time constants of 10 ms, each noise level of the five measurements is comparatively high. The background noise level drops to 0.2 mG for 300 ms integration time, before rising again to 0.4 mG at 1 s integration. This is probably due to drifts in the signal

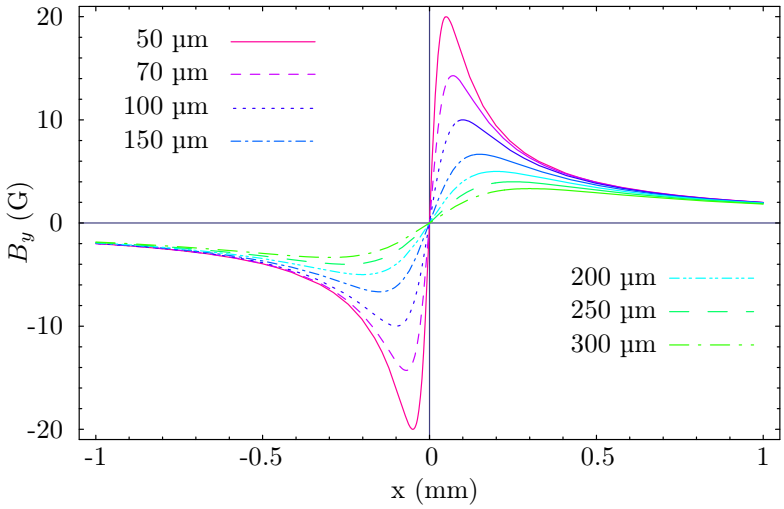

Figure 4.2: Calculated one-dimensional profiles of the vertical component B_y for different heights above the chip and for a current of 1 A. With increasing height above the wire, the signal becomes flatter and broader. The shape of the measured curve therefore is a good indicator of the sensor height even without the signal calibration.

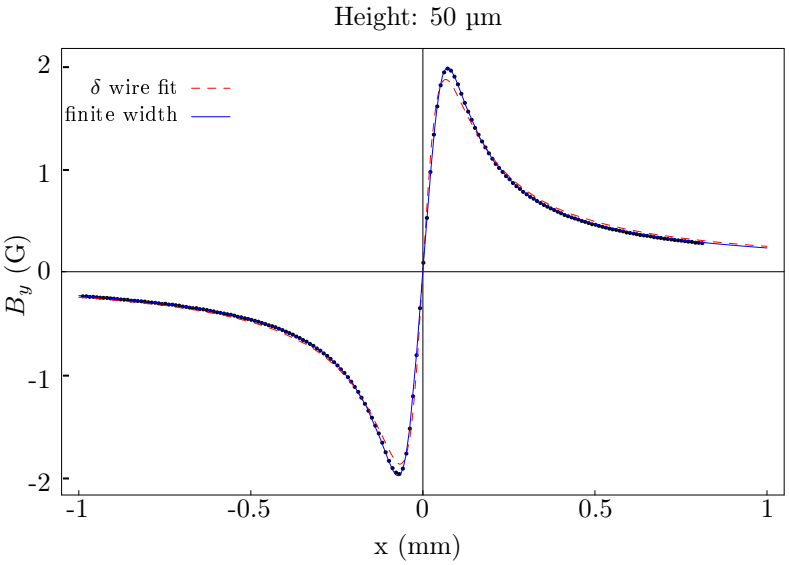

Figure 4.3: MRM measurements of the vertical component B_y (dots) for a current of 100 mA through a wire of 100 µm width. The data was fitted using equation 4.2 for an infinitely thin wire (red dashes) and using equation 4.4 for a finite width wire (blue line). The signal of the MRM is proportional to the magnetic field. The calibration factor is calculated afterwards by comparing the signal to the calculated magnetic field.

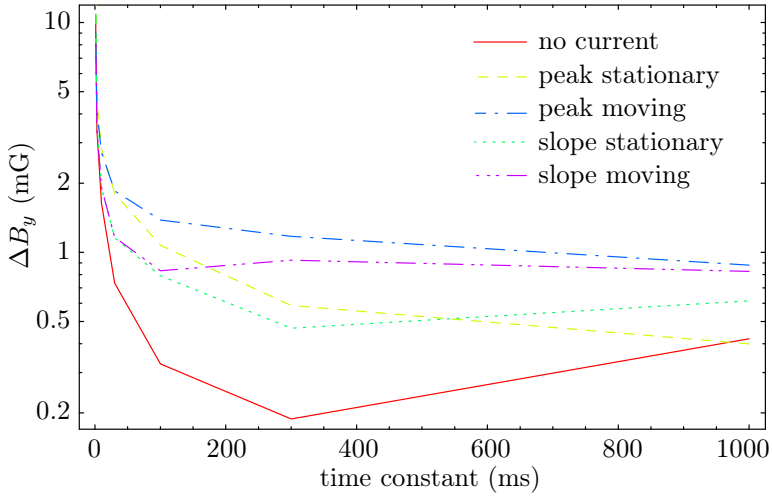

Figure 4.4: Measurements of the different error sources of the magnetic tunnel junction sensor. By measuring the same field many times, the uncertainty of the MRM corresponds to the width of the distribution of these results. At very short time constants, there is considerable noise on the measurement. The solid red line corresponds to the measurement on the background field. The apparent increase in uncertainty at 1000 ms time constant is explained by the drift of the background magnetic field during the extended measurement time. The dashed yellow and the dotted green line correspond to the stationary measurements on the peak (B_y max, $\partial B_y/\partial x = 0$) and the slope ($B_y = 0$, $\partial B_y/\partial x$ max) respectively. The dash-dotted blue line (peak) and the purple dash-dot-dotted line (slope) correspond to the measurement series where the tip was moved between each single measurement. For time constants longer than 100 ms all of the error levels are below 2 mG, which means that the MRM should be able to resolve magnetic features down to a few milligauss.

which become more dominant when larger integration times extend the required time for each measurement. At 300 ms integration times, the uncertainty in stationary measurements both for the gradient and the peak has dropped below 0.7 mG, while the moving measurements stay around 1 mG. The most interesting aspect is that the uncertainties on the flanks are actually smaller than the uncertainties on the peak, even though an additional error source has arisen. We attribute this small difference to the increased amplitude of the magnetic field. It is safe to assume that the positioning error itself is negligible. At time constants larger than 100 ms, the error due to the movement seems to play the dominant role. This could be due to the inaccuracy of the translation stage, an increased influence of the drift

because the longer duration of the measurement, or due to a remaining effect of the measured field during the movement. The movement inaccuracy is less than one micrometer, probably less than 200 nm, as we repeatedly observe during the femtosecond ablation. Considering the gradient, this would induce a noise of about 0.8 – 4 mG. Due to the drift of the magnetic background, no enhancement can be achieved with time constants longer than 300 ms.

4.1.2 Measuring $\Delta B/B$ above the Straight Wire

The MRM can only measure the component of the magnetic field perpendicular to the chip surface. B. J. Roth *et al.* [Rot89][†] have shown how it is possible to reconstruct the two-dimensional current distribution by measuring the magnetic field component perpendicular to the surface at a known height above the surface. Since the height of the tip above the sample (20 – 200 µm) is large compared with the wire thickness (0.3 µm), we can assume the current to be two-dimensional. The current distribution then allows the reconstruction of all the magnetic field components. However, we do not calculate the current density, but instead directly reconstruct the full magnetic field from one of its components. Firstly, the magnetic field component B_y, perpendicular to the chip surface, is measured using the MRM for an area $x = x_0 \ldots x_m$, $z = z_0 \ldots z_n$. With this, the Fourier components $b_z[k_x, k_z]$ are calculated using the fast Fourier transform algorithm of Mathematica 5.2 for Linux. Then, the Fourier components $b_x[k_x, k_z]$ and $b_y[k_x, k_z]$ can be calculated according to:

$$\begin{aligned} b_x[k_x, k_z] &= \mathrm{i}\,\frac{k_x}{k}\, b_z[k_x, k_y] \\ b_z[k_x, k_z] &= \mathrm{i}\,\frac{k_z}{k}\, b_z[k_x, k_z] \\ k &= \sqrt{k_x^2 + k_z^2} \end{aligned} \tag{4.5}$$

[†]Roth *et al.* postulate a quasistatic current distribution, which is not the case here, as an AC current is used in the MRM. However, since we can assume that there are no inductances or capacitances, and the AC frequency is low enough to not emit noticeable electromagnetic waves, the condition $\nabla . J = 0$ is still valid.

Here it is important to note two issues. Firstly, at $k_x = k_z = 0$, the algorithm above is undefined. Secondly, in many math programs (Mathematica was used here), the result of a fast Fourier transformation is an array in which the Fourier components are ordered so that the corresponding k vectors are in the order $0, 1, \ldots, m/2, -m/2, 1-m/2, \ldots, -1$. To correct for this, it is necessary to evaluate k manually:

$$k_x = \begin{cases} x - 1 - \epsilon & \text{for} \quad x \leq m/2 \\ x - m - 1 - \epsilon & \text{for} \quad x > m/2 \end{cases} \tag{4.6}$$

where ϵ is a minuscule offset to ensure that $k \neq 0$. k_z is calculated equivalently using n instead of m. An inverse Fourier transform on $b_x[k_x, k_z]$ and $b_z[k_x, k_z]$ will then return the magnetic field components B_x and B_z. Often it is necessary to just retain the real component of the complex numbers to accurately describe the magnetic field in the x and z direction.

Figure 4.5 demonstrates this for a 100 µm wide, 1 mm long wire with a current of 70 mA: The top left image displays a contour plot of the y component of the magnetic field. This was measured with the MRM at a height of 60 µm. Beneath this is a profile of the potential. The middle and right figures display the field strength in the x and z directions, calculated from the B_y field as noted above. Some artefacts from the conversion can still be seen, for example the negative offset in the B_x figure, and the peaks in the lower and upper centre of the B_z figure are not physical structures but derive from the limited resolution (5 µm) and area (64 mm^2) of the scan.

After eliminating these artefacts, the noise of the magnetic field component in the z direction can be observed. This is shown in figure 4.6. Ideally, the line should remain zero at all points; the noise in the magnetic field ($B_{||} = B_z$) has an rms roughness of 1.8 mG, compared with the full magnetic field produced by the wire at this distance ($B_\perp = B_x$) of 2.4 G[†], this translates to a $\Delta B_{||}/B_\perp$ of $7.5{\times}10^{-4}$. More importantly, the noise in the figure exhibits a strong component corresponding to a period of 5 µm, which is unlikely to be 'real data': No length scale of the fabrication process is in this range. The diameter (1 µm), and the

[†]Figure 4.5 middle shows that the magnitude of the magnetic field goes from 2 G down to -0.4 G, which is an artefact of the calculation, the total amplitude is therefore 2.4 G, which corresponds to the analytical expression for $B_\perp$

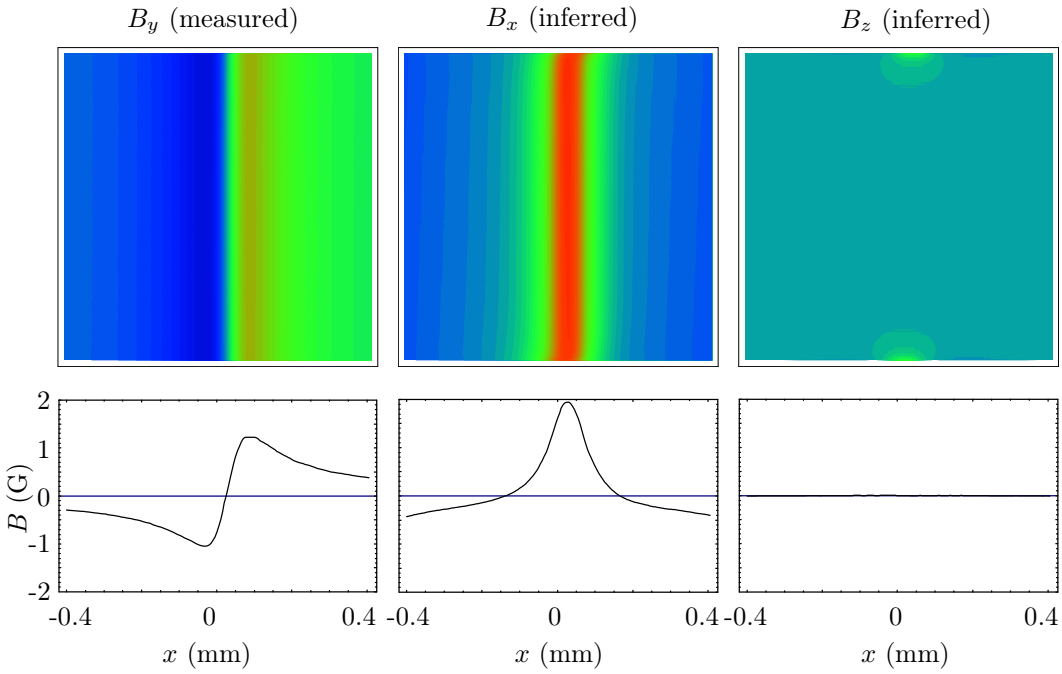

Figure 4.5: MRM measurement on a straight wire. Left: The measured B_y component of the magnetic field produced by a current carrying 100 µm wide wire. Middle: The B_x component of the magnetic field, as calculated by equations 4.5. Right: The B_z component of the magnetic field, as calculated by equations 4.5. Top: 0.8 × 0.8 mm^2 2D representations of the magnetic field. Bottom: Horizontal profiles of the graph above. All three figures are scaled. Towards the edges of the area, artefacts from the calculations play a dominant role, resulting in seemingly high values.

distance between successive pulses (0.1 µm) of the laser as well as the accuracy of the translation stages (0.1 µm) are of a smaller range. High frequency components decay quickly with distance [Whi07b]

$$b_z[k_z, h] \propto \sqrt{K_1[4\pi k_z h]} \tag{4.7}$$

where K_n is the modified Bessel function of the second kind. As $K_1[x]$ asymptotes to zero for large x, frequency components with $k \gg 1/h$ would be strongly suppressed at larger distances from the wire, and 5 µm period structures should not be visible at the measurement height $h = 60$ µm. Therefore the noise with this period is much more likely to stem from the MRM itself. Since 5 µm was the resolution with which the original magnetic scan was acquired, it is likely that any unexpectedly high noise

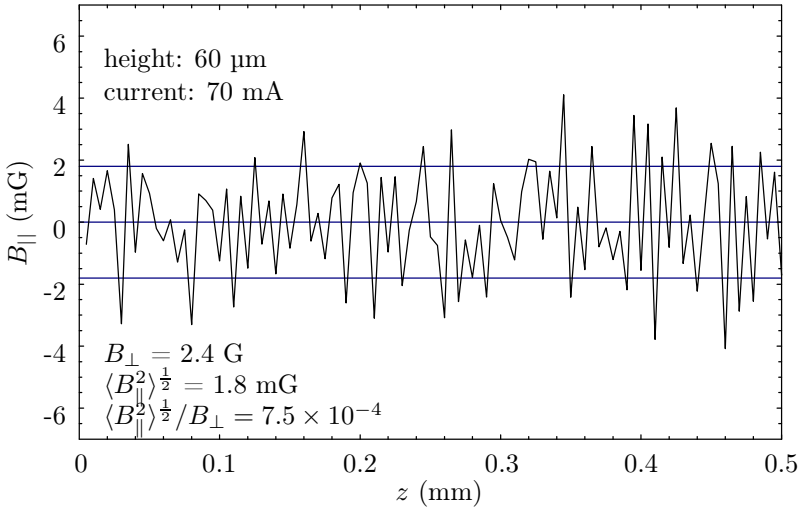

Figure 4.6: The magnetic field component in z direction $B_{||}$ of a straight wire produced by femtosecond ablation. The MRM was used to measure B_y of the field; from this, the magnetic field components in the x direction ($B_\perp$) and the z direction ($B_{||}$) were inferred. The data yield a value of $\langle B_{||}^2 \rangle^{\frac{1}{2}} / B_\perp$ of 7.5× 10^{-4}.

in this range has been produced by the scanning process.

To obtain an indication of how the parameter $\langle B_\parallel^2 \rangle^{\frac{1}{2}} / B_\perp$ changes with height, the data displayed in figure 4.6 was transformed into Fourier space components $b_z[k_z, h_0]$. These Fourier components are then evolved for heights $h > h_0$ according to equation 4.7 in the following way:

$$b_z[k_z, h > h_0] = b_z[k_z, h_0] \sqrt{\frac{K_1[4\pi k_z h]}{K_1[4\pi k_z h_0]}} \tag{4.8}$$

These Fourier components are transferred back into $B_z[z, h]$; the results are given in figure 4.7. The first three graphs in the figure show the corrugations relative to the radial magnetic field ($B_{||}/B_\perp$) at the heights of 100, 120, and 140 µm above the wire, where short periodic fluctuations from figure 4.6 are suppressed quickly with height, while longer period structures remain until larger distances. The apparent evolution of $\langle B_\parallel^2 \rangle^{\frac{1}{2}} / B_\perp$ is given in the final graph, and it shows a particular two-stage behaviour: While at heights above 100 µm, the decline is steady and only slightly flatter than expected ($\propto e^{-2.07y}$ as opposed to $\propto e^{-2.5y}$), in the region between 60 and 100 µm, the values decrease much faster. This is another strong indication of the MR sensor inducing high-frequency noise into the

data which is eliminated by the processing of the data in Fourier space, supporting the assumption that the real noise floor of the magnetic field is more appropriately described by extending the graph shown for heights larger than 100 µm. Whether the exponential decaying fit, displayed as a line in figure 4.7d, indicates the real magnetic field roughness $\langle B_{\parallel}^2 \rangle^{\frac{1}{2}} / B_{\perp}$ probably has to be evaluated using cold atoms and Bose-Einstein condensates.

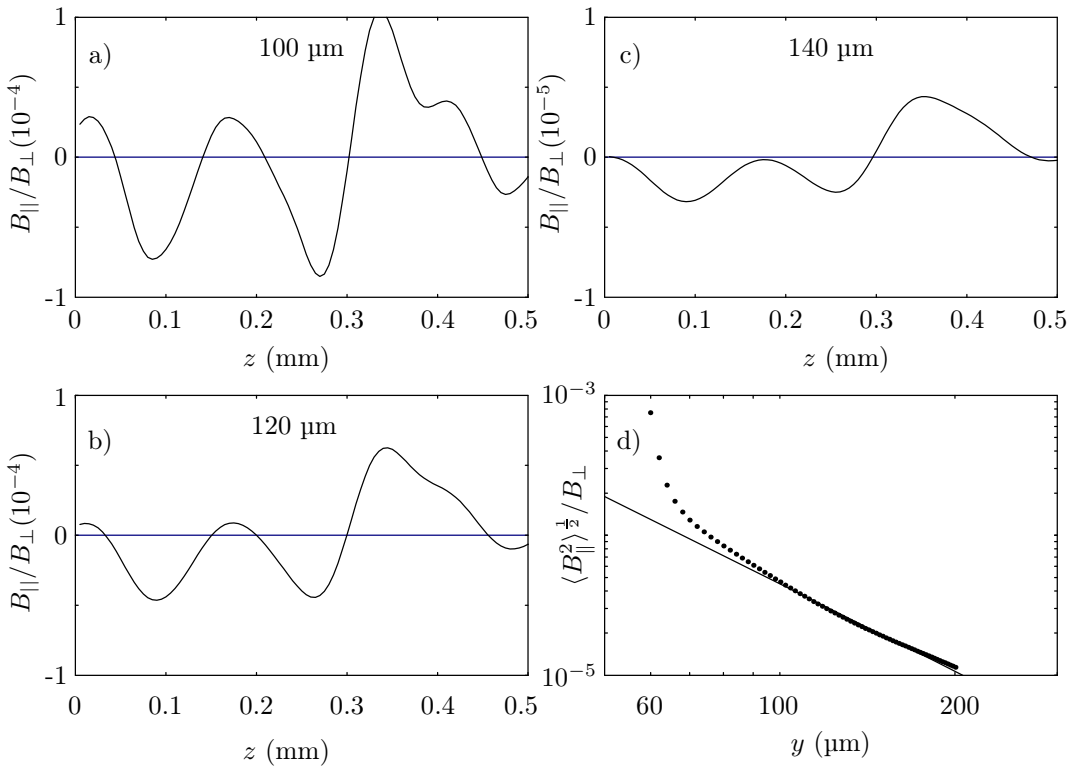

Figure 4.7: To obtain an indication of the noise levels at higher distances from the wire, the initial data was transformed into Fourier space and there multiplied by the factor $\sqrt{K_1[4\pi k_z h]/K_1[4\pi k_z h_0]}$ where h is the height and h_0 is the height of the measurement (60 µm).

Top left: Even at a height of 100 µm, most of the high frequency noise is already suppressed (compare to figure 4.6), suggesting that this noise is actually more likely to stem from the measurement instead of being real magnetic noise.

Bottom left and top right: At even higher distances, the short-ranged fluctuations are gone and only larger range features remain.

Bottom right: The characterising value of $\langle B_{\parallel}^2\rangle^{\frac{1}{2}}/B_{\perp}$, which defines the magnitude of the fragmentation, is numerically calculated for different heights. Again, the fast decay of the noise level for the region between 60 and 100 µm suggests that the high frequency noise stems not from the real magnetic field but instead is very likely instrument noise from the MRM.

4.2 Sculpting a Wire with Femtosecond Laser Ablation

While roughness of the microwire edges leads to unwanted and random fragmentation of ultracold clouds, recent experiments by [Hal07] used this deleterious effect encountered above a permanent magnetic film atom chip as the basis of a sensitive probe of the field gradient. In this realisation the corrugated potential above the TbGdFeCo atom chip [Whi07a] was due to random magnetic domain inhomogeneity which resulted in a surprisingly symmetric double-well potential close to the film edge [Whi07b]. In their experiments an ^{87}Rb Bose-Einstein condensate was split axially from being localised in a single well to being distributed across a double well. The barrier between the wells was increased (decreased) by moving the trap towards (away) from the film surface. The sensitivity of this experiment relied on i) the asymmetry of the potential which determined how evenly the BEC was split and ii) the extremely low energy scale of the BEC chemical potential which yields the order of magnitude of the detectable asymmetry. After the splitting process the number of atoms in each well is determined by a destructive absorption image taken after a short (2 ms) free fall. The potential asymmetry Δ [Hal07] is related to the relative atom number asymmetry $\Delta N/N$ by the following expression:

$$\frac{\Delta N}{N} = \frac{1.65\Delta}{cN^{2/5}} \qquad \text{with} \qquad c = \frac{\overline{\omega}}{4\pi}\left(\frac{15a}{a_0}\right)^{2/5}, \tag{4.9}$$

where $\Delta N/N$ is the atom number difference divided by the total atom number $(N_L - N_R)/(N_L + N_R)$, $\overline{\omega}$ is the geometric mean of the trap frequencies, a is the rubidium scattering length (109 a_0) and a_0 is the Bohr radius. From this expression one observes that if the atom detection signal is set to the shot noise limit $\Delta N/N \approx 1/\sqrt{N}$ then increased sensitivity in measuring a given Δ is obtained by either increasing N (scaling weakly as $N^{-0.1}$) or by reducing $\overline{\omega}$. These concepts are depicted in figure 4.8 which shows a) the adiabatic transformation of an idealised single-well potential into a double-well potential with the BEC fractions marked, b) how $\Delta N/N$ behaves as a function of applied asymmetry ([Hal07]), c) the realised microwire potential shape along with the parameters of interest (spacing s, barrier

height β, asymmetry Δ, well depth γ).

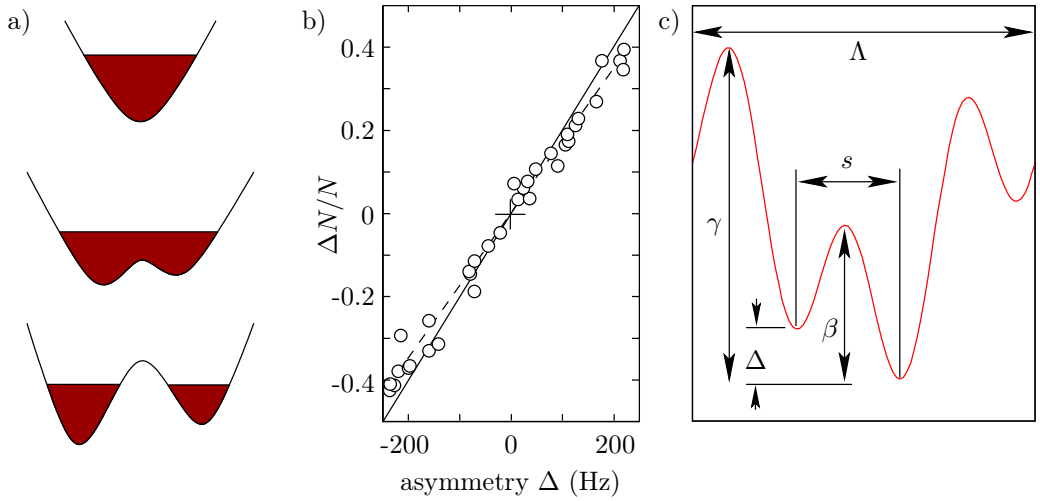

Figure 4.8: Adiabatic splitting of a double well: a) Adiabatically splitting a BEC from a single into a double well results in the atom number in each well being dependant on the relative potential bottom. b) Behaviour of $\Delta N/N$ as a function of the asymmetry in the wells. The straight line is the theoretical prediction, the datapoints are results of a measurement in [Hal07], and the dashed line is the best fit to these datapoints. c) Schematic of the important parameters of a double well.

Rather than rely on random chance, in this project our aim was to fabricate a structured microwire using the processing techniques of femtosecond ablation such that the wire was capable of creating arrays of identical single/double-well potentials. One way of achieving this goal is to fabricate two periodic structures (λ, Λ), one on each wire edge, where the wavelength of each structure determines the spatial period of the corrugating potential, along with the characteristic length that $B_{||}$ decays with from the wire, $B_{||} \approx K_1\left[\frac{2\pi y}{\lambda}\right]$ where K_n is a Bessel function of the second kind [Jon04]. Since the long wavelength Λ decays less rapidly with height above the wire (y), this quantity determines the single-well potential features, leaving the shorter wavelength λ as the scaling parameter for the double-well potential. In addition, the amplitudes of the sculptured edges are variables which tune the relative magnitude of the two field components $B_{||}^{\Lambda}$ and $B_{||}^{\lambda}$. For this sculptured microwire the double-well potentials were designed with a maximum separation of λ=100 µm which is sufficient for site specific addressability while maintaining a low $\overline{\omega}$.

To determine the fabrication path that is required for this goal we first start with an ideal analytic expression for the potential that is desired. In this case an array

of symmetric double-well potentials is given by

$$U(x) = \frac{d_c}{\alpha}\cos\left[\frac{2\pi x}{\lambda}\right] - d_c\cos\left[\frac{2\pi x}{\Lambda}+\delta\right] \tag{4.10}$$

where the new parameter d_c represents the depth of the corrugation in Gauss; α is a unitless parameter which relates the relative strengths of the two $B_{||}$ components, and its choice determines the height (y) at which the potential is evaluated above the wire:

$$\alpha = \frac{\xi_\Lambda}{\xi_\lambda}\left(\frac{\lambda}{\Lambda}\right)^2 \frac{K_1[2\pi y/\Lambda]}{K_1[2\pi y/\lambda]} \tag{4.11}$$

In the above equation ξ_λ resp. ξ_Λ is the physical edge deviation that is sculptured by the ablation and δ is a phase shift term which is responsible for the asymmetry of the potential. For an array of perfectly symmetric double wells the phase-shift term should be zero and Λ should be an integer multiple of λ. In our case this integer is 3. Once the potential is known we can use the previously derived [Sch05a] response function of a magnetic field to a wire edge fluctuation $|B(x,y)|^2 = R(k,y)\xi^2$ to approximate the current path required and the scale of the amplitude of the edge fluctuations $\xi_{\lambda,\Lambda}$

$$I(x) \propto \frac{2\pi}{3}\sin\left[\frac{2\pi x}{3\lambda}\right] - 2\pi\sin\left[\frac{2\pi x}{\lambda}\right] \tag{4.12}$$

where the parameter d_c, the corrugation depth in Gauss, is related to the physical size of the edge fluctuation $\xi(m)$ by

$$d_c = \xi_{3\lambda}(m)\ 10^4\ 4\,\pi I\left(\frac{2\pi}{3\lambda}\right)^2 K_1\left[\frac{2\pi y}{3\lambda}\right]. \tag{4.13}$$

With these equations it is possible to estimate the functionality and the scaling of the parameters of interest (separation s and barrier height β) with distance from the wire, as depicted in figure 4.8c. For quantitative values we set $\lambda = 100$ µm, $\Lambda = 300$ µm, $\xi_\lambda = 3$ µm, $\xi_\Lambda = 1$ µm, $I = 100$ mA. With these values s and β can be determined from the analytic expressions

$$s = \frac{6\lambda}{\pi}\arccos\left[\sqrt{\frac{1}{2}+\frac{\alpha+3}{4\sqrt{3}}}\right] \tag{4.14}$$

$$\beta = \frac{d_c}{\alpha}\left(1-\alpha+\left(\frac{3+\alpha}{3}\right)^{\frac{3}{2}}\right) \tag{4.15}$$

In the derivation of the response function the wire is approximated to be flat such that a uniform current density only propagates in the x-z plane. Furthermore the response function is derived for distances from the wire which are greater than the width of the wire. While the first approximation is valid for our thin (400 nm) high microwires, the second is not as the microwire width is about 100 µm wide. An additional uncertainty arises from the fact that the above calculations assume a sinusoidal edge corrugation, which is hard to fabricate. Instead, it was decided to fabricate a square wave edge. The Fourier series of a periodic, equidistant square wave has more than 81% of the amplitude in the first cosine term, and about 9% in the third cosine term. The quantitative findings of the analytical expressions detailed above are therefore not applicable to this experiment, but the qualitative results give a starting point for further examination using approximating simulation methods.

4.2.1 Finite Element Analysis of the Sculptured Wire

To verify that the broad assumptions and simplifications (most importantly that using a step function instead of sinusoidal edge deviations) still allow one to produce a suitable magnetic field and to compare experimental measurements to accurate simulations of "what should be", a finite element method was used to assess the current distribution and thereby the complete magnetic field. The electric potential V inside a current-carrying wire is given by the partial differential equation

$$-\vec{\nabla}.\vec{\nabla}\,V = 0 \tag{4.16}$$

with the boundary conditions

$$\vec{n}.\vec{\nabla}V\Big|_{\text{edge}} = 0 \quad \text{where } \vec{n} \text{ is the vector perpendicular to the edge} \tag{4.17}$$

$$V\Big|_{\text{input}} = 1 \quad \text{where the current enters the wire, and} \tag{4.18}$$

$$V\Big|_{\text{output}} = 0 \quad \text{where the current exits the wire.} \tag{4.19}$$

In complex geometries, this can not be solved analytically, but it can be approximated with finite element analysis (FEA). For FEA, the object is divided into smaller objects, usually triangles. The method assumes that the potential inside such a triangle will be in the plane generated by the three corners. In this way, only the potential at the corners needs to be calculated. The method for finding an appropriate mesh is complex: Using fewer triangles makes the calculation faster, but loses some resolution. For this reason, the mesh should be fine in the interesting areas, whereas large triangles should cover the areas where the electric potential is assumed to be linear anyway. We have used the automated mesh generation of MatLab 7.4, which we found to be quite adequate. MatLab also allows us to refine the mesh by substituting every triangle with four new ones. With this method, the number of triangles in the final meshes was approximately 25,000 – 60,000, covering the whole wire. An example of such a mesh with many small triangles in the corners and fewer, larger triangles in the centre of the wire can be seen in figure 4.9, top image.

Several different wire geometries were tested using this method. In the end we decided on the geometry shown in figure 4.9: One edge has a 300 µm period (1.6 µm out, 150 µm across, 1.6 µm in, and 150 µm across), while the other has a 100 µm period (5 µm out, 50 µm across, 5 µm in, and 50 µm across). Note that the outward steps on both sides do coincide, as do the inwards steps.

Once the program has solved the partial differential equations, the mesh is substituted by a grid of equidistant points. In our case, a distance of 0.5 µm has been shown to be sufficiently small. The potential is calculated for each of these points. The current is proportional to the gradient of the potential ($\vec{j} \propto -\vec{\nabla} V$); the factor can be easily calculated by determining the sum of the gradients along one line across the wire and comparing it to the current that must flow through there. The remainder is just adding the magnetic fields produced by the currents in each point of the grid, resulting in the full magnetic field of the wire. The interesting magnetic field component parallel to the wire B_z at a height of 35 µm above the sample is shown in figure 4.9, bottom. Atoms, normally trapped above the centre of the wire, experience a double-well potential. This particular wire geometry allows two ways to change the double wells into single wells: a) Increasing the current in the wire,

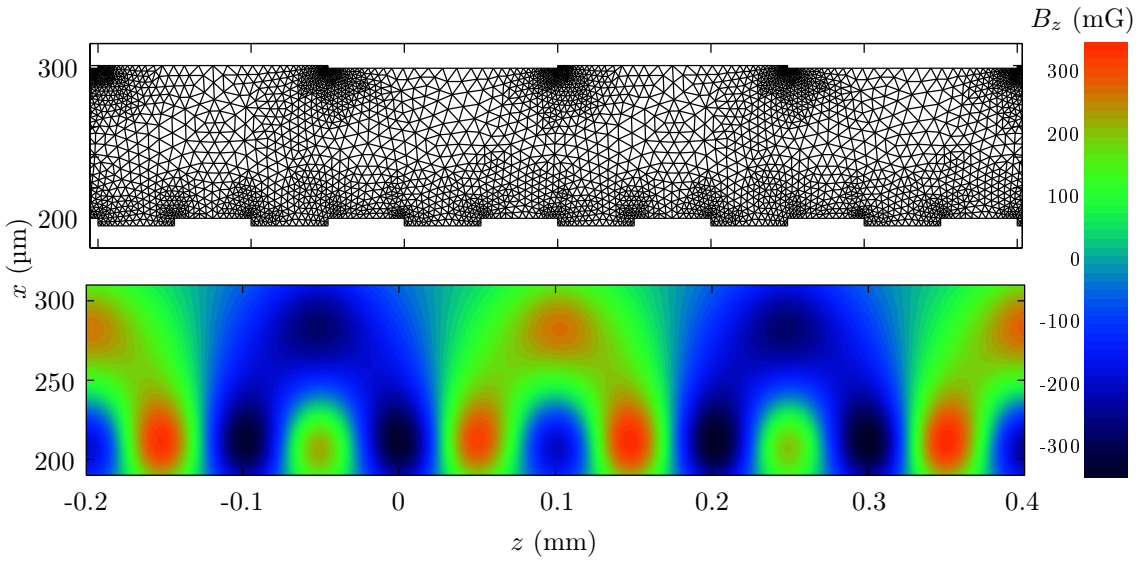

Figure 4.9: Top: The wire geometry is filled in a mesh of triangles. The finite element analysis assumes that inside each triangle, the potential follows a planar surface which is given by the potentials at the tree corners. Bottom: The calculated magnetic field in the z-direction, 35 µm above the surface of the wire. The magnitude of the magnetic field is given per Ampère. Using this wire as the centre piece of a Z-wire magnetic trap configuration, this B_z field will corrugate the magnetic trap bottom.

or reducing the bias magnetic field will both result in the atoms moving further away from the surface of the chip, where the high frequency part of the corrugation becomes less effective and the double-well structure decreases towards a single well. b) A second possibility is to move the atoms across the wire towards larger x values, as can be seen in figure 4.9. This can be done by applying a small magnetic field perpendicular to the atom chip's surface. The advantage of this method is that the trapping potential remains relatively constant compared to moving the atoms further away from the chip.

Observing just the centre of the wire, where the atoms will be confined in the experiment, the Finite Element Analysis allows us to assess the amplitudes of the double-well parameters, as well as their change with distance from the wire. These results are given in figure 4.10. Left graph: The separation of the two wells s is just over 80 µm at low heights, but steadily decreases until at a height of about 80 µm the two wells turn into a single well. The centre graph shows how the barrier height β and the well height γ between adjacent double-well structures decrease

relative to the radial magnetic field produced by the wire. The right graph shows the dependence of the absolute values of β and the asymmetry Δ on the height above the wire.

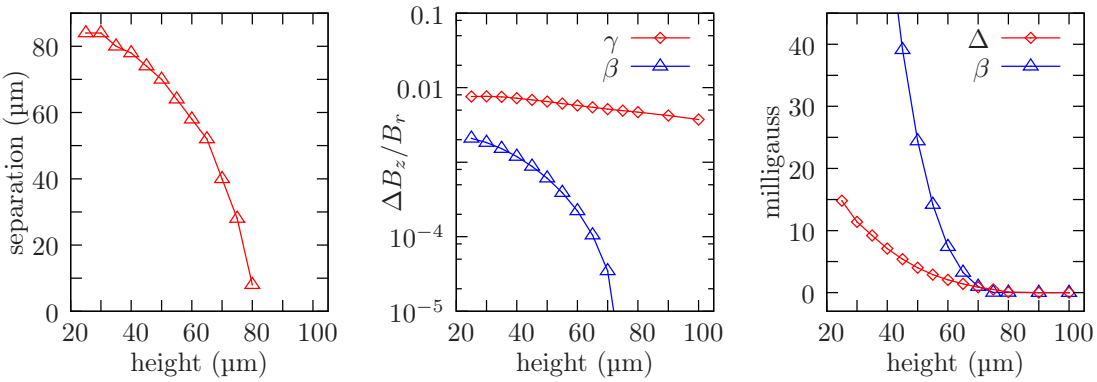

Figure 4.10: Properties of the double-well system, derived by analysing the results of the finite element calculations of the magnetic field produced by a current of 1 A in the wire.
Left: Separation of the wells over the centre of the wire, depending on height. Above 80 µm, the wells merge into one.
Middle: Potential γ between adjacent double-well structures and barrier height β between the two wells of each structure relative to the radial magnetic field B_r of the wire.
Right: Absolute values for the asymmetry Δ and the barrier height β depending on the height above the wire.

4.2.2 Mapping the Magnetic Field above the Sculptured Wire

Having decided on this structure, such a wire was created using femtosecond ablation. The magnetic field was then measured with the MR sensor, as described in section 4.1.1. The tip of the sensor was placed as close to the surface of the chip as possible, and an ac current of 150 mA at 1.75 kHz was sent through the wire. The height above the surface was found to be about 17 µm. The scan range was 1 mm by 1.5 mm. The result can be seen in figure 4.11. The interesting B_z field component clearly shows the expected structure, where the fields produced by the shorter range, yet higher amplitude, 100 µm frequency (left side) dominate over the lower amplitude 300 µm frequencies due to the small elevation of the sensor.

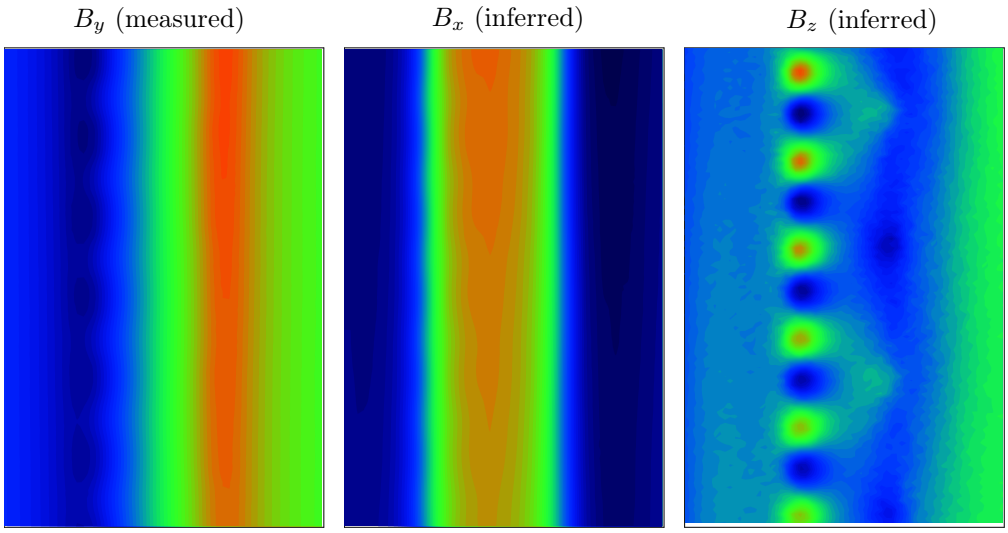

Figure 4.11: The magnetic fields of a corrugated wire perpendicular to the surface (B_y, measured), perpendicular to the wire in plane (B_x) and parallel to the wire (B_z) 17 µm above the wire over an area of 1.5 mm by 0.8 mm.

Figure 4.12 shows the comparison of the experimental data from figure 4.11 with a finite element calculation of the field at this elevation. Both amplitude and overall shape agree well. The bottom graph in figure 4.12 shows the real magnetic potential of all three dimensions with a 6 G bias and a 1 G offset field. It is clearly seen that the potential creates double wells over the centre of the wire, and the higher (lower) values of the B_z field closer to the edge are dominated by the Ioffe-Pritchard trapping potential. This proves not only that a double-well structure can be created with a sculptured wire, but even more, validates the methods of femtosecond ablation, magneto-resistance microscopy and magnetic field conversion, as well as the finite element analysis due to the close correspondence between the empiric and theoretic results. This comparison is also shown one-dimensionally in figure 4.13 along the centre of the wire. The data points stem from the MRM, while the red line shows the result of the finite element calculations. The small deviations between the two graphs can be explained by the uncertainties of assessing the height and tilt of the sensor, together with the limited resolution which results in an uncertainty in the actual location of the wire centre.

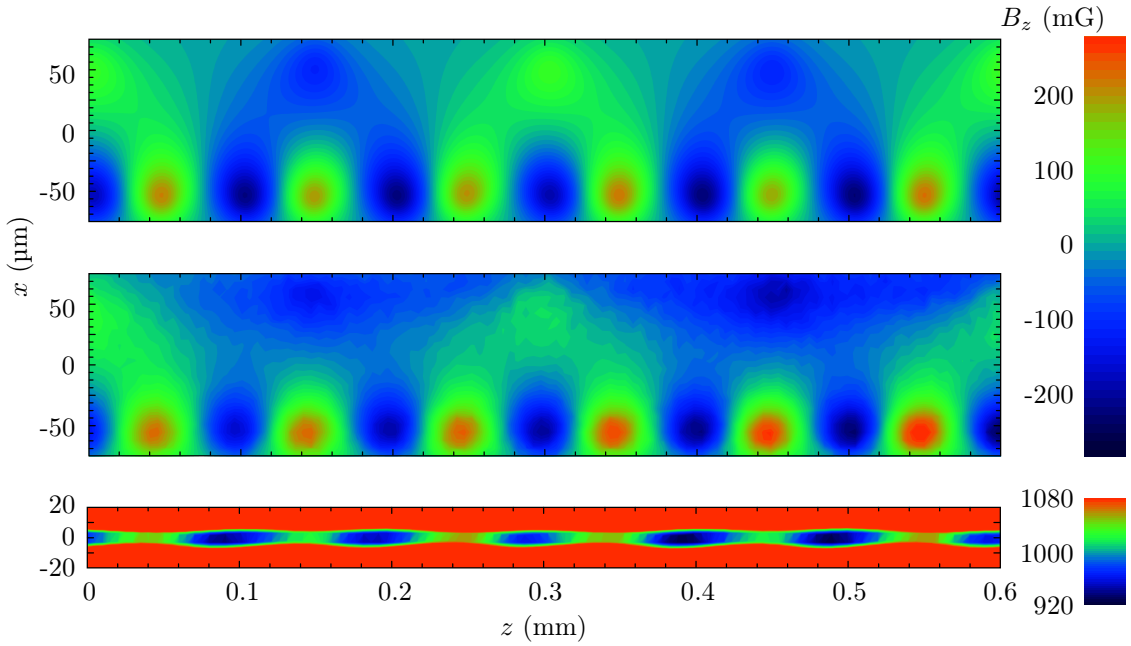

Figure 4.12: Magnetic field component B_z above the corrugated wire. A current of 150 mA was sent through the corrugated wire, and the magnetic field 17 µm above the wire was calculated (top) using Finite Element analysis and measured (middle) using the MRM. In the Finite Element Method image, the range is ±230 mG. The results of the MR measurement are in the same region (ca. -380 mG - 300 mG). Bottom: The total magnetic field strength $|B| = \sqrt{(B_x - 6\,\mathrm{G})^2 + B_y^2 + (B_z - 1\,\mathrm{G})^2}$ where B_x, B_y and B_z are the values measured with the MRM.

4.2.3 Sensing near-surface forces

In 1948, Casimir and Polder investigated the effect of retardation on the short-range, attractive London-van der Waals force between a neutral atom and a perfectly conductive wall [Cas48]. They found a monotonically decreasing correction factor, which approaches unity for $y \ll \lambda/2\pi$ and scales as y^{-1} for $y \geq \lambda/2\pi$ where y is the atom-wall separation and $\lambda/2\pi$ is the distance associated with the wavelengths λ corresponding to possible transition energies of the atom. In this region, the Casimir-Polder potential is

$$U(y) = -\frac{3}{8\pi}\,\hbar\,c\,\alpha(0)\,y^{-4} \tag{4.20}$$

where $\alpha(0)$ is the static polarisability of the atom. This interaction is a direct result of the electromagnetic vacuum whose interest has motivated numerous theoretical

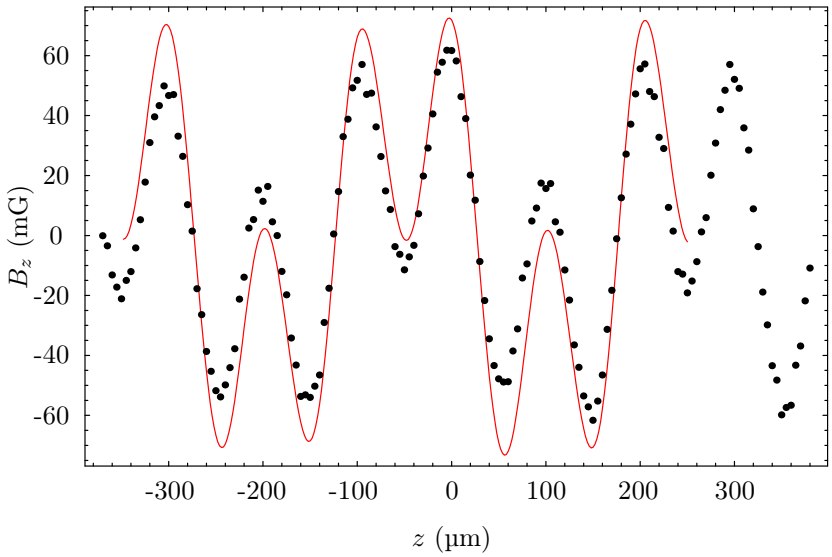

Figure 4.13: $B_z(z)$ at the centre of the wire. Points: MRM measurement on the corrugated microwire, ca. 17 µm above the surface of the chip. This low elevation results in a clear separation of the two wells. Line: Result from finite element analysis trying to mimic the conditions under which the measurement was taken (17 µm height, 150 mA, centre of wire).

extensions to equation 4.20 to account for real world effects, such as material composition, geometry, and finite temperature [Bab05]. In addition, recent precision measurement techniques using the BEC as a probe have enabled this interaction to be investigated quantitatively [Pas04, Har05, Obr07]. A schematic representation of the proposed experiment is shown in figure 4.14 which uses an atom chip with a central conductive wire sculptured in the pattern indicated (figure 4.9). Initially, ultracold ^{87}Rb atoms are trapped in the $F = 1, m_F = -1$ state and evaporatively cooled to a BEC using the long-period axial array that is localised on the left-hand side of the wire at a height of ≈100 µm. For a 300 mA wire current which is sustainable for microwires [Gro04], the typical radial trap frequency $\omega_r/2\pi = 220$ Hz where the offset field is chosen as $B_z = 3.2 \times 10^{-4}$ T. For the 300 µm long period, the axial trap frequency is $\omega_z/2\pi = 28$ Hz. With each well in the array containing 10^4 condensed atoms, the chemical potential $\mu = 910$ Hz.

Since the condensate only samples a restricted fraction of the B_z landscape, it is straightforward to adiabatically transport it horizontally across the wire transforming the axial confinement from a single well into a double-well potential. In figure 4.14 this double well is localized above the short period, right side of the

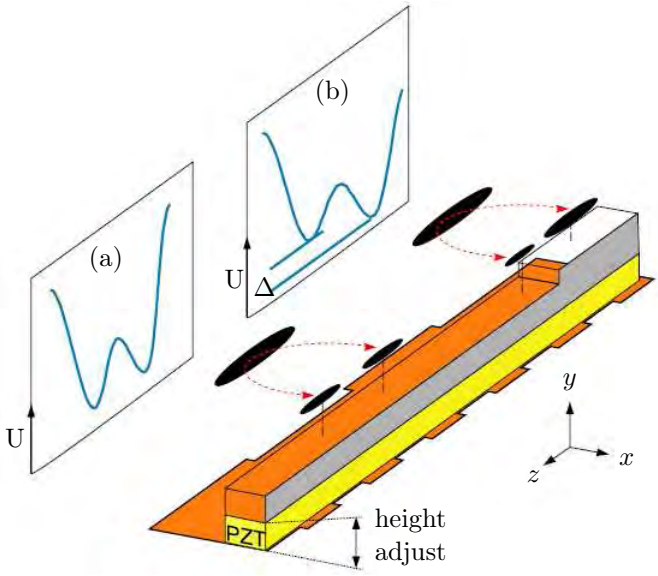

Figure 4.14: Schematic of an adiabatic splitting experiment that uses the sculpture wire pattern of figure 4.9). In (a), the attractive C-P potential is both balanced and strongly attenuated due to the increasing distance between the dw potential and the surface under study. In (b), the right well is lowered by the attractive C-P potential due to the close proximity of the raised surface. This results in a larger condensate fraction in the right well. The height of the structured surface is controllable at the nanometre level by a piezo-electric disk.

wire edge. At this edge, a structured sapphire surface is introduced whose height is controllable with a piezoelectric transducer. In section (a), the surface is uniformly flat in addition to being recessed by 20 µm when compared to the surface below section (b). This recessed section attenuates the C-P potential such that its effect is unobservable thus making (a) a calibration sensor which enables non-C-P effects to be corrected for, for example a slow drift in the magnetic field gradient along z over time. The half-raised section above (b) introduces a spatially localised C-P effect which introduces an asymmetry in the double-well potential.

The magnitude of this asymmetry is dependent upon the distance between the surface and the trapping minimum and can be calculated using established parameters for alkali atoms such as ^{87}Rb [Ant04]; for example at 1 µm separation an asymmetry of $\Delta/2\pi = 3$ Hz develops. This level of asymmetry should be discernable with just a single measurement using the adiabatic splitting technique goven above parameters and shot-noise-limited atom detection capability. This

can be further improved with averaging over multiple measurements provided statistical fluctuations dominate. Moreover in a recent paper, it was theoretically shown that a phase separable two-component BEC could be used to improve the mapping accuracy for potential energy landscapes over that performed with a single BEC [Bho08]. This improvement requires that the scattering parameters are comparable and that both BEC components experience essentially the same potential landscape. Both of these criteria are met using the $F = 1, m_F = -1$ and $F = 2, m_F = 1$ states in ^{87}Rb which can be easily prepared using a two-photon microwave plus radio frequency transition [Mat98]. The chemical potential of a single condensate sets the accessible energy scale of the splitting measurement and cannot be arbitrarily lowered without reducing the density and the atom imaging signal. A better strategy is to adopt a two-component system where the effective potential that the components experience is scaled by $1 - (a_{11}/a_{22})^{1/2}$, where a_{11} and a_{22} are the interstate scattering amplitudes. Using ^{87}Rb parameters, a possible $35\times$ improvement in sensitivity motivates future exploration of this concept.

4.3 Concluding Remarks

A magneto-resistance microscope was presented that can quickly and 'in air' evaluate the magnetic field of a given microwire in one dimension with a resolution of 5 µm, and a magnetic field sensitivity that is comparable to cold atoms (though not BEC). This sensor was the basis of the work published in [Vol08]. A method was presented that allows to calculate the full, three dimensional field produced by a two-dimensional current by measuring just one of its dimensions and knowing the distance. This was used to acquire the full, three dimensional magnetic field produced by a straight, femtosecond ablated microwire. This allows to make an early comparison between the fs-ablated microwire and microwires produced lithographically elsewhere. This can be seen in figure 4.15, where the fs-microwire's characteristics are added to the initial figure taken from [Krü07].

The idea of using sculptured edges for magnetic field shaping was introduced, and the geometry of the edge of a microwire that produces an array of double wells was presented. Corrugating both edges with periodic shapes, where the ratio of the

periods on each side is integer and the two corrugations are in phase can produce a potential of the magnetic field parallel to the wire that produces a string of double wells. The validity of this shape was assessed both by computation (finite element analysis) and fabrication and testing with the MRM. Both assessments agree very well.

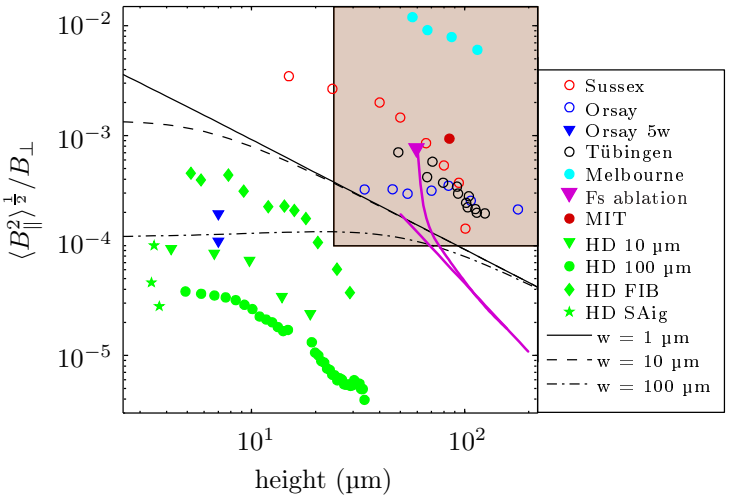

Figure 4.15: Revisiting figure 3.2 with the addition of the femtosecond ablated wire where the magnetic field roughness is measured using the MRM (dark magenta). The magenta curve originating from this point and its exponential fit are the ones given in figure 4.7d)

Chapter 5

Cold Atoms Apparatus for the Atom Chip Characterisation

Measurements with the SEM and MRM reveal excellent quality of physical and magnetic properties of the ablated straight and structural microwires. The next logical step is to use ultracold atoms for probing and mapping the magnetic fields and compare the results with the data from the MRM measurements. The aim is to expand on the expertise acquired from our first atom chip experiment, described in [Whi07a], with some modifications:

Firstly, the atom chip includes the femtosecond ablation created microwires instead of permanent magnetic films, secondly, the setup was to be more compact and more modular, and thirdly the turnaround time between successive creations of cold clouds/BECs was to be considerably shortened by implementing a scheme to directly inject cold atoms into the trapping region, thereby combining high loading rates with low vapour pressures.

5.1 Dual Layer Atom-Chip

The atom chip is composed of two layers: The bottom layer of machined silver foil and the top layer of femtosecond laser ablated microwires.

5.1.1 Silver Foil Layer of the Atom Chip

The microwires lack the ability to withstand the high currents needed for large volume on-chip traps that should capture around 10^8 atoms. Such a large number of trapped atoms is required because the evaporative cooling process reduces the atom number by several orders of magnitude on the way to condensation. Therefore, a second layer of a 250 µm thick silver foil is located beneath the microwire atom chip, and 1.4 mm wide wires were milled as given in figure 5.1.

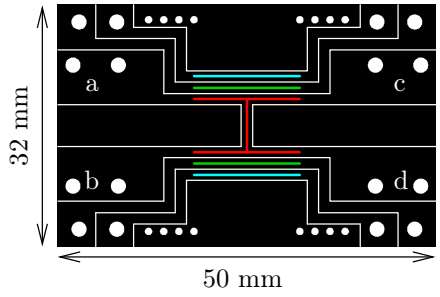

Figure 5.1: The structure of the silver foil layer of our atom chip. High currents of up to 30 A allow for capturing large numbers of atoms. The H-shaped structure (red) in the centre can be used for trapping in both a U-shape (current going from b to a) for a quadrupole trapping potential and a Z shape (going from c to a) for a Ioffe-Pritchard trap. Next to the H structure are the end wires (green) to confine the atoms in the magnetic trap, and the rf wires (blue) for rf evaporation.

A QuickCircuit 5000 milling machine was used for machining the required structure. Once the pattern was transferred into the controller, it was tested on a 1 oz single sided copper clad piece of VERO board using a #20 mil endmill with a diameter of 508 µm. This endmill can cut the roughly 30 µm thick copper layer and additional 20 µm of the fibreglass/resin backboard in a single pass, so the whole pattern was milled in less than 10 minutes.

The silver foil used to fabricate the bottom layer of our atom chip has a thickness of 250 µm. This thickness was chosen as a reasonable compromise between increased thickness of the wires (resulting in lower resistance and heating, thereby allowing more current) and the closest possible proximity between the centre of the wire and the atom cloud. To enhance its flatness, the silver foil was clamped between two steel flat plates, gauge blocks, and thus heated to about 220°C for two hours. This annealing process relieves internal stress, thereby resulting in a flat foil. Before the

milling, the silver foil was bonded to a Cu clad VERO board using Loctide 406 epoxy. This epoxy has a high tensile strength for bonding metals together (about 3000 psi), fixes in under a minute, and its recommended maximum temperature is 80°C. During the fixation, the silver foil is pressed to the VERO board by the gauge blocks.

The milling of the silver foil was performed with a #20 mil endmill with a diameter of 508 µm at 25 krpm (thousand rotations per minute), and a velocity of 5 mm/s. This cut was repeated five times while increasing the milling depth by 50 µm until the silver foil was completely cut. The holes, both ⌀ 1 mm and ⌀ 2 mm, were cut with a M1 drill, as the M2 drill had damaged the silver foil in previous attempts. After the milling, a 100 nm Cr layer was deposited at room temperature onto the silver foil. This Cr layer ensures the bonding between the silver foil and the epoxy used in the next step. The ceramic base is then glued to the silver foil using EPOTEK H77 epoxy, which is coated generously on the silver foil to fill the insulating grooves as well as to bond the foil to the ceramic. This should improve the heat dissipation in the wires. The ceramic base has to be carefully aligned to the holes in the foil, and fixed there using some alignment screws and wires. The H77 epoxy is then cured at 150°C, which exceeds the maximum temperature of the loctide bonding the foil to the VERO board.

While the foil is glued between the ceramic and the VERO board, the holes have to be cut through the whole structure, using diamond coated drills, as the steel and cobalt impregnated drills were blunted by the ceramic. Afterwards, the VERO board is no longer needed and has to be removed. The loctide is already weakened by the excess temperature during the bonding of the H77 epoxy, but still too strong to be easily removed. Therefore, the VERO board was hand polished using coarse sandpaper and water until the VERO board was reduced to a thickness of about 100 µm. Now the VERO board can be carefully locally lifted using a scalpel and copious amounts of acetone to dissolve the glue. Once the board and the loctide is completely removed, the atom chip can be cleaned using an ultrasound bath in an Extran detergent (10% Extran, 90% H_2O). Excess H77 epoxy, which had filled the gaps which extended through the foil further into the now-removed VERO board has to be carefully removed by polishing the foil with very fine sand paper.

These wires can withstand currents of up to 30 A, which is enough to produce the magnetic field gradients for magnetic and magneto-optic trapping. The central wire is an H-structure, which is similar to the one described in [Hal06]. It allows a current to be applied both in a U configuration, which together with a homogeneous bias magnetic field generates a quadrupole magnetic field, as well as in a Z-configuration, which in turn results in a Ioffe-type magnetic potential. Two wires next to the H structure are so-called end wires, used by running a small dc current in parallel. This closes off the waveguide shaped Ioffe-trap and prevents atoms from spilling out at the sides. Finally, two rf wires can be used for rf evaporation. The small rf current runs anti-parallel through these wires. For perfect electrical contact, the high-current H structure is connected to the power supply by broad-area clamps with two screws each to minimise resistance and localised heating.

5.1.2 Microwire Chip

With the findings presented in section 4.2, a microwire atom chip was fabricated on a 22 mm by 22 mm, 400 µm thick sapphire substrate. The sandwich structure of the deposition is as follows (from bottom to top):

1. 20 nm of chromium to improve adhesion,
2. 300 nm copper
3. 20 nm chromium
4. 80 nm gold for protection and better reflectivity.

Into this multilayer structure a pattern forming five wires (see figure 5.2) was written using femtosecond laser ablation. The centres of the wires are equidistant with a spacing of 100 µm. The wires 1, 3, and 5 are 40 µm wide wires that can be used for rf dressed potentials. Wire 4, a straight, 100 µm wide wire can be used for radial trapping. The measurement of fragmentation of ultracold atoms in a magnetic trap produced by this wire is meant to quantify the quality of the femtosecond ablation process by measuring $\Delta B_{||}/B_{\perp}$ to a better accuracy than that produced by the MRM in section 4.1.2. Furthermore, the rf wires 3 and 5 can be used to perform rf dressed potential experiments similar to [Les06].

Wire 2 finally is a sculptured wire as described in section 4.2. The edge facing wire 1 has the following 300 µm period pattern: 150 µm along the wire, 1.6 µm out, 150 µm along the wire, 1.6 µm in. The edge facing wire 3 has the short range, higher amplitude pattern: 50 µm along, 5 µm out, 50 µm along, 5 µm in. To create a double-well potential, the steps out and in must coincide on both edges. The whole pattern can be seen in figure 5.2.

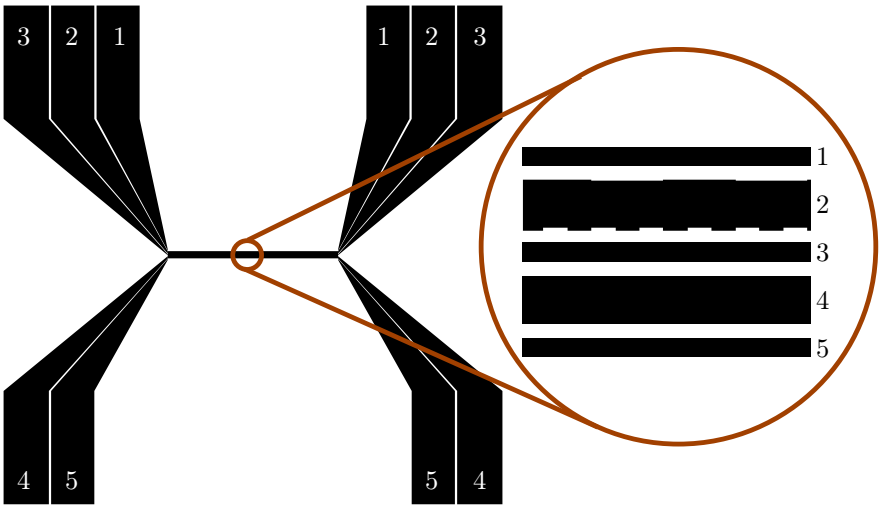

Figure 5.2: The microwire layer of the atom chip: The microwire atom chip has an area of 22 mm by 22 mm. Large, 5 mm by 2 mm pads are created to attach the wires leading to the chip. In the centre, the five wires have a straight, 7.5 mm long experimental region, where they are parallel to each other with a distance of 100 µm. Wires 1, 3, and 5 are 40 µm wide rf wires, wire 4 is a straight, 100 µm wide wire and wire 2 is a 100 µm wide wire with sculptured edges.

The femtosecond laser ablation was performed according to table 5.1. After

Table 5.1: The fabrication map for the microwire atom chip. Note that the cuts #3 to #8 were only performed on the sensitive experiment region.

	Distance	Intensity	Velocity
cut #1	5.5 mm	280 nJ	200 µm/s
cut #2	4.0 mm	280 nJ	200 µm/s
cut #3	3.0 mm	55 nJ	100 µm/s
cut #4	2.5 mm	55 nJ	100 µm/s
cut #5	2.0 mm	55 nJ	100 µm/s
cut #6	1.5 mm	55 nJ	100 µm/s
cut #7	1.0 mm	55 nJ	100 µm/s
cut #8	0.5 mm	55 nJ	100 µm/s

fabrication, the wires were tested for shorts by measuring the resistance between the pads and by optical imaging. Two areas between the pads had to be insulated again by ablating squares around defects in the sapphire surface where copper and gold had been deposited and was not ablated due to being out of focus, but no defects on the experiment region were found.

The femtosecond ablation fabricated microwire layer was glued to the silver foil using EpoTek H77 epoxy. Wires were attached to the pads of the microwire chip using EpoTek H21D conductive epoxy and guided through the small 1 mm diameter holes seen in figure 5.1. Spillage of the conductive epoxy caused additional shorts between the pads, but this too was corrected by placing the whole structure into the ablation apparatus and ablating at high power in air around the spillage. The resistivity between the connections was measured by running a fixed current of 50 mA through each wire and measuring the voltage drop across each connection between copper wire, epoxy and atom chip. The resistance of the thinner rf wires (40 µm) is about 35 Ω, whereas the thicker 100 µm wide dc wires (2 and 4) have a resistivity of about 17 Ω. The biggest uncertainty in the resistance was found in the connection between epoxy and the atom chip, where the values vary between 12 Ω and 70 Ω. The resistance between copper wires and the epoxy was with one exception beneath the measurement threshold of 1 Ω.

Table 5.2: The resistances in the microwire atom chip factored into the different occurrences. Note: due to an error during the measurement the data for wire 4 was lost.

Wire	1	2	3	4	5
current type	rf	dc	rf	dc	rf
Cu wire to epoxy	0 Ω	0 Ω	0 Ω		0 Ω
epoxy to chip	12 Ω	70 Ω	8 Ω		14 Ω
pad to pad	34 Ω	18 Ω	38 Ω		36 Ω
chip to epoxy	26 Ω	62 Ω	36 Ω		32 Ω
epoxy to Cu wire	0 Ω	0 Ω	12 Ω		0 Ω
Sum	72 Ω	150 Ω	84 Ω		51 Ω

A photograph of the assembled atom chip is shown in figure 5.3.

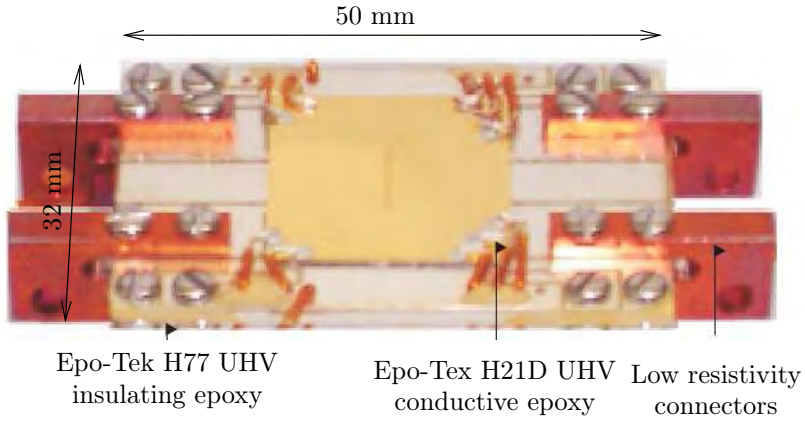

Figure 5.3: Photo of the final atom chip. The square 22 mm by 22 mm microwire chip is attached to the 50 mm by 32 mm silver foil layer using insulating epoxy (EpoTek H77). Copper wires are attached to the microwire pads using conductive epoxy (EpoTek H21D). To have a low resistivity for the high current silver foil layer, the connectors for the H structure are copper blocks with a large area for optimal connection, whereas simple screws conduct the current into the end and rf wires of the silver foil structure.

5.2 Vacuum Chamber

The background pressure of thermal atoms and molecules must be reduced to some 10^{-9} Torr to prevent excessive losses due to collisions of these with the cold atoms in the magneto-optical trap. Evaporative cooling towards BEC requires even lower pressures of several 10^{-11} Torr or below. Vacuum systems are therefore essential for atom optics experiments. In this section, a short introduction into vacuum systems is given, the preparation of vacuum components is described, and finally a description about our vacuum system is presented.

5.2.1 Basic Principles of Vacuum

The measure of vacuum is the measure of the pressure inside the system. The SI unit of pressure is Pascal (Pa); however, when describing very high and ultrahigh vacuum systems, it is more common to use the units Torr or mbar. In this thesis, pressure is measured in Torr: 1 Torr $\approx$ 1.33 mbar = 133 Pa. The classification of vacuum according to the pressure can be seen in [O'H03, p.4], this vacuum system has to rate in the very high vacuum (10^{-6} – 10^{-9} Torr) and ultrahigh vacuum (10^{-9} –

10^{-12} Torr) range.

Pumps Depending on the desired vacuum, several different types of pumps are utilised during different stages of the evacuation process. The most important characteristics of a pump are its speed and its base pressure. The speed, given in litres per second (l/s), measures the volume of gas (V) displaced by the pump per unit time. The actual amount of gas displaced is dependent upon the vessel's pressure (P). The product of pressure and pumping speed yields the throughput K which is the number of particles removed per unit time and is given in Torr l s^{-1}. The base pressure is the minimum pressure obtainable when pumping on no load (i. e. a blind flange attached directly to the pump). At the base pressure, backstreaming and other adverse effects equal the throughput of the pump and thereby negate any effect of the pump. Backstreaming describes the effect that when the pressure differential between the inlet of the pump and its exhaust is sufficiently large, some particles (atoms, molecules) will pass the pump in the reverse direction. For a real vacuum system with finite vessel size, the base pressure of the pump is rarely obtained due to loads arising from other parts of the system. These loads, which are described in detail below are, with the exception of leaks (the first list item) usually lumped into the term outgassing.

- **Leaks:** Small unsealed holes in the vacuum chamber allow atmospheric gases to pass into the vacuum vessel. The most likely locations of such leaks are the connections where parts of the vessel are attached together, transitions between different kinds of materials (glass-to-metal in viewports, metal-to-ceramic in feedthroughs, etc.), and welded links. While leaks in the connections can often be overcome by re-tightening the screws or replacing the gasket, the other two cases mean that this component has to be replaced. In our experiment, all parts of the hull of the vacuum system have been manufactured by companies specialising in ultra-high vacuum components.

- **Virtual leaks:** Small pockets of air locally trapped inside the vacuum system can slowly penetrate into the main vacuum vessel. A common example of this is a blind tapped hole, a hole with only one opening in which a screw is secured. The air beneath the screw is released only slowly during the

evacuation process, and can easily become the dominant and persistent load on the pumps. To counter this, good engineering practise requires that no pockets of air remain inside the system without a high conductivity path to the vacuum vessel/pumps.

- **Desorption:** Once the volume of gas has been removed, the rate of decrease of the pressure is quickly limited by the process of desorption. Particles that are attached to the inside walls of the chamber desorb into the system. This is countered in two different steps: First, it is important to clean the components thoroughly to remove molecules that desorb slowly (i.e. molecules with low vapour pressure, like oils). The second step is to bake the chamber to a high temperature which increases the desorption rate, thus raising the vessel pressure and the pump throughput. This is usually done while operating the displacement pump so that the desorbed material is completely removed from the vessel. Upon returning to room temperature, resorption to the depleted inner surface of the vessel dominates desorption, resulting in an increased pumping speed and a rapid reduction in pressure of up to three orders of magnitude.

- **Permeation:** Gases (mostly H_2) can transverse through the material of the vacuum chamber; however, the gases transverse with different speeds through different material. Thick stainless steel walls reduce the permeation to irrelevant amounts; however, viton O-rings used as gaskets can have noticeable high permeation characteristics. For this reason, copper gaskets are used instead of viton gaskets in the vacuum vessel. If needed, permeation can also be reduced by placing the vacuum system inside a vacuum system, but that is relevant only for extreme ultrahigh vacuum, or when strongly permeating components are needed (an example of this is given in [Die01, p. 31]).

- **Diffusion:** Gases (mostly H_2) that have been trapped inside the chamber wall materials during the manufacturing process are released into the vacuum chamber. Raising the temperature enhances this effect, so during the baking with the displacement pumps these gases are released into the chamber and pumped away. For certain experiments, it might be useful to pre-bake the

components, which means heating them up to temperatures that other parts of the vacuum system could not withstand (several hundred degrees Celsius) under vacuum before the assembly of the final chamber to reduce the amount of trapped hydrogen gas.

- **Vaporisation:** The material of the vacuum system itself dissolves into the air. Different materials vaporise differently. In our system, the most readily vaporising material is the rubidium reservoir, but wire coatings and glues also vaporise.

Vacuum pumps can be distinguished in two different classes: Displacement pumps transfer the gas from inside the vacuum chamber to the atmosphere. This is needed early in the evacuation process, when there is still a lot of gas inside the vacuum chamber. Examples for displacement pumps are rotary pumps, diaphragm pumps, and turbo-molecular pumps. However, because they have a real connection to the atmosphere, they are prone to backstreaming. Thus to improve the pumping, this connection must be closed and a different type of pump used. Vacuum getter pumps securely trap the gas inside the vacuum chamber, such that it cannot reenter the vacuum. Examples of getter pumps are ion getter pumps, non-evaporative getter pumps and titanium sublimation pumps.

5.2.2 Preparation of Vacuum Components

To achieve ultrahigh vacuum, all components have to be carefully inspected and prepared. The inspection mainly focuses on the knife edge, which will bite into the copper gaskets and form the seal. Damages to the knife edge usually disqualify the component from reaching ultrahigh vacuum with a reasonable amount of pumps. However, at one point pressures below 10^{-10} Torr in a 6-way cross with a noticeable scratch across the knife edge have been achieved. Still, components with damaged knife edges should be avoided if possible, as they are most likely a cause for a leak.

After the inspection, to prevent excessive outgassing, the stainless steel components should be washed. (Copper gaskets should remain in their plastic seal until just before assembly and should not be cleaned. The soft copper might bend or scratch easily, which is a risk not worth taking.) Even new, sealed

components have occasionally been dirty; older parts which have been stored will most likely have attracted dust and other contamination. The procedure for cleaning vacuum components at this laboratory has been tried and produces clean and usable components:

First the components are cleaned in soap water, which removes larger dirt particles. Then they are submerged in an ultrasonic bath with an Extan solution for 15 to 30 minutes. This removes residual grease and similar contamination. For excessively dirty components, this procedure can be repeated once or twice (as deemed necessary). The component is then washed with tap water to remove remaining Extan, distilled water to remove remaining dirt from the tap, and finally acetone to remove any residual water. Afterwards, the component is blow-dried in a clean nitrogen jet, after which it is ready for assembly. All this should be done shortly before the actual implementation of the components, as prolonged exposure to air (weeks, months) can reduce the effects of the cleaning.

Suggested screw dimensions (diameter and pitch) as well as the optimum torque are usually given with the components, however, we found that a torque wrench is not necessary for assembly. The thread of the bolts should be coated in anti-seize to allow easier disassembly when the vacuum chamber has to be opened again. During the assembly, unpowdered latex gloves should be worn to protect the inner surface of the vacuum chamber from natural grease of the fingertips. Handling both the anti-seize coated bolts and the vacuum components that must be kept clean inside at the same time is tricky, and using more than one person for this helps a lot. Once two components are joined and the copper gasket is secure in between, the screws are tightend slowly and evenly, so that the knife edges of the two parts cut evenly and deep into the gasket.

When opening the vacuum chamber for minor changes (e.g. fixing a leak or replacing an atom chip), it is advantageous to flush the chamber with a noble gas (helium or better argon) instead of air, as these gasses are far less absorbed into the inner surface of the chamber. This accelerates the next evacuation.

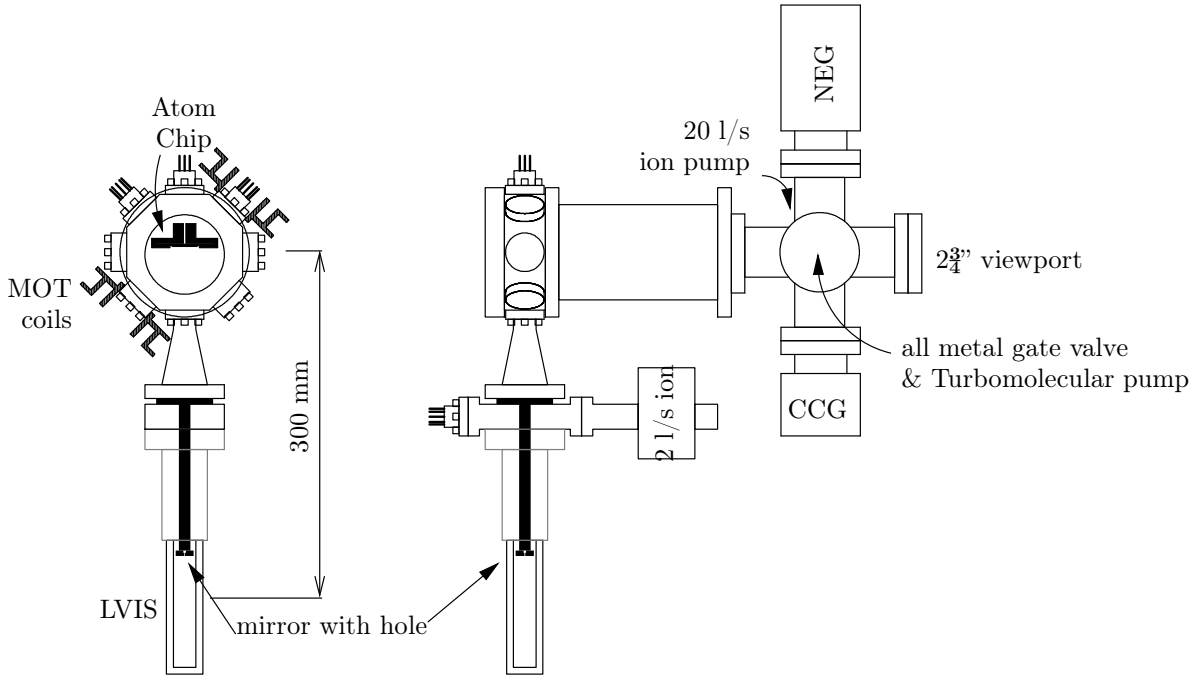

Figure 5.4: The schematic of the vacuum system: On the top is the atom chip chamber. It has a main $4\frac{1}{2}$" viewport on one side, the other side connects to the pumps (a 20 l/s ion pump, a 120 l/s NEG and a turbomolecular pump behind an all metal gate valve) and to another $2\frac{3}{4}$" viewport. Of the eight conflat mini connectors, the three at the top are used for feedthroughs for the atom chip, the two horizontal ones are used for absorption imaging of the cold atoms, the two connectors halfway down are for the mirror MOT beams, and the bottom one connects to the LVIS chamber. This chamber itself consists mainly of a glass cell, attached to a $2\frac{3}{4}$" connector with 2 additional conflat mini connectors, one having the feedthrough for the Rb source, the other connecting to a compact 2 l/s ion pump.

5.2.3 The Vacuum System

To combine the faster loading rate of a MOT at rubidium pressures around 10^{-8} Torr with the requirement of ultrahigh vacuum for evaporative cooling towards BEC, we have adopted a two-chamber system: The atom chip chamber with a UHV of about 6×10^{-11} Torr, which yields an estimated lifetime of more than 30 s, and an LVIS chamber with a pressure of about 2×10^{-8} Torr. These two regions are connected by a small hole through which a cold atom beam can propagate vertically into the trapping region inside the atom chip chamber.

The conductance between the two chambers is small enough to allow for a pressure differential between the two chambers of up to a factor of 1000.

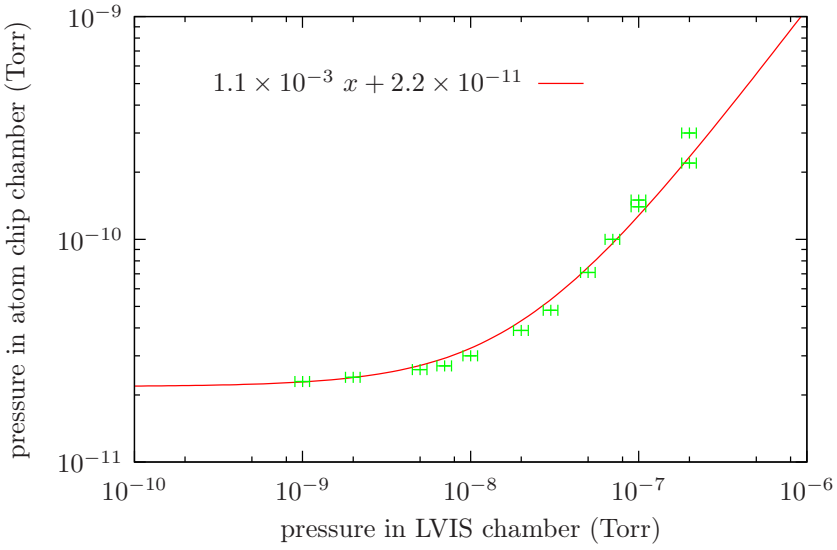

Figure 5.5: The dependence of the pressures in the atom chip and the LVIS chamber. The pressure in the LVIS chamber was raised by releasing rubidium from the dispenser. When the pressure in the LVIS chamber reaches about 10^{-8} Torr, it becomes the main load on the atom chip chamber. The red line is a linear fit which reveals the ratio to be nearly 1:1000.

The LVIS Chamber is designed to be small and compact. It consists of a glass cell (dimensions: outside: 32×32×118 mm^3, inside: 20×20×112 mm^3) on a conflat $2\frac{3}{4}$" flange, a small, 2 l/s ion getter pump, and a rubidium source. Inside the LVIS chamber, at the connection to the atom chip chamber, a quarter wave plate (Comar 195CM25, ⌀ 25 mm), coated with silver on the far end, is mounted as a retroreflector for the LVIS operation. An 0.5 mm diameter, 5 mm long hole is drilled through the centre and provides a low conductivity pathway between the LVIS chamber and the atom chip chamber.

The main part of the atom chip chamber is a Kimball physics spherical octagon (MCF450-5020008) mounted on top of the LVIS Chamber. It has two conflat $4\frac{1}{2}$" and eight conflat mini connectors. Of its conflat mini flanges, one connects to the LVIS chamber (the bottom one), two have viewports for the mirror MOT beams, two more have viewports for imaging and optical pumping, and the other three have electrical feedthroughs for the atom chip, which is located upside down in the centre of the octagon. On the one side of the octagon, a $4\frac{1}{2}$" viewport gives access for another MOT beam, a second imaging axis, and other access as required (eg. a photo diode for fluorescence measurements). The other side is connected to a $2\frac{3}{4}$"

six-way cross, which in turn connects to a turbo pump, a 20 l/s ion getter pump, a non-evaporative getter pump with 120 l/s for H_2, and a cold cathode gauge for measuring the pressure. The far side of the cross has a viewport connected to allow retroreflecting of the horizontal MOT beam.

5.3 Laser System

The optical fields needed to trap, manipulate and image the atom cloud are created by diode lasers. Before describing the lasers it is elaborated how these lasers were locked with a precision of around 1 MHz to the hyperfine levels or at the desired frequency at a certain detuning from the hyperfine transition.

5.3.1 Frequency Locking Scheme

It is crucial that the laser frequency is locked in a region less than one Megahertz, as frequency fluctuations can hugely affect the interaction characteristics between the atoms and the light, which could make trapping, cooling and observation of the atoms unreliable at best and likely impossible. Lasers are therefore locked to required transitions using gases in reference glass cells. To lock a laser, it is necessary to obtain an error signal, a signal whose sign describes the sign of the frequency error, and preferably with an amplitude that shows the magnitude of the error.

At room temperature, gases have a Doppler broadening which is much larger than the hyperfine splitting of the excited states or the required resolution of the lock, so a saturated absorption system has to be used. Commonly this is realised by having a pump beam transversing the gas in the opposite direction of the probe beam, where the pump beam is more intense than the probe beam. Often, probe and pump beam are originating from the same laser and have the same frequency, though that is not necessary. When scanning the frequency over the Doppler broadened absorption line of the gas, at certain frequencies the two beams will interact with the same velocity class of atoms in the gas. As the pump beam is stronger than the probe beam, it will shift a large portion of the atoms into the excited state, thereby reducing the absorption of the probe beam. This happens when the laser is on resonance with one of the hyperfine transitions, where both beams interact with atoms with negligible

velocity parallel to the propagation direction, but also when the frequency is exactly in the centre between two hyperfine transitions, where the Doppler shift, added to the frequency on one beam, subtracted from the other, results in the same atoms being resonant to both beams (albeit on different hyperfine transitions).

One option to lock the laser to such a feature is to modulate the frequency of the laser and to correlate this modulation to the signal of the probe beam using a lock-in amplifier. If the base frequency of the laser is located at the maximum of a transmission line, the intensity fluctuations of the probe beam will oscillate dominantly with twice the frequency of the laser modulation, as during one cycle the signal will drop slightly once left and once right of the top. If the base frequency, however, is on the flank of the transmission peak, the lock-in amplifier will show a clear correlation between the two signals, with the sign of the correlation indicating the direction of the offset.

This method is reliable and often used, for example at locking the lasers in the magnetic mirror experiment described in chapter 6 in this thesis. However, one drawback is that the frequency of the laser has to inherently oscillate, a feature usually not desired. In this experiment it was therefore decided to use a polarisation spectroscopy lock. This scheme utilises the effect that a probe beam close to resonance counterpropagating to a circularly polarised pump beam in a gas will experience a highly frequency dependant rotation of its polarisation plane [Wie76, Lan99, Pea02, Yos03]. The circular polarisation of the pump beam results in a change in the refractive index for the left-handed and the right-handed circular polarised part that make up the linearly polarised probe beam. This effect is called *Doppler-free Light Induced Birefringence*, or DLIB. This birefringence rotates the plane of polarisation of the probe beam proportionally to the detuning of the frequency, an effect that can be measured by running the so-altered probe beam through a polarising beam splitter and then onto two photodiodes. Subtracting the signal from one photodiode from that of the other results in a Doppler-free, jitter free error signal which can be used to lock the laser. Once the lasers are locked, their frequencies can be precisely and coherently changed by acousto-optical modulators (AOM). This is shown in figure 5.6.

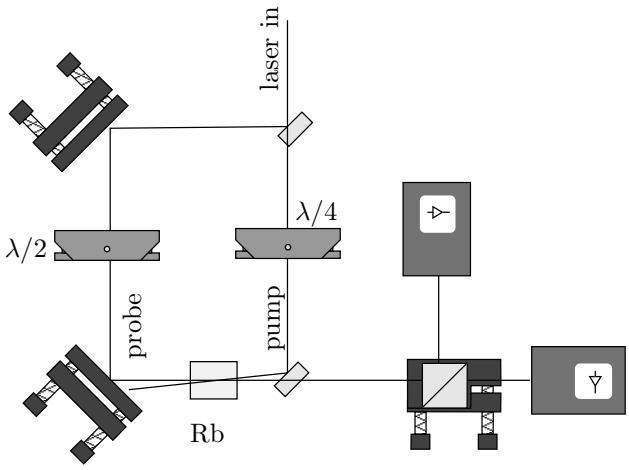

Figure 5.6: Schematic of the polarisation spectroscopy locking scheme: The circular polarisation of the pump beam introduces a rotation of the polarisation of the probe beam via Doppler-free light induced birefringence close to a hyperfine transition. This is measured using the difference in intensities of the two outputs of a polarising beam splitter.

5.3.2 Toptica DLX110

A Toptica DLX110 laser which is frequency stabilised by a polarisation spectroscopy lock to the ^{87}Rb resonance at 780 nm produces more than 500 mW of coherent light with its frequency tuned at 18 MHz below the $F = 2 \rightarrow F' = 3$ transition. The laser has two output beams, one of which is used for locking, and one for the experiment. The lock arm double passes an AOM tunable around (2×)55 MHz before entering a polarisation spectroscopy frequency lock. There, the light is locked to the $F = 2 \rightarrow F' = 3$ cycling transition, where the differential signal is linear over about 10 MHz, and can be used directly as error signal for the Toptica Lock-Box. A second, fixed frequency AOM in the operation beam is used in single pass to shift the laser frequency back to resonance. Between these two AOMs, the frequency can be shifted between -60 and +15 MHz and the laser instantly switched on and off without any change to the propagation path. However, for this experiment, the laser is held constant at -18 MHz detuning. The light from the DLX laser is split into two parts, with one required for the operation of the Atom Chip 1 experiment. The other part is again split using a halfwave plate and a polarising beam cube. Each beam is then steered using two independent two stage mirrors in a horizontal periscope configuration to enter a single mode polarisation preserving fibre. The polarisation

of the laser beam is rotated by a halfwave plate to match one of the polarisation preserving axes in the fibre to minimise uncontrolled polarisation drifts in the fibre. One of these fibres supplies the trapping light for the LVIS, the other fibre brings the laser light to another laser table. Prior to injection locking the slave diode laser, the beam is double passed through an AOM with a frequency of 40 – 85 MHz (called Master AOM in the rest of this document). This arrangement allows the frequency of the slave laser to be modulated over a range of -180 – -95 MHz relative to the $F = 2 \rightarrow F' = 3$ trapping transition.

Coupling light into polarisation preserving single mode fibres As this experiment used more than six polarisation preserving single mode fibres, this section should give a suggestion as to how to best couple the light into these fibres. Two high accuracy mirror mounts should be used to steer the beam into the in-coupler, and the laser needs to be locked as it might have different beam characteristics when it is unlocked as opposed to when it is locked. It is highly advantageous if either the in-coupler or the final fibre has the option to carefully change the distance between lens and fibre, otherwise any convergence or divergence of the laser beam will reduce the efficiency of the in-coupling.

If the end of a fibre with coupled light is already available, it can be used to pre-align the laser light: The output port of the fibre already carrying light is connected to the fibre in-coupler so that the two laser beams counter-propagate. This way it is possible to align the desired beam with the beam coming out of the fibre. If this is not possible, the fibre should still be detached from the in-coupler, and the strongly diverging spot of the light behind the in-coupler can be observed. The laser is sufficiently pre-aligned if this spot is round, without additional reflections or shadows at the corners, and its centre is aligned with the axis of the in-coupler.

The fibre should now be loosely attached to the in-coupler, just enough that its tooth interlocks with the notch in the in-coupler. The further the fibre is out of the in-coupler, the less the efficiency, but the easier it is to maximise that efficiency. Pointing the output of the fibre directly onto a camera will allow any coupled light to be seen immediately, and the first iteration of beam steering to maximise the light intensity at the output can be done this way. As more and more light is coupled into the fibre, the observation of the light intensity should be done with

a powermeter, firstly because a security camera is not made to observe laser light of high intensities and might be damaged, but also because this allows for a more quantitative measurement.

The coupling is maximised on both the horizontal and the vertical axis independently of each other, but using both mirrors at the same time. Once it is found that one has reached more or less the maximal coupling, the fibre is carefully screwed into the in-coupler a bit more, until the light intensity at the output has seriously diminished (however, it should not go down to zero, as this might make it harder), and then the maximisation process is repeated. This is done until the fibre is all the way in the coupler. The maximal achievable efficiency depends mainly on the transverse mode of the beam and its divergence. The minimum should be about 40% to 50%, high quality beams can have efficiencies exceeding 80%.

The final step is to align the polarisation of the light with the fibre. For this, a half wave plate is positioned before the in-coupler (and will remain there); another half wave plate and a polarising beam splitter are located behind the outcoupler. A powermeter measures the light intensity coming from one arm of the beam splitter. The wave plate before and after the fibre are rotated alternately to minimise the signal on the powermeter. The final value should be well below 1% of the original transmission. If that can not be achieved, rotate both wave plates by 45° to test the other polarisation plane.

5.3.3 Slave Laser

The laser light from the fibre is then coupled into the Sanyo 80 mW diode laser using the optical isolator where the input and output polarising elements have been replaced by two polarising beam cubes mounted with their bases at 45° above the horizontal (input) and at the horizontal (output). This configuration allows light to be coupled through the isolator via the vertical polarised output port (see figure A.2). The injection beam not only sets the frequency of the slave laser, it also transfers some of its good transversal mode that it acquired in the single mode fibre onto the slave laser mode. To verify that the laser is locked, part of its lasing mode is outcoupled by a glass plate and sent through saturated absorption measurement in a Rb glass cell. When the DLX is unlocked and scanning over the resonances,

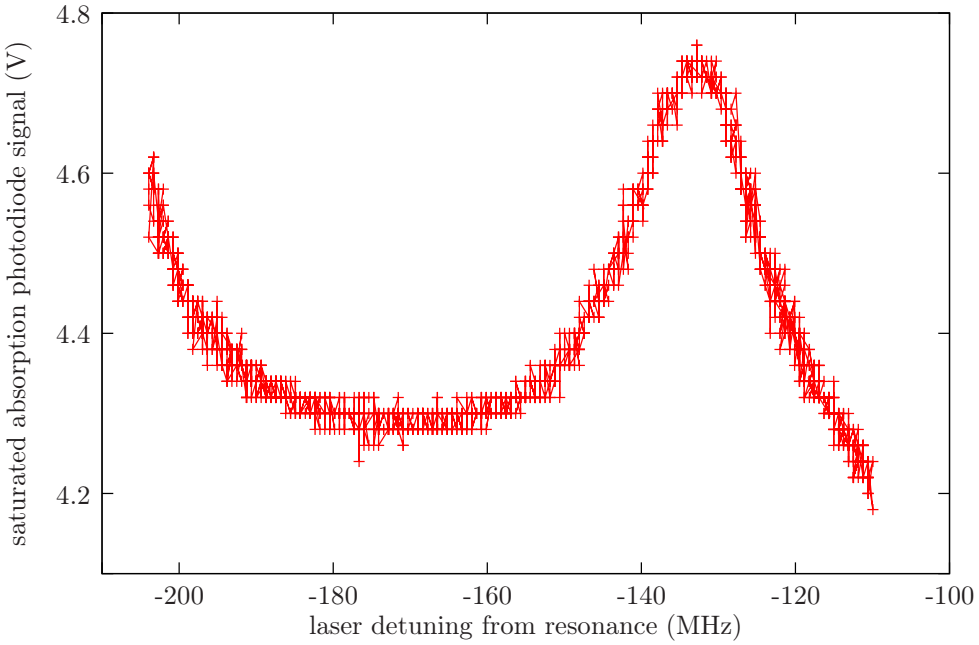

Figure 5.7: Demonstration of the control over the frequency of the slave laser: By modulating both the amplitude and the frequency of the Master AOM, the slave laser follows the injection laser over a range of more than 90 MHz. This resolves the crossover peak of the $F = 2 \rightarrow F' = 2$ and $F = 2 \rightarrow F' = 3$ transitions in the saturated absorption spectroscopy sensor. On the left the start of the crossover peak $F = 2 \rightarrow F' = 1$ and $F = 2 \rightarrow F' = 3$ can be seen.

the presence of the saturated absorption signal of the slave laser beam is used to verify that the injection lock is working. The light then passes once through an AOM (called Slave AOM) with a fixed frequency of +120 MHz, and a computer controllable amplitude. By changing the frequency of the light with the Master AOM and the intensity with the Slave AOM, the light produced by the slave laser can be used for trapping, where the detuning is set to -21 – -8 MHz and maximum amplitude, as well as for optical pumping and imaging (where the light is put onto resonance and the intensity is attenuated). When controlling the intensity of the Master AOM as well as its frequency, thereby keeping the light intensity in the injection beam constant, the frequency can be shifted over a range of more than 90 MHz (see Figure 5.7).

As both intensity and detuning of this configuration are highly controllable with the two acousto-optic modulators, the slave laser can be used simultaneously for

- MOT trapping: This is the most needed one of the operations, generating

the trapping light for the mirror MOT. The majority of the light (40 mW) is directed using a half-wave plate/polarising beam splitter arrangement through a shutter and, via two mirrors, into a single mode polarisation preserving fibre.

- Optical Molasses with far detuning: Increasing the detuning to about 40-50 MHz reduces the capture velocity considerably, but reduces the average velocity of captured atoms as well. When atoms are already captured in a MOT, it is possible to reduce the temperature shortly before the transfer or the release by just changing the frequency of the laser using the Master AOM.

- Optical pumping: During the transfer from the MOT into a magnetic trap, the atoms have to accumulate in the low field seeking $F = 2, m_F = 2$ state. This is done by shining a low intensity, σ^+ polarised on-resonance light field at the atoms. For this, the slave AOM intensity is reduced and the small fraction of light passing through the other exit of the beam splitter mentioned above is used. The light is then sent through a shutter into a second, single mode polarisation preserving fibre.

- Imaging: To observe the cold atom cloud and the BECs, an absorption scheme is used. The same path as for the optical pumping is used, except the intensity is raised by running the slave AOM at a higher intensity.

5.3.4 Repump Laser

The repump transition $F = 1 \rightarrow F' = 2$ is too far detuned (6.8 GHz) from the trapping transition to be conveniently generated by the same laser and shifted using AOMs or other means. A home built extended cavity diode laser with a Sanyo 80 mW laser diode was locked using the error signal from a polarisation spectroscopy lock.

The distinct features of the hyperfine transitions are not as resolved on the $F = 1 \rightarrow F' = 2$ transition as they are on the $F = 2 \rightarrow F' = 3$, so it was actually locked to the flank of a broader peak and then shifted using an AOM to the transition line.

The light is then equally distributed into two beams, each injected into its own single mode fibre, and guided to the LVIS and the mirror MOT respectively.

5.4 Computer Control of the Experiment

During every cycle of the experiments, many changes have to be made with sub-millisecond precision. An example is the change in frequency of a laser, the switching on or off of magnetic field coils, or the triggering of the imaging camera. Since this is not possible to achieve by hand, a computer control system was used. The system itself consists of two computers, the control computer and the acquisition computer.

5.4.1 Computer 1: The Control Computer

The control computer was fitted with a National Instruments PXI system, consisting of

- two PXI-6733 analogue output cards with 8 channels each,
- one PXI-6289 multifunction card, from which 32 digital output channels and the two counters were used, and
- one PXI-5404 function generator card meant to perform the rf evaporation.

Furthermore, NI LabView 8.0 was installed on this computer.

The LabView program that runs on the computer is shown in figures C.1 and C.2. The dominant item on the front panel is a tab control, in which the sequence is displayed. If the first tab, labelled 'All' is activated, the whole sequence is shown. It is displayed as a list of states, with each state represented by one line on the array. Such a line can be seen in figure 5.8.

Figure 5.8: Representation of a single state in the LabView experiment control program.

Each line contains firstly three buttons, 'copy', 'paste', and 'delete', which are implemented for convenience, as it is hard to use the LabView in-built functions for this array due to the complex topology of the array. The next item of the line is a green button, showing whether this state should actually be executed during the run of the sequence. This allows the operator to quickly deactivate parts of

the sequence without actually deleting them. The next item can be used to mark a state as 'interesting' – with consequences described later. Next is a short text field where the operator can write a description of the state, which has no impact on the sequence itself, but will be stored.

The next field sets the time that the experiment should remain in this state, in milliseconds. Following are two arrays of double values (length 8 each) representing the voltages that the analogue outputs will have at the end of the state (if the transition selector is set to 'Step', these voltages will be set during the whole time of the state). Similarly, the next item is an array of Boolean values representing the digital output lines. While only 16 are shown at the moment, the program already uses the whole 32 digital output lines of port 0 of the PXI-6289. The final item is the transition selector mentioned earlier. It selects how the voltages on the analogue output channels are to be changed to the new value. The simplest method is 'Step', where all channels are set to the new values immediately and held at that voltage. Other options are 'Linear', where the voltage is linearly raised or lowered until it reaches the given setting at the end of the state, 'Exponential' where the voltage is changed exponentially[†], and 'Sine' where the values change in a sinusoidal approximation. This has no effect on the digital channels.

Next to 'All', there are two other tabs labelled 'Interesting' and 'Batch'. Only those states marked as interesting on the 'All' selection are shown in these tabs, even though all that are marked 'active' will be executed. The 'Interesting' tab is meant for the operator to focus on a single or few states. As an example, the operator might want to optimise the frequency of the image beam for best absorption imaging. He would then mark the lines corresponding to the absorption image and the reference image as interesting and switch to the interesting tab, where he then only has these two states one beneath the other. He will therefore not accidentally change values in the wrong state, nor does he have to scroll up and down through the list of states between the two occurrences.

The 'Batch' allows the program to execute a number of sequences changing certain states between successive runs. Here, there are three lists beneath each other, showing the same state(s). The top list shows the state as it is; the other

[†]As an exponential sweep can only work if the old and the new value are both positive or both negative, it will default to linear for all channels that do not meet this criterion.

two lists are used to set the initial and the final versions of these states. A numeric control is used to set the number of intermediate runs. As an example, the operator might want to perform a time of flight measurement, and to image the atom cloud in 2 ms time intervals between 4 ms and 30 ms. For this, he would mark the state containing the free fall of the atoms as interesting and switch to the 'Batch' tab. This state will then be shown in all three lists. The operator would then enter '4' into the 'From' time field, '30' into the 'To' time field, and 14 into the number of steps, and then press 'Execute'. As it is only viable to change analogue values or the time for each step in this manner, the digital channels, the transition selector or the active flag are not changed.

Beneath the tab control, one button is for storing the currently selected sequence into the cards, two others are to trigger the execution. One of those will trigger a single execution of the sequence, whereas the other button will continue executing the sequence until pressed again. The 'Save' and 'Load' buttons can save or load a sequence into or from the file given in the line. If the 'Autosave' button is activated, every time a sequence is run, the sequence is stored on the hard disk with an incrementing run number. The files are saved in comma separated values format, so they can be imported, for example, into MS Excel. Finally, the IP address of the computer is displayed and an indicator is shown whether another client is connected via TCP/IP to this program, in which case the program will transmit the run number of each sequence whenever a sequence is run. This can be used to synchronise the control computer with the acquisition computer.

Some simple error handling is performed, for example it is checked if the arrays for the different channels of the AO and DI/O cards have the right number, or whether the transition selector is set to 'Step' for the first state. (The program wouldn't know what setting to transition from for the first step.) When changing the number of lines in the 'Interesting' or 'Batch' tabs, the program automatically discards these changes and reverts to the 'All' tab, as it could not know which line to remove or where to enter the new line. But there are some issues worth noting: Right-clicking on an array opens a menu in which elements can be added or removed from the array. This would result in the voltage settings being sent to different channels if used on the channel arrays instead of the sequence array. It is

best to not right-click on the program and instead use the copy/paste/delete buttons provided at the left side of each state in the 'All' tab. Auto-saving short sequences set to continuously execute will quickly create hundreds of files on the hard disk. While it is encouraged to have auto-save on when performing sequences that have even a slight chance of being used later on, it is best to disable autosaving when not performing measurements.

In the back panel (figure C.2), the program performs several things simultaneously, like writing sequences, validating the integrity of the sequence, but most importantly converting the sequences and storing them onto the cards. From the PXI system's point of view, to execute a sequence, the following has to be performed:

1. Create a task.
2. Set the timebase to the output of the sample clock.
3. Write the converted data onto the cards.
4. Start the task. As the sample clock is not running yet, this just arms the system.
5. Set up the sample clock to generate a pulse train with the right frequency and duration.
6. Start the pulse train. Now the sequence starts.
7. Wait for the pulse train to finish, then stop the task.
8. Clear the task.

Items 4-7 can be repeated a number of times as long as the sequence is not changed. When the user presses the 'Write to Cards' button, it actually executes steps 8, 1, 2, and 3 of this list. When the program starts, a task is created just so that it can be cleared when the 'Write' button is pressed for the first time without producing an error. 'Execute' similarly executes steps 4, 5, 6, and 7.

In the PXI chassis, the cards can share internal signals on a common bus. This is used here to transfer the pulse train as a synchronised timing source through all cards. As expected, it was not possible even with an oscilloscope on nanosecond resolution to observe a timing offset between different cards.

Not yet implemented is the control of the function generator card. This card does not have on-board memory and cannot be programmed, instead, it needs to be updated by the LabView program itself. However, LabView 8 offers a structure called 'timed loop' where the execution of program parts can be triggered and synchronised to external sources like the pulse train that triggers the other channels.

5.4.2 Computer 2: The Acquisition Computer

The data is gathered and pre-analysed on the acquisition computer. This computer runs LabView 6.1 and is connected to a comparatively inexpensive Prosilica GigE GC-1380 CCD camera using an additional Ethernet port. This camera has a resolution of 1380x1024 pixel with a depth of 12 bit. Each pixel has a size of 6.45 µm by 6.45 µm. The frame rate is 20 Hz, meaning the shortest possible time between successive images is 50 ms. It has a very fast software shutter which can be triggered either by software or by hardware, and has a shortest possible shutter time of just under 20 µs. The limited depth (other experiments use cameras with 16 bit or more) is somewhat compensated by the very low dark count of less than 10.

On the LabView program running on this computer, a tab control is used to distinguish between the different views on the front panel. On the first tab, several important parameters can be set. Among them are the area represented by each pixel, the cross section of the atoms (which can either be set directly or calculated from the detuning), but also which files to store and where. As the program is designed to be triggered by a notification over a TCP/IP connection, the target IP can be set here and the connection can be initialised. When connected to the control computer in this way, the program will receive the run number every time a sequence is activated and uses this notification to arm the camera and wait for the images. The camera itself is then triggered using its SyncIn 2 port via a digital I/O channel from the PXI-6289 card.

The second tab allows to set the time in microseconds that the shutter will be open for after each trigger. Note that due to the camera operation, another 8.2 µs will be added to that time, which normally is of no consequence as the time will often be set to some milliseconds.

Also the three raw images taken by the camera during the last sequence are shown, the absorption image, the reference image, and the background image. In the absorption image, the first image, the region of interest can be set using two cursors. For more detail on how to calculate the atom number and distribution, please see section 5.6.3 later in this chapter. In the third tab, a larger image shows the optical density or the atom number for the region of interest in a larger window. A cursor can be manually set into the centre of the cloud, which in turn results in the cross sections being shown in the two graphs next to the larger image. A button 'Fit' can be used to fit Gaussian curves to these two cross sections. As the cursor is moved automatically to the fitted centre of the cloud when fitting, pressing this button two or three times should also automatically place the cursor in the centre of the cloud and calculate the optimal fit for the cloud. From these fits, the following parameters are extracted:

1. The atom number,

2. the centre of mass for both x and z coordinates, and

3. the $1/e^2$ width of the cloud in both x and y coordinates.

Apart from each value being displayed independently of each other, a small text box shows all values in a single line so that marking this line and copying it (Ctrl-C, not using the mouse) allows it to be conveniently transferred into an MS Excel spreadsheet. All data is also added to a table in the fourth tab, where the data can be displayed in a graph.

On the back panel, the program interacts with the camera using self-created LabView subprograms (VI). Most of these VIs access certain methods of a dynamically linked library (DLL) downloaded and installed from the Prosilica Website (`http://www.prosilica.com`). The actual interface to acquire the images is a VI containing a C interface node; the source code of this CIN is given in appendix B.3.

5.5 Low Velocity Intense Source of Atoms

While atom chips have numerous advantages over conventional cold atom trapping schemes, as described in section 2.4, one disadvantage is the comparatively small trapping region, especially as the capture velocity scales with the fourth power of the trap diameter. Combined with the requirement of ultrahigh vacuum during evaporation, this imposes a serious limitation to the use of atom chips which needs to be overcome.

One possibility to overcome this limitation is to vary the pressure: During a first stage, rubidium dispensers are heated for several seconds, to release large amounts of Rb vapour and raise the pressure to over 10^{-8} Torr. During this stage, the atoms are captured in a surface MOT. When the dispenser heating is switched off, the untrapped Rb atoms quickly absorb on the inner surfaces of the chamber or are pumped by the getter pumps, reducing the pressure into the lower 10^{-11} Torr range within a few dozen seconds. Then the trapped atoms can be loaded into the atom chip and cooled evaporatively [Whi07a].

However, in the 'Atom Chip 1' experiment, this method increases the turnaround time for successive experiments to just under one minute. Common experiments with BECs often require hundreds of successive measurements. With such a long turnaround time, this not only elongates the measurement itself, it also amplifies the chance that something might happen during the measurement which will change the outcome. Examples for this are changes in the laser intensity, laser locking problems, temperature fluctuations, etc. One aim in this experiment was to enhance the turnaround time by injecting a flux of slow atoms directly into the trapping region of the atom chip. Three options for collimated, bright and compact sources for cold atoms have been presented in the past:

- The 2D MOT [Ber98, Sch02] works similar to a standard MOT, except in only two dimensions. This means that two anti-Helmholtz coils are used to create a 2D quadrupole field, and two pairs of red detuned circular polarised laser beams along these two axes intersect in the centre. The result are two slow beams of atoms into both directions of the third axis.

- The $2D^+$ MOT [Die98] is an extension to the 2D MOT. In addition, a fifth

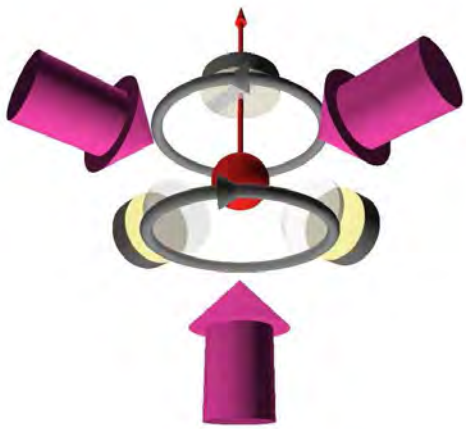

Figure 5.9: Schematic of the LVIS: A quadrupole field with the strong axis in the vertical direction is generated by two counterpropagating coils. Two circular polarised MOT beams (with repumper) enter horizontally and pass after the atom cloud through a quarter wave plate before they are retroreflected on a gold coated mirror. The double passing of the quarter waveplate means that the handedness of the circular polarised beam is flipped. The vertical beam is similar, but it hits a quarter waveplate/mirror that has a hole in the centre. This hole has two effects: Firstly, the retroreflected beam has a shadow in the centre, so that the cold atoms in the centre of the trap are accelerated upwards. Secondly, the hole allows these atoms to pass through the mirror into the atom chip chamber which is located atop.

beam pushes the atoms into the desired direction.

- The low velocity intense source (LVIS) [Lu96] consists of a full 3D MOT with one exception: One of the six laser beams has a shadow in the centre. Just like in a standard MOT, atoms are captured and cooled, however, once they are cooled and in the trap centre, they observe a pressure differential and are slowly accelerated towards the beam with the shadow.

The goal with all these sources is to produce an intense beam of slow atoms. So, the atom flux and the mean velocity of this beam are the major defining properties, and as such they have been compared in some experiments. Table 5.3 gives an overview of some experiments. While none of these sources have ever achieved a flux of cold atoms comparable with a Zeeman slower [Phi82], which was shown to produce up to 3.2×10^{12} atoms per second [Slo05], this was not considered for two

reasons: First, a Zeeman slower is not a compact, modular source, and secondly, the flux of thermal atoms in a Zeeman slower is even larger than the cold atom flux.

Table 5.3: Comparison of different cold atom sources

Author	ref.	Element	Method	Flux (10^9/s)	Velocity (m/s)	Pressure 10^{-8} Torr
Berthoud *et al.*	[Ber98]	Cs	2D MOT	0.13	0.7-3	3
Schoser *et al.*	[Sch02]	Rb	2D MOT	60	50	120
Castagna *et al.*	[Cas06]	Cs	$2D^+$ MOT	13	20	3
Ovchinikov	[Ovc05]	Rb	LVIS	8.0	8.5	24
			$2D^+$ MOT	8.0	11.0	24
Kohel *et al.*	[Koh03]	Cs	P-LVIS	2.2	15.0	0.19
Lu *et al.*	[Lu96]	Rb	LVIS	5.0	14.0	10
Dieckmann *et al.*	[Die98]	Rb	LVIS	0.03	26.0	11
			$2D^+$ MOT	9.0	8.0	11

It was decided to implement the LVIS layout in this experiment. Figure 5.9 displays the basic operation of the LVIS. To minimise gravity effects, the LVIS has been constructed in such a way that the atomic beam is progressing directly upwards. Similar to a MOT, which is described in section 2.2, red detuned, circular polarised laser beams are made to intersect from all six spatial directions at the minimum of a 3D magnetic quadrupole field, created by a set of anti-Helmholtz coils. The axis of these coils coincides with the vertical extraction direction. The beams are actually three sets of retro-reflected laser beams. A quarter wave plate between the vacuum chamber and the retroreflected beam changes the circular polarisation into a linear one on the way towards the mirror and into the correct circular polarisation on the way back. The difference between an LVIS and a standard MOT is realised in the vertical beam. It is guided into the vacuum chamber from below, and its retro-reflecting mirror is mounted inside the vacuum vessel, forming the boundary between the LVIS and the atom chip chamber. It consists of a Comar quarter wave plate on which a silver layer has been coated at the upper side, thereby forming mirror and polarisation optics in a single element. Additionally, a 0.5 mm diameter hole has been drilled in the centre of this mirror, at the same time creating the connection between the two chambers and the shadow in the reflected beam that is required to turn the MOT into an LVIS.

In this experiment, the LVIS chamber is located directly beneath the atom chip chamber. A glass cell (32 mm by 32 mm square, 100 mm high, 6 mm thick) surrounds

the trapping region. The glass cell is attached to a transition stage via a $2\frac{3}{4}$ inch connection. This transition stage has two Conflat Mini connectors at the side, one of which connects to a Varian MicroVac 2 l/s ion pump, and the other to a feedthrough, through which the current for the Rb dispenser is supplied. Opposite the glass cell, the transition stage connects to a reducer, which in turn is connected to the bottom conflat mini port of the octagon of the atom chip chamber. However, in the connection between the transition stage and the reducer, not a standard copper gasket is used; instead, a single copper piece was fabricated which combines the functions as, firstly, a gasket, secondly, as the separation between the LVIS and the atom chip chamber, and thirdly, as the mount of the specific LVIS mirror with the hole. This copper block consists of a 5 mm thick disk, but in the centre, a hollow tube with an outer diameter of 15 mm runs 9 cm down into the glass cell before terminating in the mirror mount. The whole copper block is milled from a single piece. The hole mirror is a Comar quarter wave plate with a 1 inch diameter and a thickness of 3 mm. The backside of this wave plate is silver coated for reflection, and a 0.5 mm diameter hole is drilled co-axially through the mirror and the copper block, culminating in a total length of 5 mm.

The trapping light for the LVIS is outcoupled from two single mode fibres (one from the Toptica DLX and one from the repump laser) into a Thorlabs cage mount system. The trapping light supplied a total power of 80 mW, while the repump light totalled 8 mW. The beams are expanded to 10 mm diameter by 50 mm lenses in the appropriate distance to the end of the fibres, and joined in a polarising beam cube. The same cube is also used to split light off for the vertical z beam, while the remaining light is expanded to a diameter of 35 mm using two lenses. This is described in figure 5.10

The coils producing the magnetic quadrupole field have a diameter of 90 mm and are 60 mm apart from each other. Each has 81 turns of coated, 0.527 mm diameter copper wire. Initially the coils were mounted along the y-axis of the LVIS, and additional Helmholtz coils along both x- and z axis were used to move the centre of the quadrupole field. Later the quadrupole coils were mounted along the vertical y-axis, and placed on a x-z micrometer adjustable translation stage. This improves the access to the glass cell and also promises to reduce the average velocity of the

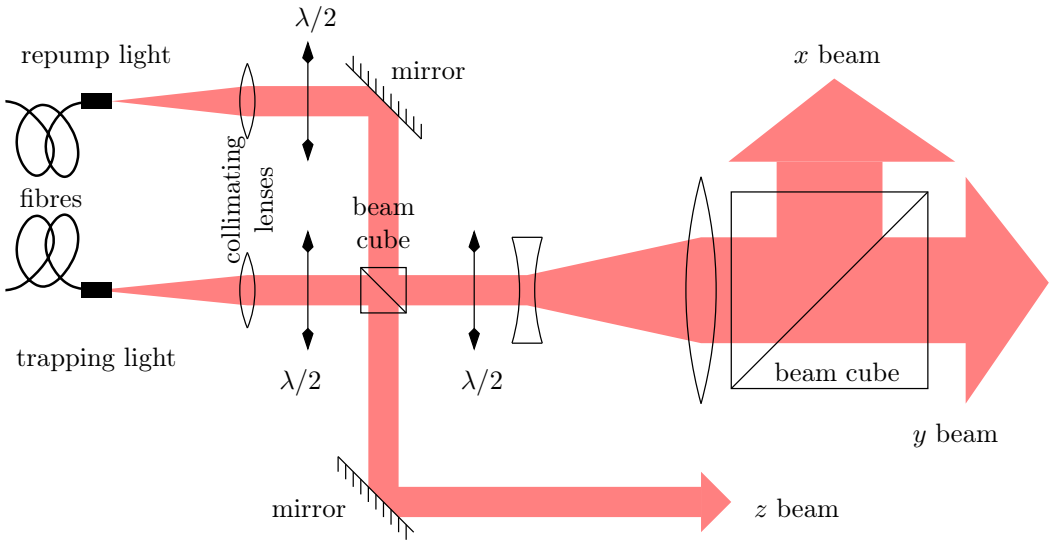

Figure 5.10: The LVIS laser cage: Trapping and repump light arrive from single mode fibres, are collimated at a diameter of 10 mm and joined on a polarising beam cube. The same cube also separates the light for the vertical LVIS beam. The rest of the light is expanded even further to 35 mm diameter using a telescope, and is split with a 50 mm polarising beam cube into the two horizontal arms for the LVIS.

cold atom beam as the strong gradient of the magnetic quadrupole field will shift the atoms faster out of resonance from the accelerating LVIS laser beam. The resulting magnetic field has a strong field gradient $\partial B/\partial z$ of 4 Gauss per centimetre for 1 A, and was usually run at the maximum of 4.5 A. A calculation of the magnetic field is given in figure 5.11, showing a near linear magnetic field dependence with a gradient of 18 G/cm in the region 20 mm around the centre.

The coils are mounted on a manual $x-y$ translation stage so that the position of $|B| = 0$ can be moved horizontally. This is of particular interest for aligning the centre of the trap with the hole in the LVIS mirror; however, it can also be used to move the trap away from the hole and operate it as a standard MOT. This allows to measure the influx of atoms into the trap by observing the intensity of the light scattered from the atom cloud. The number of scattered photons per atom is given in equation 2.2:

$$\gamma_p = \frac{\Gamma}{2} \frac{s_0}{1 + s_0 + 4\left(\delta/\Gamma\right)^2}$$

The saturation parameter $s_0 = I/I_{sat}$ depends on the laser intensity and the saturation intensity. For Rb in a MOT on the $F = 2 \rightarrow F' = 3$ transition the

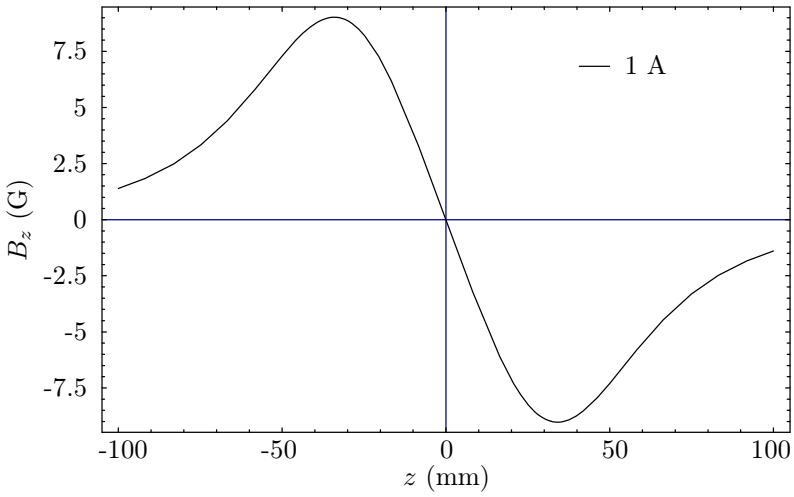

Figure 5.11: The calculated on-axis magnetic field produced by the LVIS coils at 1 A. Typically, 4.5 A were run through the coils, resulting in a magnetic field gradient of 18 G/cm.

saturation intensity is hard to calculate, as the atoms will see different magnetic fields. [Ste01] suggests using the saturation intensity corresponding to an isotropic pump field, which is $I_{sat} = 3.58$ mW cm^{-2}. Of these photons, some transverse a lens which is placed at a distance $d = 2f$ (f is the focal length) from the atom trap and are thus collected. This is schematically presented in figure 5.12. The percentage of scattered photons collected by the lens can be easily calculated as the solid angle α:

$$\alpha = \frac{\text{area of lens with radius } r}{\text{surface of a sphere with radius } d} = \frac{\pi\, r^2}{4\,\pi\, d^2} = \frac{r^2}{4\, d^2} \tag{5.1}$$

$$N = \frac{S - S_0}{\alpha\, \zeta\, \hbar\omega_l\, \gamma_p} \tag{5.2}$$

where S is the signal of the photo diode, S_0 is the background signal, measured with all lights on, but the magnetic field off, and ζ is the measured sensitivity of the photo diode, giving the signal per Watt of light intensity. Note that usually a silicon photo diode has a sensitivity given in A/W; however, in this experiment, photo diodes are embedded in a circuit which returnes a voltage proportional to the light intensity (V/W) which was carefully measured by observing the signal when shining a weak laser beam with different known intensities directly onto the photodiode. The circuit diagram of the photodiode is given in figure D.1 in the appendix. This form of measurement is particularly convenient as it can monitor the atom number

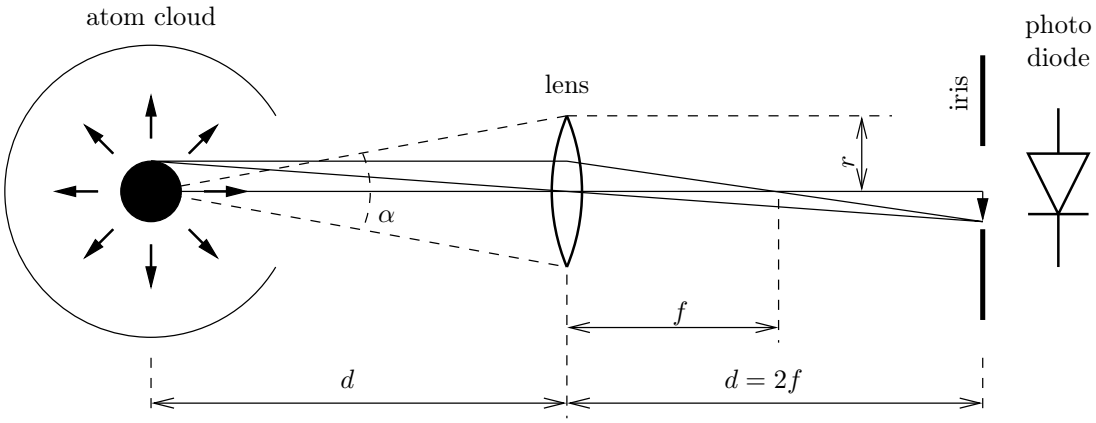

Figure 5.12: Measurement of trapped atom fluorescence: The atom cloud in the centre scatters light in all directions homogeneously. A lens with the radius r and the focal range f is located at a distance $d = 2\ f$ from the atom cloud outside the vacuum chamber. The solid angle α gives the percentage of these photons which are measured. After another distance d, the image of the atom cloud is located inside an iris diaphragm to minimise the amount of light coming from other sources. Directly after this diaphragm, a high gain photodiode is placed, giving a signal proportional to the number of photons and therefore proportional to the number of atoms. By knowing the light intensity of the trapping beams I, the scattering rate γ_p, α, and the gain of the photodiode ζ, this proportional factor can be calculated.

in the MOT without interfering with it, with a signal which is proportional to the atom number. The loading of atoms into the MOT can be observed by monitoring the development of the signal over time. In first order approximation, the number of the trapped atoms obeys the equation:

$$\dot{N} = \phi - \gamma\ N, \tag{5.3}$$

where ϕ is the loading flux of the atoms, and γ is the loss rate. Even in dense magneto-optic traps, higher order terms proportional to the density (N^2) can be omitted. The behaviour of the MOT can more easily be seen by separating the variables in equation 5.3 and considering the appropriate initial conditions. Assuming the MOT is empty at $t = 0$ ($N(0) = 0$), the atom number development over time follows a saturated curve.

$$N(t) = N_{sat}\ \left(1 - \exp\left[-\frac{t}{\tau}\right]\right) \tag{5.4}$$

with the fill time $\tau = 1/\gamma$ and the saturation atom number $N_{sat} = \phi/\gamma$. Counterintuitively, higher flux does not load the MOT faster, as the fill time does not depend on the flux. Rather, the higher flux will lead to a higher saturation number N_{sat}. When increasing the loss rate, the MOT will load faster, but to a lower total number. In effect, the flux defines the initial gradient of the fill curve, while the loss defines how soon it turns over. From monitoring the loading of a MOT with a photo diode and fitting the data to equation 5.4, N_{sat} and τ can be extracted, the flux calculates to

$$\phi = \frac{N_{sat}}{\tau}. \tag{5.5}$$

This is shown in figure 5.13. It has been shown that the fill rate is approximately

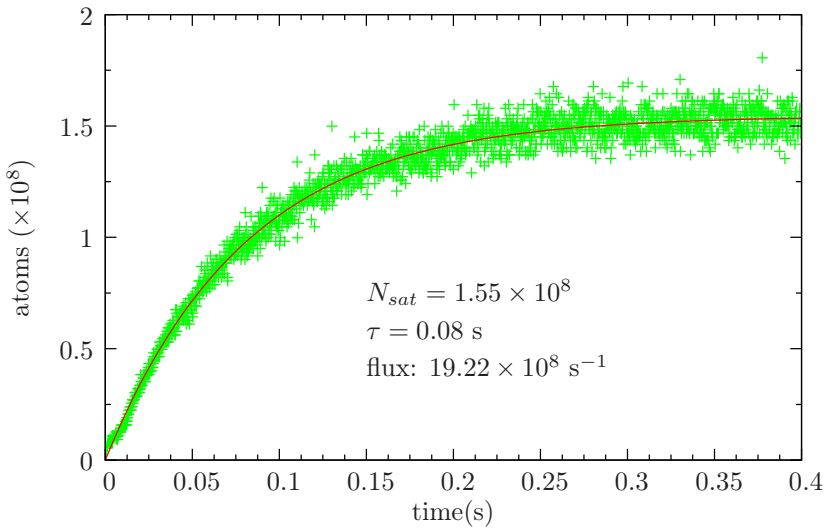

Figure 5.13: MOT filling curve in the LVIS chamber. The fluorescence measured by a photodiode is linearly proportional to the atom number in the MOT, with the proportionality factor being calculated according to equation 5.2.

equal to the flux of the LVIS, provided that the 'loss' of the trapped atoms into the atomic beam is larger than the loss due to background collisions [Lu96]. For this reason, the fill rate is the most important characteristic of the LVIS, and several measurements were performed to optimise and verify the fill rate.

One of these experiments is measuring the fill rate at different pressures. This was done by stepwise increasing the current through the Rb dispenser, which heated up and released more atoms into the chamber, and measuring fill curves when the pressure had equilibriated at a new value. The results of this measurement are given

in figure 5.14, showing that the fill rate increases at first, but levels out at pressures over 3×10^{-8} Torr as the losses due to background collisions become more dominant. Eventually it would turn over and reduce again.

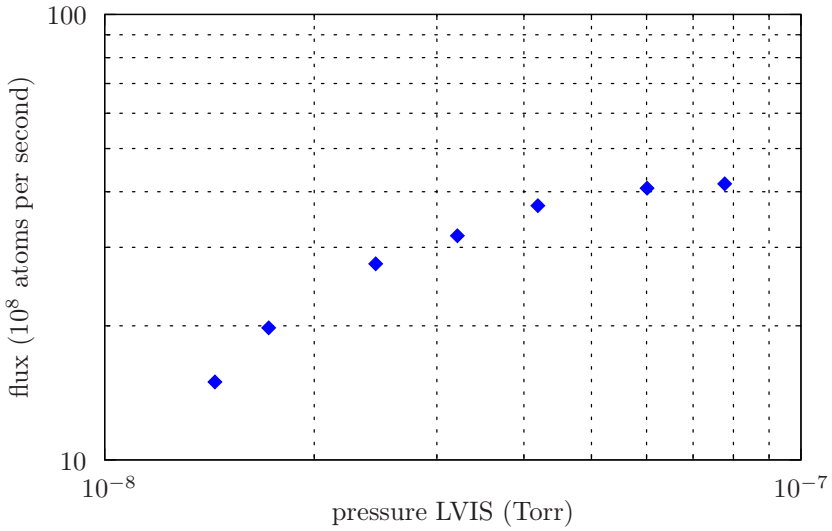

Figure 5.14: LVIS fill rate versus pressure. To observe the optimal conditions, several fill curves were taken for different pressures, where the pressure was increased by running higher current through the Rb dispenser, thereby releasing more Rb into the LVIS chamber. The fill rate increases at first, but equilibirates still well below 10^{-7} Torr, as the loss rate due to background collisions limits the trap. The fill rate would eventually turn over,

Another measurement was taken at different detunings of the LVIS laser frequency; the results are shown in figure 5.15. As under normal conditions the laser frequency is fixed to -17 MHz, the reason for this measurement was to verify that the LVIS operates at a reasonable rate with this given detuning. At smaller values of the detuning the fill rate was only slightly higher.

5.6 Atom Chip Measurements

5.6.1 Magnetic Fields

Four different magnetic trapping potentials are needed in the top chamber to create a BEC in the microwire atom chip. In the first stage, atoms are to be trapped in a MOT with the quadrupole magnetic field created exclusively by external coils. The atom chip operates in this configuration as a mirror for the MOT beams. The

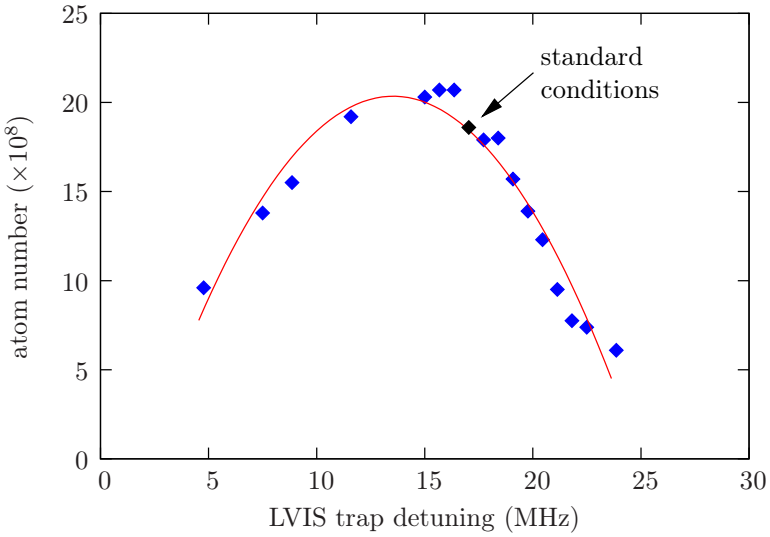

Figure 5.15: LVIS atom number versus laser detuning: To verify that the LVIS was working under reasonable conditions at the fixed detuning of -17 MHz, the fill rates of the trap in the LVIS chamber was measured at different detunings. It can be seen that the LVIS fill rate is not optimal, but reasonably good at the given detuning.

configuration has one laser beam parallel to the surface, and the two other beams at an angle of 45° to the surface, forming each other's counter-propagating beam. The handedness of the circular polarisation is changed during the reflection of the atom chip, therefore one of these two beams has to be co-axial with the strong axis of the quadrupole field. This configuration is valid and widely used. It is visualised in figure 5.16.

The coils which produce this magnetic quadrupole field in the experiment described in this thesis had several constraints with respect to their dimensions: The diameter of the octagon is 11.5 cm, giving a lower limit for the separation of the coils. At the same time, the position and dimension of the reducer leading to the LVIS chamber limited the radius of the coils to 4.5 cm. These constraints are far from the optimum setting for anti-Helmholtz coils, where the separation of the coils should be between 1 and 1.5 times the radius of the coils. Under these constraints it was decided that each coil should hold 275 turns of ⌀ 0.527 mm copper wire, and run a current of 2.5 A, which would result in a magnetic field gradient of 12 G/cm. 30 Watts of power are dissipated by a water cooling system located inside the coils formers. The schematic of this coil can be found in the Appendix D.3. In figure 5.17 these coils can be seen in green colour.

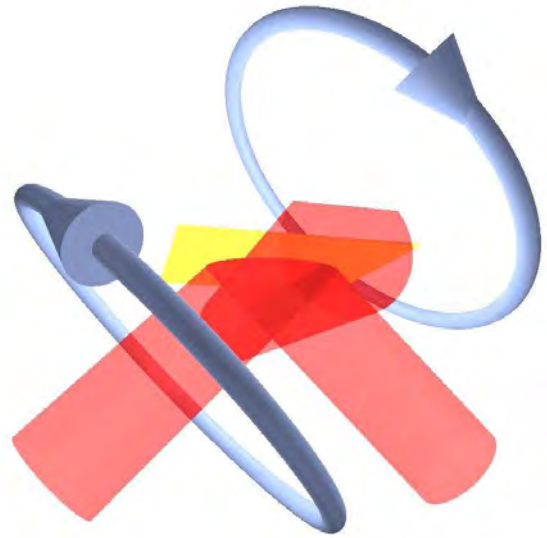

Figure 5.16: Schematic of a Mirror MOT: One laser beam passes parallel to the surface of the chip in close distance, the other two beams counterpropagate at an angle of 45° to the surface. A set of anti-Helmholtz coils creates a magnetic quadrupole field with the strong axis coinciding with one of the angled laser beams.

The second required magnetic field is the magnetic quadrupole trap produced by the silver layer of the atom chip and an external B_x bias field. The B_x field is produced by a set of large coils with a diameter of 24 cm and a separation of 10 cm. Each of the coil formers harbours two coils, one with 16 turns, and a second with 4 turns. The 4 turn coil (called $B_{x\ small}$) has a lower inductance and can therefore be switched considerably faster than the $B_{x\ large}$ coils. The orientation of the magnetic quadrupole field produced by this configuration corresponds with the orientation of the first quadrupole field. The same set of coils also produces the bias field for the third and fourth stage of the magnetic trapping: Using the U-wire on the silver foil structure, and finally using the microwires in combination with the end wires of the silver foil.

5.6.2 Lasers

The lasers needed for trapping atoms in the top chamber are guided to the experiment with single mode fibres in a similar way as for the LVIS. Inside a Thorlabs cage mount setup the light fields of the repump and the trapping light are combined and split into the three arms for the MOT trapping. Note that the trapping light of

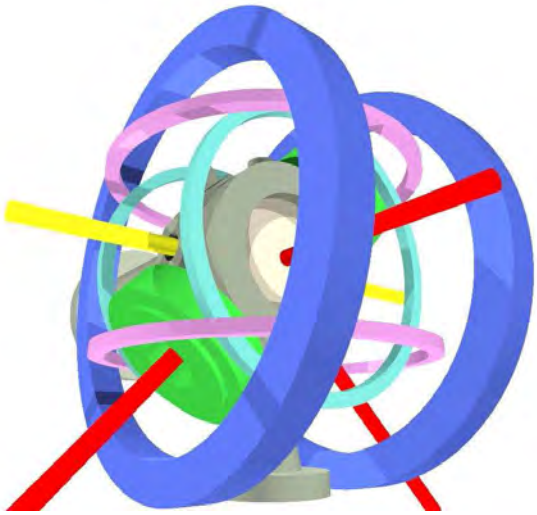

Figure 5.17: The location of the different coils around the top chamber, displaying the vacuum system (grey), the MOT beams (red), the imaging/optical pumping beam (yellow), the MOT coils (green), the B_y (purple) and B_z (cyan) Helmholtz coils, and the B_x bias field coils (blue).

Table 5.4: The details of the bias field coils for the experiment chamber. For each direction, two coils are wound on one former. The first line gives the dimensions of the former in diameter as well as width and height available for the coils itself, and the separation of the two formers. The second and third lines give the details of the actual coils, with the diameter of the wire used, the number of turns per width and height, the calculated resistance of the wires, the magnetic field strength per Ampère, and the power dissipation for the large coils at 10 A.

Coil Name	colour in fig. 5.17	diameter (mm)	width (mm)	height (mm)	sep. (mm)	resistance Ω	Gauss per Amp	Power @ 10 A
B_x former	blue	240	20	20	100			
B_x large		4.5×3	4	6		0.029	1.75	2.9 W
B_x small		1.57	4	1		0.007	0.46	
B_y former	purple	200	6.8	8.5	110			
B_y large		1.57	4	4		0.099	1.33	9.8 W
B_y small		1.57	4	1		0.025	0.33	
B_z former	cyan	172	7	8.2	100			
B_z large		1.57	4	4		0.086	1.49	8.5 W
B_z small		1.57	4	1		0.021	0.37	

the horizontal beam is separated from the rest before it is mixed with the repump light, therefore the horizontal beam does not carry any repump light. The setting is shown in figure 5.18. The diameter of the beams is limited to about 14 mm, as this is the size of the viewport on the side of the octagonal atom chip chamber.

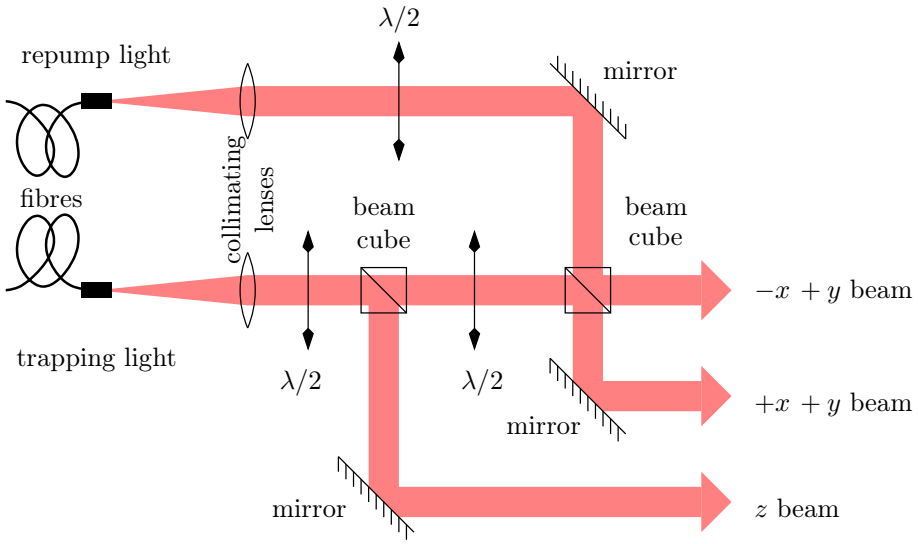

Figure 5.18: The trapping beam and the repumping beam are delivered through two single mode polarisation preserving fibres in a Thorlabs Cage Mount system. The light in both arms is first collimated using two f=50 mm lenses at 50 mm from the end of the fibre. Then, using a $\lambda/2$ half waveplate and a polarising beam splitter cube, about a third of the trapping light intensity is removed and guided into the vacuum chamber from the $+z$ direction as the first MOT beam. The rest of the trapping light is then guided through another of these half waveplate/beam splitter cube setups to reliably distribute laser power into the two transversal beams entering from the bottom left $(+x, +y)$ and bottom right $(-x, +y)$. The same beam splitter is used to combine the trapping and the repump light. While the repump beam has only a negligible impact on the momentum of the atoms, and therefore does not need to be balanced, a half waveplate nevertheless was installed in the repump arm to be able to distribute the whole repump light into a single beam, which simplifies alignment considerably.

5.6.3 Detection

In the top chamber, two distinct detection systems were realised. One is a photodiode measurement identical to the one used in the LVIS chamber. This is used to observe the atom number during filling and release of the atoms. The other is an absorption imaging scheme, shown in figure 5.19. In this scheme, the atom cloud is illuminated with resonant light, which is then collected in a lens and focused on a CCD camera.

The absorption imaging allows not only to measure the atom number with a higher accuracy than the photodiode, but also allows to assess the dimensions of the

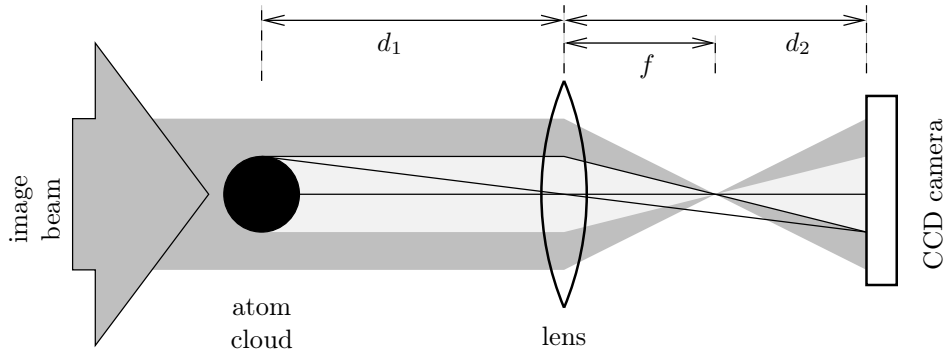

Figure 5.19: Schematic of the absorption measurement: A collimated on-resonance beam enters from the left side. The atom cloud scatters atoms out of the beam according to its density, leaving a shadow. A lens with focal length f is placed at a distance d_1 behind the atom cloud outside the chamber. It forms an image of the shadow on the CCD chip of a camera, which is placed at distance d_2 behind the lens ($1/d_1 + 1/d_2 = 1/f$). For $d_1 = d_2 = 2\,f$ the magnification of the image is unity. By comparing the image of the cloud with a second image taken under identical circumstances except the absence of the atom cloud itself, the optical density of each pixel can be observed. From this and the size of the pixel the number of atoms can be calculated.

atom cloud. In both cases, three images are taken by the camera:

1. The absorption image A: The imaging beam passes through the cloud of atoms and acquires a shadow while passing through.

2. The reference image R: This is taken as shortly after the absorption image as possible with the same settings. The atom cloud has already been destroyed while taking the absorption image, and the imaging beam passes onto the camera without a shadow.

3. The background image B: In this image, the camera shutter opens for the same amount of time as before, but the image beam remains switched off. This identifies stray light sources.

With these three images, the optical density OD of the atom cloud can be extracted for each pixel:

$$OD = -\ln\left[\frac{A-B}{R-B}\right] \tag{5.6}$$

To assess the dimensions of the atom cloud, and also the number of atoms in the cloud, it is important to know the magnification of the lens-camera system. In this experiment, a lens ($f = 5$ mm) is placed ca. 9 cm before the CCD chip. This camera-lens system was pointed at a ruler and the magnification was directly measured. Each pixel represents 8.01 µm by 8.01 µm of space.

To calculate the atom number, first the cross section σ of the atoms has to be calculated, using the appropriate equation for two-level atoms:

$$\sigma = \frac{3\,\lambda^2\ /\ (2\,\pi)}{1 + \left(2\frac{\delta}{\Gamma}\right)^2} \tag{5.7}$$

Now the number of atoms in each pixel is

$$\eta = OD\ \frac{\text{pixel area}}{\sigma} \tag{5.8}$$

As σ, and therefore OD depends on the detuning, this method can also be used to map out the maximum absorption, and calibrate the resonance frequency. To measure this, the top MOT is loaded from the LVIS for 40 s, then the atoms are released from the MOT and fall under gravity for 5 ms before an absorption image is taken of the atom cloud. By that time the cloud has acquired a Gaussian shape in both dimensions and is still clearly visible on the absorption image. The maximum is then set manually before two Gaussian functions are fitted to the x- and y-axes of the data, and the maximum of the optical density is noted. By repeating this measurement for different Master AOM detunings during the absorption imaging, the setting for the maximal absoption is found, and thereby the on-resonance frequency (here 6.63 MHz against the arbitrarily selected origin of the measurement). The result can be seen in figure 5.20: The full width half maximum of the curve is 5.6 MHz, which is also in good agreement with the natural linewidth of the transition.

The total number of atoms in the surface MOT remains low, even with long loading times. Observing the loading with a timed fluorescence measurement, it can be seen that the rate of captured atoms is just 10^6 atoms per second, as seen in figure 5.21. This is considerably less than the capture rate of the LVIS, which was 10^9 atoms per second. Ideally, the fill rate of the LVIS, the flux of atoms from the

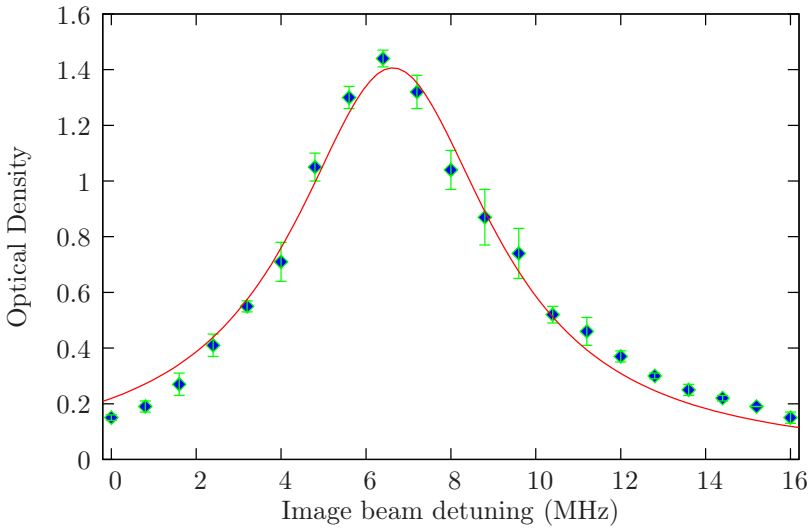

Figure 5.20: Dependence of the absorption of the probe beam on the image beam detuning. The image beam detuning was changed by changing the Master AOM frequency from an arbitrarily selected value. Each data point is the average (with standard deviation) of four independent measurements. Each time, the top MOT was loaded in the same manner, it was then released for 5 ms before taking the image. A Gaussian function was then fitted through the optical density, and the maximum of this Gaussian function is given here. A Lorentz function was fitted to the data (red line).

LVIS to the atom chip, and the fill rate of the atom chip should all be the same.

Several re-calibrations and optimisations did not significantly enhance the fill rate of the top MOT, so it is unlikely that the poor fill rate is due to improper alignment. One possibility is a blockage in the hole for the extraction beam, but that is unlikely as a clear spot of the LVIS pushing beam can be seen in the centre of the microwire atom chip, which is bright and round. A blockage that would reduce the number of atoms by three orders of magnitude would also probably noticeably block this beam.

Another possible reason is that the cold atom beam divergence is too large and most atoms miss the trapping region. To measure the diameter of the atomic beam close to the trapping region (ca. 27 cm above the hole), a probe beam was directed into the atomic beam through a 1 mm wide vertical slit, thereby only illuminating a small slice of the atomic beam. A photomultiplier tube was used to observe the fluorescence of the atoms in the beam. The result can be seen in figure 5.22; the

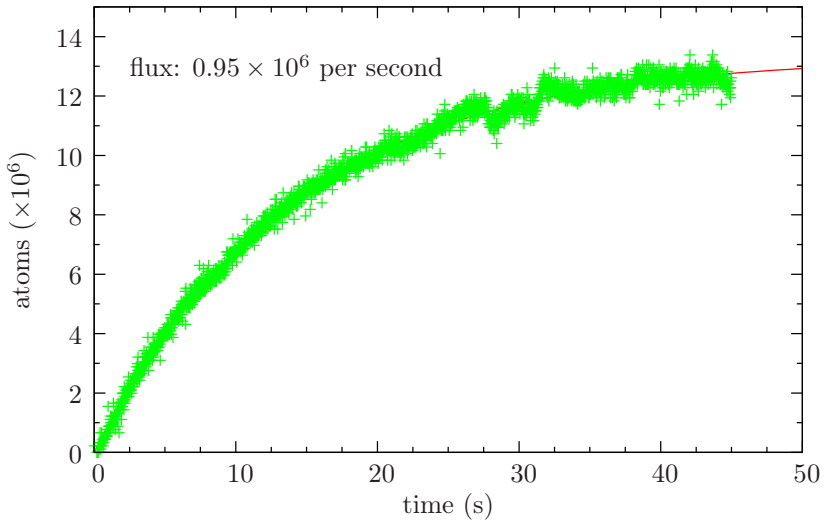

Figure 5.21: Loading curve of the MOT loaded by the LVIS. The data is taken using a fluorescence measurement as described in figure 5.12. The loading usually follows an equation $N(t) = N_{sat}\,(1 - \exp[-t/\tau]$, which is fit onto the data returning N_{sat} and τ. The flux is the derivative of the equation at the position $t = 0$, which is N_{sat}/τ.

diameter of the cold atomic beam is measured to be 7±2 mm (divergence in the order of 1°), not large enough to account for 99.9% losses.

The most likely explanation for the low fill rate of the atom chip would be a high average velocity of the atoms in the beam, so that only a small fraction of the atoms has a velocity smaller than the capture velocity. However, while a measurement of the atomic beam velocity was set up, first the rubidium reservoir was depleted and then the DLX laser broke. This measurement will be performed later.

Finally, it is possible that due to defects in the LVIS mirror close to the hole the extraction region is larger than the hole itself. This would result in a large number of atoms in the cold atomic beam to miss the hole and hit the mirror. However, again, visual assessment of the mirror does not suggest any effect that would account for the huge difference in fill rates.

While the fill rate of the top MOT was insufficient to load enough atoms to reliably transfer these atoms into the atom chip or perform evaporative cooling, the MOT itself could be assessed using the imaging setup. Time of flight measurements were performed to measure the temperature of the atomic cloud inside the MOT. After capture, the trap lasers were detuned farther to -40 MHz, and the atoms

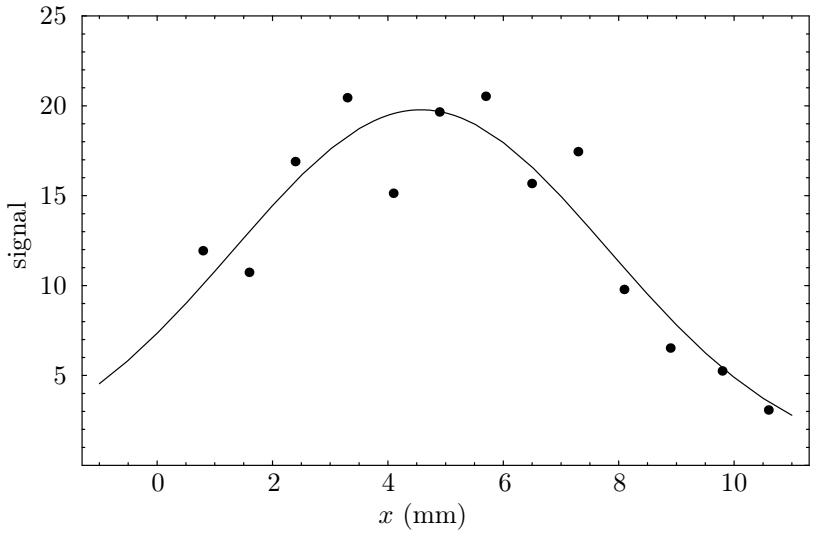

Figure 5.22: Measurement of the cold atom beam diameter. A probe laser is set to illuminate only a small vertical slice of the atomic beam, while a photomultiplier tube observes the fluorescence of the atomic beam from the side. The signal here is the signal of the PMT divided by the intensity of the probe beam at the position. It is an arbitrary number, but it gives a good relative beam intensity, which is all that is needed to assess the diameter of the atomic beam. The diameter of 7±2 mm is not wide enough to account for the difference between LVIS fill rate and top MOT fill rate.

released afterwards. They were allowed to fall and expand for up to 15 ms before an absorption measurement was taken. At longer times the small number of atoms became too widely spread out and too thin to measure the spread with any certainty. The measured expansion over time yields a temperature of the atomic cloud of 55-60 µK. This can be seen in figure 5.23.

5.7 Conclusion

This chapter presented the experimental environment in which the femtosecond ablated microwire chip was to be assessed. A flexible measurement control software was presented and tested. The flexibility of the laser system was shown. The dual-chamber vacuum system with the high pressure cold atom source chamber and the low pressure atom chip chamber was introduced and the assembly explained. The small hole for the atoms between the two chambers was shown to allow for pressure differentials of factors up to 1000. The implementation of the Low-Velocity

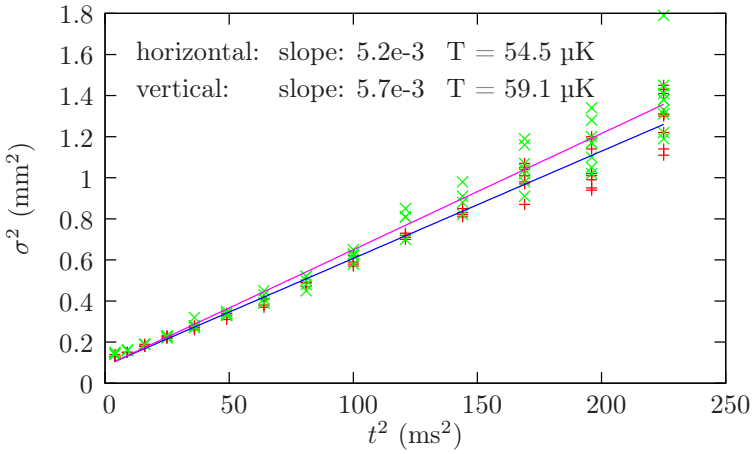

Figure 5.23: Expansion of the free-falling cloud: A very important measurement for cold atoms are 'time of flight' measurements, where the cold atom cloud is released and falls under gravity. Here, the temperature of the cloud is measured: The expansion of the cloud is plotted in square against the square of the time since the release. The slope of this line is $\frac{1}{2}\bar{v}^2$, which, multiplied by the mass of an atom M, gives the mean energy, which is equal to $k_B T$.

Intense Source of atoms (LVIS) was described and initial measurements presented that suggested a expected flux of more than 10^9 atoms per second.

The dual layer atom chip was introduced with the high-current H-wire silver foil structure and the copper/gold layer with five femtosecond laser ablated microwires. Three of these microwires are designed for rf currents and two are for dc currents for trapping. One of these two is a sculptured wire able to produce a magnetic potential forming a string of double wells.

A large discrepancy between the fill time of the LVIS and the fill rate of the top MOT of three orders of magnitude was observed, even though in theory those two rates should be about equal. A great effort has been applied to the alignment, with some major changes, but while a flux of about 10^6 atoms per second could usually be achieved, higher yields were not obtained. This strongly suggests a fundamental problem limiting the flux. This is most likely due to the very limited capture velocity of the mirror MOT, which in turn is due to the very limited beam size, its proximity to the surface of the chip, and the fact that the atom jet is injected perpendicularly to the chip's surface. Most likely, the average velocity of the atoms from the LVIS still exceeds the small capture velocity, so that a large fraction of the atoms is not

trapped.

A solution to this is the implementation of a $2D^+$-MOT scheme. For this, two sets of anti-Helmholtz coils need to be used along the x and z-axis, with the majority of the trapping light in the LVIS chamber being directed along these axes as well. The pushing y-beam should contain only a smaller fraction of the intensity.

Other possible reasons are:

- Defects around the centre of the LVIS mirror hole resulting in an extraction region wider than the hole of the mirror, so that the majority of the atoms in the beam hit this mirror and are not transferred into the atom chip chamber.

- A wider-than anticipated spread of the atomic beam, with most atoms hitting the inside of the reducing cone. However, measurements performed to assess the spread of the beam do not hint at such a problem.

- Contamination might have blocked or partially blocked the extraction hole. However, even if contamination had occurred despite the careful handling of this central piece of the LVIS, it would also block the laser light, but a round spot originating from the LVIS push beam can be seen on the atom chip, which strongly suggests that the extraction hole is clear.

Chapter 6

Characterisation of Magnetic Mirror Quality with Ultracold Atoms

This chapter presents the results of an experimental investigation of the reflection of cold atoms from an atomic mirror constructed from the permanent magnetic material GdTbFeCo, which is also used in commercial mini-disc players. To adapt the material for use in ultra-high vacuum atom optics experiments, the composition and relative ratios of the elements were optimised and thin films were deposited on substrates in-house using the CAOUS microfabrication facilities [Wan05a]. Atom optical elements such as mirrors are of interest to the atom optics community as they represent a fundamental building block for more complex systems. For example, an optical interferometer relies on the coherent reflection of light from mirrored surfaces and also on the partial reflection/transmission of photons through partially reflective mirrors called beam splitters. By analogy mirrors for atoms can be created by establishing a large repulsive potential for atoms. Two such approaches have been investigated in this field:

1) Use of the repulsive conservative electric dipole potential of a far blue-detuned optical field [Bal88]. The spontaneous scattering rate from the field must be low to remain conservative and the potential barrier must be high for reflection of atoms with velocities up to 1 m s^{-1}. These two requirements can be met by using focused laser light of high intensity and large blue-detuning. In addition, the potential should have little spatial dependence perpendicular to the direction of incidence, that is, the mirror should be flat in order to yield good specular reflection. These potentials are

commonly realised using evanescent light field created from total internal reflection of a prism [Lan96].

2) Use of a periodic array of magnets giving a magnetic field that decays exponentially with distance above the surface of the array [Opa92]. This creates a gradient that repels atoms which have a magnetic dipole moment and which are in low-field-seeking states ($m_F g_F > 0$), as shown in section 2.2. Different approaches have been used to realise such a periodic magnetic array. The two main types are based on current carrying wires (e.g. used in [Lau99a]) and permanent magnets [Sid02]. While it is not possible to switch or modulate the magnetic fields with permanent magnets, the advantages of these include the 'plug and play' usage, the absence of heating or current fluctuations, and the inherent absence of short or open circuits. The first atomic mirror based on permanent magnets was made by recording a sinusoidal pattern of period about 10 µm onto commercial audio tape [Roa95]. Subsequent mirrors based on recording media used video tape [Sab99], floppy disks [Hug97], and hard disks [Lev03b, Boy07]. Such media offer good magnetic properties, but because they magnetise in-plane, it is very difficult to record micron-scale patterns onto them.

Films that magnetise perpendicular to the surface are more attractive in this respect. GdTbFeCo, developed in the magneto-optical recording industry and used in the mirrors discussed in this work, offers several other advantages [Wan05a]. These include a high remanent field, good homogeneity, high coercivity, and high Curie temperature. A high coercivity prevents the mirror from being demagnetised by stray magnetic fields, while a high Curie temperature is needed for the magnetisation of the mirror to survive the baking of the vacuum chamber.

The specularity of the mirrors, or angular spread resulting from the reflection process, must be thoroughly characterised. Other important characteristics of these mirrors are the decay length, end-effects (due to the finite size of the mirror) and the field strength. The decay length depends on the periodicity and decreases as the period of the array becomes smaller. Mirrors with short decay length are called 'hard' mirrors. End-effects, and their effect on the specularity, and possible counter measures, are discussed in section 6.3.2.

A diffraction grating can be produced by applying a bias magnetic field [Opa92,

Dav01], by applying an oscillating magnetic field [Opa99] or by physically vibrating the structure. Since the period of the grating should be comparable with the deBroglie wavelength of the atoms, short-period hard mirrors are required.

6.1 Basic Principles of Magnetic Mirrors

Magnetic mirrors rely on the fact that an array of magnets of alternating polarity with period a will produce a magnetic field whose strength decreases exponentially with distance y above the surface (see figure 6.1).

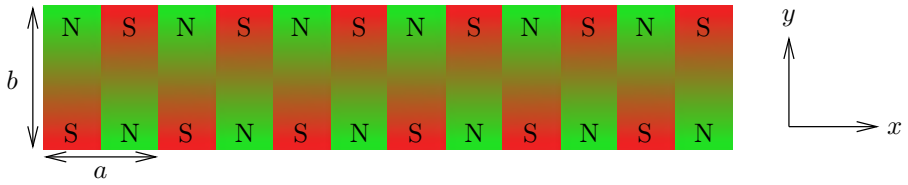

Figure 6.1: Schematic of a magnetic mirror: An array of magnets of alternating polarity produces a magnetic field with a strength that decays exponentially with decay length $k = 2\pi/a$ above the surface.

We assume the surface of the magnetic structure is in the x-z-plane with the magnetic polarity in the $\pm y$ direction alternating along the x-axis. For an infinite array the amplitude of such a field is [Lau99b]:

$$|B[x,y]| = B_0\, e^{-ky}\Big\{ \left(1-e^{-kb}\right) + \underbrace{\frac{1}{3}\left(1-e^{-3kb}\right) e^{-2ky}\,\cos[2kx] + \ldots}_{\text{corrugations close to surface}} \Big\} \tag{6.1}$$

where the decay constant

$$k = \frac{2\pi}{a} \tag{6.2}$$

The characteristic surface magnetic field is $B_0 = 2\,\mu_0\, M_0/\pi$ where M_0 is the magnetisation of the magnetic material, and the factors $(1-\exp[-nkb])$ account for the finite thickness b of the magnetic material. For heights $y \gg a/4\pi$, this simplifies to:

$$|B[x,y]| \approx \left(1-e^{-kb}\right)\, B_0\, e^{-ky} \tag{6.3}$$

At a given height above the surface, the magnetic field direction rotates around the z axis as one moves across the mirror in the x-direction:

$$\begin{pmatrix} B_x \\ B_y \end{pmatrix} = |B[y]| \begin{pmatrix} \sin[kx] \\ \cos[kx] \end{pmatrix}. \tag{6.4}$$

The first mirror made by the CSIRO/University of Melbourne group was an array of magnets with alternating polarity, comprising 16 NdFeB magnets of width 1.04 mm (period 2.08 mm) with a 0.52 mm magnet on each end to compensate for end-effects [Sid96]. Such magnets provide large magnetic fields, but the reflecting potential was quite uneven. Also, the period needs to be short for the mirror to be hard and to turn the mirror into a diffraction grating, as described in section 6.2. Therefore, much effort has been put into constructing mirrors and structures with micron-scale periods. Grooved structures are attractive for this purpose as they are considerably easier to fabricate than mirrors with alternating polarities. They are similar to the magnetic mirrors described above, except that every second magnet (for example every south up facing magnet) is missing, thereby circumventing the tedious task of producing magnetic fields with alternating polarities. In this case all equations remain unchanged except for the surface magnetic field, which is only half of the original: $B_0 = \mu_0 M_0/\pi$. The interaction potential between an atom with magnetic dipole moment $\vec{\mu}$ and a magnetic field $\vec{B}[x, y]$ is

$$U_{int} = -\vec{\mu}.\vec{B}[x, y]. \tag{6.5}$$

The potential exerts a gradient force on the atom given by:

$$F_{grad} = \nabla(\vec{\mu}.\vec{B}) = m_F g_F \mu_B \nabla B. \tag{6.6}$$

Low-field-seeking atoms approaching the mirror therefore encounter a repulsive force as the magnetic field amplitude increases (see figure 6.2). How close the atoms come to the mirror surface depends on the field strength. For example ^{87}Rb atoms in the $F = 2, m_F = 2$ ground state dropped from a height of 10 mm are reflected at a distance where the field amplitude is about 15 G. According to equation 6.1, the further away the reflection occurs, the less the atoms are susceptible to higher order

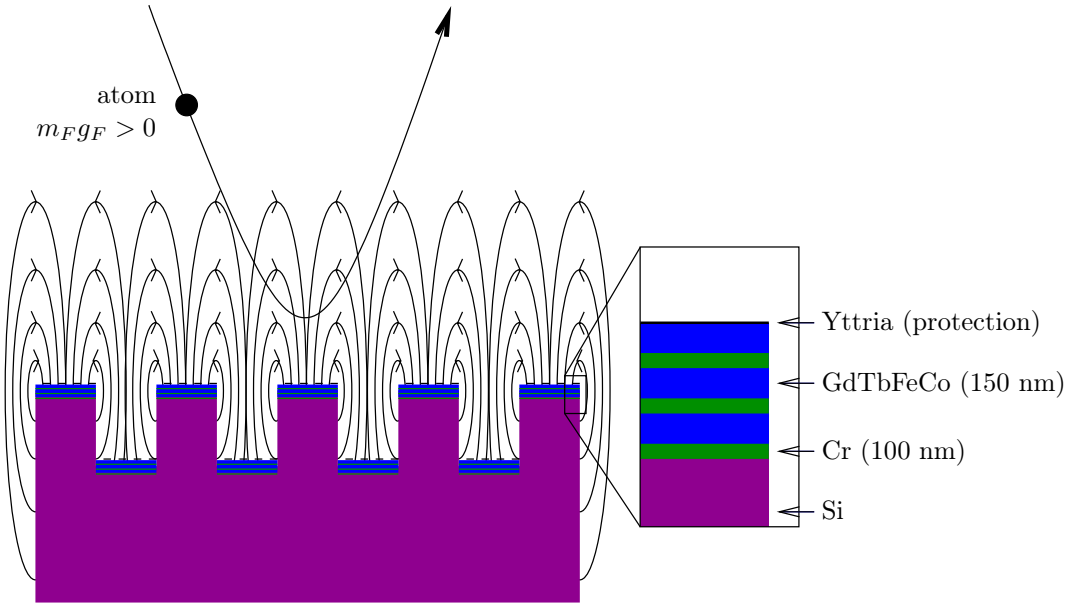

Figure 6.2: Reflection of an atom in a low-field-seeking state by a periodic grooved magnetic structure with perpendicularly magnetised film as in this experiment: a sandwich structure of three layers each of GdTbFeCo (the permanent magnetic film) and non-magnetic chromium (for better adhesion and to prevent parallel magnetisation). A thin yttria protection layer finishes the structure. The field lines are drawn only for the upper magnetic layer.

harmonics of the magnetic field or to imperfections of the mirror itself. In order to achieve micron-scale periodicity, our group initially attempted to construct periodic grooved micro-structures of ferromagnetic Ni, Co and AlNiCo [Sid97, Lau99b] using electron beam lithography and followed by sputtering and electroplating processes. All of the grooved part of the structure and some distance below it therefore consisted of the ferromagnetic material. However, this material tended to magnetise in-plane along the grooves, which does not produce a suitable magnetic field.

A solution to this is to use materials with a perpendicular magnetic anisotropy. Perpendicularly magnetised $Co_{0.8}Cr_{0.2}$ films on a non-magnetic grooved substrate produced successful magnetic mirrors [Sid02]. However, the magnetic properties of CoCr films were not ideal. Hysteresis loop measurements showed that the remanent magnetisation was only about one quarter of the saturation magnetisation. Furthermore, the magnetic domains of the mirror were observed to be not completely oriented, resulting in magnetic inhomogeneities.

The mirrors described in this chapter consisted of micro-fabricated grooved sili-

con structures, on to which several alternating layers of ferrimagnetic $Tb_6Gd_{10}Fe_{80}Co_4$ and non-magnetic Cr were coated [Wan05a]. Three double layers of Cr (100 nm) and TbGdFeCo (150 nm) were sputtered onto the silicon substrate (see figure 6.2). On top, a 20 nm layer of yttria was evaporated as a protection coating. Details of the fabrication of the mirrors used in this work, and the magnetic characteristics of the film are discussed in [Wan05a]. The advantages of this film include:

- a high perpendicular magnetic anisotropy,
- a high remanent field of more than 3.8 kG (see figure 6.3),
- a high coercivity of more than 4 kOe, protecting the magnetic structure from stray fields (see figure 6.3),
- a high expected Curie temperature of about 300°C, necessary for allowing the film to survive the baking of the vacuum chamber, and
- excellent magnetic homogeneity.

The field at the surface ($B_0(1-\exp[-kb])$) for this film and this grooved structure is about 1 kG. Figure 6.4 shows scans performed on a 10 mm×10 mm mirror (period $a = 1.5$ µm) with atomic force microscopy (AFM) and magnetic force microscopy (MFM).

The suitability of the micro-structure for atom optics is verified by taking MFM scans at various heights above the surface and plotting the relative magnetic field seen by the MFM logarithmically as a function of height (see figure 6.4). The straight line confirms the exponential decay, and the decay constant is consistent with the periodicity of the mirror.

6.2 Magnetic Diffraction Gratings for Atoms

Coherent splitting of atomic beams and the construction of efficient beam splitters are of great significance in atom optics. This, too, is currently usually done by manipulating the atoms with laser light [Gri94, Pfa93]. But ideas to use permanent magnetic structures for beam splitting have been discussed [Opa92].

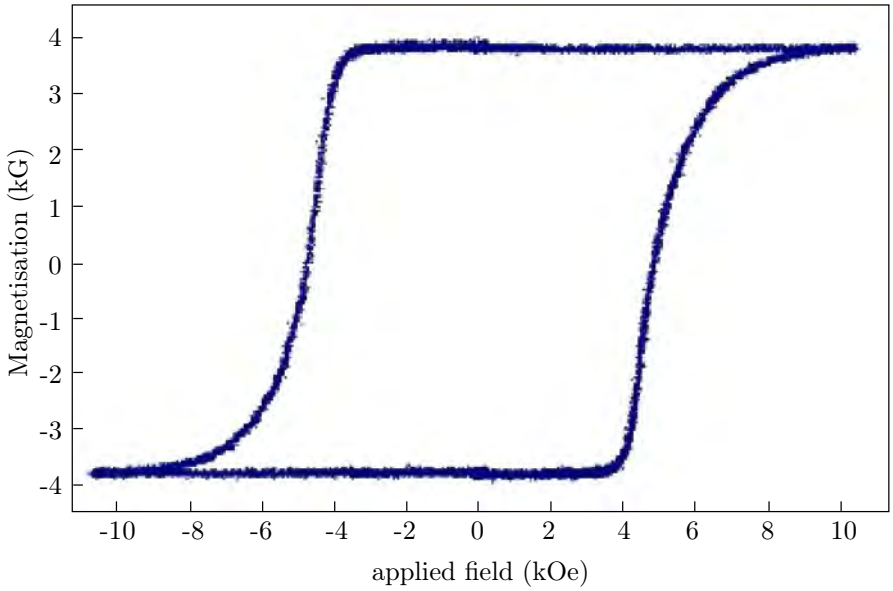

Figure 6.3: Hysteresis loop of the GdTbFeCo film measured using the magneto-optical Kerr effect (MOKE) before installation. The magnetisation is calibrated using SQUID-measurements. This displays the advantageous characteristics of the material, namely the high remanent field (3.8 kG) and the high coercivity (4 kOe)

The main idea is to use a periodic grooved structure as a diffraction grating. For this, the flatness of the equipotentials has to be broken. This can be done by:

- applying a bias field in the x or y-direction,
- applying a rotating bias field in the x-y plane, or
- physically vibrating the mirror.

When a bias field is applied along the y direction, a corrugation term results that varies with a period of a along the x direction:

$$\begin{aligned} B_x &= -b_1 e^{-ky} \cos[kx] \\ B_y &= \underbrace{b_1 e^{-ky} \sin[kx]}_{\text{magnetic array}} + \underbrace{b_0}_{\text{appl. field}} \end{aligned}$$

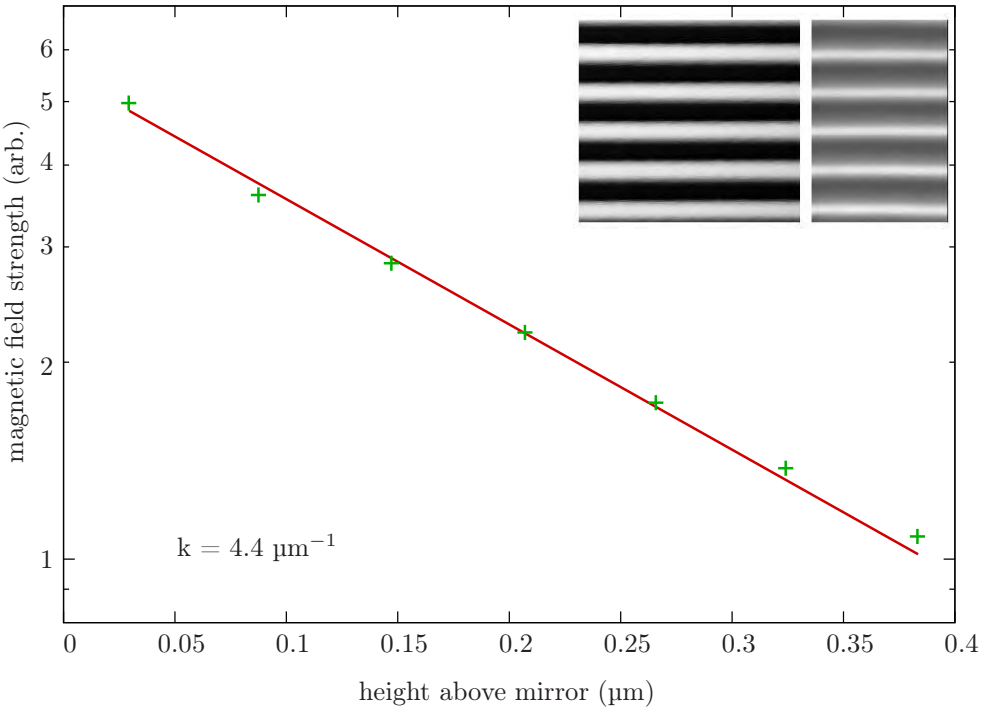

Figure 6.4: Decay of the magnetic field strength (log scale) as a function of height measured with a magnetic force microscope. The measured k of (4.4±0.2) µm^{-1} is in good agreement with the predicted value of 4.19 µm^{-1} calculated from equation 6.2 for a period a of 1.5 µm. Inset: Structure of the 10 mm by 10 mm mirror: Left: Surface scan (AFM), the period is 1.5 µm. Right: Magnetic field scan (MFM).

$$\begin{aligned} B &= \sqrt{B_x^2 + B_y^2} \\ &= \Bigg(\underbrace{b_0^2}_{\text{dc field}} + \underbrace{b_1^2 e^{-2ky}}_{\text{mirror term}} + \underbrace{2b_0 b_1 e^{-ky} \sin[kx]}_{\text{grating}} \Bigg)^{\frac{1}{2}} \end{aligned} \tag{6.7}$$

This corrugation is not to be confused with the higher order corrugation term in equation 6.1. The atoms see this periodic corrugation as a grating and the atomic matter waves are diffracted from it. The nth order of diffraction of a grating (at normal angle of incidence) is given by:

$$\sin \Theta_{diff} = \left(\frac{n \lambda_{dB}}{a} \right) \tag{6.8}$$

where Θ_{diff} is the angle of diffraction, $\lambda_{dB} = h/mv$ the deBroglie wavelength of the atom and a the period of the grating. Assuming the incident atom's velocity is

50 cm s^{-1}, and $a = 1.5$ µm, we expect the angle of the first order diffraction to be 6.1 mrad.

Larger diffraction angles can be obtained with non-normal incidence. For an angle of incidence of 45° and the other parameters the same as above, the diffraction angle is $\Theta_{diff} = 10$ mrad. This emphasises the point that micron-scale periods or less are needed to observe diffraction. This also puts a limit on the angular spread that may result from a lack of specularity in the reflection process. Another issue that needs to be considered in using these structures as gratings is the diffraction efficiency into the different orders [Dav01].

6.3 Theory of Atomic Reflection from a Corrugated Mirror

This section describes the reasons and sources of angular spread associated with reflection of atoms from a magnetic mirror, and explains how they can be calculated or approximated.

6.3.1 Angular Spread

Ideally, the velocity vectors of an atom directly before and after the reflection should have the same angle with respect to the mirror's surface, as stated by the law of reflection. This is a characteristic of specular reflection. In diffuse reflection the angle of the velocity vector after the reflection has no correlation with the incident velocity vector. As a measure of the *specularity* of the reflection, we use the value of the angular spread Θ. The angular spread is the rms difference between the horizontal components of the incident and reflected velocity vectors of all atoms. The main reason for angular spread are corrugations in the equipotentials of the magnetic field, which can arise from imperfect magnetisation, higher order corrugations, stray magnetic fields (see section 6.2), and effects due to the finite size of the array (end effects, discussed in section 6.3.2). As described in section 6.2, for the array of magnets to be used as a diffraction grating, the angular spread resulting from the reflection process Θ should be less than about 5 mrad. To calculate the angular spread, the forces due to magnetic gradients parallel to the mirror surface must be

determined. If the total magnetic field has an oscillating component of amplitude $B_G/2$, which for example would occur by adding an homogeneous bias field of magnitude B_G to an otherwise uniform field above the array, then the resulting force on an atom is [Ros00]:

$$F_x \approx k\,\mu_B\,B_G\,\sin[kx] \tag{6.9}$$

The time the atom is in the mirror field is approximately given by [Ros00]

$$T_{int} \approx \frac{4}{k\sqrt{2\,g\,h}} = \frac{4}{k\,v_v} \tag{6.10}$$

We can evaluate the maximum change in the horizontal velocity:

$$\Delta v = \frac{F_x}{M} \times T_{int} = \frac{4\,\mu_B\,B_G}{M\,v_v}\,\sin[kx] \tag{6.11}$$

Note that the maximum change in horizontal velocity is not dependent on the period $2\,\pi/k$ of the magnetic array. While shorter period mirrors expose the atom to a higher force, they are also harder and reduce the interaction time in such a way that the period is eliminated. For a single atom, we can obtain the maximum angle θ_{max} that results from reflection off the corrugated surface of the mirror from the change in the horizontal velocity Δv.

$$v_{out} = \begin{pmatrix} v_2 \\ v_{v,o} \end{pmatrix} = \underbrace{\begin{pmatrix} \cos[2\theta] & \sin[2\theta] \\ -\sin[2\theta] & \cos[2\theta] \end{pmatrix}}_{\text{rotation}} \underbrace{\begin{pmatrix} 1 & 0 \\ 0 & -1 \end{pmatrix}}_{\text{reflection}} \underbrace{\begin{pmatrix} v_1 \\ -v_v \end{pmatrix}}_{v_{in}} \tag{6.12}$$

$$\begin{aligned} v_2 &= v_1\,\cos[2\theta] + v_v\,\sin[2\theta] \\ &\approx v_1 + v_v\,2\theta \qquad (6.13) \\ \theta &\approx \frac{v_2 - v_1}{2v_v} = \frac{\Delta v}{2v_v} \\ \theta_{max} &\approx \frac{2\,\mu_B}{M\,v_v^2}\,B_G \approx 33 \text{ mrad} \qquad (6.14) \end{aligned}$$

for ^{87}Rb dropping from 2 cm height ($v_v = 0.63$ m/s) and for $B_G = 1$ G.

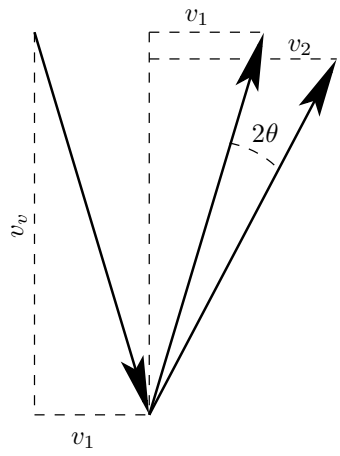

Figure 6.5: Schematic of a single atom reflection: An atom arrives at the mirror with a vertical velocity v_v and a horizontal velocity v_1. In a specular reflection, the sign of the vertical component of the velocity vector changes, whereas the horizontal component would stay the same. However, due to corrugations, its velocity vector might be rotated by 2θ, where θ is the angle of the equipotential at the point of reflection.

To observe the angular spread, the average horizontal velocities of the atom cloud have to be compared. For this, $\Delta v = v_2 - v_1$ has to be replaced by the "root mean square" value $\Delta v_{rms} = \sqrt{\bar{v}_2^2 - \bar{v}_1^2}$:

$$\Theta = \frac{\Delta v_{rms}}{2v_v} = \frac{\sqrt{\bar{v}_2^2 - \bar{v}_1^2}}{2v_v} \tag{6.15}$$

where $\bar{v}_1$ and $\bar{v}_2$ are the average horizontal velocities.

6.3.2 End-Effects

The finite size of the mirror can produce strong corrugations in the magnetic field, especially close to the edges. End-effects are more pronounced when the number of elements in the magnetic array is small. For mirrors using current carrying wires, these end effects can be suppressed by so called end-wires. These end-wires are placed at half the distance to where the next wire would be $(a/4)$, and carry half the current [Lau99a]. The magnetic field from the current in such wires approximates the magnetic field that would have been produced by the missing semi-infinite array. This is shown in figure 6.6. The magnetic field at a distance d from a wire is given

by the equation

$$B = \frac{\mu_0 I}{2 \pi d} \quad . \tag{6.16}$$

The resulting magnetic field of a finite wire array combined with these end-wires is in very good agreement with equation 6.1 for the region encompassed by the magnetic mirror and is a big improvement over non-corrected mirrors as can be seen in figure 6.6. A similar scheme has been used with permanent NdFeB magnets [Sid96] (in-plane magnetisation), where one magnet of half the thickness of the others was added to each end of the array to minimise the end-effects.

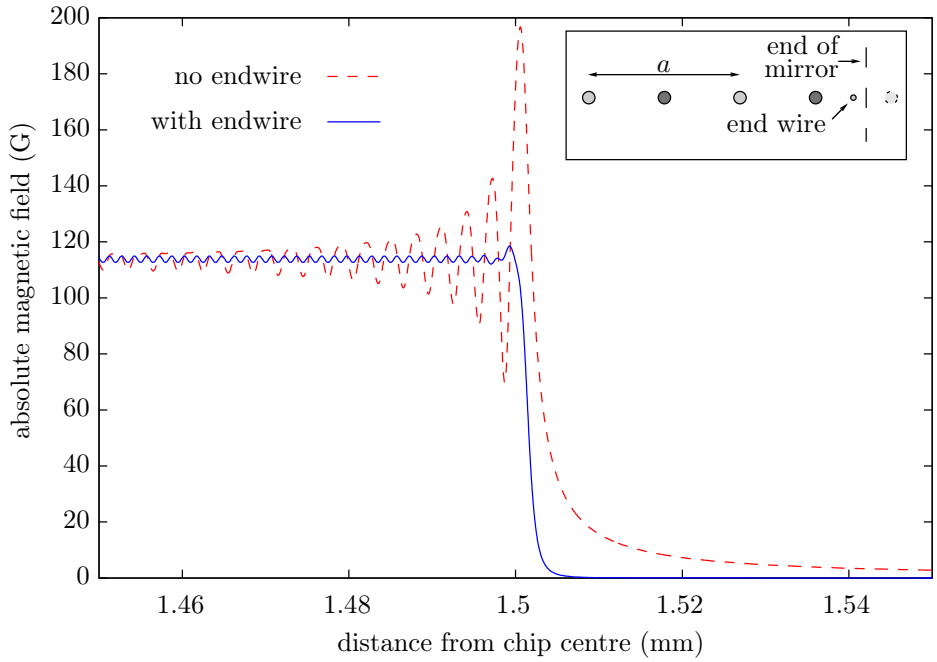

Figure 6.6: Computer calculations of the magnetic field 1 µm above a 3 mm×3 mm mirror with a period of 3 µm. The red dotted line represents a mirror without compensation for end-effects, which acquires strong corrugations towards the edge of the chip. The blue line represents the magnetic field with an additional end wire. There are no noticeable end-effects. The small residual corrugations on the blue line correspond to the higher order terms of equation 6.1. Inset: Schematic of the end-wire: End-wires with half the current of the other wires are positioned exactly in the centre between the last existing wire and where the next wire ought to have been (distance $a/4$ from the last wire).

Just as the magnetic field due to the end-wires can compensate the end-effects in finite length mirrors, similarly such a magnetic field would introduce corrugations to an *infinite* mirror, whose variation would then mimic the end-effects of a finite

size mirror with the edges at the position of the wires in the region between these two wires. This Gedankenexperiment allows one to approximate the magnetic field strength distortion resulting from the abrupt end of the magnetic array. This magnitude can then be used to approximate the corrugation of a finite size mirror in relation to the distance from its edge (see equation 6.9). The effective current I (discussed in section 6.4.1) of our magnets is about 140 mA, so the end-wires should carry about 70 mA. With this value, we calculate that 1 mm from the edge, the equivalent corrugating field has an amplitude of about 150 mG, which should result in a maximum angular spread of about 6 mrad (equation 6.14). This means that as long as most of the atoms are hitting the mirror further than 1 mm away from the edge, the end-effects will cause an angular spread smaller than this.

Considering a Gaussian width σ of the atom cloud of 3.0 mm, table 6.1 shows the percentage of atoms reflected from the parts of the mirror that satisfy this criterion 'less than 1 mm from edge', for the two types of mirror used in this experiment.

Table 6.1: Fraction of atoms incident on the different areas of the mirror. With the 3 mm mirror, only 35% of the reflected atoms are reflected from the uncorrugated area.

	3 mm mirror 3.0 µm period	10 mm mirror 1.5 µm period
max. spread due to end effects		
$<$ 6 mrad	13 %	82 %
$>$ 6 mrad	25 %	9 %
atoms missing the mirror	62 %	9 %
atom reflected from 'uncorrugated' region	35 %	90 %

6.4 Monte-Carlo Simulations

To better understand and verify our observations, a computer simulation of the experiment was created. The motion of the atoms was assumed to be classical, with the pre-cooled atoms exhibiting random initial velocities and positions with a Gaussian distribution, following pathways determined by these initial parameters and the prevailing conditions (gravity and the magnetic mirror).

6.4.1 Overview

Monte-Carlo simulations are named after a well-known area of Monaco, famous for gambling and casinos. In a Monte-Carlo simulation, a random initial configuration is chosen, and from this initial configuration the phase space is evolved deterministically in time. By averaging over many of these iterations, it is possible to make predictions about the reality. In this case, the random initial configuration consisted of a random positioning of the atoms in the x (horizontally perpendicular to the grooves) direction and z (vertical) direction and giving them random velocities v_x and v_z. The calculation then evolves the position according to the atom's velocities, and changes the velocities according to the forces experienced at the position.

The calculation does this by incrementing time by a certain amount (`timeStep`), calculating the new position of the atom considering the time increment and the speed of the atom in each direction, and changing the speed of the atom according to its current acceleration. To speed the calculation up, `timeStep` is comparatively large when the atom is far away from the mirror (10 µs, `timeStep1`), but smaller for accuracy when close to the mirror (10 ns, `timeStep2`). The complete source code (Fortran 77) can be found in the appendix B.1. Note that the source code needs the `/dev/urandom` random number device, which is supplied by Linux and most Unixes.

Gaussian random numbers

The initial position and velocity in the x- and z-direction are determined by a random number generator that produces a Gaussian distribution. Such a random number generator is not usually part of the programming environment and had to be implemented. Equation 6.17 (Box-Muller Transformation) transforms two random numbers x_1 and x_2 between 0 and 1 into a new random number y that follows a Gaussian distribution with width $\sigma^2 = 1$.

$$y = \sqrt{-2\,\ln[x_1]}\,\cos[2\,\pi\,x_2] \tag{6.17}$$

Calculation of the magnetic field

The magnetic field was calculated in two different ways:

- Using equation 6.1 with or without the higher-order harmonic term. Without the higher-order term the magnetic equipotentials are flat, and the reflection is perfectly specular. While this is not realistic, we can use this to compare our experimental data to the ideal case.

  The advantage of this method is the short time of the numerical simulations.

- Using the analogy between a magnet and current carrying wires: A magnet has the same magnetic effect as a wire around the boundary of the magnet that carries a current of magnitude

$$I = M \times h \tag{6.18}$$

  where M is the magnetisation, h the height of the magnet and I the effective current.

  The magnetic field above the centre of a wire again is given by the Biot Savart law for finite length wires

$$B = \frac{\mu_0 I}{2\,\pi\,d}\,\frac{l}{\sqrt{l^2+d^2}} \tag{6.19}$$

  where l is the length of the wire and d the distance from the wire. The magnetic fields of all wires have to be added up by vector-addition to generate the total field. In this method, higher-order terms and end-effects are automatically included.

The force on an atom with a magnetic moment ($g_F m_F \mu_B$) can be calculated from the gradients of the magnetic field in the x and y direction. For a Rb atom in the $F = 2$, $m_F = 2$ stretch state, the equation is as follows:

$$F = -\,\mu_B\,\nabla\,B \tag{6.20}$$

where μ_B is the Bohr magneton.

6.4.2 Determining the Angular Spread

To determine the angular spread (equation (6.15)), two transverse velocities need to be measured, one for a perfectly specular mirror (v_1), and the other for the mirror which is to be characterised (v_2). This is done by a 'time of flight' method. The algorithm generates an atom with random position and speed, according to the observed sizes of the atom cloud in the MOT, and then follows this atom along its trajectory. At certain preselected times (every 5 ms in this case), the position of the atom is stored. By repeating this 10,000 to 100,000 times, images of virtual atom clouds at these given times are generated. By fitting the Gaussian function

$$f[x] = n_0 \exp\left[-\frac{x^2}{2\,\sigma^2}\right] \tag{6.21}$$

to the cross section of each atom cloud, the transverse size σ is determined. If the atom cloud has the initial size σ_0, then the size $\sigma(t)$ at time t is given by

$$\sigma^2[t^2] = \sigma_0^2 + v^2\,t^2 \tag{6.22}$$

A standard fitting algorithm can easily determine v^2. The velocities before and after the reflection are determined in this way and equation 6.15 used to calculate Θ.

6.5 The Magnetic Mirror Experiment Setup

This section describes the actual experiment. Initially a brief description of the experiment hardware is given, followed by the procedure of each experiment. Finally the results of two experiments with different permanent magnet grooved mirrors are presented.

6.5.1 The Magneto-Optical Trap

A Toptica DL 100 diode laser was locked to the $F = 2 \rightarrow F' = 2$ transition of the ^{87}Rb D2 line using a standard Doppler-free saturated absorption locking scheme. A double-passed 110 MHz centre frequency AOM was used to shift the frequency close to the desired $F = 2 \rightarrow F = 3$ trapping transition. This light was used to

injection-lock the slave laser.

This scheme offered three important features:

- The frequency of the laser could be adjusted as needed for the MOT or optical molasses use by changing the AOM frequency.

- Switching the AOM off resulted in a far-off-resonance lasing mode of the slave laser within less than a microsecond, overcoming the negative effects of the comparatively slow mechanical shutter(400 µs). Figure 6.7 demonstrates the importance of this. In this sequence, atoms were trapped in a MOT, cooled for 10 ms in an optical molasses, and they then received different treatments over the next 10 ms, before the picture was taken. As can be seen, the number of atoms in the trap is reduced by more then 50% if the laser remains on frequency during the closing and opening of the shutter.

- A fraction of the unshifted master laser beam could be used for optical pumping the atoms into the $F = 2$, $m_F = 2$ state.

The optical pumping laser was expanded to fill a cross section of 9 mm^2 around the trap, and retro-reflected to minimise the pushing of the atoms. The 60 mW output of the slave laser was coupled into a single-mode fibre with an efficiency of roughly 50% for beam shaping. The light emanating from that fibre with a near-perfect Gaussian transverse shape was then split into six separate beams using $\lambda/2$ wave plates and polarising beam splitters to allow independent control of the shape and position of the MOT. The scheme can be seen in figure A.1. A second Toptica DL 100 laser was used as a probe laser. This laser was locked using a simple saturated absorption lock to the peak of the crossover resonance between the $F = 2 \rightarrow F' = 2$ and $F = 2 \rightarrow F' = 3$ transitions, and then frequency-shifted onto the $F = 2 \rightarrow F = 3$ resonance by an AOM that also worked as a fast shutter. The repumping laser, a home-made extended cavity diode laser, was locked to the $F = 1 \rightarrow F' = 2$ D2 line. The quadrupole field gradient for the MOT was about 10 G/cm in the axial direction. It could be switched off in about 1 ms. Three sets of coils were used to eliminate residual magnetic fields including the Earth's magnetic field. Rubidium was contained in a separate oven (usually kept at room temperature). A valve between the oven and the main chamber provided control

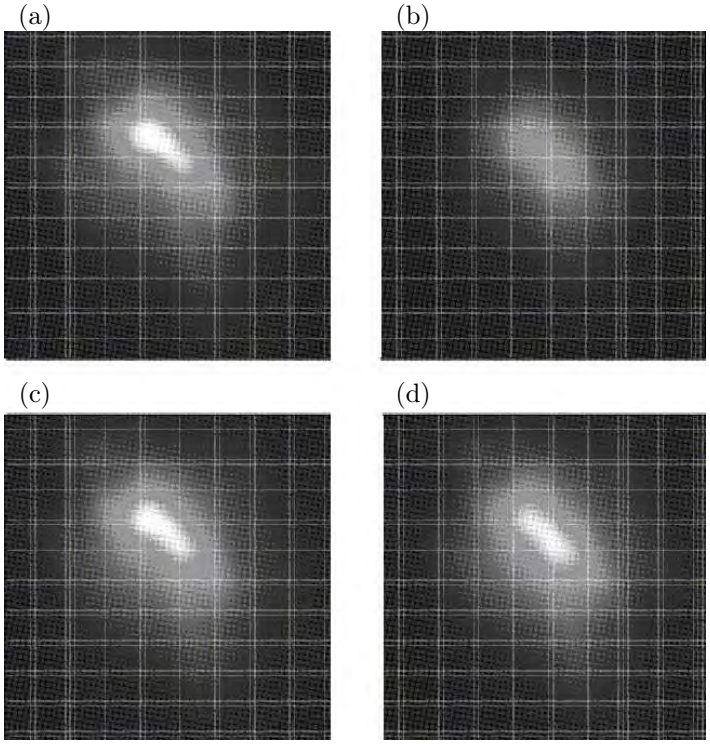

Figure 6.7: Comparison of different techniques to release the atoms from the MOT/molasses: (a) Atoms are not released, all atoms remain in the molasses. (b) The laser has been switched off using a shutter, as is the standard technique. More than half of the atoms are lost. (c) The laser remained on, but the injection lock was destroyed by switching off the AOM. The molasses laser immediately jumps off resonance, until the AOM is switched on again. Most atoms are preserved. (d) The laser is unlocked shortly before switching it off. Again, most atoms are preserved. All of this indicates that during the switching off of the trapping laser, a considerable fraction of the atoms is blown away. Switching the laser far-off-resonance by switching the injection beam off preserves the atoms.

over the amount of rubidium vapour entering the chamber. The MOT trapped the atoms out of the tail of the Maxwellian velocity distribution of the background Rb vapour. The density of the cloud was high enough to absorb 95% of the probe laser sent through the trap, which corresponds to roughly 10^8 atoms in the trap.

6.5.2 Measurement Procedure

The experiment was controlled by a computer running LabView 6.1. A National Instruments analog output card with 8 analog channels (PCI-6713) and a National Instruments digital I/O card with 32 channels (PCI-6534) were used to connect to

the experiment. These cards were synchronised using the RTSI bus. The atom cloud was monitored by fluorescence images taken by a CCD camera positioned above the atom cloud. To operate the camera reliably, the shutter needed to be opened for more than 5 ms. The precise timing was therefore done by opening the camera's shutter 5 ms before the intended time, and closing it 5 ms afterwards, and illuminating the cloud for only 1 ms by switching on and off an on-resonance probe beam. A typical timing procedure of the experiment can be seen in table 6.2.

Table 6.2: Typical experiment sequence: the 1st block describes the cooling in the molasses and the optical pumping into the low-field-seeking state; the 2nd block shows the taking of the fluorescent image; the 3rd block is the background image; and the 4th block switches the MOT back on.

time	description
-10 ms	quadrupole field off
	detuning to ca. -40 MHz
-4 ms	optical pumping beam switched on
0 ms	MOT beams switched off
1 ms	optical pumping switched off
	repumping laser switched off
t - 5 ms	CCD camera opened
t	probe beam switched on
t + 1 ms	probe beam switched off
t + 5 ms	CCD camera closed
1895 ms	CCD camera opened
1900 ms	probe beam switched on
1901 ms	probe beam switched off
1905 ms	CCD camera closed
2000 ms	MOT-beams on
	repumper on
	quadrupole field on
	detuning to ca. -5 MHz

The cycle was repeated every 5 to 10 seconds. The CCD output data was collected by a second computer, running a NI LabView 6.1 program that was synchronised to the control computer via TCP/IP, and gathering the data by interfacing to a Princeton Instruments WinView 4 using ActiveX and analysing the data 'on the fly'. This included fitting a Gaussian to the fluorescence image, plotting the squares of the cloud's width against the squares of the time, and extracting the change of the horizontal velocity thereby calculating the angular spread during the

reflection. At longer drop times, the density of the atom cloud is small and several images are taken and averaged, which also was automatically done by the LabView program.

6.5.3 Experimental Observations with the 10 mm Mirror

The first mirror had a size of 10 mm×10 mm. The period a of the magnetic grooved structure was 1.5 µm resulting in an array of more than 6,500 periods. The magnetic properties of this mirror were discussed in section 6.1. The distance between the centre of the MOT and the surface of the mirror could be adjusted between 14 mm (at shorter distances, the mirror started cutting into the MOT beams) and 20 mm (lowest possible adjustment). Parallel to the grooves, no significant increase in the angular velocity of the atom cloud was observed. This is expected for geometrical reasons. An example of such a measurement is presented in figure 6.8. The slight apparent decrease in the horizontal velocity seen in that figure is due to atoms with the highest velocity missing the mirror. Measurements of the angular velocity of the atom cloud perpendicular to the grooves, however, showed a much higher spread. An example of the observed transverse velocities is given in figure 6.9 with the following results:

$$\begin{array}{rrcl} \text{before reflection} & v_1^2 & = & (15.3 \pm 0.5)\ \text{cm}^2\ \text{s}^{-2} \\ \text{after reflection} & v_2^2 & = & (53.3 \pm 2.3)\ \text{cm}^2\ \text{s}^{-2} \\ \text{vertical} & v_v & = & (54 \pm 2)\ \text{cm s}^{-1} \end{array}$$

$$\Theta \;=\; \frac{\sqrt{v_2^2 - v_1^2}}{2\,v_v} \;=\; (57 \pm 3)\,\text{mrad} \tag{6.23}$$

These errors only consider the standard deviation, systematic errors might also apply.

By taking fluorescent images along the grooves (z-direction) from the side of the vacuum chamber strong curvature of the reflected atom cloud was observed (see figure 6.10). This curvature is clear evidence that the magnetic potential from which the atoms are reflecting is not flat.

This could be caused by:

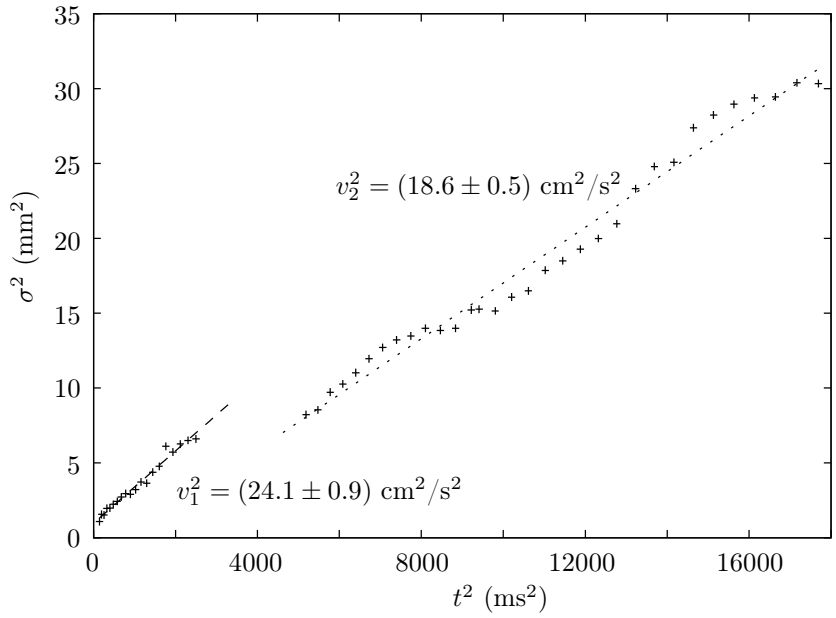

Figure 6.8: Transverse velocity (parallel to the grooves) of the atom cloud before and after the reflection on the 10 mm mirror. σ is the width of the Gaussian distribution of the atom cloud (see equation 6.21). This measurement does not suggest a noticeable heating of the atom cloud, which would result in v_2^2 to be higher than v_1^2.

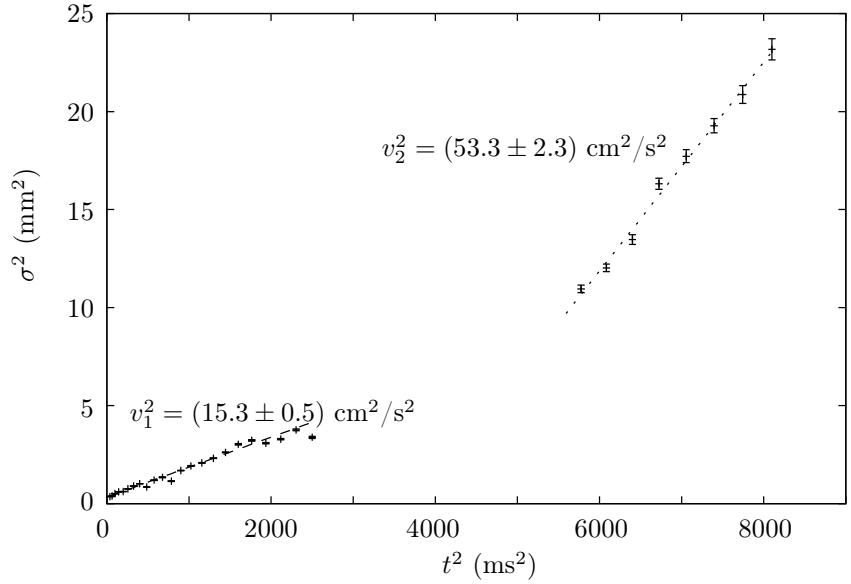

Figure 6.9: Transverse velocity (perpendicular to the grooves) of the atom cloud before and after the reflection on the 10 mm mirror. Here, a definitive and large increase in the angular velocity is observed. The angular spread Θ is calculated to (57$\pm$3) mrad.

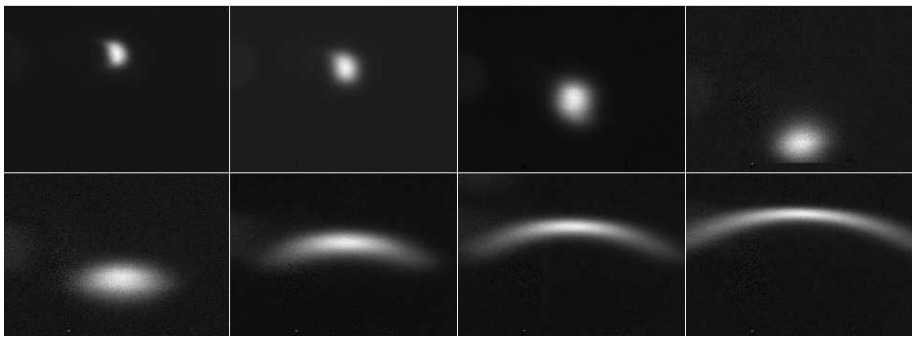

Figure 6.10: Sequence of fluorescence images of atoms incident on the 10 mm mirror. The camera is viewing from the side of the chamber along the z-direction (direction of the grooves). The images in the top row show the atom cloud before the reflection at 10, 20, 30, and 40 ms. The images in the bottom row are taken after the reflection at 60, 70, 80, and 90 ms.

- Decay of the magnetic properties during baking. The Curie temperature for the GbTdFeCo film used was about 300°C. During the baking, a temperature of about 150°C was reached, well below the Curie temperature. Tests performed later by Timothy Roach [Roa06], however, showed signs of serious deterioration of the magnetic film at temperatures as low as 120 °C during baking, making this the most likely reason for the diffuse reflection.

- The rubidium could have chemically reacted with the magnetic film, despite the protective layer.

- Stray magnetic field or field gradient.
  Externally applied magnetic fields (up to 1 G) or magnetic field gradients were not able to improve the mirror's quality.

The observation of curvature in the fluorescence images provides a direct method to check for the presence of diffuse reflection. In order to see a curvature in the Monte Carlo simulations, a magnetic field strength of only 10% of that expected from the characterisation of the film after fabrication was combined with a 1 G bias field, to produce the spatial atom number distribution (after a simulated 100 ms drop time) in figure 6.11. Both the weak magnetic field strength and the bias field were necessary to produce the curvature which is still much less than the observations in figure 6.10. Similar observations of diffuse reflection of a BEC from a evanescent

light field and a similar approach to modelling this behaviour is shown in [Per06].

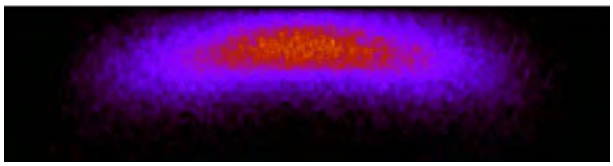

Figure 6.11: Monte Carlo simulation of the reflection of cold Rb atoms from a 10 mm magnetic mirror with a 90% weaker magnetic field strength at 1 G bias field after a simulated drop time of 100 ms. The onset of a curvature in the reflected cloud is clearly seen, though small compared to the observed curvatures in the last frame of figure 6.10.

After verifying the poor quality of the mirror, it was decided to remove the mirror from the chamber. The mirror's magnetic properties were reevaluated with the magnetic force microscope (MFM). Severe deterioration in the magnetic properties was observed (see figure 6.12) compared to before the mirror was installed (figure 6.4, right part of inset). Apart from the deterioration of the magnetic film, which is easily recognised in the figure, the contrast has also decreased by more than an order of magnitude. (It is difficult to quantify the contrast reliably because of the use of different MFM tips, which usually give different results.)

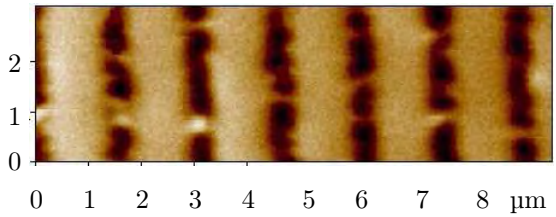

Figure 6.12: Magnetic structure measured by a MFM scan after removing the 10 mm mirror 15 months after installation in the vacuum chamber.

Attempts to re-magnetise the mirror produced negligible improvements.

6.5.4 3 mm Mirror

It was not possible at that time to fabricate a new mirror. Because of this, a previously fabricated 'proof of concept' mirror was installed in the chamber. This mirror had a size of 3 mm x 3 mm. The periodicity a is 3.0 µm resulting in an

array of 1,000 magnets. The mirror had a 1 mm ungrooved area around the grooved section. The magnetic film consisted of one layer each of Cr (140 nm), GdTbFeCo (250 nm), and Y_2O_3 (30 nm) for protection. Assuming a magnetisation of 3.8 kG, we expect a field at the surface of 320 G, significantly less than for the first mirror. End-effects will have a considerably larger effect (see table 6.1).

The magnetic properties of this mirror were measured before and after baking and evacuation of the chamber at 110-120°C. No effects of this procedure on the magnetic film could be seen. The mirror was raised as close to the MOT as possible, 10 mm, without obstructing the MOT beams. This was to minimise the size of the atom cloud at the time of the bounce and so minimise the number of atoms missing the mirror or suffering large horizontal acceleration due to the end-effects. The expansion of the atom cloud after the reflection seemed to indicate that the effective temperature did not change significantly, but this is misleading:

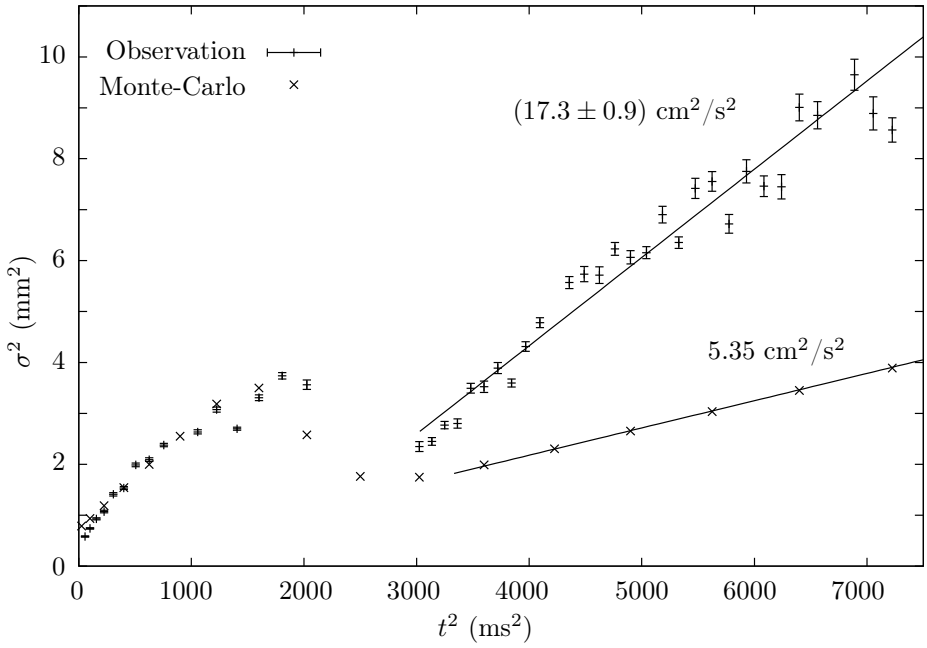

Figure 6.13: Transverse rms size of atom cloud after reflection on the 3 mm mirror: Observation and simulation. As the small size of the mirror removes the 'hotter' atoms by reflecting just the centre, it is no longer viable to compare the angular velocity before and after the reflection. Instead the angular spread of the reflected atoms is compared to a Monte-Carlo simulation of a perfect mirror. This procedure gives an angular spread Θ of (39.1±2.4) mrad.

The sudden decrease in the width of the cloud at the time of the reflection

occurs because a considerable fraction of the atoms have missed the mirror. Since these atoms are the hottest atoms, a significant decrease of temperature is expected. Because of this, the angular spread from the reflection process had to be estimated by comparing the observed expansion after the reflection with the results of a simulation to give the expected expansion. Also an image taken from the side shows a slight curvature of the atom cloud (figure 6.14).

Both propagations are compared in figure 6.13. The observed velocities are given below. The vertical speed v_v was calculated from the drop height (10±1) mm.

$$\begin{array}{rrcl} \text{simulation} & v_1^2 & = & 5.35 \text{ cm}^2 \text{ s}^{-2} \\ \text{observed} & v_2^2 & = & (17.3 \pm 0.9) \text{ cm}^2 \text{ s}^{-2} \\ \text{vertical} & v_v & = & (45 \pm 2) \text{ cm s}^{-1} \end{array}$$

Using the equation for the diffusive component (6.15) Θ for this mirror can be calculated:

$$\Theta = \frac{\sqrt{v_2^2 - v_1^2}}{2\, v_v} = (39.1 \pm 2.4)\,\text{mrad} \tag{6.24}$$

Figure 6.14: Fluorescence image taken of the atom cloud 100 ms after release from the MOT 10 mm above the 3 mm mirror. Again a slight curvature is seen, though less dominant than for the 10 mm mirror.

6.6 Conclusion

The reflection of ultracold atoms from two magnetic mirrors based on micron-scale periodic grooved magnetic structures was evaluated. Considerable angular spread was observed on both mirrors with the appearance of a curved profile of the reflected cloud. On the smaller, 3 mm mirror, this could be explained by end-effects, originating from the limited size of the mirror itself. The diffuse reflection on the larger, 10 mm mirror was due to a degradation of the magnetic film.

Supplementary work by Timothy Roach [Roa06] and Shannon Whitlock [Whi07b] strongly suggests that the increased temperatures in the vacuum chamber during the bake out deteriorated the magnetic film. Annealing magnetic films with similar compositions to the ones used during the evacuation of the vacuum chamber in this experiment showed serious degradation of the magnetic properties as well as demagnetisation after having been submitted to a procedure similar to the bakeout of the vacuum chamber (130°C for 2 days), whereas at lower temperatures (100°C) the characteristics remained good and unchanged.

Unfortunately, it was not possible to fabricate another mirror to replace the tested mirrors. It is possible that measurement of the specularity of a mirror immediately after installation in the vacuum chamber may have produced better results. Our experiments with the 3 mm mirror showed that under favourable conditions, the quality of the mirror could be evaluated within a few weeks after installation.

Developing materials with a higher Curie Temperature, combined with baking at a lower temperature, will allow for for the fabrication of hard, specular mirrors that then can be converted into diffraction gratings.

Chapter 7

Conclusion

7.1 Summary

The research area of atom optics in general and Bose-Einstein condensate research in particular have in recent years more and more embraced the idea of microwires on atom chips to produce steep and complex magnetic potentials. Since the observation of fragmentation in atomic clouds and BECs close to current carrying wires and magnets, and the explanation thereof through deviations in the current path through the wire due mainly to corrugations in the edges of microwires, considerable effort has gone into the precise creation of smooth edged complex microwire geometries on atom chips.

In chapter 3 of this thesis, it was shown that femtosecond laser ablation is a tool completely unlike the common techniques based on photolithography to produce a microwire atom chip, with the distinct advantage of needing considerably fewer intermediate steps. An apparatus to create two-dimensional patterns was presented; its development is comparatively inexpensive for research groups that already have access to a femtosecond laser system. Consequent testing and characterisation revealed that copper is the most suitable metal to produce the cleanest possible edges; however, for reasons of reflectivity and protection, it is advisable to coat the copper with a thinner gold layer. Scanning electron microscope images revealed that the edge roughness is only 16 nm, a value to match and exceed the quality of edge roughnesses reported by some other microwire atom chip groups. Furthermore, the analysis of the edge over a range of 650 µm revealed no dominant frequencies of the

corrugations, which could have created serious fragmentation in BECs.

Following up on these promising optical evaluations of the femtosecond laser ablation created microwires, chapter 4 characterised the magnetic fields produced by these microwires. A magneto-resistance microscope (MRM) was presented, which used a magnetic tunnel junction sensor to accurately map the magnetic field component perpendicular to the surface of the atom chip with a spatial resolution of 5 µm, and a noise floor for the magnetic field of 2 mG. A method was presented to use this data to completely calculate the magnetic field components in the other two dimensions, thereby giving the full magnetic field. This was used to infer the magnetic corrugations in the direction parallel to the wire, which are most dominantly responsible for fragmentations of the atom cloud. The best accuracy of the magnetic potential measured by the MRM is comparable with that of cold, thermal atoms. In this way it was possible, even before installing the atom chip in the vacuum chamber, to compare its potential corrugations with that of comparable conventional microwire atom chips, and assess that the ablated microwires achieve similarly low corrugations.

Also in chapter 4, the idea was developed that since corrugations in the edges can cause fragmentation, intentionally shaping the edges can produce interesting complex patterns in much the same way. This chapter explained how from initial qualitative considerations a final wire geometry was evolved, and simulated using finite element analysis (FEA), that would produce a string of double wells. Such a wire was then produced using femtosecond laser ablation, and measured with the MRM. The very good agreement between the simulation and the results from the MRM validates that (a) the shaping of the edge can produce such a potential, (b) the MRM is able to resolve it, (c) the method of inferring the two other dimensions of the magnetic field from a single one works, and (d) FEA can reliably predict the magnetic field of a microwire even before it is fabricated.

Finally, chapter 5 described the path towards testing the femtosecond laser ablated microwire atom chip with a Bose-Einstein condensate (BEC). The full dual-layer atom chip was presented, consisting of a high-current silver foil layer beneath the microwire layer which is needed to produce the initial strong magnetic fields to trap enough atoms for evaporative cooling. A Low Velocity Intense Source of

atoms (LVIS) was presented, and its modus operandi explained. It was used to load atoms into the MOT created close to the atom chip. Initial measurements of loading atoms into the LVIS and the surface MOT were presented and the imaging system was tested. While the temperature in the surface MOT was about 55-60 µK, the number of atoms loaded into the MOT was unfortunately too low, about 10^7, to successfully start evaporative cooling or to load the atoms into the atom chip. The basis for the low number of atoms was a lower than expected loading rate: Only about 10^6 atoms per second were loaded into the surface MOT, while initial experiments suggested that the flux could be as high as 10^9 atoms per second. The suspected reason is that the mean velocity of the atomic beam is considerably higher than the capture velocity, so only a small fraction of atoms are captured.

Chapter 6 described research performed earlier in the studies, where the reflection of a cold atomic cloud from two permanent magnetic mirrors was evaluated. Atoms were dropped under gravity about 15-20 mm onto a magnetic mirror consisting of a grooved structure with a perpendicularly magnetised magnetic film. The resulting magnetic field decays exponentially with distance, where the period of the structure corresponds to the decay constant. Atoms in high-field seeking states are repelled, and thus reflected. It was found that a considerable curvature of the atomic cloud indicates strong diffuse components in the reflection, a feature verified by Monte-Carlo simulations. Whereas this diffuse reflection can be attributed to end effects in the case of the small 3 mm mirror, the magnetic field pattern in the case of the larger 10 mm mirror was found to have degenerated, probably during baking. The findings relate to similar experiments on the reflection of a BEC from an evanescent wave, presented in [Per06].

7.2 Outlook

As has been shown in chapter 4, the measurement of the magnetic field component parallel to the wire is limited by the noise level of the MRM. The MRM is a very useful tool during initial assessment and characterisation, being comparable with the use of cold thermal atoms. However, to really assess the full potential of the new fabrication method of femtosecond laser ablation, the author strongly suggests

to try and map the magnetic potential with a BEC. A BEC has a considerably higher precision and lower noise level ($\Delta B_{||}/B_r \approx 10^{-6}$ as opposed to 10^{-4}), a feature required to compare the new microwires to their 'conventionally' fabricated counterparts of other experiments.

To achieve this, primarily the loading of the surface MOT needs to be analysed and optimised. The number of atoms in the trap has to be enhanced by at least one order of magnitude to supply enough atoms for evaporative cooling. A suggestion is to replace the LVIS with a 2D$^+$-MOT, something that can be done by changing the magnetic configuration into a 2D quadrupole field and reducing the intensity in the vertical trapping beam. The atomic flux and its velocity distribution has to be studied and optimised. When the loading of the surface MOT is found to be sufficient, the next tasks are to load the atom cloud into a MOT created by currents in the silver foil layer combined with the large B_x external coils. In this trap, the atoms will be compressed and prepared for the transition into the magnetic trap. This is done by switching off the trapping lasers, shining in weak (100 µW) σ^+ polarised on-resonant light to optically pump the atoms into the $F = 2, m_F = +2$ low field seeking state, and changing the current through the silver foil layer from the U- into the Z-shape. Once the atoms are magnetically trapped, they can be evaporatively cooled to quantum degeneracy (BEC) and then loaded into the magnetic trap created by a current in the microwires. Imaging the BEC evolving inside the straight, femtosecond laser ablated microwire will provide data to assess the spatial noise of the magnetic field produced by the femtosecond laser ablated microwires to an accuracy $\Delta B_{||}/B_r$ at least two orders of magnitude better than the MRM.

The sculptured microwire on the atom chip can be used to carefully map short-ranged forces. The source of the to-be-measured force would be placed close to one of the double-well structures so that the potential imbalance will result in a measurable difference in condensed atoms in one of the two wells. At the same time, other wells will be unaffected and can be used as a reference measurement.

The sharp threshold for femtosecond laser ablation could be used in future atom chip fabrication to create multi-layer microwire atom chips reliably: Without having to re-position the chip itself, just by tuning the fluence of the laser pulses, the

ablation depth can be tuned to ablate just certain layers of a multilayer coated atom chip. Similarly, a permanent magnetic layer could be combined with current carrying layers to combine the low thermal heating rate of magnetic traps created by permanent magnetic films with the flexibility of manipulation by microwires with tunable DC and AC currents.

Bibliography

[And95] M. H. Anderson, J. R. Ensher, M. R. Matthews, C. E. Wieman, and E. A. Cornell. "Observations of Bose-Einstein condensation in a dilute atomic vapor." *Science*, 269:198–201 (1995).
URL http://www.bec.nist.gov/PDF/bose-einst.pdf

[And97] M. R. Andrews, C. G. Townsend, H.-J. Miesner, D. S. Durfee, D. M. Kurn, and W. Ketterle. "Observation of Interference Between Two Bose Condensates." *Science*, 275(5300):637–641 (1997). doi: 10.1126/science.275.5300.637.
URL http://www.sciencemag.org/cgi/content/abstract/275/5300/637

[And00] B. P. Anderson, P. C. Haljan, C. E. Wieman, and E. A. Cornell. "Vortex Precession in Bose-Einstein Condensates: Observations with Filled and Empty Cores." *Phys. Rev. Lett.*, 85(14):2857–2860 (Oct 2000). doi: 10.1103/PhysRevLett.85.2857.

[Ant04] M. Antezza, L. P. Pitaevskii, and S. Stringari. "Effect of the Casimir-Polder force on the collective oscillations of a trapped Bose-Einstein condensate." *Phys. Rev. A*, 70(5):053619 (Nov 2004). doi: 10.1103/PhysRevA.70.053619.

[Bab05] J. F. Babb. "Long-range atom-surface interactions for cold atoms." *Journal of Physics: Conference Series*, 19:1–9 (2005).
URL http://stacks.iop.org/1742-6596/19/1

[Bal88] V. I. Balykin, V. S. Letokhov, Y. B. Ovchinnikiv, and A. I. Sidorov. "Quantum-State-Selective Mirror Reflection of Atoms by Laser Light." *Phys. Rev. Lett.*, 60:2137 (1988).

[Bar01] M. D. Barrett, J. A. Sauer, and M. S. Chapman. "All-Optical Formation of an Atomic Bose-Einstein Condensate." *Phys. Rev. Lett.*, 87(1):010404 (Jun 2001). doi:10.1103/PhysRevLett.87.010404.
URL `http://prola.aps.org/abstract/PRL/v87/i1/e010404`

[Ber98] P. Berthoud, A. Joyet, G. Dudle, N. Sagna, and P. Thomann. "A continuous beam of slow, cold cesium atoms magnetically extracted from a 2D magneto-optical trap." *EPL (Europhysics Letters)*, 41(2):141–146 (1998).
URL `http://stacks.iop.org/0295-5075/41/141`

[Bho08] S. G. Bhongale and E. Timmermans. "Phase Separated BEC for High-Sensitivity Force Measurement." *Physical Review Letters*, 100(18):185301 (2008). doi:10.1103/PhysRevLett.100.185301.
URL `http://link.aps.org/abstract/PRL/v100/e185301`

[Bon01] J. Bonse, J. M. Wrobel, J. Krüger, and W. Kautek. "Ultrashort-pulse laser ablation of indium phosphide in air." *Applied Physics A*, 72(1):89 – 94 (January 2001). doi:10.1007/s003390000596.
URL `http://www.springerlink.com/content/lr44vefg1c583vuv`

[Bos24] S. N. Bose. "Plancks Gesetz und Lichtquantenhypothese." *Zeitschrift für Physik*, 26(1):178–181 (December 1924). doi:10.1007/BF01327326.
URL `http://dbserv.ihep.su/~elan/src/bose24/eng.pdf`

[Bou08] I. Bouchoule, J.-B. Trebbia, and C. L. G. Alzar. "Limitations of the modulation method to smooth wire-guide roughness." *Physical Review A (Atomic, Molecular, and Optical Physics)*, 77(2):023624 (2008). doi:10.1103/PhysRevA.77.023624.
URL `http://link.aps.org/abstract/PRA/v77/e023624`

[Boy07] M. Boyd, E. W. Streed, P. Medley, G. K. Campbell, J. Mun, W. Ketterle, and D. E. Pritchard. "Atom trapping with a thin magnetic film." *Physical*

Review A (Atomic, Molecular, and Optical Physics), 76(4):043624 (2007). doi:10.1103/PhysRevA.76.043624.
URL `http://link.aps.org/abstract/PRA/v76/e043624`

[Bru00] K. Brugger, T. Calarco, D. Cassettari, R. Folman, A. Haase, B. Hessmo, P. Krüger, T. Maier, and J. Schmiedmayer. "Nanofabricated atom optics: Atom chips." *Journal of Modern Optics*, 47(14–15):2789–2809 (November 2000). doi:10.1080/09500340008232197.
URL `http://www.informaworld.com/10.1080/09500340008232197`

[Bur99] S. Burger, K. Bongs, S. Dettmer, W. Ertmer, K. Sengstock, A. Sanpera, G. V. Shlyapnikov, and M. Lewenstein. "Dark Solitons in Bose-Einstein Condensates." *Phys. Rev. Lett.*, 83(25):5198–5201 (Dec 1999). doi: 10.1103/PhysRevLett.83.5198.

[Cas48] H. B. G. Casimir and D. Polder. "The Influence of Retardation on the London-van der Waals Forces." *Phys. Rev.*, 73(4):360–372 (Feb 1948). doi:10.1103/PhysRev.73.360.

[Cas00] D. Cassettari, B. Hessmo, R. Folman, T. Maier, and J. Schmiedmayer. "Beam Splitter for Guided Atoms." *Phys. Rev. Lett.*, 85(26):5483–5487 (Dec 2000). doi:10.1103/PhysRevLett.85.5483.
URL `http://prola.aps.org/abstract/PRL/v85/i26/p5483_1`

[Cas06] N. Castagna, J. Guéna, M. D. Plimmer, and P. Thomann. "A novel simplified two-dimensional magneto-optical trap as an intense source of slow cesium atoms." *Eur. Phys. J. Appl. Phys.*, 34:21–30 (2006). doi: 10.1051/epjap:2006037.

[Cer07] L. R. Cerami, E. Mazur, S. Nolte, and C. B. Schaffer. "Femtosecond laser micromachining." In R. Trebino and J. Squier, editors, "Ultrafast Optics," Trafford Publishing (2007).
URL `http://mazur-www.harvard.edu/publications.php`

[Dal89] J. Dalibard and C. Cohen-Tannoudji. "Laser cooling below the Doppler limit by polarization gradients: simple theoretical models." *J. Opt. Soc.*

Am. B, 6(11):2023 (1989).
URL http://josab.osa.org/abstract.cfm?URI=josab-6-11-2023

[Dav95] K. B. Davis, M.-O. Mewes, M. A. Joffe, M. R. Andrews, and W. Ketterle. "Evaporative Cooling of Sodium Atoms." *Phys. Rev. Lett.*, 74(26):5202–5205 (Jun 1995). doi:10.1103/PhysRevLett.74.5202.

[Dav01] T. J. Davis. "Modelling the diffraction of laser-cooled atoms from magnetic gratings." *Eur. Phys. J. D*, 14:111–118 (2001).

[Den99a] J. Denschlag, D. Cassettari, A. Chenet, S. Schneider, and J. Schmiedmayer. "A neutral atom and a wire: towards mesoscopic atom optics." *Applied Physics B*, 69(4):291–301 (October 1999). doi:10.1007/s003400050809.

[Den99b] J. Denschlag, D. Cassettari, and J. Schmiedmayer. "Guiding Neutral Atoms with a Wire." *Phys. Rev. Lett.*, 82(10):2014–2017 (Mar 1999). doi:10.1103/PhysRevLett.82.2014.
URL http://prola.aps.org/abstract/PRL/v82/i10/p2014_1

[Die98] K. Dieckmann, R. J. C. Spreeuw, M. Weidemüller, and J. T. M. Walraven. "Two-dimensional magneto-optical trap as a source of slow atoms." *Phys. Rev. A*, 58(5):3891–3895 (Nov 1998). doi:10.1103/PhysRevA.58.3891.

[Die01] K. Dieckmann. *Bose-Einstein Condensation with High Atom Number in a Deep Magnetic Trap*. Ph.D. thesis, University of Amsterdam (2001).

[Dik05] V. Dikovsky, Y. Japha, C. Henkel, and R. Folman. "Reduction of magnetic noise in atom chips by material optimization." *The European Physical Journal D*, 35(1):87–95 (aug 2005). doi:10.1140/epjd/e2005-00203-9.
URL http://www.springerlink.com/content/h156607323771850/

[Ein24] A. Einstein. "Quantentheorie des einatomigen idealen Gases." *Sitzungsberichte der Preussichen Akademie der Wissenschaften*, Physikalisch – Mathematische Klasse:261–267 (1924).

[Est04] J. Esteve, C. Aussibal, T. Schumm, C. Figl, D. Mailly, I. Bouchoule, C. I. Westbrook, and A. Aspect. "Role of wire imperfections in micromagnetic

traps for atoms." *Physical Review A (Atomic, Molecular, and Optical Physics)*, 70(4):043629 (2004). doi:10.1103/PhysRevA.70.043629.
URL `http://link.aps.org/abstract/PRA/v70/e043629`

[Fer26] E. Fermi. "Zur Quantelung des Idealen Einatomigen Gases." *Zeitschrift für Physik*, 36(11–12):902–912 (November 1926). doi:10.1007/BF01400221.
URL `http://dbserv.ihep.su/~elan/src/fermi26b/eng.pdf`

[Fol00] R. Folman, P. Krüger, D. Cassettari, B. Hessmo, T. Maier, and J. Schmiedmayer. "Controlling Cold Atoms using Nanofabricated Surfaces: Atom Chips." *Phys. Rev. Lett.*, 84(20):4749–4752 (May 2000). doi:10.1103/PhysRevLett.84.4749.

[Fol02] R. Folman, P. Krüger, J. Schmiedmayer, J. Denschlag, and C. Henkel. "Microscopic atom optics: from wires to an atom chip." *Advances in Atomic, Molecular and Optical Physics*, 48:263–356 (December 2002). ISSN 0-12-003848-X.
URL `http://www.bgu.ac.il/atomchip/physics/clean_final.pdf`

[For02a] J. Fortágh, H. Ott, S. Kraft, A. Günther, and C. Zimmermann. "Surface effects in magnetic microtraps." *Phys. Rev. A*, 66(4):041604 (Oct 2002). doi:10.1103/PhysRevA.66.041604.
URL `http://prola.aps.org/abstract/PRA/v66/i4/e041604`

[For02b] J. Fortágh, H. Ott, G. Schlotterbeck, C. Zimmermann, B. Herzog, and D. Wharam. "Microelectromagnets for trapping and manipulating ultracold atomic quantum gases." *Applied Physics Letters*, 81(6):1146–1148 (2002). doi:10.1063/1.1495086.
URL `http://link.aip.org/link/?APL/81/1146/1`

[Gri94] R. Grimm, J. Söding, and Y. B. Ovchinnikov. "Coherent beam splitter for atoms based on a bichromatic standing light wave." *Opt. Lett.*, 19(9):658–660 (1994).
URL `http://ol.osa.org/abstract.cfm?URI=ol-19-9-658`

[Gro04] S. Groth, P. Krüger, S. Wildermuth, R. Folman, T. Fernholz, J. Schmiedmayer, D. Mahalu, and I. Bar-Joseph. "Atom chips: Fabrication and thermal properties." *Applied Physics Letters*, 85(14):2980–2982 (2004). doi:10.1063/1.1804601.
URL `http://link.aip.org/link/?APL/85/2980/1`

[Güd98] J. Güdde, J. Hohlfeld, J. G. Müller, E. Matthias, et al. "Damage threshold dependence on electron-phonon coupling in Au and Ni films." *Applied Surface Science*, 127-129:40–45 (1998). doi:10.1016/S0169-4332(98)00002-6.

[Haa01] A. Haase, D. Cassettari, B. Hessmo, and J. Schmiedmayer. "Trapping neutral atoms with a wire." *Phys. Rev. A*, 64(4):043405 (Sep 2001). doi:10.1103/PhysRevA.64.043405.
URL `http://prola.aps.org/abstract/PRA/v64/i4/e043405`

[Hal06] B. V. Hall, S. Whitlock, F. Scharnberg, P. Hannaford, and A. Sidorov. "A permanent magnetic film atom chip for Bose-Einstein condensation." *Journal of Physics B: Atomic, Molecular and Optical Physics*, 39(1):27–36 (January 2006). doi:10.1088/0953-4075/39/1/004.
URL `http://stacks.iop.org/0953-4075/39/27`

[Hal07] B. V. Hall, S. Whitlock, R. Anderson, P. Hannaford, and A. I. Sidorov. "Condensate Splitting in an Asymmetric Double Well for Atom Chip Based Sensors." *Physical Review Letters*, 98(3):030402 (2007). doi:10.1103/PhysRevLett.98.030402.
URL `http://link.aps.org/abstract/PRL/v98/e030402`

[Hän01a] W. Hänsel, P. Hommelhoff, T. W. Hänsch, and J. Reichel. "Bose–Einstein condensation on a microelectronic chip." *Nature*, 413:498 (2001). doi:10.1038/35097032.

[Hän01b] W. Hänsel, J. Reichel, P. Hommelhoff, and T. W. Hänsch. "Magnetic Conveyor Belt for Transporting and Merging Trapped Atom Clouds." *Phys. Rev. Lett.*, 86(4):608–611 (Jan 2001). doi:10.1103/PhysRevLett.86.608.
URL `http://prola.aps.org/abstract/PRL/v86/i4/p608_1`

[Har05] D. M. Harber, J. M. Obrecht, J. M. McGuirk, and E. A. Cornell. "Measurement of the Casimir-Polder force through center-of-mass oscillations of a Bose-Einstein condensate." *Phys. Rev. A*, 72(3):033610 (Sep 2005). doi:10.1103/PhysRevA.72.033610.

[Hee63] C. V. Heer. "Feasibility of Containment of Quantum Magnetic Dipoles." *Review of Scientific Instruments*, 34(5):532–537 (1963). doi:10.1063/1.1718426.
URL `http://link.aip.org/link/?RSI/34/532/1`

[Hen03] C. Henkel, P. Krüger, R. Folman, and J. Schmiedmayer. "Fundamental limits for coherent manipulation on atom chips." *Applied Physics B*, 76(2):173–182 (February 2003). doi:10.1007/s00340-003-1112-z.
URL `http://www.springerlink.com/content/ygbn30aca9de83dn/`

[Hug97] I. G. Hughes, P. A. Barton, T. M. Roach, M. G. Boshier, and E. A. Hinds. "Atom optics with magnetic surfaces: I. Storage of cold atoms in a curved 'floppy disk'." *J. Phys. D: Appl. Phys.*, 30:647–58 (1997).

[Jee88] Y. Jee, M. F. Becker, and R. M. Walser. "Laser-induced damage on single-crystal metal surfaces." *J. Opt. Soc. Am. B*, 5(3):648–659 (1988).
URL `http://josab.osa.org/abstract.cfm?URI=josab-5-3-648`

[Jo07] G.-B. Jo, Y. Shin, S. Will, T. A. Pasquini, M. Saba, W. Ketterle, D. E. Pritchard, M. Vengalattore, and M. Prentiss. "Long Phase Coherence Time and Number Squeezing of two Bose-Einstein Condensates on an Atom Chip." *Physical Review Letters*, 98:030407 (January 2007). doi:10.1103/PhysRevLett.98.030407.
URL `http://link.aps.org/abstract/PRL/v98/e030407`

[Jon03] M. P. A. Jones, C. J. Vale, D. Sahagun, B. V. Hall, and E. A. Hinds. "Spin Coupling between Cold Atoms and the Thermal Fluctuations of a Metal Surface." *Phys. Rev. Lett.*, 91(8):080401 (Aug 2003). doi:10.1103/PhysRevLett.91.080401.
URL `http://prola.aps.org/abstract/PRL/v91/i8/e080401`

[Jon04] M. P. A. Jones, C. J. Vale, D. Sahagun, B. V. Hall, C. C. Eberlein, B. E. Sauer, K. Furusawa, D. Richardson, and E. A. Hinds. "Cold atoms probe the magnetic field near a wire." *Journal of Physics B: Atomic, Molecular and Optical Physics*, 37(2):L15–L20 (2004).
URL `http://stacks.iop.org/0953-4075/37/L15`

[Kas02] M. A. Kasevich. "Coherence with Atoms." *Science*, 298(5597):1363–1368 (2002). doi:10.1126/science.1079430.
URL `http://www.sciencemag.org/cgi/content/abstract/298/5597/1363`

[Kau94] W. Kautek and J. Krüger. "Femtosecond pulse laser ablation of metallic, semiconducting, ceramic, and biological materials." In E. Beyer, M. Cantello, A. V. L. Rocca, L. D. Laude, F. O. Olsen, and G. Sepold, editors, "Laser Materials Processing: Industrial and Microelectronics Applications," volume 2207, pages 600–611. SPIE, Vienna (1994). doi: 10.1117/12.184768.
URL `http://link.aip.org/link/?PSI/2207/600/1`

[Ket96] W. Ketterle and N. J. van Druten. "Evaporative Cooling of trapped Atoms." *Adv. At. Mol. Opt. Phys.*, 37:181–236 (1996).

[Koh03] J. M. Kohel, J. Ramirez-Serrano, R. J. Thompson, L. Maleki, J. L. Bliss, and K. G. Libbrecht. "Generation of an intense cold-atom beam from a pyramidal magneto-optical trap: experiment and simulation." *J. Opt. Soc. Am. B*, 20(6):1161–1168 (2003). doi:10.1364/JOSAB.20.001161.
URL `http://josab.osa.org/abstract.cfm?URI=josab-20-6-1161`

[Kou04] E. Koukharenko, Z. Moktadir, M. Kraft, M. E. Abdelsalam, D. M. Bagnall, C. Vale, M. P. A. Jones, and E. A. Hinds. "Microfabrication of gold wires for atom guides." *Sensors and Actuators A*, 115:600–607 (September 2004). doi:10.1016/j.sna.2004.03.069.

[Kra02] S. Kraft, A. Gunther, H. Ott, D. Wharam, C. Zimmermann, and J. Fortagh. "Anomalous longitudinal magnetic field near the surface of copper conductors." *Journal of Physics B: Atomic, Molecular and Optical*

Physics, 35(21):L469–L474 (2002). doi:10.1088/0953-4075/35/21/102. URL `http://stacks.iop.org/0953-4075/35/L469`

[Krü07] P. Krüger, L. M. Andersson, S. Wildermuth, S. Hofferberth, E. Haller, S. Aigner, S. Groth, I. Bar-Joseph, and J. Schmiedmayer. "Potential roughness near lithographically fabricated atom chips." *Physical Review A (Atomic, Molecular, and Optical Physics)*, 76(6):063621 (2007). doi:10.1103/PhysRevA.76.063621.
URL `http://link.aps.org/abstract/PRA/v76/e063621`

[Lan96] A. Landragin, G. Labeyrie, C. Henkel, R. Kaiser, N. Vansteenkiste, C. I. Westbrook, and A. Aspect. "Specular versus diffuse reflection of atoms from an evanescent-wave mirror." *Opt. Lett.*, 21(19):1591–1593 (1996).
URL `http://ol.osa.org/abstract.cfm?URI=ol-21-19-1591`

[Lan99] G. P. T. Lancaster, R. S. Conroy, M. A. Clifford, J. Arlt, and K. Dholakia. "A polarisation spectrometer locked diode laser for trapping cold atoms." *Optics Communications*, 170(1–3):79–84 (October 1999). doi:10.1016/S0030-4018(99)00433-2.

[Lau99a] D. C. Lau. *A Novel Magnetic Mirror for Slowly Moving Atoms.* Ph.D. thesis, School of Physics, University of Melbourne (November 1999).

[Lau99b] D. C. Lau, R. J. McLean, A. I. Sidorov, D. S. Gough, J. Koperski, W. J. Rowlands, B. A. Sexton, G. I. Opat, and P. Hannaford. "Magnetic mirrors with micron-scale periodicities for slowly moving neutral atoms." *J. Opt. B*, 1:371–377 (1999).

[Lea02] A. E. Leanhardt, A. P. Chikkatur, D. Kielpinski, Y. Shin, T. L. Gustavson, W. Ketterle, and D. E. Pritchard. "Propagation of Bose-Einstein Condensates in a Magnetic Waveguide." *Phys. Rev. Lett.*, 89(4):040401 (Jul 2002). doi:10.1103/PhysRevLett.89.040401.

[Lea03] A. E. Leanhardt, Y. Shin, A. P. Chikkatur, D. Kielpinski, W. Ketterle, and D. E. Pritchard. "Bose-Einstein Condensates near a Microfabricated

Surface." *Phys. Rev. Lett.*, 90(10):100404 (Mar 2003). doi: 10.1103/PhysRevLett.90.100404.
URL http://prola.aps.org/abstract/PRL/v90/i10/e100404

[Les06] I. Lesanovsky, T. Schumm, S. Hofferberth, L. M. Andersson, P. Kruger, and J. Schmiedmayer. "Adiabatic radio-frequency potentials for the coherent manipulation of matter waves." *Physical Review A (Atomic, Molecular, and Optical Physics)*, 73(3):033619 (2006). doi: 10.1103/PhysRevA.73.033619.
URL http://link.aps.org/abstract/PRA/v73/e033619

[Let88] P. D. Lett, R. N. Watts, C. I. Westbrook, W. D. Phillips, P. L. Gould, and H. J. Metcalf. "Observation of Atoms Laser Cooled below the Doppler Limit." *Phys. Rev. Lett.*, 61(2):169–172 (Jul 1988). doi: 10.1103/PhysRevLett.61.169.
URL http://prola.aps.org/abstract/PRL/v61/i2/p169_1

[Lev03a] B. Lev. "Fabrication of Micro-Magnetic Traps for Cold Neutral Atoms." *Quantum Information and Computation*, 3(5):450 (2003).
URL http://minty.stanford.edu/Publications/Lev03b.pdf

[Lev03b] B. Lev, Y. Lassailly, C. Lee, A. Scherer, and H. Mabuchi. "Atom mirror etched from a hard drive." *Applied Physics Letters*, 83(2):395–397 (2003). doi:10.1063/1.1592305.
URL http://link.aip.org/link/?APL/83/395/1

[Lon03] R. Long, T. Steinmetz, P. Hommelhoff, W. Hänsel, T. W. Hänsch, and J. Reichel. "Magnetic microchip traps and single-atom detection." *Philosophical Transactions of the Royal Society A: Mathematical, Physical and Engineering Sciences*, 361(1808):1375–1389 (July 2003). doi:10.1098/rsta.2003.1207.
URL http://journals.royalsociety.org/content/v9fq54j86jrlygqc

[Lu96] Z. T. Lu, K. L. Corwin, M. J. Renn, M. H. Anderson, E. A. Cornell, and C. E. Wieman. "Low-Velocity Intense Source of Atoms from a

Magneto-optical Trap." *Phys. Rev. Lett.*, 77(16):3331–3334 (Oct 1996). doi:10.1103/PhysRevLett.77.3331.

[Luo06] L. Luo, B. Clancy, J. Joseph, J. Kinast, A. Turlapov, and J. E. Thomas. "Evaporative cooling of unitary Fermi gas mixtures in optical traps." *New Journal of Physics*, 8(9):213 (2006). doi:10.1088/1367-2630/8/9/213. URL `http://stacks.iop.org/1367-2630/8/213`

[Mad98] M. Madou. *Fundamentals of Microfabrication*. CRC Press, 2000 N.W. Corporate Blvd., Boca Raton, FL 33431, 1 edition (1998). ISBN 0-8493-9451-1.

[Mat98] M. R. Matthews, D. S. Hall, D. S. Jin, J. R. Ensher, C. E. Wieman, E. A. Cornell, F. Dalfovo, C. Minniti, and S. Stringari. "Dynamical Response of a Bose-Einstein Condensate to a Discontinuous Change in Internal State." *Phys. Rev. Lett.*, 81(2):243–247 (Jul 1998). doi:10.1103/PhysRevLett.81.243.

[Met99] H. J. Metcalf and P. van der Straten. *Laser Cooling and Trapping*. Springer, New York (1999).

[Mig85] A. L. Migdall, J. V. Prodan, W. D. Phillips, T. H. Bergeman, and H. J. Metcalf. "First Observation of Magnetically Trapped Neutral Atoms." *Phys. Rev. Lett.*, 54(24):2596–2599 (Jun 1985). doi:10.1103/PhysRevLett.54.2596.
URL `http://prola.aps.org/abstract/PRL/v54/i24/p2596_1`

[Mom96] C. Momma, B. N. Chichkov, S. Nolte, F. von Alvensleben, A. Tunnermann, H. Welling, and B. Wellegehausen. "Short-pulse laser ablation of solid targets." *Optics Communications*, 129(1–2):134–142 (August 1996). doi:10.1016/0030-4018(96)00250-7.

[Mom97] C. Momma, S. Nolte, B. N. Chichkov, F. v. Alvensleben, and A. Tünnermann. "Precise laser ablation with ultrashort pulses." *Applied Surface Science*, 109-110:15–19 (1997). doi:10.1016/S0169-4332(96)00613-7.

[Ned04] N. N. Nedialkov, P. A. Atanasov, S. E. Imanova, A. Ruf, P. Berger, and F. Dausinger. "Dynamics of the ejected material in ultra-short laser ablation of metals." *Applied Physics A*, 79(4-6):1121–1125 (July 2004). doi:10.1007/s00339-004-2659-1.
URL `http://www.springerlink.com/content/rr425wd99q9llx24`

[Nir06] T. Nirrengarten, A. Qarry, C. Roux, A. Emmert, G. Nogues, M. Brune, J.-M. Raimond, and S. Haroche. "Realization of a Superconducting Atom Chip." *Physical Review Letters*, 97(20):200405 (2006). doi: 10.1103/PhysRevLett.97.200405.
URL `http://link.aps.org/abstract/PRL/v97/e200405`

[Nol97] S. Nolte, C. Momma, H. Jacobs, A. Tünnermann, B. N. Chichkov, B. Wellegehausen, and H. Welling. "Ablation of metals by ultrashort laser pulses." *J. Opt. Soc. Am. B*, 14(10):2716–2722 (1997). doi: 10.1364/JOSAB.14.002716.
URL `http://josab.osa.org/abstract.cfm?URI=josab-14-10-2716`

[Obr07] J. M. Obrecht, R. J. Wild, M. Antezza, L. P. Pitaevskii, S. Stringari, and E. A. Cornell. "Measurement of the Temperature Dependence of the Casimir-Polder Force." *Physical Review Letters*, 98(6):063201 (2007). doi: 10.1103/PhysRevLett.98.063201.
URL `http://link.aps.org/abstract/PRL/v98/e063201`

[O'H03] J. F. O'Hanlon. *A Users Guide to Vacuum Technology*. John Wiley and Sons, New Jersey (2003).

[Opa92] G. I. Opat, S. J. Wark, and A. Cimmino. "Electric and magnetic mirrors and gratings for slowly moving neutral atoms and molecules." *Appl. Phys. B*, 54(5):396–402 (May 1992). doi:10.1007/BF00325385.

[Opa99] G. I. Opat, S. N. Chormaic, B. P. Cantwell, and J. Richmond. *J. Opt. B: Quant. Semiclass. Opt*, 1:415 (1999).

[Ott01] H. Ott, J. Fortagh, G. Schlotterbeck, A. Grossmann, and C. Zimmermann. "Bose-Einstein Condensation in a Surface Microtrap." *Phys. Rev. Lett.*, 87(23):230401 (Nov 2001). doi:10.1103/PhysRevLett.87.230401.

[Ovc05] Y. B. Ovchinnikov. "Compact magneto-optical sources of slow atoms." *Optics Communications*, 249(4-6):473–481 (May 2005). doi: 10.1016/j.optcom.2005.01.047.

[Pas04] T. A. Pasquini, Y. Shin, C. Sanner, M. Saba, A. Schirotzek, D. E. Pritchard, and W. Ketterle. "Quantum Reflection from a Solid Surface at Normal Incidence." *Phys. Rev. Lett.*, 93(22):223201 (Nov 2004). doi: 10.1103/PhysRevLett.93.223201.

[Pau05] T. Paul, P. Leboeuf, N. Pavloff, K. Richter, and P. Schlagheck. "Nonlinear transport of Bose-Einstein condensates through waveguides with disorder." *Physical Review A (Atomic, Molecular, and Optical Physics)*, 72(6):063621 (2005). doi:10.1103/PhysRevA.72.063621.
URL `http://link.aps.org/abstract/PRA/v72/e063621`

[Pea02] C. P. Pearman, C. S. Adams, S. G. Cox, P. F. Griffin, D. A. Smith, and I. G. Hughes. "Polarization spectroscopy of a closed atomic transition: applications to laser frequency locking." *Journal of Physics B: Atomic, Molecular and Optical Physics*, 35(24):5141–5151 (2002). doi: 10.1088/0953-4075/35/24/315.
URL `http://stacks.iop.org/0953-4075/35/5141`

[Per06] H. Perrin, Y. Colombe, B. Mercier, V. Lorent, and C. Henkel. "Diffuse reflection of a Bose-Einstein condensate from a rough evanescent wave mirror." *Journal of Physics B: Atomic, Molecular and Optical Physics*, 39(22):4649–4658 (2006).
URL `http://stacks.iop.org/0953-4075/39/4649`

[Pet99] A. Peters, K. Y. Chung, and S. Chu. "Measurement of gravitational acceleration by dropping atoms." *Nature*, 400:849–852 (August 1999). doi:10.1038/23655.

[Pfa93] T. Pfau, C. Kurtsiefer, C. S. Adams, M. Sigel, and J. Mlynek. "Magneto-optical beam splitter for atoms." *Phys. Rev. Lett.*, 71(21):3427–3430 (Nov 1993). doi:10.1103/PhysRevLett.71.3427.

[Phi82] W. D. Phillips and H. Metcalf. "Laser Deceleration of an Atomic Beam." *Phys. Rev. Lett.*, 48(9):596–599 (Mar 1982). doi: 10.1103/PhysRevLett.48.596.

[Pre95] S. Preuss, A. Demchuk, and M. Stuke. "Sub-picosecond UV laser ablation of metals." *Appl. Phys. A*, 61(1):33–37 (November 1995). doi: 10.1007/BF01538207.
URL `http://www.springerlink.com/content/p6t732u61452t6t7/`

[Pri83] D. E. Pritchard. "Cooling Neutral Atoms in a Magnetic Trap for Precision Spectroscopy." *Physical Review Letters*, 51(15):1136–1139 (October 1983).

[Pri86] D. E. Pritchard, E. L. Raab, V. Bagnato, C. E. Wieman, and R. N. Watts. "Light Traps Using Spontaneous Forces." *Phys. Rev. Lett.*, 57(3):310–313 (Jul 1986). doi:10.1103/PhysRevLett.57.310.
URL `http://prola.aps.org/pdf/PRL/v57/i3/p310_1`

[Raa87] E. L. Raab, M. Prentiss, A. Cable, S. Chu, and D. E. Pritchard. "Trapping of Neutral Sodium Atoms with Radiation Pressure." *Phys. Rev. Lett.*, 59(23):2631–2634 (Dec 1987). doi:10.1103/PhysRevLett.59.2631.
URL `http://prola.aps.org/pdf/PRL/v59/i23/p2631_1`

[Rei99] J. Reichel, W. Hänsel, and T. W. Hänsch. "Atomic Micromanipulation with Magnetic Surface Traps." *Phys. Rev. Lett.*, 83(17):3398–3401 (Oct 1999). doi:10.1103/PhysRevLett.83.3398.
URL `http://prola.aps.org/abstract/PRL/v83/i17/p3398_1`

[Roa95] T. M. Roach, H. Abele, M. G. Boshier, H. L. Grossman, K. P. Zetie, and E. A. Hinds. "Realization of a Magnetic Mirror for Cold Atoms." *Phys. Rev. Lett.*, 75:629–632 (1995).

[Roa06] T. Roach. "Vacuum Annealing of Magnetic Films & MOK Analysis." (May 2006). Experiment project at Swinburne University 2006.

[Ros00] P. Rosenbusch, B. V. Hall, I. G. Hughes, C. V. Saba, and E. A. Hinds. "Manipulation of cold atoms using a corrugated magnetic reflector." *Phys. Rev. A*, 61(3):031404 (Feb 2000). doi:10.1103/PhysRevA.61.031404.

[Rot89] B. J. Roth, N. G. Sepulveda, and J. J. P. Wikswo. "Using a magnetometer to image a two-dimensional current distribution." *Journal of Applied Physics*, 65(1):361–372 (1989). doi:10.1063/1.342549.
URL `http://link.aip.org/link/?JAP/65/361/1`

[Sab99] C. V. Saba, P. A. Barton, M. G. Boshier, I. G. Hughes, P. Rosenbusch, B. E. Sauer, and E. A. Hinds. "Reconstruction of a Cold Atom Cloud by Magnetic Focusing." *Phys. Rev. Lett.*, 82:468 (1999).

[Sch02] J. Schoser, A. Batär, R. Löw, V. Schweikhard, A. Grabowski, Y. B. Ovchinnikov, and T. Pfau. "Intense source of cold Rb atoms from a pure two-dimensional magneto-optical trap." *Phys. Rev. A*, 66(2):023410 (Aug 2002). doi:10.1103/PhysRevA.66.023410.

[Sch05a] T. Schumm, J. Estève, C. Figl, J.-B. Trebbia, C. Aussibal, H. Nguyen, D. Mailly, I. Bouchoule, C. I. Westbrook, and A. Aspect. "Atom chips in the real world: the effects of wire corrugation." *Europ. Phys. J. D*, 32(2):171–180 (2005). doi:10.1140/epjd/e2005-00016-x.

[Sch05b] T. Schumm, S. Hofferberth, L. M. Andersson, S. Wildermuth, S. Groth, I. Bar-Joseph, J. Schmiedmayer, and P. Krüger. "Matter-wave interferometry in a double well on an atom chip." *Nature Physics*, 1(1):57–62 (2005). doi:10.1038/nphys125.

[Sid96] A. I. Sidorov, R. J. McLean, G. I. Opat, W. J. Rowlands, D. C. Lau, J. E. Murphy, M. Walkiewicz, and P. Hannaford. "Specular reflection of cold caesium atoms from a magnetostatic mirror." *Quantum Semiclass. Opt.*, 8:713 (1996). doi:10.1088/1355-5111/8/3/030.
URL `http://www.iop.org/EJ/abstract/1355-5111/8/3/030`

[Sid97] A. I. Sidorov, D. C. Lau, G. I. Opat, R. J. McLean, W. J. Rowlands, and P. Hannaford. "Microfabricated magnetic mirror for cold atoms." In

"Proc. of the 13th Int. Conf. on Laser Spectroscopy," page 252. World Scientific, Singapore (1997).

[Sid02] A. I. Sidorov, R. J. McLean, F. Scharnberg, D. S. Gough, T. J. Davis, B. J. Sexton, G. I. Opat, and P. Hannaford. "Permanent-Magnet Microstructures for Atom Optics." *Acta Phys. Pol. B*, 33:2137–2155 (2002).

[Ska06] B.-S. K. Skagerstam, U. Hohenester, A. Eiguren, and P. K. Rekdal. "Spin Decoherence in Superconducting Atom Chips." *Physical Review Letters*, 97(7):070401 (2006). doi:10.1103/PhysRevLett.97.070401.
URL `http://link.aps.org/abstract/PRL/v97/e070401`

[Slo05] C. Slowe, L. Vernac, and L. V. Hau. "High flux source of cold rubidium atoms." *Review of Scientific Instruments*, 76(10):103101 (2005). doi: 10.1063/1.2069651.
URL `http://link.aip.org/link/?RSI/76/103101/1`

[Ste01] D. A. Steck. "Rubidium 87 D Line Data." (September 2001).
URL `http://steck.us/alkalidata`

[Tre07] J.-B. Trebbia, C. L. G. Alzar, R. Cornelussen, C. I. Westbrook, and I. Bouchoule. "Roughness Suppression via Rapid Current Modulation on an Atom Chip." *Physical Review Letters*, 98(26):263201 (2007). doi: 10.1103/PhysRevLett.98.263201.
URL `http://link.aps.org/abstract/PRL/v98/e263201`

[Tri08] M. Trinker, S. Groth, S. Haslinger, S. Manz, T. Betz, S. Schneider, I. Bar-Joseph, T. Schumm, and J. Schmiedmayer. "Multilayer atom chips for versatile atom micromanipulation." *Applied Physics Letters*, 92(25):254102 (2008). doi:10.1063/1.2945893.
URL `http://link.aip.org/link/?APL/92/254102/1`

[Val04] C. J. Vale, B. Upcroft, M. J. Davis, N. R. Heckenberg, and H. Rubinsztein-Dunlop. "Foil-based atom chip for Bose-Einstein Condensate." *Journal of Physics B*, 37:2959–2967 (July 2004). doi: 10.1088/10.1088-4075/37/14/009.

[Vol08] M. Volk, S. Whitlock, C. H. Wolff, B. V. Hall, and A. I. Sidorov. "Scanning magnetoresistance microscopy of atom chips." *Review of Scientific Instruments*, 79(2):023702 (2008). doi:10.1063/1.2839015.
URL `http://link.aip.org/link/?RSI/79/023702/1`

[Wan05a] J. Y. Wang, S. Whitlock, F. Scharnberg, D. S. Gough, A. I. Sidorov, R. J. McLean, and P. Hannaford. "Perpendicularly magnetized, grooved GdTbFeCo microstructures for atom optics." *Journal of Physics D: Applied Physics*, 38(22):4015–4020 (2005). doi:10.1088/0022-3727/38/22/003.
URL `http://stacks.iop.org/0022-3727/38/4015`

[Wan05b] Y.-J. Wang, D. Z. Anderson, V. M. Bright, E. A. Cornell, Q. Diot, T. Kishimoto, M. Prentiss, R. A. Saravanan, S. R. Segal, and S. Wu. "Atom Michelson Interferometer on a Chip Using a Bose-Einstein Condensate." *Physical Review Letters*, 94(9):090405 (2005). doi:10.1103/PhysRevLett.94.090405.
URL `http://link.aps.org/abstract/PRL/v94/e090405`

[Wei95] J. D. Weinstein and K. G. Libbrecht. "Microscopic magnetic traps for neutral atoms." *Phys. Rev. A*, 52(5):4004–4009 (Nov 1995). doi:10.1103/PhysRevA.52.4004.
URL `http://prola.aps.org/abstract/PRA/v52/i5/p4004_1`

[Wel99] S.-S. Wellershoff, J. Hohlfeld, J. Güdde, and E. Matthias. "The role of electron-phonon coupling in femtosecond laser damage of metals." *Appl. Phys. A*, 69(7):99–107 (December 1999). ISSN 0947-8396. doi:10.1007/s003390051362.
URL `http://www.springerlink.com/content/90at27ttlwwna2y9/`

[Whi07a] S. Whitlock. *Bose-Einstein condensates on a magnetic film atom chip.* Ph.D. thesis, Swinburne University of Technology (January 2007).

[Whi07b] S. Whitlock, B. V. Hall, T. Roach, R. Anderson, M. Volk, P. Hannaford, and A. I. Sidorov. "Effect of magnetization inhomogeneity on magnetic microtraps for atoms." *Physical Review A (Atomic, Molecular, and*

Optical Physics), 75(4):043602 (2007). doi:10.1103/PhysRevA.75.043602. URL `http://link.aps.org/abstract/PRA/v75/e043602`

[Wie76] C. Wieman and T. W. Hänsch. "Doppler-Free Laser Polarization Spectroscopy." *Phys. Rev. Lett.*, 36(20):1170–1173 (May 1976). doi: 10.1103/PhysRevLett.36.1170.
URL `http://prola.aps.org/abstract/PRL/v36/i20/p1170_1`

[Wil05] S. Wildermuth, S. Hofferberth, I. Lesanovsky, E. Haller, L. M. Andersson, S. Groth, I. Bar-Joseph, P. Krüger, and J. Schmiedmayer. "Bose–Einstein condensates: Microscopic magnetic-field imaging." *Nature*, 435:440 (May 2005). doi:10.1038/435440a.

[Yan07] J. Yang, Y. Zhao, N. Zhang, Y. Liang, and M. Wang. "Ablation of metallic targets by high-intensity ultrashort laser pulses." *Physical Review B (Condensed Matter and Materials Physics)*, 76(16):165430 (2007). doi: 10.1103/PhysRevB.76.165430.
URL `http://link.aps.org/abstract/PRB/v76/e165430`

[Yos03] Y. Yoshikawa, T. Umeki, T. Mukae, Y. Torii, and T. Kuga. "Frequency Stabilization of a Laser Diode with Use of Light-Induced Birefringence in an Atomic Vapor." *Appl. Opt.*, 42(33):6645–6649 (2003). doi: 10.1364/AO.42.006645.
URL `http://ao.osa.org/abstract.cfm?URI=ao-42-33-6645`

[Zha02] Y. Zhang, R. M. Lowe, E. Harvey, P. Hannaford, and A. Endo. "High aspect-ratio micromachining of polymers with an ultrafast laser." *Applied Surface Science*, 186(1-4):345–351 (2002). ISSN 0169-4332. doi: 10.1016/S0169-4332(01)00673-0.

Glossary

2D$^+$ MOT	A modification of the 2D-MOT where a low-intensity push beam is added to improve the efficiency and lower the velocity, 108
2D-MOT	A method of creating two jets of cold atoms by omitting one pair of trapping lasers from a standard MOT, 107
A	Weak field gradient, 13
a	Period of the periodic magnetic surface of the atom mirror, 129
AFM	Atomic force microscope, 132
AO	Analogue output channel, 101
AOM	Acousto-optic modulator, 95
α	A unitless parameter which relates the relative strengths of the corrugations on the two edges of the wire, 71
α	Angle between MTJ sensor and normal of the chip surface, 59
$\vec{B}$	Magnetic field, 13
b	Thickness of the magnetic film, 129
$B_\perp$	Strength of the magnetic field produced by a current carrying wire, 31

$B_{\|\|}$	Corrugation of the magnetic field produced by a current carrying wire, parallel to this wire, 31
B_0	Surface magnetic field, 129
BBO	β-barium borate (β-BaB_2O_4), 41
BEC	Bose-Einstein condensate, 8, 27
B_G	Magnitude of the corrugation of the potential of a magnetic mirror, 135
B_{OS}	Magnetic offset field parallel to the wire, 22
β	Barrier height in double well, 69
CCD	Charge-coupled device, 29
CIN	LabView C interface node, 106
Γ	Decay rate of the excited state, 9
γ	Depth of the well, 69
γ	Loss rate, 113
γ_p	Scattering rate, 10
dark state	Hyperfine level in the ground state that is not resonant to trapping light, 12
DI/O	Digital input/output channel, 101
DLIB	Doppler-free Light Induced Birefringence, 95
Δ	Asymmetry in double well, 69
δ	Laser detuning, 9
δ'	Corrected detuning, 10
$\|e\rangle$	Excited state of a 2-level system, 9
$\Delta E_{\|F\, m_F\rangle}$	Linear Zeeman shift, 13
F	Hyperfine level quantum number of the ground state, 12

F' Hyperfine level quantum number of the excited state, 12

FEA Finite element analysis, 73

FET Field-effect transistor, 199

Fragmentation The breaking up of cold atomic clouds due to roughness in the magnetic potential bottom, 31

$|g\rangle$ Ground state of a 2-level system, 9

g_F Landé g-factor, 13

η Number of atoms per pixel, 120

h Planck's constant (6.626×10^{-34} m^2kg/s), 8

$\hbar$ Reduced Planck's constant ($h/2\pi$), 9

I Laser intensity, 10

I_{sat} Saturation Intensity, 10

K Throughput, the amount of gas displaced per second, 87

$\vec{k}$ Wave vector of the light field, 10

k k-vector of the periodic magnetic structure and decay constant of the magnetic field, 129

k wave vector, 16

k_B Boltzmann constant, 8

LVIS Low velocity intense source of atoms, 107

Λ Mean free path for collisions, 42

Λ Period of the lower frequency corrugated edge, 70

λ Period of the higher frequency corrugated edge, 70

$\lambda_{\mathbf{material}}$	Thermal conductivity of the material, 30
M	Mass of one atom, 15
M_0	Magnetisation of the magnetic material, 129
Majorana losses	Loss of atoms due to spinflip because of non-adiabatical change in magnetic field direction, 17
m_F	Magnetic quantum number, 12
MFM	Magnetic force microscope, 132
MOT	Magneto-optic trap, 12
MRM	Magneto-resistance microscope, 58
MTJ	Magnetic tunnel junction, 59
$\vec{\mu}$	Magnetic dipole moment of an atom, 130
μ_0	Vacuum permeability ($4\,\pi\,10^{-7}$ N/A), 21
μ_B	Bohr magneton ($\approx 9.274 \times 10^{-24}$ J/T), 13
n	Number density, 8
N	Number of atoms, 112
NI	National Instruments, 101
N_{sat}	Saturation atom number, 114
OD	Optical Density, 119
P-LVIS	Pyramid LVIS, 108
PSD	Power spectral density, 32
PXI	PCI eXtensions for Instrumentation, a modular instrumentation platform, 101
ξ	A material specific parameter governing the incubation effect in fs ablation, 53
ξ	Physical derivation of the edge of the wire, 71

Rb	Rubidium, 8
ρ	Electrical resistivity, 29
ρ	Phase space density, 8
S	Wire cross section, 24
s	Double well separation, 69
s_0	Saturation parameter (I/I_{sat}), 10
SEM	Scanning electron microscope, 32
SQUID	Superconducting quantum interference device, 132
σ	Scattering cross section, 119
$\sigma_{\mathbf{Xx}}$	Electrical conductivity of element Xx, 29
$\sigma_{x/y}$	Root mean square width of the atom cloud in x or y direction, 14
T	Temperature, 8
TCP/IP	Transfer control protocol/Internet protocol, 105
T_D	Doppler temperature, 12
ToF	Time of flight measurement, 14
T_{rc}	Recoil temperature, 16
τ	MOT fill time, 114
Δv	Change in the horizontal velocity component of an atom during reflection, 136
v_c	Capture velocity, 10
VI	LabView Virtual Instrument (LabView subprogram), 106
Δy_{rms}	Roughness of the ablated edge, 54
Φ	Fluence of ablation laser, 49
ϕ	Capture rate, 113

Φ_{th}	Threshold fluence for laser ablation, 49
z_0	Rayleigh Length, 43
Ω	Rabi frequency, 9
Ω'	Off-resonant Rabi frequency, 9
ω_0	Waist of laser beam, 43
ω_D	Doppler shift, 10
ω_a	Atomic resonant frequency, 9
ω_l	Laser frequency, 9
ω_t	Trapping frequency, can have a for axial or r for radial, 18
ω_{rf}	Radio-frequency, 20

Appendix A

Laser Systems

A.1 Magnetic Mirror Experiment

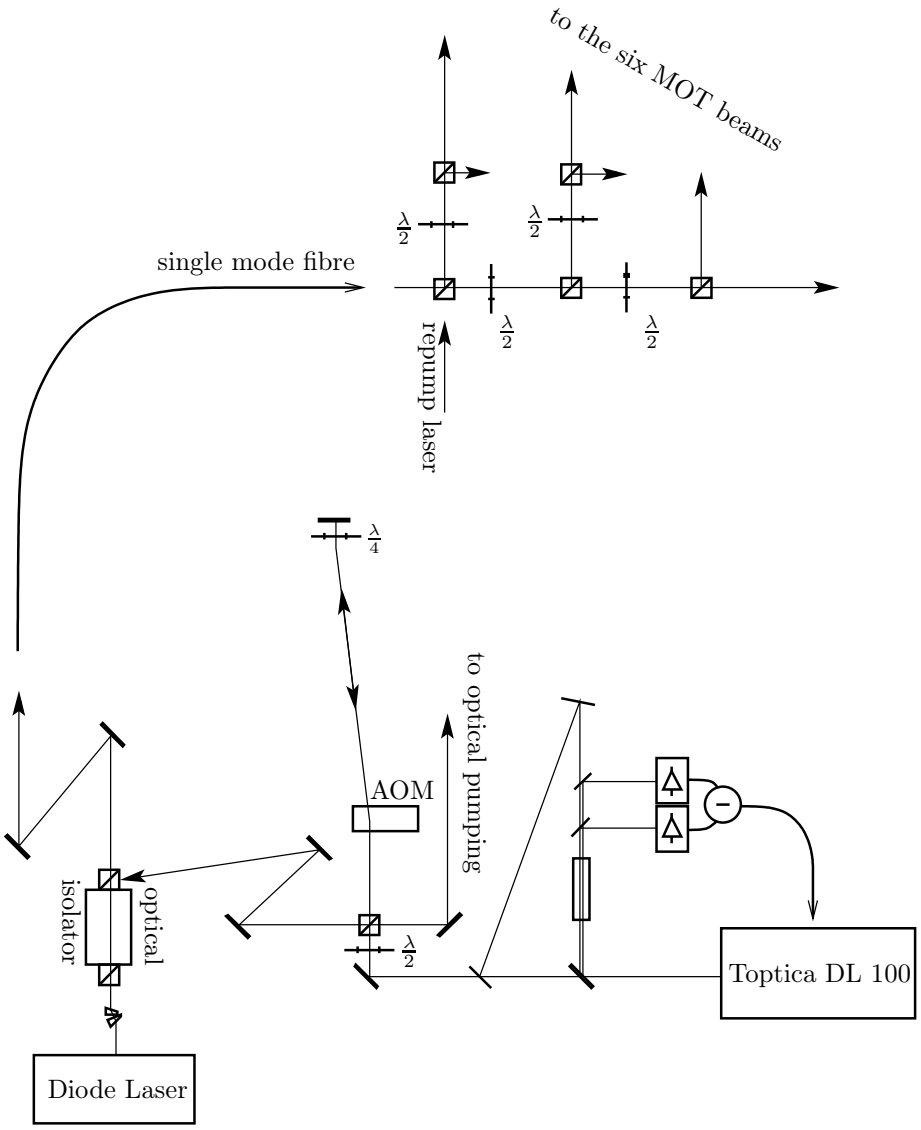

Figure A.1: Schematic of the trapping laser setup. The DL100 laser is locked to the $F = 2 \rightarrow F' = 2$ line, gets frequency shifted to the $F = 2 \rightarrow F' = 3$ line and then injection locks the diode laser. This laser is beam shaped and mode cleaned by a single mode fibre and then splits into 6 separate beams.

A.2 Atom Chip Experiment

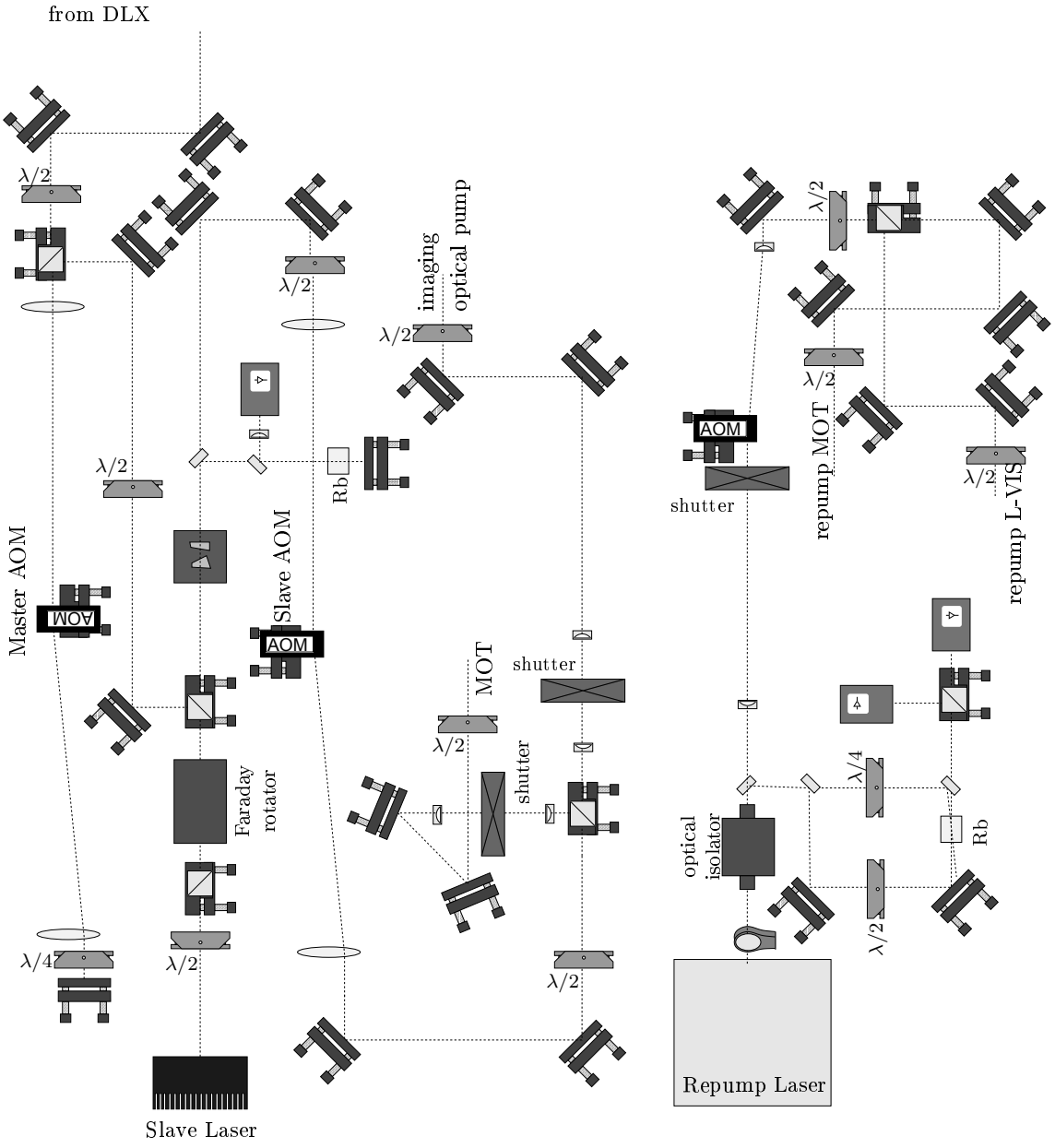

Figure A.2: The laser table: On the left had side the slave laser, injection locked by the DLX, with two AOMs allowing to set the detuning and the intensity. On the right hand side the repump system with polarisation spectroscopy lock, and fixed frequency AOM.

Appendix B

Numerical Codes

B.1 Monte-Carlo Simulations of the Magnetic Mirror Experiment

The following FORTRAN77 code modells the propagation of atoms in the potential of the mirror experiment. For this, an atom is created with a gaussian distribution in space and velocity according to typical values observed in the experiment, and then progressed in time steps. At each timestep, the atom is moved in space according to its velocity, and then the velocities are adjusted according to the forces onto the atom at the particular position. In the vicinity of the mirror, the time resolution of this procedure is strongly enhanced to better follow the fast changing potential in that region. At regular intervals, the horizontal position of the atom is stored in an array, mimicking the experimental procedure of 'taking an image of the cloud'.

On a standart Office PC with a Intel Pentium 4 CPU (2.8 GHz) and 1.5 GB RAM the simulation of 1,000 atoms took about 2 hours. The amount of time required should increase linearly with the number of atoms.

```
C     +------------------------+
C     | Calculate the Mirror   |
C     +------------------------+
      PROGRAM mirror
      IMPLICIT NONE
      REAL pi, e, g
      PARAMETER (pi = 3.14159265, e = 2.71828183, g = 9.81)
C     +-------------------------------------------------+
C     | declaration of variables                        |
C     +-------------------------------------------------+
C     | timeStep1 and 2 is in ms (2 is critical region)  |
C     | numberAtoms is the number of followed atoms      |
C     | height is the hight of the MOT above the mirror  |
C     | droptimes is an array of times when a measurement|
C     |    shall be taken                                |
C     | next is an arbitrary number to remember which    |
C     |    droptime is next                              |
C     | motRadius is in mm, motTemperature in K          |
```

```
C     | x and z are in mm, vx and vz are m/s             |
C     | picture(10x) is the number of atoms at x mm      |
C     | x, z is the position in mm                       |
C     | vx, vz is the speed in m/s (=mm/ms)              |
C     | xn and vxn are x and vx if mirror was perfect    |
C     | cont is set to FALSE if atom misses the mirror   |
C     | follow is whether trajectories shall be printed  |
C
      REAL timeStep1, timeStep2
      INTEGER numberAtoms
      REAL height
      INTEGER droptimes(20)
      INTEGER next
      REAL initialCloudsize
      REAL initialVelocityDistribution
      REAL bias
      DOUBLE PRECISION x, z, r, v, vx, vz, time, vxn, xn
      INTEGER picture(20, -150:150), picture2(20, -150:150)
      INTEGER i,current
      LOGICAL cont, follow
      INTEGER px
      DOUBLE PRECISION accelX, accelZ, maxAccelX, maxAccelZ
      REAL currents(5400), rf
C     +----
C     | These are actually functions
C     +----
      DOUBLE PRECISION magAccelX, magAccelZ, myAbs, magField
      REAL myrand, gaussrand
      LOGICAL mydiv

C     +-------------------------+
C     | User questions          |
C     +-------------------------+
      numberAtoms = 10000
cc      print *, "please enter number of atoms: "
cc      read *, numberAtoms
      print *, numberAtoms, " atoms will be followed"
      initialCloudsize = 1.
cc      print *, "initial cloudsize [mm]: "
cc      read *, initialCloudsize

      initialVelocityDistribution = 3.7
cc      print *, "initial velocity distribution [cm/s]: "
cc      read *, initialVelocityDistribution
      initialVelocityDistribution = initialVelocityDistribution/100
      height = 14.
cc      print *, "dropheight [mm]: "
cc      read *, height
      bias = 1.
cc      print *, "biasfield (Gauss): "
cc      read *, bias
      bias = bias/10000.
      follow = .TRUE.
cc      follow = (numberAtoms .lt. 100)
cc      print *, "follow trajectories? (yes=1) "
cc      read *, i
cc    follow = (i .eq. 1)
C     +--------------+
C     | Set default  |
C     +--------------+
      timeStep1 = 1e-2
      timeStep2 = 1e-5
      do i=1, 20
         droptimes(i) = 5*i
         do px = -150, 150
            picture(i, px) = 0
            picture2(i, px) = 0
         end do
      end do
      maxAccelX = 0.
      maxAccelZ = 0.
      i = 0

C     +-------------------+
C     | begin of the loop |
C     +-------------------+
      OPEN(UNIT=99, FILE='/dev/urandom')
      OPEN(UNIT=20, FILE='error.log')
```

```
      rf = .006
      call randomcurrents(currents, rf)
      if (follow) then
         open (unit=11, file='trajectories.dat')
      end if
      print *, "random currents generated"
      print *, "Beginning loop"
      do current=1, numberAtoms
         cont = .TRUE.
         x = gaussrand(initialCloudsize)
         xn = x
         z = gaussrand(initialCloudsize) + height
         vx = gaussrand(initialVelocityDistribution)
         vxn = vx
         vz = gaussrand(initialVelocityDistribution)
         next = 1
         time = 0.
         if (current.eq.1) then
            print *, "starting fall"
         end if
         do while ((cont) .and. (time.lt.100) .and. (z.gt.0))
C     +----
C     | Atoms missing the mirror
C     +----
            if ((z.lt.0.01) .and. ((x.gt.4) .or. (x.lt.-4))) then
               cont = .FALSE.
               write (20, *) "atom ", current, " off mirror:"
               write (20, *) "x:", x, " z:", z, " vx, vz: ", vx, vz
               write (20, *) "Field: ", magField (x, z, bias, currents)
            end if

C     +----
C     | Bouncing
C     +----
            if (z.lt.1e-2) then
               if (z.lt.2e-4) then
                  cont = .FALSE.
                  write (20, *) "atom ", current, " fell through:"
                  write (20, *) "x:", x, " z:", z, " vx, vz: ", vx, vz
                  write (20, *) "Field: ", magField (x, z,bias,currents)
               else
                  time = time + timeStep2
                  x = x + vx*timeStep2
                  xn = xn + vxn*timeStep2
                  z = z + vz*timeStep2
                  vz = vz - g*timeStep2/1000.
                  if (z.lt.5e-3) then
                     accelX = magAccelX(x, z, bias, currents)
                     if (myAbs(accelX).gt.maxAccelX) then
                        maxAccelX = myAbs(accelX)
                     end if
                     accelZ = magAccelZ(x, z, bias, currents)
                     if (myAbs(accelZ).gt.maxAccelZ) then
                        maxAccelZ = myAbs(accelZ)
                     end if
                  else
                     accelX = 0
                     accelZ = 0
                  end if
                  vx = vx + accelX*timeStep2/1000.
                  vz = vz + accelZ*timeStep2/1000.
               end if
            else
               time = time + timeStep1
               x = x + vx*timeStep1
               xn = xn + vxn*timeStep1
               z = z + vz*timeStep1
               vz = vz - g*timeStep1/1000.
            end if

cc            if (follow) then
cc               write (11, *) current, time, x, z, xn
cc            end if
C     +----
C     | Get picture
C     +----
            if (next.le.20) then
               if (time.gt.droptimes(next)) then
```

```
                  if (x.gt.-15. .and. x.lt.15.) then
                     px = 150 + (x * 10);
                     picture(next, px-150) = picture(next, px-150)+1
                  end if
                  if (xn.gt.-15. .and. xn.lt.15.) then
                     px = 150 + (xn * 10);
                     picture2(next, px-150) = picture2(next, px-150)+1
                  end if
                  next = next + 1
                  if (follow) then
                    write (11, *) current, time, x, z, xn
                  end if
               end if
            end if
         end do
         if (mydiv(current, numberAtoms/100)) then
            print *, (current*100)/numberAtoms, "% finished     "
         end if
      end do
C     +----
C     | Write out the crossections
C     +----
      open (unit=10, file='pictures.dat')
      do next=1, 20
         do px = -150, 150
            x = px/10.
            write (10, *) droptimes(next), x, picture(next, px),
     c                    picture2(next, px)
         end do
      end do
      write (10,*) "# number:", numberAtoms, "   bias:", bias*10000,
     c             "  initial:", initialVelocityDistribution*100,
     c             "  randomness of the field: ", rf
      close(10)
C     +-----+
C     | End |
C     +-----+
      close(99)
      if (follow) then
         close(11)
      end if
      CLOSE (20)
      print *, 'max. accel. in X:', maxAccelX, '    in Z:', maxAccelZ
C     1001: i/o Format: droptime [ms], x [mm], number of atoms
C                                       (first real, then perfect mirror)
 1001 FORMAT (I5, T4, F7.2, T4, I6, T4, I6)
C     1001: trajectories: atom, x, z, xn
 1002 FORMAT (I5, T4, F7.2, T4, F7.2, T4, F7.2)
C     1010: random
 1010 FORMAT (F10.2)
      STOP
      END

C     +----
C     | magnetic force acceleration
C     | in Z and X direction
C     +----
      DOUBLE PRECISION function magAccelZ(x, z, v, currents)
      DOUBLE PRECISION x, z
      REAL v
      REAL currents(5400)
      DOUBLE PRECISION pi, e, a, mu, m
      PARAMETER (pi = 3.14159265, e = 2.71828183, a = .0015,
     c           mu = 9.274e-24, m = 1.443e-25)
      DOUBLE PRECISION k, deriv, force, magField, field1, field2, dz
      k = (2*pi)/a
      dz = 1e-5
      if ((x.gt.-4) .and. (x.lt.4)) then
         field1 = magField(x, z-dz, v, currents)
         field2 = magField(x, z+dz, v, currents)
         deriv = 1e3 * (field2-field1)/(2*dz)
         force = -mu * deriv
         magAccelZ = force/m
      else
         magAccelZ = 0.
      end if
      RETURN
```

```
      END
      DOUBLE PRECISION function magAccelX(x, z, v, currents)
      DOUBLE PRECISION x, z
      REAL v
      REAL currents(5400)
      DOUBLE PRECISION pi, e, a, mu, m
      PARAMETER (pi = 3.14159265, e = 2.71828183, a = .0015,
     c           mu = 9.274e-24, m = 1.443e-25)
      DOUBLE PRECISION k, deriv, force, magField, field1, field2, dx
      k = (2*pi)/a
      dx = 1e-5
      if ((x.gt.-4) .and. (x.lt.4)) then
         field1 = magField(x-dx, z, v, currents)
         field2 = magField(x+dx, z, v, currents)
         deriv = 1e3 * (field2 - field1)/(2*dx)
         force = - mu * deriv
         magAccelX = force/m
      else
         magAccelX = 0.
      end if
      RETURN
      END
C     +---
C     | Enter magnetic field here
C     +---
      DOUBLE PRECISION FUNCTION magField(x, z, v, currents)
      DOUBLE PRECISION x, z
      REAL v
      REAL currents(5400)
      REAL a
      PARAMETER (a=.0015)
      DOUBLE PRECISION dx, magX, magZ
      REAL cur, c
      magX = v
      magZ = 0
      cur = .136
C      cur = .06
      i = 0
      do dx = -4., 4., a
         c = cur + currents(i)
         i = i+1
         call wire(dx-(a/4.)+x, z,  c, 4., magX, magZ)
         call wire(dx+(a/4.)+x, z, -c, 4., magX, magZ)
      end do
      call wire(x-5., z, -cur, 5., magX, magZ)
      call wire(x+5., z,  cur, 5., magX, magZ)
      magField = sqrt(magX**2 + magZ**2)
      RETURN
      END
C     +----
C     | returns magX, magZ (in Tesla) according to an
C     | additional wire (y=-4mm..4mm) at dx and dz
C     +----
      SUBROUTINE wire(dx, dz, cur, l, magX, magZ)
      DOUBLE PRECISION dx, dz, magX, magZ
      REAL cur, l
      DOUBLE PRECISION mu0, pi
      PARAMETER (pi=3.14159265359)
      DOUBLE PRECISION b, bx, bz, d
      mu0 = 4 * pi * 1e-7
      d = sqrt(dx**2 + dz**2)
      b = (l/d)*(mu0 * cur)/(2.*pi*sqrt(l**2 + d**2)) * 1000.
      bx = -b * dz/d
      bz =  b * dx/d
      magX = magX + bx
      magZ = magZ + bz
      RETURN
      END

cc      DOUBLE PRECISION function magField(x, z, v)
cc      DOUBLE PRECISION x, z
cc      REAL v
cc      DOUBLE PRECISION pi, e, a, mu, m
cc      PARAMETER (pi = 3.14159265, e = 2.71828183, a = .0015,
cc     c           mu = 9.274e-24, m = 1.443e-25)
cc      DOUBLE PRECISION k, field, fieldX, fieldZ
```

```
cc      REAL b0
cc      b0 = 500.
C     convert Gauss to Tesla
cc      b0 = b0/10000.
cc      k = (2*pi)/a
cc      field = b0*e**(-k*z)*(1.+e**(-2.*k*z)*cos(2.*k*x)/3.)
cc      if (v.gt.1e-7) then
cc         fieldX=field*sin(k*x)+v
cc         fieldZ=field*cos(k*x)
cc         field=sqrt(fieldX**2 + fieldZ**2)
cc      end if
cc      magField = field
cc      return
cc      END
      SUBROUTINE randomcurrents(currents, s)
      REAL currents(5400)
      INTEGER i
      do i=0, 5399
         currents(i) = gaussrand(s)
      end do
      RETURN
      END

C     +------
C     | Produces random number with gaussian distribution
C     |  d(x) ~= exp(-.5 * (x/sigma)^2)
C     +------
      REAL function gaussrand(sigma)
      REAL sigma
      REAL pi, e, g
      PARAMETER (pi = 3.14159265, e = 2.71828183, g = 9.81)
      REAL x1, x2, y1, y2
      REAL myrand
      x1 = log(myrand(1.))/.434294481903
      x2 = myrand(2*pi)
      y1 = sqrt(-2. * x1) * cos(x2)
cc      y2 = sqrt(-2. * x1) * sin(x2)
      gaussrand = y1/1.514 * sigma
      RETURN
      END

C     +------
C     | produces random numbers between 0 and max
C     | needs linux /dev/urandom random generator
C     +------
      REAL function myrand(max)
      REAL max
      BYTE r1, r2, r3
      INTEGER int
      REAL RANF
      read (99, 1020) r1, r2, r3
      int = (r1+128)*2**16 + (r2+128)*2**8 + (r3+128)
      myrand = (.0+int)/(2**24) * max
 1020 FORMAT(A1, A1, A1)
c     alternative: use function below:
cc      myrand = max * RANF()
      RETURN
      END
C     +----
C     | true, if m is dividable by n
C     +----
      LOGICAL function mydiv(m, n)
      INTEGER m, n
      if (n.lt.m) then
         if (n.gt.0) then
            mydiv = (m.eq.((m/n)*n))
         else
            mydiv = .TRUE.
         end if
      else
         mydiv = .FALSE.
      end if
      RETURN
      END
C     +---
C     | myAbs
```

```
C     +---
      DOUBLE PRECISION function myAbs(x)
      DOUBLE PRECISION x
      if (x.lt.0) then
         myAbs = -x
      else
         myAbs = x
      end if
      RETURN
      END

C     +-----
C     | random number generator
C     | Source: http://www.physics.unlv.edu/~pang/comp/code211.f
C     +-----
      REAL FUNCTION RANF()
      DATA IA/16807/,IC/2147483647/,IQ/127773/,IR/2836/
      COMMON /CSEED/ ISEED
      IH = ISEED/IQ
      IL = MOD(ISEED,IQ)
      IT = IA*IL-IR*IH
      IF(IT.GT.0) THEN
         ISEED = IT
      ELSE
         ISEED = IC+IT
      END IF
      RANF = ISEED/FLOAT(IC)
      RETURN
      END
```

B.2 Calculating the Ablation Laser Path

The following code for MatLab 7.4.0 (Linux) generates a new list of coordinates which trace a path parallel to a given path. This was used to generate the path the ablation laser must take over a sample. Assume that the x- and y-coordinates of the desired pattern are stored inside two arrays called xpos and ypos, and that d is the distance that the laser center should have to that pattern. Then this code will generate two new arrays nxpos and nypos which give the coordinates of intersections of the parallels of the original pattern at distance d.

```
%   make sure the line is closed
if (xpos(1)~=xpos(end) || ypos(1)~=ypos(end))
    xpos = [xpos, xpos(1)];
    ypos = [ypos, ypos(1)];
end
todelete = [];
if length(xpos) == length(ypos)
%    dx = xpos(2:end)-xpos(1:end-1);
%    dy = ypos(2:end)-ypos(1:end-1);
    dx = [xpos(2:end),xpos(1)]-xpos;
    dy = [ypos(2:end),ypos(1)]-ypos;
% delete identical points
    for n = 1:length(dx)-1
        if (dx(n)==0 && dy(n)==0)
            todelete = [todelete,n];
        end
    end
    dx(todelete)=[];
    dy(todelete)=[];
    xpos(todelete+1)=[];
    ypos(todelete+1)=[];
% calculate the offset-vector
    ndx = dx;
    ndy = dy;
    for n = 1:length(dx)
        ndx(n)=-dy(n)/sqrt(dx(n)^2+dy(n)^2)*d;
        ndy(n)=dx(n)/sqrt(dx(n)^2+dy(n)^2)*d;
```

```
    end
% calculate the interactionpoints
    nxpos = xpos;
    nypos = ypos;
    todelete = [];
    for n=1:length(dx)-2
        A = [dx(n),-dx(n+1);dy(n),-dy(n+1)];
        B = [ndx(n+1)-ndx(n)+xpos(n+1)-xpos(n); ...
             ndy(n+1)-ndy(n)+ypos(n+1)-ypos(n)];
        a1 = (B'/A');
        if ((a1(1)>0 && a1(2)<2) || nocorrection)
            nxpos(n+1) = ndx(n)+xpos(n)+a1(1)*dx(n);
            nypos(n+1) = ndy(n)+ypos(n)+a1(1)*dy(n);
        else
            if (a1(1)<=0)
                A = [dx(n-1),-dx(n+1);dy(n-1),-dy(n+1)];
                B = [ndx(n+1)-ndx(n-1)+xpos(n+1)-xpos(n-1); ...
                     ndy(n+1)-ndy(n-1)+ypos(n+1)-ypos(n-1)];
                a1 = (B'/A');
                nxpos(n+1) = ndx(n+1)+xpos(n+1)+a1(2)*dx(n+1);
                nypos(n+1) = ndy(n+1)+ypos(n+1)+a1(2)*dy(n+1);
                todelete = [todelete, n];
            else
                A = [dx(n),-dx(n+2);dy(n),-dy(n+2)];
                B = [ndx(n+2)-ndx(n)+xpos(n+2)-xpos(n); ...
                     ndy(n+2)-ndy(n)+ypos(n+2)-ypos(n)];
                a1 = (B'/A');
                nxpos(n+1) = ndx(n)+xpos(n)+a1(1)*dx(n);
                nypos(n+1) = ndy(n)+ypos(n)+a1(1)*dy(n);
                todelete = [todelete, n+2];
            end
        end
    end
    nxpos(todelete)=[];
    nypos(todelete)=[];
    A = [dx(end-1),-dx(1);dy(end-1),-dy(1)];
    B = [ndx(1)-ndx(end-1)+xpos(1)-xpos(end-1); ...
         ndy(1)-ndy(end-1)+ypos(1)-ypos(end-1)];
    a1 = (B'/A');
    nxpos(end) = ndx(end-1)+xpos(end-1)+a1(1)*dx(end-1);
    nypos(end) = ndy(end-1)+ypos(end-1)+a1(1)*dy(end-1);
    nxpos(1) = nxpos(end);
    nypos(1) = nypos(end);
end
```

B.3 LabView C Interface Node to Access the Prosilica GigE Camera

The following C code is used to collect the data from the camera and store it in a three dimensional array to be used by the camera control LabView software.

```
/*
 * CIN source file
 */

#include "extcode.h"
#include "PvApi.h"
#include <malloc.h>
#include <stdio.h>
#include <stdlib.h>

/*
 * typedefs
 */
#define ReturnParamNum 4
```

```
typedef struct {
int32 dimSizes[3];
uInt16 Value[1];
} TD1;
typedef TD1 **TD1Hdl;

CIN MgErr CINRun(uInt32 *PvErr, uInt32 *TimeOut, uInt32 *CameraHandle,
                 uInt32 *NumberOfFrames, TD1Hdl ImagesOut);

CIN MgErr CINRun(uInt32 *PvErr, uInt32 *TimeOut, uInt32 *CameraHandle,
                 uInt32 *NumberOfFrames, TD1Hdl ImagesOut) {

MgErr mgErr = noErr;
tPvFrame* MyFrame = (tPvFrame*) calloc(sizeof(tPvFrame), *NumberOfFrames);
tPvHandle MyCamera = (tPvHandle) *CameraHandle;
unsigned long imageSize;
unsigned long imageWidth;
unsigned long imageHeight;
unsigned long MyError;
unsigned long MyTimeout = *TimeOut;
unsigned int errorHappened = 0;
unsigned int i = 0;
unsigned long x, y, f;
uInt16* MyImageBuffer;
char* DummyString=calloc(sizeof(char), 256);
unsigned long DummyUint16;
tPvFrame* DummyFrame;
unsigned int SizePerPixel;
unsigned int MyPvErr = 0;
uInt16* PointerToArrayElement;
int32 WholeArraySize;

MyTimeout = (MyTimeout == 0) ? PVINFINITE : MyTimeout;


if((MyError = PvAttrUint32Get(MyCamera, "TotalBytesPerFrame", &imageSize))>0) {
MyPvErr = MyError+800;
goto returnLabel;
} // getBytesPerFrame

if((MyError = PvAttrUint32Get(MyCamera, "Width", &imageWidth))>0) {
MyPvErr = MyError + 100;
goto returnLabel;
} // get Width

if((MyError = PvAttrUint32Get(MyCamera, "Height", &imageHeight))>0) {
MyPvErr = MyError + 200;
goto returnLabel;
} // get Height

if((MyError = PvAttrEnumGet(MyCamera, "PixelFormat",
                                    DummyString, 256, &DummyUint16))>0) {
MyPvErr = MyError + 300;
goto returnLabel;
} // get PixelFormat
if(!strcmp(DummyString, "Mono16")) {
SizePerPixel=2;
} // if Mono16
if(!strcmp(DummyString, "Mono8")) {
SizePerPixel=1;
} // if Mono8

for(i = 0; i < *NumberOfFrames; i++) {
if((MyFrame[i].ImageBuffer = malloc(imageSize))!= NULL) {
MyFrame[i].ImageBufferSize = imageSize;

if(errorHappened == 0) {
if((MyError=PvCaptureQueueFrame(MyCamera, &MyFrame[i], NULL))>0) {
MyPvErr = MyError + (10+i)*100;
errorHappened = 1;

} // if QueueFrame successful
} // if !errorHappened
} // if calloc successful
} // for i

if (errorHappened==1) goto returnLabel;

DummyFrame = &MyFrame[*NumberOfFrames-1];
```

```
PvCommandRun(MyCamera, "AcquisitionStart");
if(0<(MyError=PvCaptureWaitForFrameDone(MyCamera, DummyFrame, MyTimeout))) {
MyPvErr = MyError + 900;
PvCommandRun(MyCamera, "AcquisitionStop");
goto returnLabel;
}
PvCommandRun(MyCamera, "AcquisitionStop");

// ( *ImagesOut )->dimSizes[ 2 ] = 0; //imageWidth;
// ( *ImagesOut )->dimSizes[ 1 ] = 0; //imageHeight;
// ( *ImagesOut )->dimSizes[ 0 ] = 0; //*NumberOfFrames;

WholeArraySize = imageWidth * imageHeight * (*NumberOfFrames);

if (mgErr > 0) goto returnLabel;
PointerToArrayElement = ( *ImagesOut )->Value;

for(f = 0; f < *NumberOfFrames; f++) {
if (MyFrame[f].Status == ePvErrSuccess) {

MyImageBuffer = (uInt16*) MyFrame[f].ImageBuffer;
for(x = 0; x < imageWidth; x++) {
for(y = 0; y < imageHeight; y++) {
*PointerToArrayElement = MyImageBuffer[y+x*imageHeight];
PointerToArrayElement++;
} // for y
} // for x
} // if MyFrame[f].Status successful
} // fo f


returnLabel:

for (i=0; i<*NumberOfFrames; i++) {
free(MyFrame[i].ImageBuffer);
} // for i
free(MyFrame);

*PvErr = MyPvErr;

return mgErr;
} // CINRun
```

Appendix C

Labview Programs

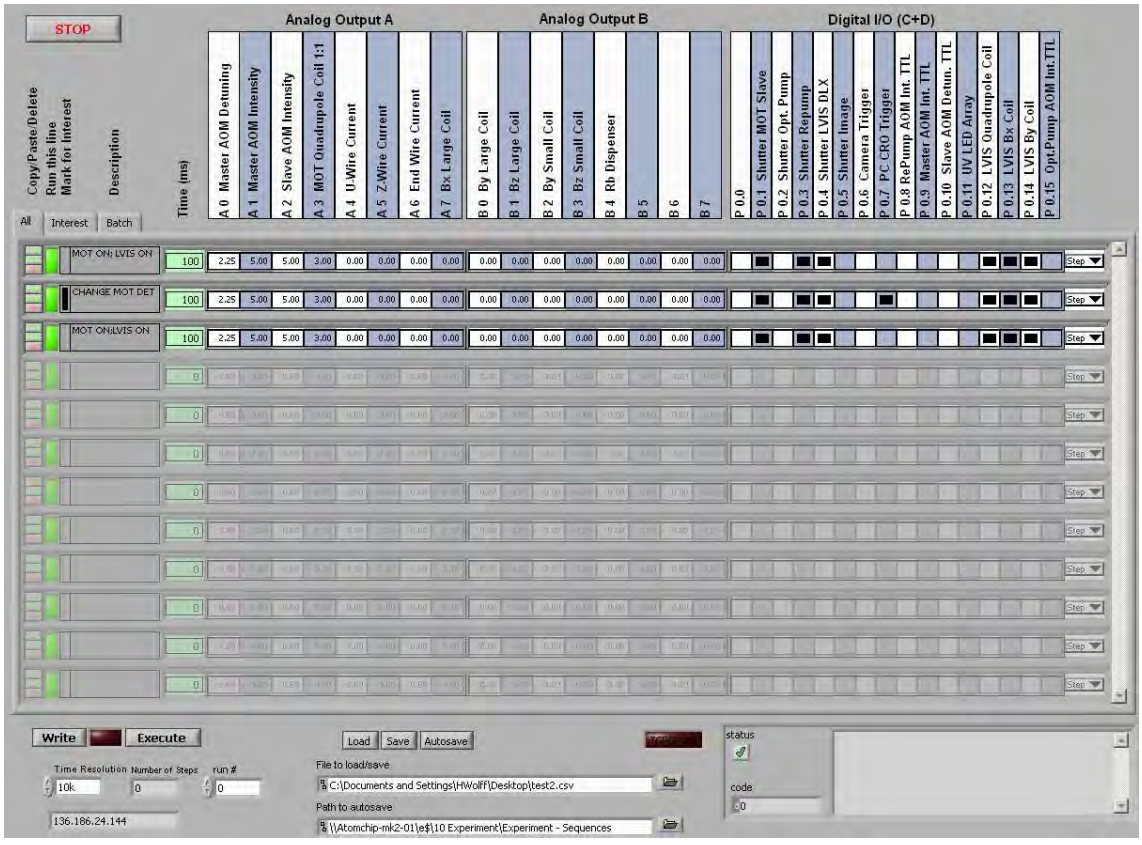

Figure C.1: Frontpanel of the experiment control program.

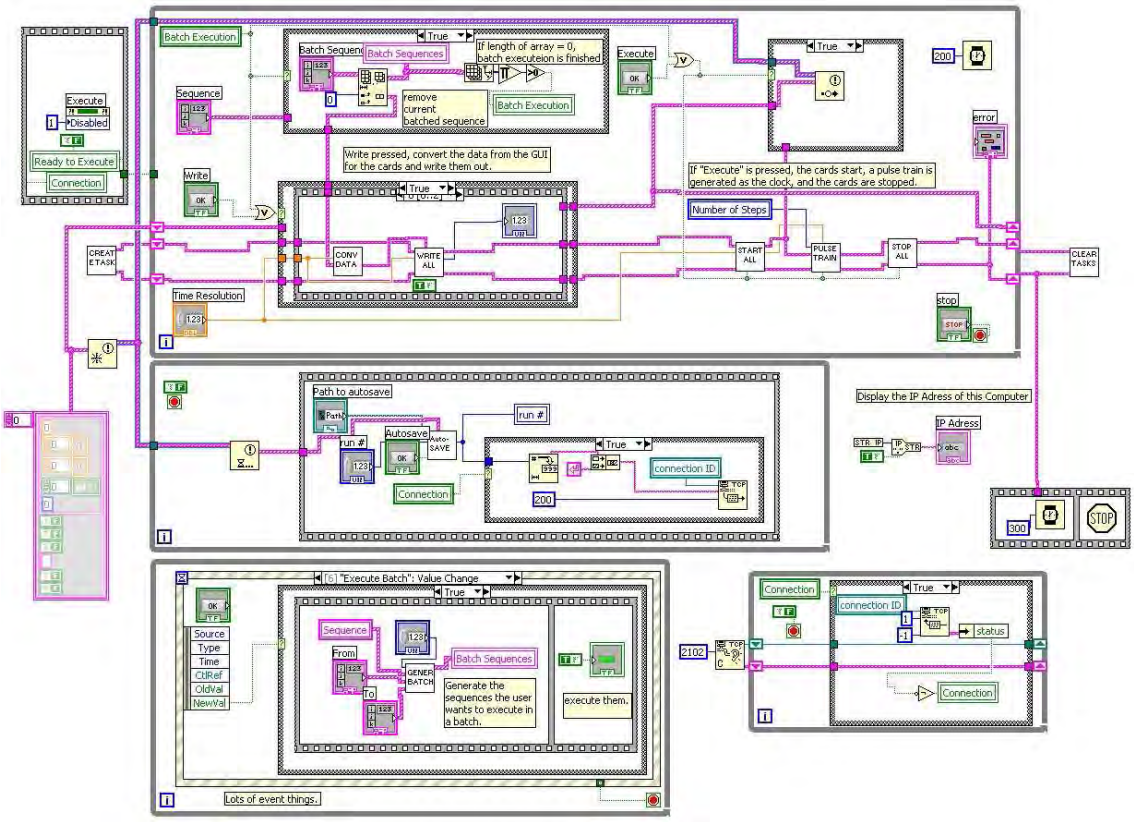

Figure C.2: Diagram panel of the experiment control program.

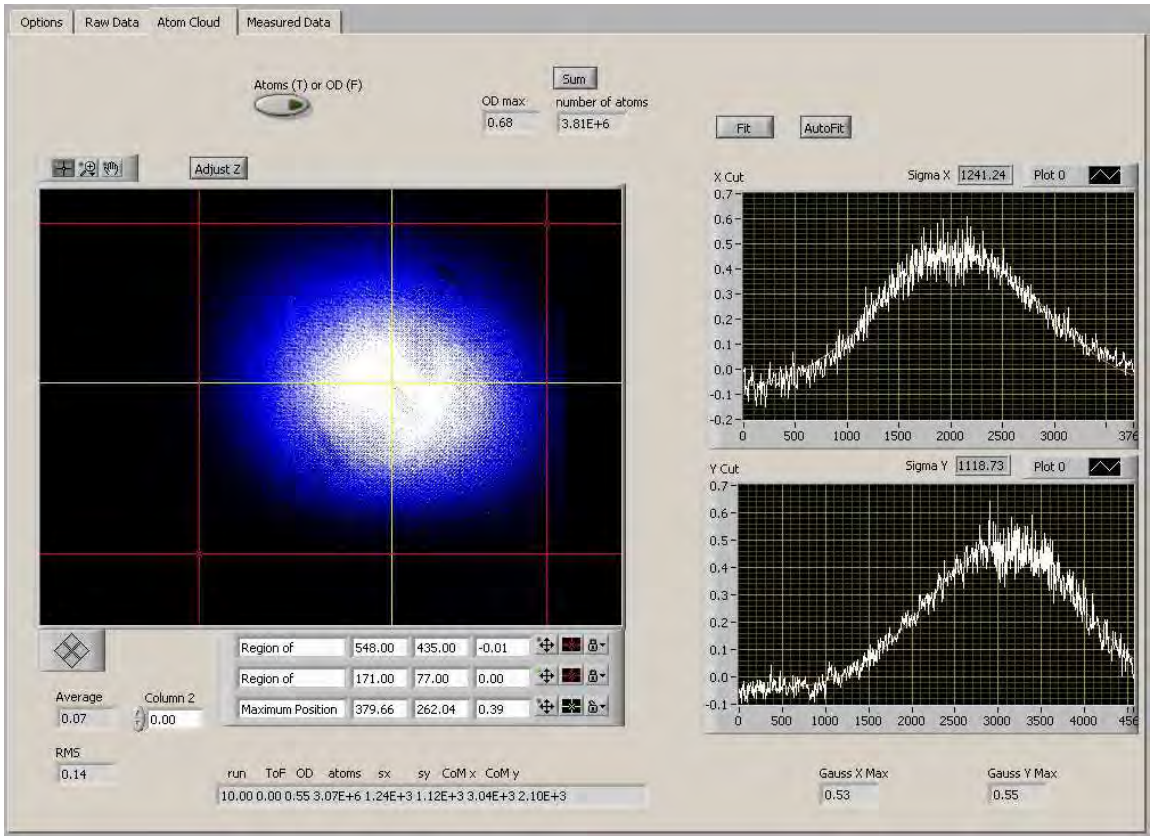

Figure C.3: Frontpanel of the image acquisiton program.

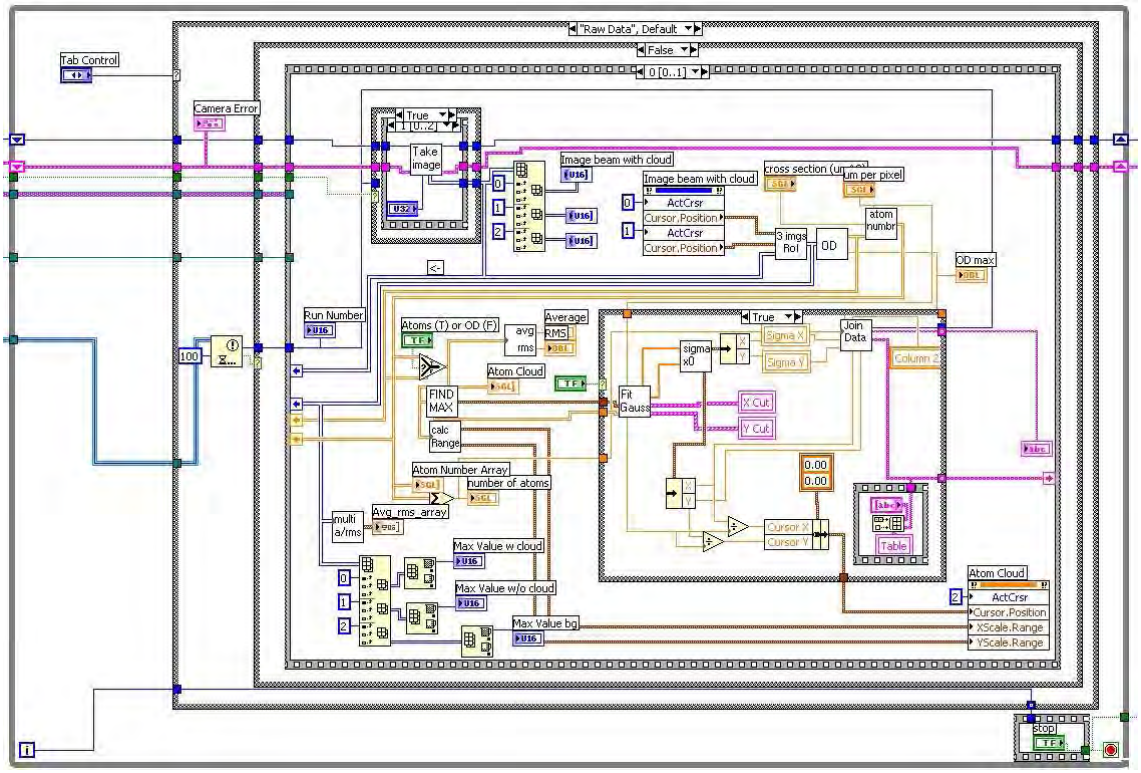

Figure C.4: Diagram panel of the image acquisiton program.

Appendix D

Technical Drawings

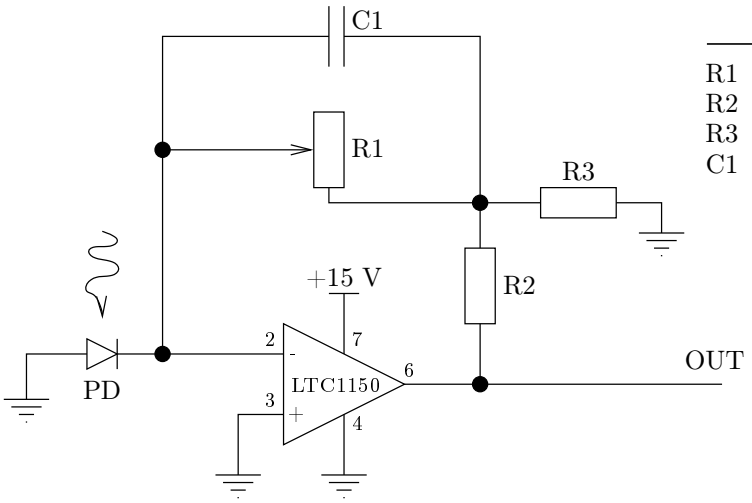

	normal	high gain
R1	1 MΩ pot	1 MΩ pot
R2	10 kΩ	10 kΩ
R3	10 kΩ	10 Ω
C1	15 pF	100 pF

Figure D.1: Diagram of the Photodiode Circuit. Photodiodes used for laser lock and similar tasks, where the intensity of a direct laser is measured, have a lower gain than the high gain photodiodes used for MOT fluorescense measurements. The resistance R1 is a potentiometer to to allow fine tuning of the gain. The total signal at the output calculates to $V = I_p \times R1 \times R2/R3$ (for dc signals), where I_p is the photocurrent (ca. 0.5 A per Watt for silicon photodiodes).

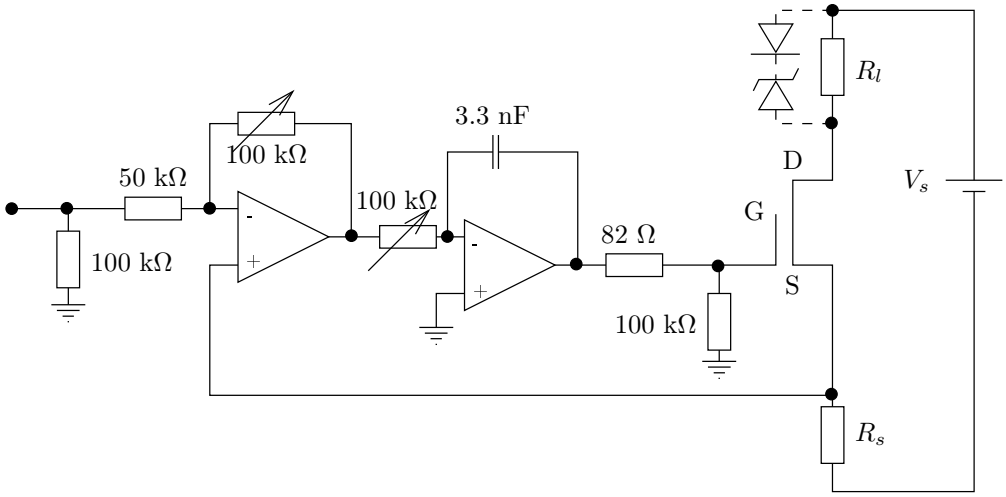

Figure D.2: Diagram of the FET driver circuit. These devices are used to computer control an electric current through setting an analogoue output voltage. The current circuit is shown on the right side of the diagram: From a power supply it passes through the load R_l (for example a coil or a wire on the atom chip), and then into a field-effect transistor (FET). Between the negative output of the power source and the FET, a sense resistor R_s. The electronics tries to equalise the voltage before the R_s (which for a fixed R_s is proportional to the current) and the voltage setting. If the load has a large inductance, it is advisable to implement a Zener diode setting parallel to the load so that the excessive voltages produced by the inductance upon rapid switching do not harm the FET.

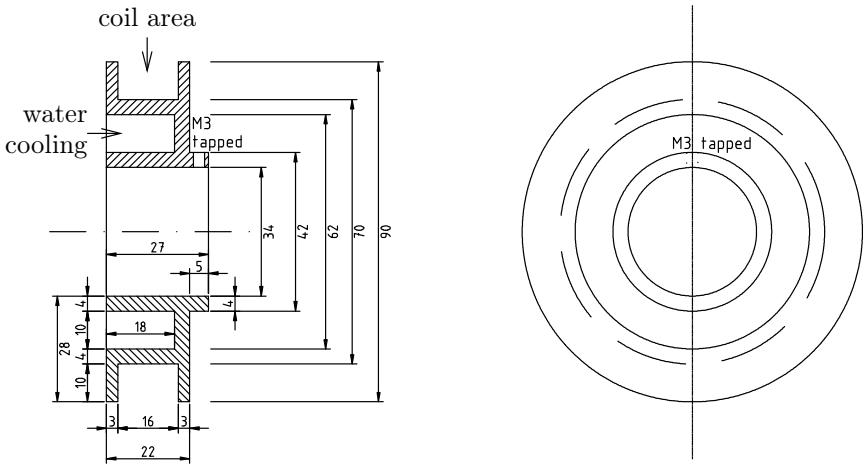

Figure D.3: The coils which generate the quadrupole field for the MOT in the top chamber had several constraints: They could not have a diameter larger than 90 mm, while having to be spaced at least 126 mm apart, which is much more than the optimum Anti-Helmholtz configuration, where the spacing is $\frac{3}{4}$ of the diameter. To get a similar gradient, a much higher current has to be used, resulting in higher power dissipation. This was conpensated by water cooling. The water cooling channel is located inside the coil mount, as can be seen in the figure, and was closed of by welding a circular plate with attached water in- and outlets (not shown).